Developing Nucleic Acid-Based Tool For Precision Medicine

by

Ricky Whitener

A dissertation submitted to the Graduate Faculty of
Auburn University
in partial fulfillment of the
requirements for the Degree of
Doctor of Philosophy

Auburn, Alabama
August 3, 2019

Keywords: Aptamer, bionanocarrier, drug delivery, nanotechnology

Approved by

Dr. Mark Byrne, Co-chair, Professor
Dr. Jacek Wower, Co-chair, Professor
Dr. Allan David, committee member, John W. Brown Associate Professor
Dr. Elizabeth Lipke, committee member, Mary and John H. Sanders Associate Professor
Dr. Robert Chambers, committee member, Professor

Abstract

Nucleic acid aptamers are new therapeutic tools that are growing in use in the bionanotechnology field. Understanding their behavior and engineering their structure is desirable for many applications due to unique advantages over antibodies and other current therapeutic methods. In this work, aptamer platforms compatible with hydrogels were designed and aptamers were explored as targeting and drug delivery molecules attached to the surface of gold nanoparticles and by utilizing a quartz crystal microbalance. **We have shown that DNA structure and stability, which dictates function, can be engineered and maintained for multiple platforms and therapeutic purposes.**

The tear fluid in a human eye only contains one type of RNase, molecules that degrade RNA strands. Furthermore, this molecule, RNase 4, is known to only cut after the nucleotide Uracil. By designing a nucleic acid platform consisting of both a DNA anchor strand capable of binding to a hydrogel and RNA that can modified to regulate cut sites and additionally act as a drug, we were able to create a triggered release mechanism for aptamers within a hydrogel to release into the eye. This platform was made so that it is versatile and adaptable to a range of aptamers and other ligands. **Results show that we can form a homogenous sample of our nucleic acid platform that maintains a structure capable of controlled release of aptamers from hydrogels into the eye for treatment of ocular diseases.**

A Quartz crystal microbalance with dissipation was used to characterize and optimize DNA behavior and binding to a gold surface in real time and with high sensitivity. In this work, it is desired to maximize drug loading onto a nanoparticle. Since the drug is binding to double

stranded DNA in our system, this means it is essential to understand how to bind the most amount of double stranded DNA possible and maintain a DNA structure that has high affinity towards binding the drug. Dissipation monitoring tracked how flexible or rigid the DNA behaved when bound to the gold sensor, which in turn was used to determine if a highly dense surface is affecting DNA structure in a significant manner that will reduce drug binding affinity. The real time binding is based on traceable changes in frequency and was used to determine salt and DNA concentrations that maximize binding of double stranded DNA to the gold surface. If too much anchor DNA was bound, the surface area available decreased, which resulted in a decrease in the formation of double stranded DNA. Therefore, higher amounts of salt and increased DNA concentration are not always going to produce more double stranded complexes on the gold surface. **Results indicate that different amounts of drug binding can be created by adjusting DNA and salt concentrations, while agreeing with similar experiments for DNA conjugation to gold nanoparticles, and dissipation data strongly indicates monolayer formation and behavior.**

DNA strands can also be used as drug delivery vehicles themselves. We designed a spherical DNA particle with potential for high drug loading and targeting capabilities. Modifications to DNA strands allow binding to the surfaces of many molecules, and in our case, gold nanoparticles. We used 15nm gold nanoparticles to bind approximately 101 nucleic acid strands vial Thiol chemistry. These strands can be a mixture of both drug delivery vehicles and targeting moieties. By combining research on optimizing nucleic acid intercalation of the cancer drug daunomycin with recently developed double stranded gold nanoparticles optimized with maximum DNA loading, we have engineered a therapeutic platform for treatment of cancer cells.

Results are promising towards the goal of creating a new therapeutic tool for treating various types of cancers.

Abbreviation List

A	Absorbance
AGC	Efficient nucleotide sequence for binding Daunomycin
ANC	Non-thiolated anchor DNA
ANC-ANC	Thiolated anchor DNA interactions with itself
ANC-SH	Thiolated anchor DNA
APT	Aptamer
A/T	DNA base pair Adenine with Thymine
AT cut	Crystal blank cut 35^0 25' to the z axis
ATP	Adenosine triphosphate
AuNps	Gold nanoparticles
AuNP-ANC	Gold nanoparticles conjugated with thiolated anchor DNA
AuNP-AuNP	Gold nanoparticle interactions with itself
BioSS	Biological surface science
bp	base pair
BSA	Bovine serum albumin
C	Concentration
CO_2	Carbon dioxide gas
C.S.	Cell suspension
CT	Cholera toxin
D_n	Dissipation
dcs	Dilute cell suspension
DDT	1-dodecanethiol

DLS	Dynamic light scattering
DMA	Dimethylacrylate
DNA	Deoxyribonucleic acid
DNA-AuNP	One of four engineered sequences hybridized to AuNP-ANC
DNA-DNA	Deoxyribonucleic acid interactions with itself
DNase	Deoxyribonuclease
dNTPs	Deoxynucleotide Triphosphates
dsDNA	Double stranded deoxyribonucleic acid
DTT	Dithiothreitol
ε	Extinction coefficient
E_{lost}	Energy lost
E_{stored}	Energy stored
EDC	1-Ethyl-3-(3-dimethylaminopropyl)-carbodiimide
EDTA	Ethylenediaminetetraacetic acid
EGFR	Epidermal growth factor receptor
ELISA	Enzyme-linked immunosorbent assay
EMEM	Eagle's minimum essential medium
EPR	Enhanced permeability and retention
Δf	Frequency change
f_n	Resonance frequency
Fab	Fragment antigen binding
Fc	Fragment crystallizable
ΔG	Gibbs free energy

G-25	Gel type 25 filtration size
G/C	DNA base pair Guanine with Cytosine
h	Hour
H52	52bp DNA sequence with complementary nucleotides to anchor DNA
HA	Hemagglutinin
HEMA	2-Hydroxyethyl methacrylate
HMPP	2-Hydroxy-2-methylpropiophenone
Hz	Hertz
IPA	Isopropanol
J52	52bp DNA sequence with complementary nucleotides to anchor DNA
J52-AuNP	Drug loaded AuNP-ANC hybridized with *J52*
J52H	Klenow reaction on ANC-SH + J52
K_d	Dissociation constant
L	Concentration of free Daunomycin
L52	52bp DNA sequence with complementary nucleotides to anchor DNA
L_p	Path length
LOD	Limit of detection
M	Molar concentration
Δm	Change in mass bound
M52	52bp DNA sequence with complementary nucleotides to anchor DNA
MAb	Monoclonal antibody
MβCD	Methyl-Beta-Cyclodextrin
MHL	6-mer- capto-1-hexanol

min	Minute
MIPs	Molecularly imprinted polymers
mL	Milliliter
mM	Millimolar concentration
mm	Millimeter
MUA	11-mercapto-undecanoic acid
MW	Molecular weight
n	Overtone number
n	Hill coefficient
NaCl	Sodium chloride
NAP-5	Sephadex G-25 grade column for a sample volume of 0.5mL
NAP-10	Sephadex G-25 grade column for a sample volume of 1mL
NGS	Next generation sequencing
NHS	N-hydroxysuccinimide
nm	Nanometer
ng	Nanogram
nt	Nucleotide
NTP	Nucleoside triphosphate
θ	Fraction of DNA that bound Daunomycin
^{o}C	Degrees Celsius
OEG	Oligoethylene glycol
PBS	Phosphate buffered saline
PCP	Cytidine 3', 5' bis(phosphate)

PEG	Poly(ethylene glycol)
polyT	Series of Thymine's
pM	Picomolar
PNK	Polynucleotide kinase
QCM	Quartz crystal microbalance
QCM-D	Quartz crystal microbalance & dissipation
REVS	Rupture event scanning
RES	Reticuloendothelial system
RH_2O	RNase free water
RNase	Ribonuclease
rpm	Rotations per minute
s	Seconds
SAMs	Self-assembled monolayers
SDS	Sodium dodecyl sulfate
SELEX	Systematic evolution of ligands by exponential enrichment
SPR	Surface plasmon resonance
ss	Single stranded
ssDNA	Single stranded deoxyribonucleic acid
TE	Tris-EDTA
TEM	Transmission Electron Microscopy
Γ_n	Bandwidth of crystal
U	Enzyme catalytic activity conversion of one μmole of substrate per minute
μL	microliter

μM	micromolar concentration
UV	Ultraviolet
XTT	Tetrazolium salt

Table of Contents

Acknowledgments

This research was funded by the US Department of Education GAANN Graduate Fellowship Program in Biological & Pharmaceutical Engineering Award No. P200A120244.. Additional partial funding was provided by a grant from the Auburn University Research Initiative in Cancer.

I would like to thank both Dr. Mark Byrne and Dr. Jacek Wower for their continual support and guidance throughout the course of this research as well as my graduate studies and life pursuits. I would like to thank my committee members, Dr. Allan David, Dr. Elizabeth Lipke, and Dr. Robert Chambers, for their knowledge and timely assistance in the critical review and preparation of this manuscript. I would also like to thank Jessica Kelly, Liana Wuchte, Stephen DiPasquale, Laura Osorno, Robert Mosley, Sarah Lino, Alex Kelly, Alan Hanley, Prachi Sangle, Richard Cullum, Dr. Tareq Anani, Dr. Barry Yeh, Dr. Xin Fan, and Dr. Iwona Wower for their assistance and invaluable support with many aspects of this work. Personal gratitude is also extended to Dr. Mario Eden, for his guidance and support unrelated to research.

I would like to thank Allan David in the department of Chemical Engineering in the Samuel Ginn College of Engineering at Auburn University for use of the ZetaSizer Nano for nanoparticle diameter analysis and access to cell culture room. I would like to thank James Gillespie in the College of Veterinary Medicine at Auburn University for training in cell culture passaging. A final thanks goes to Sevgi Kucuktas in the Radiation Safety program at Auburn University for her guidance in the handling of radioactivity and use of the scintillation counter for aspects of this work.

List of Tables

List of Figures

Chapter 1: Introduction and Motivation

Nucleic acids are currently underutilized as therapeutic and/or targeting agents. It is important for more researchers to focus on studying the properties and capabilities of these molecules because of their cheap production costs and batch uniformity making them readily available. It is believed by many in the field that nucleic acids have the potential to surpass antibodies and other targeting molecules, as well as behave as a smart drugs compared to current therapeutics. Explanations and demonstrations for how this is possible are covered throughout the entirety of this dissertation. As technology continues to advance, more opportunities for nucleic acids continue to rise. This is due to the fact that nucleic acid technology is a relatively new field that was limited due to lack of capabilities for replication because of primers influence on structure in the past. It is my hope that after reading this dissertation, further awareness for nucleic acid development, functions, and properties will be created, and willingness to learn more and excitement about their potential will be conjured.

This dissertation is categorized into five main sections, which are separated into chapters. Chapter 2 involves identifying challenges with current nucleic acid aptamer development and application progression as an innovative therapeutic molecule. Chapter 3 involves engineering of nucleic acid strands to assemble a platform tailored for controlled release of an aptamer acting as a therapeutic through a contact lens. Chapter 4 focuses on methods of use for quartz crystal microbalance (QCM) in biosensing and biological surface science applications. The second part of chapter 4 describes preliminary QCM tests that will aid with characterizing behavior of nucleic acid binding

to gold nanoparticles. Chapter 5 describes the use of gold nanoparticles conjugated with DNA to deliver the chemotherapeutic drug Daunomycin to MCF-7 breast cancer cells, while analyzing the mechanism of entry into the cells. It further highlights the behavior of nucleic acids based on sequence and the impact this has on drug binding and affinity. Finally, Chapter 6 summarizes the main findings from each chapter and connects each into a conclusive story that explains how engineering nucleic acid strands can be used for platform assembly, controlled drug release, and targeting

Chapter 2: Aptamers as an Innovative Therapeutic Molecule

Aptamers, shown in Figure 2.1 [1], are molecules that can specifically bind and recognize a target molecule, the most common being nucleic acid or peptide based. There are many advantages to using aptamers as a therapeutic tool compared to other molecules such as antibodies. Aptamers can be synthesized without batch variation and stored at room temperature. Since they are made of natural materials found in the body, particularly DNA based aptamers, and due to their small size and low molecular weight, they do not trigger an immune response. Aptamers can be made in vitro, in a highly controlled environment; therefore selection conditions such as temperature, pH, buffer, etc. can be manipulated. [2].

In addition to the advantages in aptamer production, there are also many advantages in the functionality of aptamers compared to other tools, such as antibodies. Aptamers can be labeled without affecting their binding affinity. Furthermore, by making slight changes in the aptamer sequence, the binding affinity becomes adjustable. Aptamers cannot only bind with drugs, but they can also bind with toxic substances and cells [2]. One of the biggest advantages of aptamers is that many aptamers can be made for a single target, which can be used to increase the specificity of a targeting delivery system. Also, they are able to distinguish between different conformations of target proteins. These production and functional advantages of aptamers are unobtainable to the same degree or not even possible for antibodies.

2.1 Development of the Aptamer Concept and Applications

A riboswitch is a naturally occurring, nucleic acid based genetic regulatory element. When these nucleic acid ligands are engineered to selectively bind to amino acids, drugs, proteins, or other molecules, they are known as aptamers [3]. Over the past decade, the popularity of aptamers has grown enormously. With this increasing attention, the number of unique aptamers and their applications has flourished. What began as a therapeutic agent has begun to enter bioanalytical applications, diagnostics, and in many cases has replaced antibodies [4].

As increasingly efficient methods for the synthesis and selection of aptamers develop, so do the variety of applications. Analytical, aptamer-based formats have been progressively exploited for use in enzyme-linked oligonucleotide assays [5], aptazymes [6], and even in the field of separation science [7]. Additionally, the use of aptamers as biocomponents in biosensors has grown into its own field of study called aptasensors [8].

In 1996, Drolet et al. published one of the first papers regarding the use of a reporter-linked aptamer assay (RLAA) to detect vesicular endothelial growth factor (VEGF) in serum. This paper revealed the potential of aptamers used as replacements for standard targeting moieties [9]. These targeting moieties, including antibodies, peptides, transferrin, and folate, each contain their own flaws [10,11]. In contrast, the uniqueness and tunability of aptamers can be harnessed through the ever-improving systematic evolution of ligands by exponential enrichment (SELEX) method. Table 2.1 lists several advantages of aptamers over antibodies. A distinct advantage of aptamers is due to their small size and their ability to be synthesized without batch variation. They are able to

bind with drugs and toxic substances [12], while the affinity of the aptamers toward their target and the selection conditions (e.g., temperature, pH, buffer, etc.) can be easily modulated [2]. Furthermore, aptamers can be labeled without having their affinity affected [13], be produced in vitro, and be stored and transported at room temperature [4].

2.1.1 Aptamer Development Through SELEX

Aptamers are produced through a process known as systematic evolution of ligands by exponential enrichment (SELEX) [14]. A schematic illustration of SELEX highlighting each step in aptamer development is shown in Figure 2.2. Similar to other selective methods used for proteins, aptamers are selected from a large library according to their specificity and binding affinity to a desired target. One major advantage of this approach is that aptamers can be developed without requiring any biological knowledge pertaining to the target molecule [15]. The SELEX process begins with the chemical synthesis of a large single stranded (ss) DNA or RNA library. The 5' and 3' ends, usually between 16-20 nucleotides (nts) long, are specific nt sequences designed for binding to primers, which will allow for amplification of desired aptamer strands. The middle portion of the ssDNA or ssRNA consists of a variable region, usually between 30-40 ntslong, containing an automated random placement of nucleotide's to produce the significant difference between each library strand.

The sslibrary is then introduced to the same environment as the desired target molecule. For example, cell-SELEX puts the sslibrary in contact with a particular cell culture [16]. After a certain incubation period, usually around 20 minutes to 1 hour, the

entire solution is washed. Unbound ssDNA or ssRNA are removed and discarded after the wash step. The bound strands, which remain after the wash steps, are eluted and amplified by PCR. The remaining strands are reintroduced to the same environment and the process is repeated. Each time the cycle is repeated the stringency of the wash is increased to continually collect the ssDNA or ssRNA samples that have a higher affinity towards the target. A typical SELEX procedure involves between 10-25 cycles. After the final cycle is completed, the selected aptamer strands undergo a cloning and sequencing process to determine the sequence of the variable region.

The amplification of each strand requires PCR. This means the ends of each strand must be predetermined sequences known not to interact with one another in order to bind readily to primers. Theoretically, the end regions of each strand should not be the functional region of an aptamer strand because the same primer sequences are found in every strand in the initial library. In reality, these primer regions can bind to the variable region, resulting in them influencing and limiting the structures that the aptamer can form. For example, the formation of a *lollipop* structure (where the two ends of a strand bind to each other creating a loop and stem) can be severely limited when the nt's at the ends of each individual strand are designed to reduce intramolecular binding. Such a hindrance would reduce the likelihood of this particular structure forming.

To further improve the specificity of selected aptamers during the SELEX process, additional steps can be incorporated into the original protocol. A counter-selection step can be introduced to the aptamer pool to protect against nonspecific binding of undesirable targets. The usefulness of this feature is particularly recognized during the selection of aptamers for cancer cells. SELEX can be used to generate

aptamers with specific targeting toward a cancer cell line while counter-selecting aptamers that do not recognize normal cells of the same type. Adding a counter-selection step to the SELEX protocol can greatly improve the specificity of aptamers [17]. However, it also highlights a major flaw in the development of aptamers using the standard SELEX process.

2.1.2 Challenges with SELEX Progression

The main challenge with the SELEX process is that the procedure is performed completely in vitro. Unlike antibodies, which are produced in vivo and are designed to only recognize one target molecule, aptamers are developed outside of the body and tested only against certain molecules under specific lab conditions that could drastically vary from an in vivo environment. An aptamer developed by the SELEX process is capable of targeting and binding to a desired target, even as a sensor by using fluorescence for detection (Figure 2.3A), but there is no evidence shown thus far to confirm that the aptamer will not bind to other, untested targets. Aptamers produced by the SELEX process cannot be considered truly specific towards their desired target unless they are counter selected against every possible cell line and molecule present in the body under the same conditions found in vivo. However, such a process is unrealistic, and more pragmatic improvements must be considered.

Adjustments can be made to the SELEX process in order to overcome some of the flaws from an in vitro based protocol. One major challenge of aptamers, particularly RNA based molecules, is their susceptibility towards degradation in vivo. RNA molecules are known to have a short half-life in the body, averaging minutes to hours

[18]. This rapid clearance is due to a number of factors: instability of the molecule, nucleases and other degradation factors, small size, and aggregation due to binding of other molecules. The small size and relative accessibility of aptamers attracts a multitude of factors able to recognize them and break them down [19]. In order to combat these challenges a variety of techniques have been developed to mitigate the impact of each.

Aptamer instability can be improved through methods such as caps on the 5' and 3' ends [20]. This method includes the well-known and reliable practice of pegylation, already shown to increase the half-life of nucleic acids [21]. Other approaches have utilized cholesterol to achieve the same effect [22]. Incorporating modified nucleotides can also stabilize the aptamer and protect it from degradation factors [23]. Figure 2.3B shows an aptamer known as Pegaptanib, currently the only approved aptamer on the market, containing pegylation on its 5' and modified nucleotides combined in order to maintain stability *in vivo*. The mechanism of action of nucleases depends on sequence specific recognition. By modifying certain nucleotides, specific nucleases are no longer able to recognize and degrade these molecules. Other methods for preventing degradation of aptamers by nucleases include the use of locked nucleic acids (LNA) and spiegelmers [24].

These issues can be tackled directly and implemented into the SELEX process. Once a small set of aptamers have been selected, these aptamers can be incorporated with a desired modification to increase their viability in vivo. These modified aptamers will need to again be tested in vitro to ensure the modifications have not affected the functionality. Fortunately, modifications have not been shown to affect aptamer behavior [13]. The addition of these modifications, however, can introduce a new challenge to the

use of aptamers in vivo: an immunological response. Aptamers made from DNA and RNA are believed to not elicit an immune response. Experiments in literature have shown this to be the case [10]. Once modifications are introduced to an aptamer, the biological response to them could change as well. Particularly, degraded products may have the potential to elicit an immune response [18]. This will require further studies before such modified aptamers can be implemented into a human patient.

Another problem with aptamer delivery in vivo is their short half-life due to renal clearance. The generally small size of aptamers and the efficiency of the body's urinary system typically results in the renal clearance of aptamers within minutes to hours [25]. Several modifications to aptamers are currently being employed to encourage longer aptamer residence times in the body. The total length of a strand can be increased [26], the aptamers can be conjugated to larger particles such as nanoparticles [27], encapsulated in liposomes or other lipid based carriers [28], or bound to other molecules to increase the molecular weight and improve stabilization such as PEG [29]. Increasing the size of the aptamer complex too much, however, may elicit an unanticipated immune response.

These new aptamer based platforms need to be re-tested in vitro to confirm if their functionality remains. This coincides with the issue of binding affinity and specificity. During the SELEX process, if there are small amounts of aptamers selected due to either low specificity towards the target molecule or unacceptable binding affinity, then unnatural bases can be incorporated into the SELEX library. Unnatural bases allow for the creation of entire new libraries for the production of aptamers in the SELEX process.

More options will allow for selection of better aptamers that have increased specificity and show a higher binding affinity towards the desired target molecule [30].

Another weakness of the SELEX process is the bias that can occur due to the amplification of the aptamers using PCR. This approach introduces limitations on the structures that the aptamers can form as well as the size of an aptamer. A new method for improving this flaw in SELEX uses nuclease sequences attached by ligation for amplification of selected aptamers [31]. This approach works by introducing the primer binding sequences to the aptamers after they have already been selected for a particular target. These sequences are able to bind to the aptamers due to a specific nuclease sequence, which can recognize the ends of the aptamer strands extended by ligation. At this point, PCR can occur as it normally would. After amplification, restriction endonucleases are introduced into the selected aptamer environment to cut a designated sequence and effectively remove the primer binding regions. These regions can then be easily removed from the solution.

The variable region of nucleotides presents another potential bias in the current SELEX method. The structures of nucleic acid strands that form in the initial nucleotide library naturally favor less complex structures that require lower amounts of energy to produce. Therefore, the high flexibility and structural diversity of nucleic acid structures are limited from the beginning. In order to obtain a more diverse range of structures, the variable region of each initial strand can be adjusted to include specific nucleotides at predetermined locations, which will aide in the development of aptamers with more complex structures, including three way junctions and quadruplexes [32]. The abundance of new three-dimensional structures in the initial SELEX library, combined with reduced

structure limitations due to the primer binding sequences, will result in a more diverse aptamer pool. This carries potential for improved specificity and binding affinity over aptamers currently in development.

Some final factors to consider are the potential loss of aptamers during the amplification process and the build-up of artifacts with increasing SELEX cycles. The rate of replication of a DNA strand will vary depending on the structure of the strand [33]. If a DNA strand contains a quadraplex, for instance, the rate at which the DNA polymerase can replicate this particular sequence will be slower than a DNA strand with a less complex structure. When nucleic acid strands are recovered from their target molecule, each strand will not be amplified to the same degree, due to the formation of three-dimensional structures. This can result in the loss of potential highly functional aptamer candidates. This effect is exacerbated with RNA aptamers because they hold the potential to undergo even more complex structures. This can result in a reverse transcription process that will show greater favoritism towards amplifying DNA strands whose RNA templates have less complex constructs. As the number of cycles increases, this phenomenon will continue to have an impact on each set of nucleic acid strands in the library for the next round of SELEX. Additionally, artifacts such as degraded materials can begin to build-up in the nucleic acid library. One way to account for this phenomenon and reduce these effects by reducing the number of cycles is by using next-generation sequencing (NGS) [34]. After two rounds of SELEX are performed, NGS can be used to analyze and compare the sequences between the two sets of samples and use them as indicators for determining which specific sequences within each strand are essential for functionality of an aptamer. At this point NGS can be used to determine

which nucleic acid strands and motif regions are likely producing functional aptamers. Therefore, the number of different strands in the library can be vastly reduced. After a few subsequent rounds, a highly functional aptamer (or set of aptamers) can be determined.

Due to time constraints, resources, and costs, in vitro SELEX cannot be used to determine if a developed aptamer is truly specific towards one particular cell line. As previously mentioned, counter-SELEX can be used to demonstrate that a selected aptamer is not able to recognize and bind to other undesired regions of an organism, such as the heart or liver. These tests are imperative to improve confidence in aptamer specificity, but they are not able to validate that the chosen aptamer will not target untested cell lines. In vivo SELEX is the best option to mitigate this problem. In Vivo SELEX involves introduction of the initial library of DNA or RNA strands to an organism directly and identifying the location of each strand using detection techniques such as fluorescence or radioactivity [35]. The desired cell line can be collected, and the library strands extracted from the cells. The strands are amplified and the process is repeated on a new organism for several rounds until a series of aptamers are identified that are specifically shown in vivo to bind to a specific cell line while not being located anywhere else in the organism. By the end of the in vivo SELEX process, a series of aptamers should be identified that have been proven to only bind to the desired target cell line in an organism.

This method sounds ideal compared to in vitro SELEX processes; however, there are several limitations to this approach. First, in vivo SELEX is currently limited to targeting cell lines that are well studied. This takes away one of the major advantages of

aptamers in that they can be created without needing to know any physiological characteristics, markers, or other proteins expressed in the desired cell line. In vivo SELEX still does not require knowledge of the binding site for the aptamer, but the growth conditions of the particular target cell type within the organism needs to be understood. The target cell line for in vivo SELEX must also be non-metastatic. This is necessary because during the procedure DNA or RNA strands will be present throughout the entire organism and the specific location of the cell line needs to be known in order to capture the aptamer strands for amplification. Since the aptamers specific to the cell line have not yet been determined, the labeled aptamers in vivo allow only for detection of the aptamers, not the particular cell line. For this reason, the exact location of the target cell line needs to be known.

The quality of the final aptamers produced in in vivo SELEX can also come into question. In the case of in vitro SELEX, the stringency of each round can be increased, giving control of the affinity of the final aptamers identified. In addition, every aptamer in the initial library is exposed to the target cell line. During in vivo SELEX, it is possible that the best aptamers for targeting a specific cell line are never placed in contact with the desired site. Furthermore, the final selected aptamers cannot be improved upon by controlling the conditions for binding as readily as in vitro, so the aptamers may have a lower affinity for the target cell line then aptamers found from in vitro methods. In Vivo SELEX is a promising method for validating the specificity of aptamers towards a particular cell line [36]. However, it is restricted by the type of cell lines it can target and the varying affinity it can produce. Due to these restrictions, it may not be suitable for application in all instances.

Once the final product of aptamers have been produced from SELEX and any desired modifications have been introduced to the nucleic acid strands, the aptamers are ready for use in experimentation. However, there is one final problem to address with the developed aptamers. Very few aptamers move onto clinical studies after the SELEX process, owing to a loss of targeting efficiency. The most likely cause for this issue involves the flexibility of the three dimensional structure of each aptamer strand. When an aptamer is identified through SELEX its structure is unknown. Experimentation and computer models can be combined to determine the structure of an aptamer, but usually more than one three dimensional structure will exist for each aptamer depending on environmental factors. Even purified aptamer strands will still contain a heterogeneous mixture of different three dimensional aptamer structures.

It is possible to determine which structure is desired for functionality by analyzing the aptamer strands from experimental results. However, if the correct structure is one of the lesser thermodynamically favorable constructs, then the percent yield will be very low during purification. Furthermore, even if the correct structure is one of the more thermodynamically favorable constructs, the aptamer structures are fluid and the purified strands will have some of their shapes switch to one of the lesser favored structures. As these aptamer strands transport towards their designated site in vivo, they will come across various proteins and salt conditions that will change their structure. At the desired in vivo site for aptamer interaction, the environmental conditions will need to be favorable for the correct structure to form. This is certainly possible, but the ever-changing conditions surrounding a cell must be considered.

In order to address this issue, there needs to be a greater understanding on the fundamental principles of intramolecular interactions within nucleic acid strands. There are certain structures that are known to form with nucleic acid strands that are so stable, they appear to be locked in that position. One example for DNA is G-quadruplexes [37], and an example for RNA would be tRNA [38]. Using the knowledge of structure formation of these highly stable constructs, it may one day be possible to design sequences that will fold in similar structures that will also be highly stable. Another potential solution is using specific nucleic acid modifications. New bases have been designed and these may have the potential to create structures that are either locked or at least much more thermodynamically favorable than without the presence of these new bases [39]. tRNA is one example of a highly stable structure that uses unorthodox bases in its sequence. LNA has also been shown to successfully create structured nucleic acid strands with higher stability [31]. By analyzing these two methods, perhaps it is possible to design aptamer sequences that will produce constructs with much higher stability.

2.2 Aptamer Functionality with Nanocarrier Applications

Successfully produced aptamers have been incorporated into platforms in order increase their efficacy, improve half-life, and increase resistance towards degradation in vivo. This incorporation has the potential to change the confirmation of the aptamer and affect their functionality in the process. There are three main mechanisms for incorporating aptamers into a platform: Attachment of other nucleic acids, encapsulation into “soft” nanoparticles, and binding onto the surface of “hard” nanoparticles. The first mechanism allows for the creation of “smart” aptamers that are self-guiding towards

specific organelles within a cell. The second mechanism allows for protection of the aptamers treated as “cargo”, as well as prevent undesired binding until the appropriate target location is reached.

The third mechanism allows for the improvement of the functionality and affinity of an aptamer by taking advantage of avidity and accessibility of the aptamer towards a target site. Avidity is when the presence of multiple aptamers increases the affinity of individual aptamers to their target site. This is done by reducing free diffusion of an aptamer away from its target during binding. Figure 2.4 shows the phenomenon in a cyclic nature and demonstrates why avidity has more impact on successful aptamer binding. The last two mechanisms also increase the half-life of an aptamer by avoiding renal clearance and degradation by nucleases [40,41]. Each of these mechanisms can potentially affect the functionality of a developed aptamer by different methods.

2.2.1 Attachment of Nucleic Acids to Aptamers

In the case of the first mechanism, the focus will be solely on the attachment of other nucleic acids to the aptamer. There are two main ways to attach additional nucleic acids to an aptamer, both of which are demonstrated by example in Figure 2.5. One is simply by the use of a linker sequence to extend the overall length of the aptamer strand so that the strand is continuous for both the aptamer and attached molecule. The second way is to use modified groups on the ends of two separate nucleic acid strands in order to covalently bind them together. Regardless of the approach the concerns are the same. The first concern is that the attached molecule needs to have the same environmental conditions to induce functionality and appropriate folding as the aptamer. The second

concern is how the attached molecule and aptamer affect the functionality of each other. The success is dependent on the design of a nucleic acid linker sequence or spacer molecule used to keep the aptamer and attached molecule apart from each other. A linker sequence should be engineered so that it creates a bridge that prevents folding over so that both components on each side are not able to readily interact. This will allow both components to first bind intramolecularly with themselves before having the chance to interact with each other. A selected spacer used to separate the two components should be made of a compound that will not provide additional hybridization sites that can interact with the nucleic acids. Furthermore, the space should be long enough to separate the two components, but not long enough to vastly change the molecular weight and size of the total strand.

2.2.2 Aptamer Binding with "Soft" Nanoparticles

The second mechanism is either encapsulation or incorporation with "soft" nanoparticles. Examples include liposomes [42], micelles [43], polymeric particles [29, 44, 45], and viral capsids [46]. For a precise list of types of "soft" nanoparticles as well as comments on their advantages and disadvantages involving specific properties, see Table 2.2. Encapsulating aptamers into a nanoparticle is great for increasing their half-life from renal clearance, as well as protecting them from degradation by nucleases. Furthermore, aggregation is reduced due to binding of positive proteins that could potentially be attracted to the negatively charged aptamers [47]. A disadvantage with these types of nanoparticles is the likelihood that leaking between the membrane will occur [48]. This could impact the environment that the aptamers are located in, as well as allow other

molecules to come into contact with the aptamers prior to their arrival at the desired target site. It is possible to conjugate aptamers to the surface of soft nanoparticles instead of encapsulating them, which would have an effect similar to that of our third mechanism.

2.2.3 Aptamer Binding with "Hard" Nanoparticles

The third mechanism is the attachment of aptamers to "hard" nanoparticles. Examples include gold nanoparticles (AuNPs) [27, 49, 50], mesoporous silica nanoparticles [51], carbon nanotubes [52], and superparamagnetic iron oxide nanoparticles (SPIONs) [53]. AuNPs and SPIONs are particularly useful due to their viability as imaging agents in cancer diagnosis [54,55]. For a precise list of types of "hard" nanoparticles as well as comments on their advantages and disadvantages involving specific properties, see Table 2.3. Although each of these nanoparticles has shown success with aptamer targeting *in vitro*, little is known about their performance *in vivo*. The negative charge of DNA can cause nonspecific binding on some metallic surfaces, which would alter the structure and therefore the function of bound aptamers. Additionally, hard nanoparticles do not show the same resistance to the RES system that is found in polymeric nanoparticles. Therefore, it must be confirmed that aptamers are bound to these nanoparticles in such a way to reduce nonspecific binding, and care must be taken to ensure RES clearance does not occur before the aptamers comes into contact with the target molecule.

2.3 Conclusions

To date a number of aptamers have been approved for clinical trials with one – Macugen - already on the market to treat macular degeneration [56,57]. As the use of aptamers becomes more prevalent, the stability of the molecules must be the foremost concern. The SELEX procedure has been used recently in tandem with a quartz crystal microbalance (QCM) to select an aptamer specific for *E. coli* [58]. Although this technique does nothing in terms of improving aptamer stability, it shows how the technology can be used in novel ways to increase its effectiveness. SELEX must be scrutinized under stricter environments to ensure that the product of the process will remain effective under *in vivo* circumstances.

An aptamer-linked nanoparticle has not yet been approved for clinical trials. Although they have been effective *ex vivo* for detection, imaging, and drug delivery, *in vivo* effectiveness has not been confirmed. More sophisticated analytical techniques are currently needed to confirm the structure and function of aptamers when conjugated to different materials. A stringent selection procedure paired with a precise structure characterization will provide insight to the types of applications one can successfully use with aptamers. Only once these problems have been solved will the door opento a new era of nucleic acid based medicine.

2.4 Tables & Figures

Table 2.1. Aptamer property advantages over antibodies. *List of distinctive traits of aptamers that make them preferable to antibodies for both production and experimentation.*

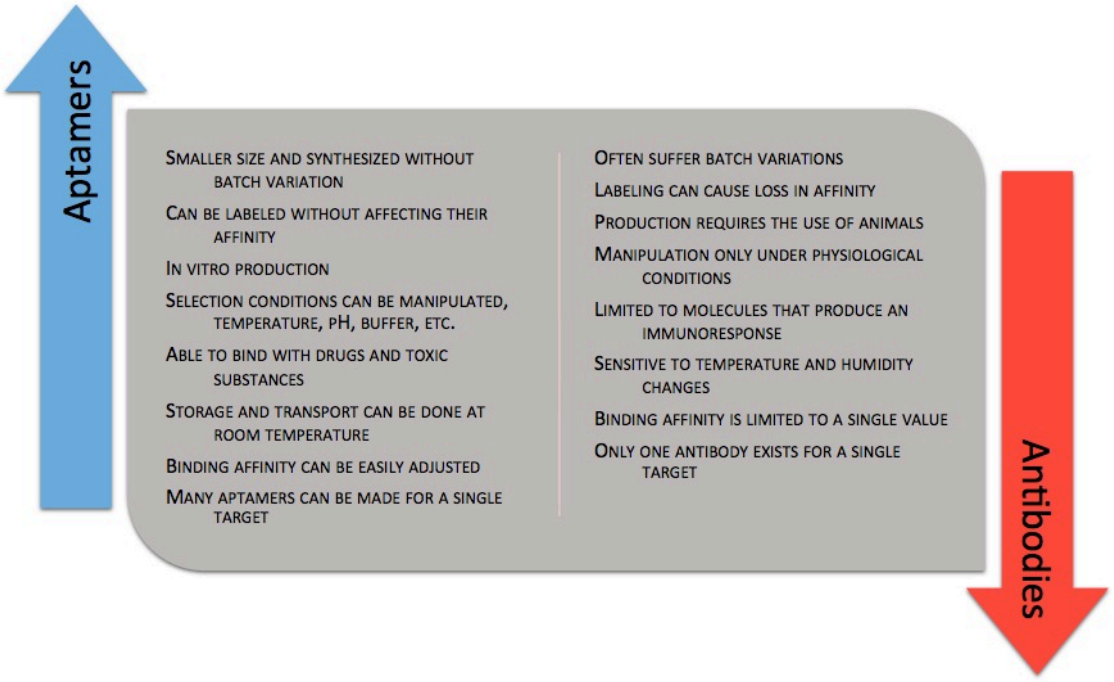

Table 2.2. Advantages and disadvantages for various "soft" nanoparticles. *"Soft" nanoparticles are made up of individual or flexible components that merge into a 3D sphere like structure. This list shows advantages and disadvantages of materials that have been used previously with aptamers.*

		Advantages	Disadvantages
"SOFT" NANOPARTICLES	**Liposomal platforms**	Can protect the cargo from premature chemical or physical break down Surface can be modified such that the liposome is targeted to a specific receptor which can also lead to a decrease in toxic side effects of the drug	Limited range of cargo, solubility and partitioning issues, chemical and physical instability Not shape or size specific leading to difficulty in precise loadability
	Polymeric Platforms/Polymer–drug (or protein) conjugates	Tend to be water soluble, exploit the enhanced permeability and retention (EPR) effect, can be captured via the endosome	Need to have high molecular mass and be biodegradable, conjugates need to move away from the heterogeneity of the carrier and to a more uniform structure.
	Polymeric Micelles	Hydrophobic core capable of carrying poorly soluble drugs with high loading capacity. Shell provides a steric protection for the micelle, thereby increasing its stability in blood, and functional groups suitable for further micelle modification Can be used to co-deliver two or more drugs with similar or different water solubility for combination therapy, or to simultaneously deliver two or more therapeutic modalities such as radiation agents and drugs	Difficult to tailor drug release rate Problems with nanoparticle disassembly in vivo
	Dendrimers	Specific molecular structure of dendrimers enables them to carry various drugs using their multivalent surfaces through covalent conjugation or electrostatic adsorption. Alternatively, dendrimers can be loaded with drugs using the cavities in their cores through hydrophobic interaction, hydrogen bond, or chemical linkage	Can cause toxicity when in contact with biological membranes
	Albumin-, polysaccharide-, and virus-based nanoparticles	Peculiar therapeutic potential because of their specific biological characteristics The core (of viruses) contains infectious agents that can control the transcription and translation machinery of the host cells. The shell is comprised of various proteins or proteins embedded in lipid membranes Conjugated with small-molecule drugs their stability and biodistribution can be significantly improved	Possibility for toxicity Recognized by the RES system

Table 2.3. Advantages and disadvantages for various "hard" nanoparticles. *"Hard" nanoparticles are made up of metals or non-flexible components that form into a 3D sphere like structure. This list shows advantages and disadvantages of materials that have been used previously with aptamers.*

"HARD" NANOPARTICLES	Metallic nanoparticles	Iron oxide: • can be used as a passive or targeting agent after being coated with dextran, surfactants, phospholipids, or other compounds to improve their stability. • magnetic field-induced excitation of iron oxide superparamagnetic nanoparticles, thermotherapy in the rat model can prolong the survival time 4.5-fold over controls Gold: • good optical and chemical properties, and thus high infrared phototherapy potential	Iron oxide: • Wide size range distribution within sample Gold • Possibility of aggregation
	Ceramic nanoparticles	Porous structures Easy to control drug release	Shown to cause immune response
	Carbon nanotubes	Can be PEGylated for high residence times within the body Low cytotoxic side effects	Not naturally water soluble No long-term biodistribution studies
	Mesoporous silica nanoparticles	High surface area Large, uniform porosity	Silanol groups on surface may cause hemolysis

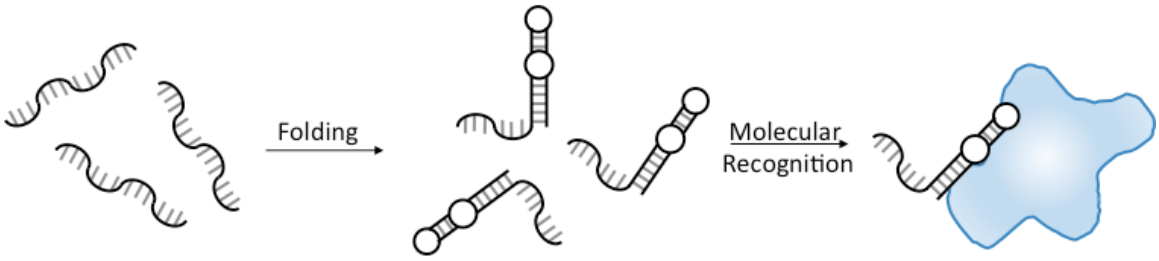

Figure 2.1. Aptamer formation and target binding mechanism. *This schematic demonstrates the folding of single stranded DNA or RNA into complex structures. These complex structures are able to specifically recognize and bind to a target molecule of choice. Adapted from [1].*

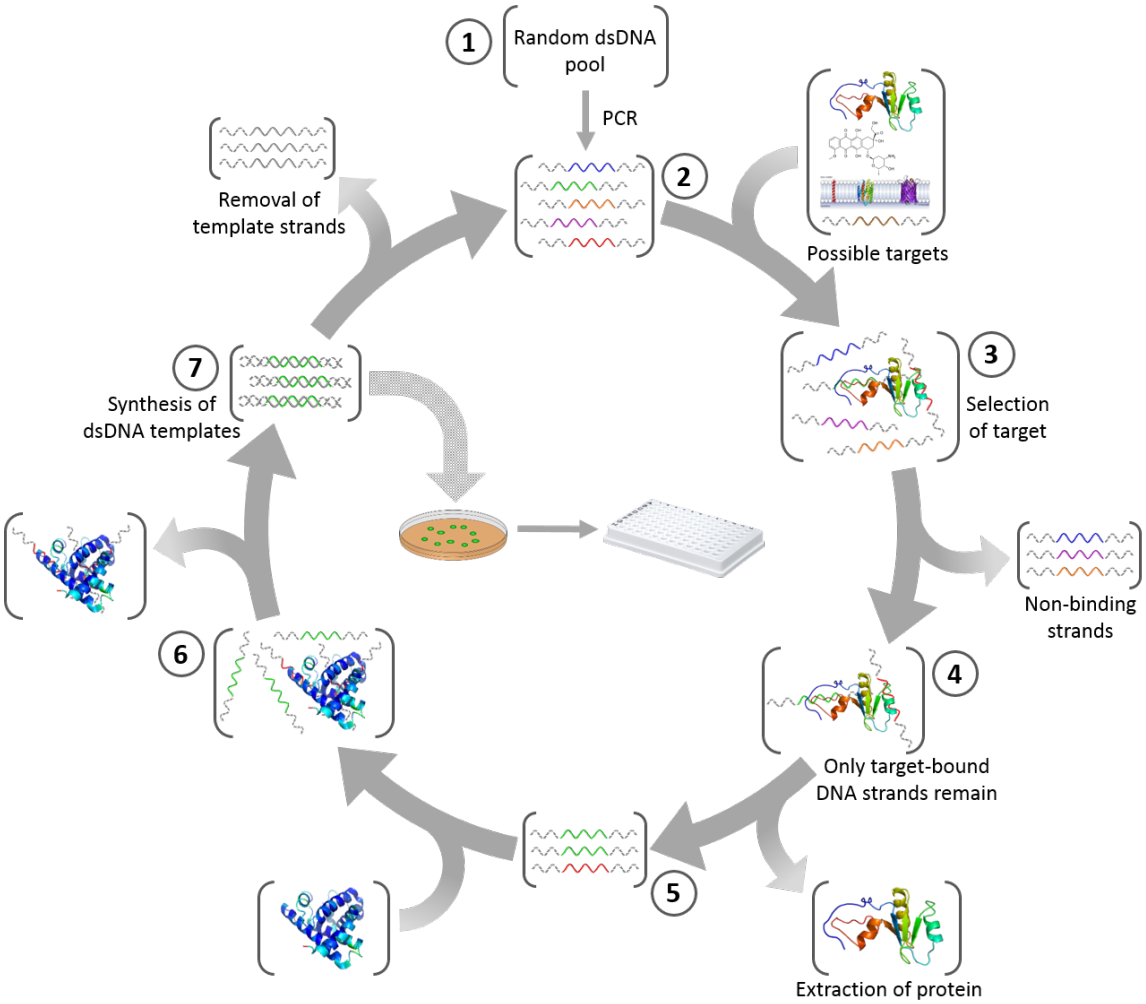

Figure 2.2. Systematic evolution of ligands by exponential enrichment (SELEX). *Diagram of the fundamental steps for aptamer production. A pool of oligonucleotides is exposed to a target molecule and non-binding strands are removed. Remaining strands are exposed to a control target and binding strands are removed. Oligonucleotides are then amplified using PCR and this cycle is repeated until a high affinity aptamer is produced.*

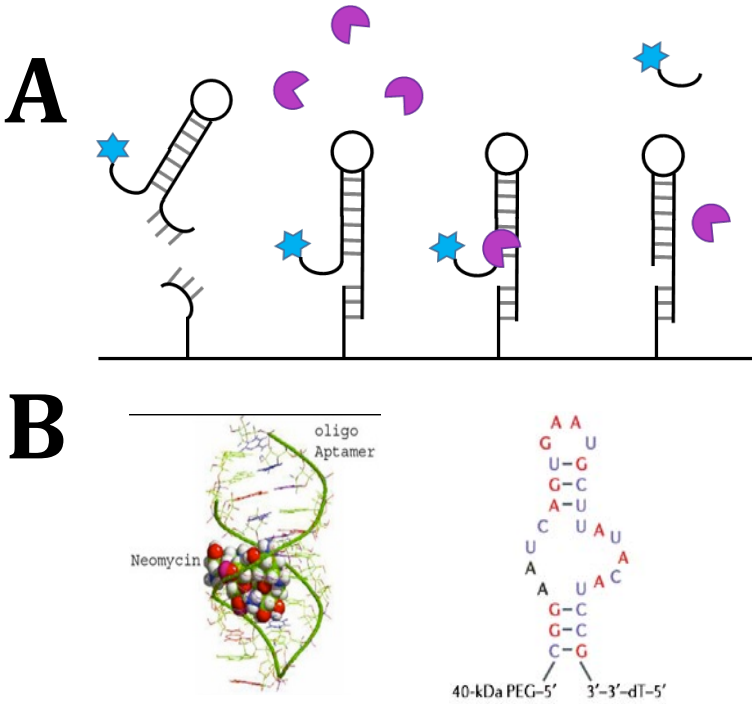

Figure 2.3. Variability of aptamer functions and modifications. *Aptamers are capable of being sensors (**A**) for detection, or specific drug delivery molecules (**B, left**). However, aptamers tend to be unstable in vivo and require many modifications including pegylation and altered nucleotides (**B, right**). This is an image of Pegaptanib, (**B, right**), currently the only approved aptamer on the market. It was modified with pegylation on the 5', as well as a cap on the 3' end. In addition, most of the nucleotides required either fluoro or iodo modifications to prevent degradation and increase half-life in vivo. Adapted from [20].*

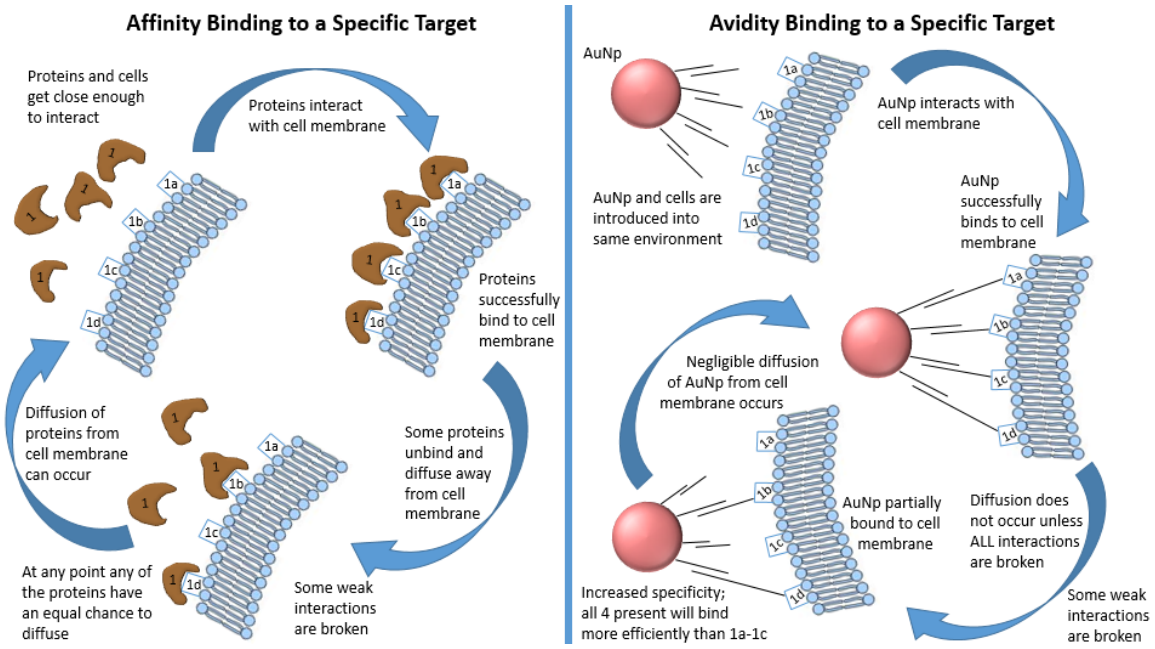

Figure 2.4. Nanoparticle construct leads to avidity effect of aptamers. *(**Left**) Affinity values decrease as a result of a molecule being allowed to diffuse away from the binding site during interactions. (**Right**) The avidity effect from nanoparticles restricts diffusion from binding site allowing the aptamer to always remain in proximity to the target, thereby increasing the affinity value.*

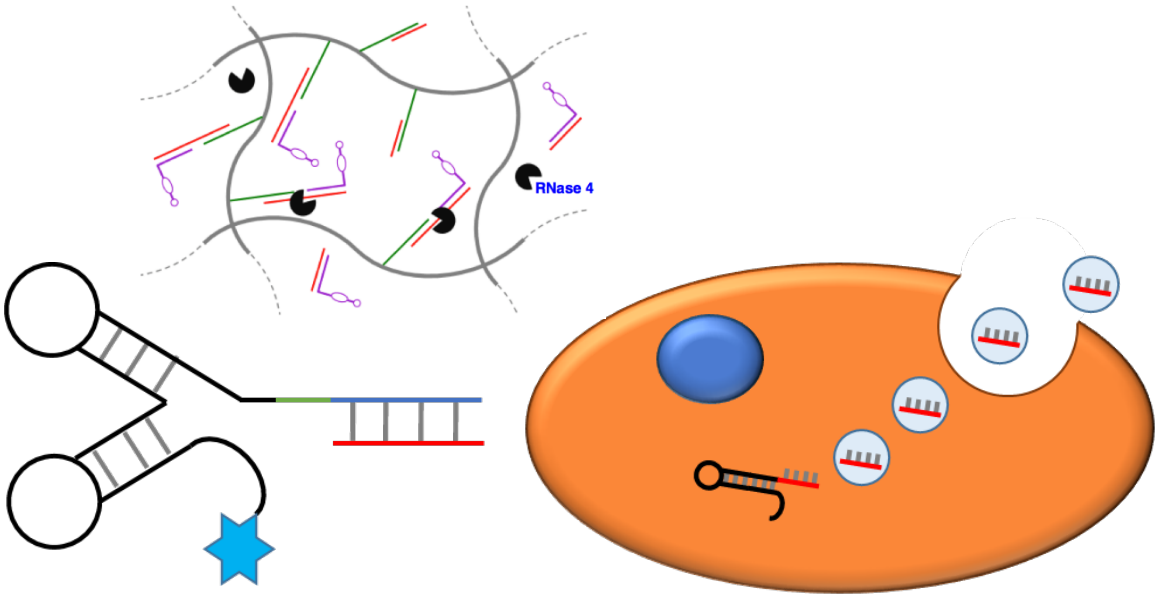

Figure 2.5. Attachment of additional nucleotides or other ligands to aptamers. *Aptamers have the potential to increase their number of functions by attachment of other molecules. This image shows additional nucleotides binding to an aptamer to allow binding to a gel, as well as a linker attachment to more specifically target an aptamer to a particular gene of interest. Adapted from [40].*

2.5 References

[1] http://technologyinscience.blogspot.com/2014/01/aptamers-new-class-of-oligonucleotide.html#.WwTSLiMrIfE. Lecture Series January 2014.

[2] Lakhin, A. V., Tarantul, V. Z. & Gening, L. V. Aptamers: Problems, solutions and prospects. *Acta Naturae* **5,** 34–43 (2013).

[3] Mairal, T. *et al.* Aptamers: Molecular tools for analytical applications. *Anal. Bioanal. Chem.* **390,** 989–1007 (2008).

[4] Mascini, M. Aptamers and their applications. *Anal. Bioanal. Chem.* **390,** 987–988 (2008).

[5] Ito, Y., Fujita, S., Kawazoe, N. & Imanishi, Y. Competitive binding assay for thyroxine using in vitro selected oligonucleotides. *Anal. Chem.* **70,** 3510–3512 (1998).

[6] Famulok, M. Allosteric aptamers and aptazymes as probes for screening approaches. *Curr. Opin. Mol. Ther.* **7,** 137–43 (2005).

[7] Ravelet, C., Grosset, C. & Peyrin, E. Liquid chromatography, electrochromatography and capillary electrophoresis applications of DNA and RNA aptamers. *J. Chromatogr. A* **1117,** 1–10 (2006).

[8] O'Sullivan, C. K. Aptasensors – the future of biosensing? *Anal. Bioanal. Chem.* **372,** 44–48 (2002).

[9] Drolet, D. W., Moon-McDermott, L. & Romig, T. S. An enzyme-linked oligonucleotide assay. *Nat. Biotechnol.* **14,** 1021–1025 (1996).

[10] Jayasena, S. D. Aptamers: An emerging class of molecules that rival antibodies in diagnostics. *Clin. Chem.* **45,** 1628–1650 (1999).

[11] Guo, K. T., Paul, A., Schichor, C., Ziemer, G. & Wendel, H. P. Cell-SELEX: Novel perspectives of aptamer-based therapeutics. *Int. J. Mol. Sci.* **9,** 668–678 (2008).

[12] Wochner, A. *et al.* A DNA aptamer with high affinity and specificity for therapeutic anthracyclines. *Anal. Biochem.* **373,** 34–42 (2008).

[13] Mayer, G. The chemical biology of aptamers. *Angew. Chemie - Int. Ed.* **48,** 2672–2689 (2009).

[14] Tuerk, C. & Gold, L. Systematic evolution of ligands by exponential enrichment:

RNA ligands to bacteriophage T4 DNA polymerase. *Science* **249,** 505–510 (1990).

[15] Sun, H. *et al.* Oligonucleotide aptamers: New tools for targeted cancer therapy. *Mol. Ther. - Nucleic Acids* **3,** (2014).

[16] Ohuchi, S. Cell-SELEX Technology. *Biores. Open Access* **1,** 265–272 (2012).

[17] Kunii, T., Ogura, S., Mie, M. & Kobatake, E. Selection of DNA aptamers recognizing small cell lung cancer using living cell-SELEX. *Analyst* **136,** 1310 (2011).

[18] Levin, A. A. A review of issues in the pharmacokinetics and toxicology of phosphorothioate antisense oligonucleotides. *Biochim. Biophys. Acta - Gene Struct. Expr.* **1489,** 69–84 (1999).

[19] Healy, J. M. *et al.* Pharmacokinetics and biodistribution of novel aptamer compositions. *Pharm. Res.* **21,** 2234–2246 (2004).

[20] Kasahara, Y. *et al.* Effect of 3′-end capping of aptamer with various 2′,4′-bridged nucleotides: Enzymatic post-modification toward a practical use of polyclonal aptamers. *Bioorganic and Medicinal Chemistry Letters* **20,** 1626–1629 (2010).

[21] Pasut, G. & Veronese, F. M. State of the art in PEGylation: The great versatility achieved after forty years of research. *J. Control. Release* **161,** 461–472 (2012).

[22] Rusconi, C. P. *et al.* Antidote-mediated control of an anticoagulant aptamer in vivo. *Nat. Biotechnol.* **22,** 1423–1428 (2004).

[23] Keefe, A. D. & Cload, S. T. SELEX with modified nucleotides. *Curr. Opin. Chem. Biol.* **12,** 448–456 (2008).

[24] Klußmann, S., Nolte, A., Bald, R., Erdmann, V. A. & Fürste, J. P. Mirror-image RNA that binds D-Adenosine. *Nat. Biotechnol.* **14,** 1112–1115 (1996).

[25] Capek, I. *DNA Engineered Noble Metal Nanoparticles: Fundamentals and State-of-the-Art of Nanobiotechnology*. (Scrivener Publishing, 2015).

[26] Liu, J. *et al.* Multifunctional aptamer-based nanoparticles for targeted drug delivery to circumvent cancer resistance. *Biomaterials* **91,** 44–56 (2016).

[27] Sundaram, P., Wower, J. & Byrne, M. E. A nanoscale drug delivery carrier using nucleic acid aptamers for extended release of therapeutic. *Nanomedicine Nanotechnology, Biol. Med.* **8,** 1143–1151 (2012).

[28] Kaneda, Y. Virosomes: Evolution of the liposome as a targeted drug delivery system. *Adv. Drug Deliv. Rev.* **43,** 197–205 (2000).

[29] Guo, J. *et al.* Aptamer-functionalized PEG-PLGA nanoparticles for enhanced anti-glioma drug delivery. *Biomaterials* **32,** 8010–8020 (2011).

[30] Kimoto, M., Yamashige, R., Matsunaga, K. I., Yokoyama, S. & Hirao, I. Generation of high-affinity DNA aptamers using an expanded genetic alphabet. *Nat. Biotechnol.* **31,** 453–457 (2013).

[31] Lai, Y. T. & DeStefano, J. J. A primer-free method that selects high-affinity single-stranded DNA aptamers using thermostable RNA ligase. *Anal. Biochem.* **414,** 246–253 (2011).

[32] Mergny, J.-L. & Hélène, C. G-quadruplex DNA : A target for drug design Compounds that stabilize G-quadruplex structures in telomeric DNA block telomerase activity and may be. *Nat. Med.* **4,** 1366–1367 (1998).

[33] Takahashi, S., Brazier, J. A. & Sugimoto, N. Topological impact of noncanonical DNA structures on Klenow fragment of DNA polymerase. *Proc. Natl. Acad. Sci.* **114,** 9605–9610 (2017).

[34] Schuster, S. C. Next-generation sequencing transforms today's biology. *Nat. Methods* **5,** 16–18 (2008).

[35] Cheng, C., Chen, Y. H., Lennox, K. A., Behlke, M. A. & Davidson, B. L. In vivo SELEX for identification of brain-penetrating aptamers. *Mol. Ther. - Nucleic Acids* **2,** e67 (2013).

[36] Darmostuk, M., Rimpelova, S., Gbelcova, H. & Ruml, T. Current approaches in SELEX: An update to aptamer selection technology. *Biotechnol. Adv.* **33,** 1141–1161 (2014).

[37] Burge, S., Parkinson, G. N., Hazel, P., Todd, A. K. & Neidle, S. Quadruplex DNA: Sequence, topology and structure. *Nucleic Acids Res.* **34,** 5402–5415 (2006).

[38] Davies, D. *Structural Molecular Biology: Methods and Applications*. (Springer US, 2013).

[39] Rohloff, J. C. *et al.* Nucleic acid ligands with protein-like side chains: Modified aptamers and their use as diagnostic and therapeutic agents. *Mol. Ther. - Nucleic Acids* **3,** e201 (2014).

[40] Alexis, F., Pridgen, E. & Molnar, L. K. Factors Affecting the Clearance and Biodistribution of. *Mol. Pharm.* **5,** 505–515 (2008).

[41] Gref, R. *et al.* Biodegradable Long-Circulating Polymeric Nanospheres. *Science (80-.).* **263,** 1600–1603 (2013).

[42] Cao, Z. *et al.* Reversible cell-specific drug delivery with aptamer-functionalized liposomes. *Angew. Chemie - Int. Ed.* **48,** 6494–6498 (2009).

[43] Wu, Y., Sefah, K., Liu, H., Wang, R. & Tan, W. DNA aptamer-micelle as an efficient detection/delivery vehicle toward cancer cells. *Proc. Natl. Acad. Sci.* **107,** 5–10 (2010).

[44] Aravind, A. *et al.* AS1411 aptamer tagged PLGA-lecithin-PEG nanoparticles for tumor cell targeting and drug delivery. *Biotechnol. Bioeng.* **109,** 2920–2931 (2012).

[45] Farokhzad, O. C. *et al.* Targeted nanoparticle-aptamer bioconjugates for cancer chemotherapy in vivo. *Proc. Natl. Acad. Sci.* **103,** 6315–6320 (2006).

[46] Tong, G. J., Hsiao, S. C., Carrico, Z. M. & Francis, M. B. Viral Capsid DNA Aptamer Conjugates as Multivalent Cell Targeting Vehicles. *Jacs* **131,** 11174–11178 (2010).

[47] Owens, D. E. & Peppas, N. A. Opsonization, biodistribution, and pharmacokinetics of polymeric nanoparticles. *Int. J. Pharm.* **307,** 93–102 (2006).

[48] Russell, L. M., Hultz, M. & Searson, P. C. Leakage kinetics of the liposomal chemotherapeutic agent Doxil: The role of dissolution, protonation, and passive transport, and implications for mechanism of action. *J. Control. Release* **269,** 171–176 (2018).

[49] Luo, Y. L., Shiao, Y. S. & Huang, Y. F. Release of photoactivatable drugs from plasmonic nanoparticles for targeted cancer therapy. *ACS Nano* **5,** 7796–7804 (2011).

[50] Wang, J. *et al.* Assembly of aptamer switch probes and photosensitizer on gold nanorods for targeted photothermal and photodynamic cancer therapy. *ACS Nano* **6,** 5070–5077 (2012).

[51] Yang, X. *et al.* Near-infrared light-triggered, targeted drug delivery to cancer cells by aptamer gated nanovehicles. *Adv. Mater.* **24,** 2890–2895 (2012).

[52] Taghdisi, S. M., Lavaee, P., Ramezani, M. & Abnous, K. Reversible Targeting and controlled release delivery of daunorubicin to cancer cells by aptamer-wrapped carbon nanotubes. *Eur. J. Pharm. Biopharm.* **77,** 200–206 (2011).

[53] Wang, Andrew Z., Bagalkot, V., Vasilliou, Christophoros C., Gu, F., Alexis, F., Zhang, L., Shaikh, M., Yuet, K., Cima, Michael J., Langer, R., Kantoff, Philip W., Bander, Neil H., Jon, S. and Farokhzad, O. C. Superparamagnetic Iron Oxide Nanoparticle–Aptamer Bioconjugates for Combined Prostate Cancer Imaging and

Therapy. *Chem Med Chem* **3,** 1311–1315 (2008).

[54] Cao, X., Ye, Y. & Liu, S. Gold nanoparticle-based signal amplification for biosensing. *Anal. Biochem.* **417,** 1–16 (2011).

[55] Wang, Y.-X. J., Hussain, S. M. & Krestin, G. P. Superparamagnetic iron oxide contrast agents: physicochemical characteristics and applications in MR imaging. *Eur. Radiol.* **11,** 2319–2331 (2001).

[56] Sundaram, P., Kurniawan, H., Byrne, M. E. & Wower, J. Therapeutic RNA aptamers in clinical trials. *Eur. J. Pharm. Sci.* **48,** 259–271 (2013).

[57] Parashar, A. Aptamers in therapeutics. *J. Clin. Diagnostic Res.* **10,** BE01-BE06 (2016).

[58] Yu, X., Chen, F., Wang, R. & Li, Y. Whole-bacterium SELEX of DNA aptamers for rapid detection of E.coli O157:H7 using a QCM sensor. *J. Biotechnol.* **266,** 39–49 (2018).

Chapter 3: Aptamers for Triggered Release

The goal of the experiments in this research is to understand how to engineer DNA and RNA sequences to hybridize, meaning base pairing between neighboring nucleic acid strands, in a specific manner. Furthermore, it is important to understand conceptually how DNA/RNA binds and behaves dynamically in various solutions because structures are not homogeneous and will change with time based on Gibbs free energy of the system. Performing the experiments in this chapter was a lesson on how to solubilize, stabilize, and purify DNA/RNA. Understanding their binding kinetics and thermodynamics, and the effects that salts have on these properties, e.g. the dielectic constant of sodium acetate allowing it to be used as a transport vehicle for nucleic acids between water and ethanol phases. It is important to also understand the differences between DNA and RNA, such as their stability in pH where RNA favors slightly acidic environments and DNA favors slightly basic environments. This difference also includes secondary structures with RNA having the dominant form (a form for RNA-RNA and RNA-DNA vs b form for DNA-DNA) when hybridized with DNA, or DNA having a stronger base pairing (A-T > A-U). The effect of secondary structures such as loops, overhangs, and mismatches, on the stability of base pairings surrounding them is also learned through these experiments.

3.1 Innovating a New Drug Delivery Approach for the Eye

Eyesight is considered by many to be the most important of the five senses in the human body [1]. This has led to a major focus on treating diseases affecting eyesight over

the past several decades. Many platforms have been developed for treating ocular diseases such as eye drops, in situ gels, laser therapy, surgery, and contact lenses. All of these methods have pros and cons associated with them and many can use the same mechanisms for drug delivery such as pH, diffusion, and enzyme cleavable polymers [2]. Our plan is to use aptamers as a new drug delivery mechanism for treating ocular diseases on a contact lens platform. In order to explain why this mechanism and platform have been chosen, the anatomy of the eye needs to first be discussed.

The human eye has a diameter of 24 mm, mass of 7.5 g, weight of 0.25 oz, and a volume of 6 mL [3]. There are three distinct layers of the eye: tear film, anterior, and posterior. Ocular diseases can be caused from defects in any of these regions. This means that finding one platform and mechanism that can treat or cure all eye diseases will be difficult. Our desire is to pick the part of the eye that is currently used the most for treatment so that our experiment will have the largest effect possible on patients with diseases in the eye. The highest cause of irreversible blindness worldwide is due to Glaucoma and the most common treatment approach for this disease is drug delivery using the tear film [4]. There are also many other diseases that are treated using properties of the tear film, which makes it the best candidate for utilizing biological molecules, if the goal is creating a general platform for treating many diseases. The best platform options for drug delivery through the tear film are eye drops and contact lenses.

In order to determine which of these remaining two platforms is the best to use for our research, it is important to learn the anatomy of the tear film. The tear film is 8-10 μm thick with a volume of 4-13 μL and turnover rate of 18% per minute [5]. It is composed of lipids that retard evaporation of the tear fluid. The normal basal drainage rate is 1.2

μL/min while the rate of removal of fluid through the puncta and lacrimal duct is about 25-50 μL in 90 seconds [6]. The rate of oxygen diffusion is 7.8 μL/(cm^2 *hr) [7]. The temperature of the cornea is slightly less than the rest of the human body at around 34-35^{0}C [8]. There are many mechanisms that use the pH of the tear film, ~7.2, for triggered release [9]. A summary of these facts can be found in Table 3.1. However, there are other physiological components of the tear film that have not been explored nearly as much and the plan was to exploit one to help create a new mechanism for eye treatment. There is only one RNase in the tear film called RNase 4 [10] and we hypothesize the use of RNA as a triggered release mechanism and with high regulation. An RNA molecule can be designed to respond to this protein and attach to a drug that can treat ocular disease.

It is also important to keep other biological properties of the eye in mind when designing drug platforms for delivery; so that potential other release mechanisms, such as temperature, may be possible for future experiments and the scope of our project is not limited. Drug permeation is affected by hydrophobicity, solubility, molecular size and shape, charge, and ionization. To reach the interior of the eye a drug would need to have both hydrophilic and hydrophobic components. In the anterior segment, the cornea is a drug transport barrier. The aqueous humor is between the cornea and the lens, it is a clear fluid that circulates through the anterior segment at 1% per minute and drains out [11]. The conjunctiva typically has high permeability for drugs [12] resulting in drugs being removed from the eye to other organs. This means we should try to engineer RNA drugs that are more likely to absorb into the cornea or sclera for less loss.

The vitreous humor, in the posterior segment,is the fluid that gives the eye its size and shape, making up two thirds of the mass and volume of the eye [13]. Drugs must pass

through the anterior of the eye into the vitreous humor and through it to the reach the back of the eye. The retina is inside the choroid, which nourishes the retina and is inside the sclera. Retinal vessel walls have poor permeation of small hydrophilic molecules, while lipophilic compounds can penetrate more easily [14].

There are two methods for drug delivery to the posterior of the eye. First is for the drug to be absorbed through the cornea route [15]. It will enter the aqueous humor, be distributed to the iris-ciliary body, then the vitreous humor, and finally the choroid-retina. The second way is by non-corneal routes. It will enter the conjunctiva and sclera; reach the vitreous, then must pass across the choroid and RPE without entering the aqueous humor [16]. Pathway two is preferred for hydrophilic drugs; the conjunctiva may allow hydrophilic drugs up to 20 Kda [17] to permeate through and the sclera up to 70 Kda [18]. The endothelium should allow drugs up to 20 nm in diameter to diffuse across [17]. The corneal epithelium is negatively charged so RNA will permeate slower than positive or neutral molecules [19]. Aptamers can be developed with molecular weights and diameters smaller than the restrictions of these regions of the eye. Knowing these properties of other regions of the eye allows us to engineer an RNA drug that has the potential to travel to other areas to further increase the range of treatments possible with our platform.

Eye drops have many disadvantages such as low residence time, patient compliance, and potential toxicity due to delivering a large excess of drug [20]. Contact lenses also have disadvantages as therapeutic tools such as drug-gel compatibility, loading quantity, and release of drug into the tear film [21]. Overcoming the main disadvantages of contact lenses is why our new mechanism for delivery has the potential

to be highly effective. Since our approach uses aptamers that are capable of overcoming the limitations of contact lenses, it is best suited for us to use contact lenses in this case.

Past approaches for use with contact lenses have been to use a diffusion gradient, pH, or enzyme cleavable polymers. Diffusion gradients have a weakness in that there is little control in the rate of release of drug, usually resulting in a burst release followed by a lack of sustained therapeutic delivery. pH mechanisms rely on using acidic storage buffers that can be damaging to the eye if not properly handled by the patient [22]. Enzyme cleavable polymers, see Figure 3.1 [23], affect the properties of the contact lens resulting in decreased function and potential for increased eye irritation. Our RNA triggered release approach allows us to modulate the release of drug, and create a harmless platform-gel hybrid that will not be damaging to the eye or affect the integrity of the contact lens, essentially correcting all the issues with current treatment approaches for ocular therapeutics in contact lenses.

3.1.1 Macugen & Contact Lenses

There are four main properties of a contact lens that need to be accounted for when introducing our platform [24]. These are optical transparency, oxygen permeability, water content, and modulus. An optical transparency value of 90% is generally deemed acceptable [25].

Oxygen transport is the main limiting factor for the time period that a lens can be worn before it is removed [26]. Overnight lenses such as silicone-based hydrogels allow for a longer period of wear compared to daytime hydrogen lenses such as HEMA [27].

Water content of the lens effects the environment of the eye. Contact lenses that can sustain wetting are capable of recovering the tear film layer smoothly after each blink [28]. The comfort of lenses is mostly dependent on water content, and when low, can result in dry eye and irritation for the user [29]. This is important to consider because it affects tear film layer properties and patient compliance towards wearing the lens. Modulus effects susceptibility of lenses to breaking down due to the movement of skin by blinking and constant washing of tear film [30]. It is important that the integrity of the lens remain intact. The shape of the lens needs to align with the optical surface without deformation occurring.

Aptamers can precipitate out of solution in hydrophobic environments. DNA and RNA are considered hydrophilic, and therefore need a hydrophilic environment in order to maintain their function and structure. Aptamers are known to have many different modifications that can be added to each base or their ends to prevent degradation, but because RNase 4 is the only protein in the tear film known for degrading RNA and none for DNA, that is the only consideration that needs to be recognized. The stability of the structure of an aptamer is dependent on its chemistry and thermodynamics, however most aptamers have structures that do not remain intact for very long. Modifications to each nucleotide such as 2'-O-methylated nucleotides or 2'-fluro pyrimidines, as well as many others, are capable of improving the stability of aptamers [31]. These changes also affect the function of RNase 4 to recognize and cleave RNA, which is a positive for the design of our platform.

The 5' and 3' ends of an aptamer can also be modified with various approaches including capping, active group attachments, and polymer extensions. Capping can be

used to help prevent degradation and improve stability of the aptamer's structure [32]. Active group attachments will be utilized with our platform for allowing our DNA to bind to the hydrogel; this will be explained in more detail in the next section. Polymer extensions, such as PEG, increase residence time and of aptamers inside the body and can be used as a tool for controlling the release rate of an aptamer drug from the contact lens due to changing its total size. Aptamer size can vary, but they are capable of being smaller than 20 kDa and 20nm in diameter, which are the size conditions required for being capable of transporting through many tissues of the eye. Finally, aptamers are natural compounds already present in the body and therefore are biocompatible.

3.1.2 Nucleic Acid/HEMA Gel Properties & Compatibility

Our contact lens formula uses a base polymer known as 2-Hydroxyethyl Methacrylate (HEMA). HEMA is a day time wear lens because it has an oxygen transport problem, however it can still be worn for an entire day until going to sleep depending on the formulation [33]. This is the window of time available for drug delivery. HEMA itself is a hydrophobic polymer, but it has a hydrophilic pendant group and can absorb anywhere from 10% to 600% of water relative to its dry weight [34]. This gives the polymer hydrophilic properties. These are the properties that make HEMA an ideal choice for incorporation of DNA or RNA, which are also hydrophilic, into the polymer. It is also already an FDA approved polymer used in current contact lens formulations. Other components that can be potentially added to the lens formulation are Dimethacrylate (DMA), Polyethylene glycol dimethacrylate (PEGDMA) of various sizes, and tris-silicone, as well as others. Variation in these other components is mainly to

control mesh size, water uptake, and hydrophobicity of the lens. This gives us leniency on the size and modifications on the aptamer.

The DNA/RNA platform incorporated into the hydrogel will be illustrated and discussed in the next section, but first it is important to explain how the nucleic acids interact with the polymer and the reactions described above. The nucleic acid strands are covalently attached to the HEMA network using an Acrydite group that is modified onto the 5' end of a DNA strand called the anchor strand. The Acrydite group reacts by using free radicals to convert a double carbon bond into a single bond connection with HEMA, see Figure 3.2. This is the same mechanism that the cross linkers used react with HEMA (monomer and macromer), therefore the same methods for polymerizing the gel can also be used for covalently binding the anchor DNA strand [36]. The other side of the Acrydite group contains the same PO_4 group found on the 5' end of DNA and is used to substitute the Acrydite molecule onto the start of the 5' DNA strand during chemical synthesis. Therefore, the nucleic acid platform can be incorporated into the lens solution before polymerization and then covalently bind to HEMA during the reaction.

DNA is used for modification with the Acrydite group instead of RNA for several reasons. RNA is much more sensitive to degradation by environmental factors and temperature so cost of transporting Acrydite modified RNA is drastically more expensive then DNA. It is also more time consuming to produce RNA and there are additional preparation steps required before a modified RNA sample could be used. Since RNA is less stable than DNA, it is usually delivered with some form of capping to protect it during transportation that then needs to be removed from the RNA sample before it is ready to use. RNA would be preferred since it is the tool necessary for cleavage with

RNase 4 in the tear film, but DNA is so stable and easily engineered to have a linear structure, that it can act as a connector between RNA and the hydrogel with very little complications.

3.2 Creating a Hydrogel-Nucleic Acid Platform

Our nucleic acid platform consists of a construct containing one DNA strand and two RNA strands. The image below shows the construct inside of a general hydrogel. The anchor DNA strand has already been explained in the previous section. The nucleotides on the 3' end of the anchor strand are used for hybridization of an RNA strand called the linker strand. The linker strand serves two purposes, it attaches the drug to the anchor strand, and it serves as the controlled cleaving site for release of the drug. The last RNA strand is the drug itself. In our case we used Pegaptanib, an aptamer created as a drug for targeting age-related macular degeneration [37], but any aptamer developed in the future for ocular diseases has the potential to be incorporated into our platform, see Figure 3.3.

Because RNase 4 cleaves RNA strands, the RNA aptamer acting as a drug needs to be modified to protect it. This means that two RNA strands are needed; the linker strand remains as unmodified RNA and is cleavable by the enzyme, while the aptamer is modified preventing its degradation. The role of all three nucleic acids strands creates a drug delivery platform that is capable of modulating release of therapeutics into the eye from a contact lens. A more in depth analysis on the sequence and segments of each of the three strands will be discussed in the next section, see Figure 3.4.

The role of the DNA anchor strand is to covalently bind to the contact lens on the 5' end, and hybridize with the linker strand through base pairing. The role of the RNA

aptamer strand is to hybridize with the linker strand so that it is not able to freely diffuse into the tear film, and to act as a drug for treating a desired ocular disease. RNA is more versatile than DNA at folding into three-dimensional structures and therefore has a wider range for successfully creating a therapeutic based on nucleic acids, which is why an RNA aptamer strand was chosen instead of DNA.

The two main roles of the RNA linker strand are to connect the drug to the anchor strand so that it is bound to the hydrogel, and to be the cleavage site for RNase 4, which will allow the drug to be released. There are many ways that engineering the linker strand can modulate the release rate of the drug. *1) Number of cut sites* - RNase 4 works by cleaving after the base uracil, by controlling the location of uracil and the number of the uracil bases present, the number of potential cleavage sites can be regulated. *2) Accessibility of RNase 4 to the cut site* - By flanking the uracil cut site with other nucleotides to create a larger single stranded area surrounding the cut site, the RNase 4 enzyme will have less obstacles around the cut site to prevent it from binding and cleaving. *3) Temperature control of hybridization* - Room temperature is between 20-25^{0}C, while the temperature at the surface of the eye is around 33-34^{0}C. This means that the composition of the nucleotides used for hybridizing the linker and aptamer strands together can be modulated so that hybridization is stable at room temperature, but begins to break down at the temperature on the surface of the eye. 4*) Concentration of linker and aptamer strands present in the hydrogel* - By controlling the number of linker and drugs present inside the contact lens, this will affect the amount of drug that gets released over time.

There are also many ways that the hydrogel can be used to regulate drug release. *1) Mesh size of the polymer network* - The accessibility of the RNase 4 enzyme to the cleavage site is mostly restricted by the pore size of the polymer. By controlling how much bigger the average pore size is compared to the size of the enzyme, the contact rate between RNase 4 and the cut site can be regulated. Pore size can be controlled by the size and amount of cross linkers used. Mesh sizes can be finely tuned by using multiple types of cross linkers as well. *2) Percentage of cross linker and presence of other components in the hydrogel* - By manipulating the properties of the contact lens, such as water swelling or hydrophobicity, the RNase 4 enzyme may travel faster or slower once inside the polymer on its way to the cut site.

Finally, there are also other factors that can regulate drug release besides the linker strand and polymer. *1) Size of the aptamer* - By attaching PEG or other molecules to either end of an aptamer strand, its size can be increased. This will affect its diffusion rate through the hydrogel and tear film layer once the linker strand has been cleaved. *2) Packaging of the nucleic acid construct* - The platform can be incorporated into the hydrogel either before or after the polymerization of the lens. This can have major implications on the three dimensional structure of the mesh surrounding the nucleic acid construct inserted into the lens.

3.2.1 Computer Modeling & Formation of Aptamer Complex

Now that we know the role of each nucleic acid strand in our drug delivery platform, it is time to engineer the sequences to meet each of the criteria. The DNA

anchor strand, which can be seen in Figure 3.5,contains three segments called 1) hydrogel binding region, 2) spacer region, and 3) hybridization of RNA linker region.

First, the hydrogel binding region is the 5' end of the DNA strand containing the Acrydite modification. This is where the DNA strand will covalently bind to the hydrogel. Second, the spacer region is the first five nucleotides consisting of only thymines. A spacer region is important because it creates separation between the polymer and the cut site for the enzyme. This allows accessibility of the enzyme to the cut site without being blocked by the polymer. In our case, five nucleotides were chosen as a starting point for proof of concept, but the length of the spacer is readily adjustable depending on the RNase 4 enzyme and mesh sizes of the polymer. Thymines are generally considered the least reactive nucleotide and therefore are less likely to attach to nearby molecules than the other nucleotides. This makes them ideal for placing near other compounds, such as a polymer in our case.. Because thymines are normal nucleotides being used as a spacer, their effect on the overall DNA structure is known and much more controllable as opposed to using a different spacer material.

The third and final segment is the hybridization of RNA linker region. It is the last twelve nucleotides on the anchor DNA strand. This is the sequence of nucleotides that will complementary base pair with the RNA linker strand. There are five considerations that need to be checked when engineering the sequence order and composition of nucleotides in this region: 1) *Desired melting temperature* - The length and nucleotide composition of this sequence can be selected so that a specific melting temperature for separation of the DNA and RNA linker strand can be chosen. Since this region is located on the left side of the cut site (see nucleic acid platform image in previous section), the melting temperature

of this region should be equal to or greater than the surface temperature of the eye. The nucleotide sequence chosen on our DNA strand shown above has a melting temperature of ~34^0C, the same as the average temperature on the eye surface. This was done because it creates a potential second mechanism for release of the drug in addition to the RNase 4 enzyme. This melting temperature can be increased as necessary to prevent strand separation in this region. 2) *Three dimensional structure of the DNA strand* - For the most part, DNA tends to not prefer intramolecular binding with itself so this constraint will most likely not be an issue. However, it is still something that needs to be checked and can be using computer modeling software such as mfold. The data from Figure 3.6, taken from using mfold, shows that no thermodynamically favorable intramolecular interactions will take place with the DNA strand containing the sequences selected. This means that the DNA will have a linear structure and the last twelve nucleotides are free for hybridization.

Gibbs free energy is the maximum amount of reversible work that can be done to a system. A negative value indicates a reaction is favorable. The Gibbs free energy values calculated from the computer models are determined using the nearest neighbor model. The nearest neighbor model works by determining Gibbs free energy values for pairs of neighboring bases and their complements on both sides of a single nucleotide meaning it gets accounted for twice. These values are all then summed together for the total Gibbs free energy of the hybridization. The individual Gibbs free energy values for the coupled base pairs were determined based on hundreds of melting temperature studies.

3) Intermolecular interactions between the anchor DNA strand with itself. It is important that the anchor DNA strand be available to bind with the RNA linker strand. If

the DNA strand wants to hybridize with another DNA strand then it will reduce the efficiency of binding to the RNA linker strand. By using computer-modeling software, such as the Vienna package, intermolecular interactions can be checked. The data below shows that our anchor DNA strand does not prefer to hybridize with itself. The dots underneath each nucleotide represent a base-pairing mismatch, meaning hybridization will not occur. Parentheses mean that base pairing is likely to occur. There are no parentheses in the data shown in Figure 3.7.

4) Undesired hybridization with linker and aptamer strands. From the layout of our nucleic acid construct discussed in the previous section it can be seen that there is a specific location for the anchor DNA strand to hybridize with the linker strand. There is also no hybridization occurring between the anchor strand and the aptamer. Intermolecular hybridization with the linker strand and aptamer needs to be checked so that inappropriate binding does not occur. The linker strand actually needs to be checked twice, once with the appropriate binding location, and again without it, in order to make sure that there are not two thermodynamically favorable binding sites for the anchor strand on the linker. The sequence selected for our anchor strand does not have any undesired hybridization, as can been seen from the data shown in Figure 3.8. Computer models showing no other preferred binding sites exist when the target-hybridized areas are removed is not shown.

5) Considerations on restrictions for complementary strand. When determining what nucleotides to place in the hybridization region it is also necessary to consider the function of the strand that is binding to the anchor. In this case that is the linker strand and it presents two issues that need to be considered when selecting the sequence of this

region. One is that there cannot be any uracils in this region on the linker strand, which means there cannot be any adenines on the anchor strand in this segment. Second, adenines are preferred in the linker strand for radioactive labeling using inexpensive α^{32}P-ATP, if possible; so a few thymines should be placed on this segment of the anchor strand. It is important to note that these five considerations each affect one another in a loop, so when adjustments are made to fix one of the problems, all of other criteria need to be checked again. This can make the engineering process difficult and a great understanding of DNA and RNA behavior is required.

The RNA linker strand sequence is shown in Figure 3.9 and also contains three different segments called the 1) anchor hybridization region, 2) cut site, and 3) aptamer hybridization region. There are several considerations that need to be recognized when engineering the linker strand. Fortunately, several of them are similar to the requirements for the hybridization region on the anchor DNA strand described above.

The first segment is the anchor hybridization region. It is located near the 3' end of the linker strand. It has five similar guidelines to follow in its design as its complementary part on the anchor strand. 1) Desired melting temperature. 2) Three dimensional structure of the RNA linker strand. Since this strand is RNA instead of DNA, this step becomes a lot more difficult. RNA very readily folds on itself to form multiple structures. Sequences must be designed so that in the presence of the anchor and aptamer strands, the linker strand will be more thermodynamically favored to hybridize with each of them in the appropriate locations then it will be to bind with itself. 3) Intermolecular interactions between the RNA linker strand with itself. 4) Undesired hybridization with anchor and aptamer strands. 5) Considerations on restrictions for

complementary strand. For our particular case there are no special restrictions for the DNA anchor strand so this step does not apply here, however the requirements in the reverse case described previously affect the sequence and still need to be considered.

All of the computer modeling data for conditions 2, and 3, are shown in the data from Figures 3.10 and 3.11. As can be seen it was not as simple to prevent unwanted hybridization for RNA. In order to ensure that all of the conditions have truly been met it is important to analyze the Gibbs free energy values calculated by the computer software. The large differences in values between the desired hybridization reactions compared to the undesired ones indicates that the RNA structure will hybridize appropriately in the presence of both the anchor and aptamer strands. However, there may be some unwanted folding prior to combining all three strands together. This is can be alleviated by heating the linker sample, which will cause it to denature, and then it will hybridize correctly in solution with the other two strands.

The second segment is the cut site. It is located in the middle of the linker strand. This region is much easier to design because it has no second strand to try to hybridize it with. There are only two considerations for this segment, rather it contains uracil, or does not hybridize with anchor or aptamer strands. Containing uracil just means that a lot of uracils are placed in this region so that RNase 4 is able to cut here. The second part about not hybridizing with the other strands is simple because this is the only segment that contains uracil. By limiting certain adjacent nucleotides on the other hybridizing segments, this region should not want to hybridize with the rest of nucleic acid construct because its nucleotide composition is drastically different then the rest of the segments.

Determining how many uracils to place in this region, or separating them with adenines has already been discussed in the previous section.

The third segment is the aptamer hybridization region. It is located on the 5' end of the linker strand. When engineering the nucleotide composition of this region there are six guidelines to follow. The first five are the same as the anchor hybridization region described earlier. The sixth condition involves the fact that this region is located on the 5' end of the linker strand as opposed to the 3' end that the anchor hybridization region is located at. Unlike DNA, which is cheap and quick to order online with a desired sequence, RNA is expensive and time consuming.

In order to get a high yield of RNA material, transcription is more efficient if the first nucleotide is guanine. The efficiency increases even further if the second nucleotide is also a guanine if possible. Therefore, when engineering the twelve nucleotides in this segment, it is ideal to have the first one or two nucleotides be a guanine so that a lot of RNA product can be readily made. It is also important to note that the 5' end of the aptamer strand begins as the complement base to the end of the region, meaning that the last one or two nucleotides should be cytosine. This will allow the aptamer strand to being with guanine. After careful design and consideration of all the guidelines and restrictions on each segment from all three nucleic acid strands, our best layout has two guanines at the start of this region and one cytosine at the end of it, and still meeting all other development requirements.

The computer modeling data for condition 4 is shown in Figure 3.12. The data for base pairing involving the RNA linker strand is in much more depth compared to the DNA data because there are other base pairings possible besides the standard Watson-

Crick base pairing that is essentially the only concern for DNA in our case. Hydrogen bonding is dependent on buffer, salt concentration, and other environmental factors. For RNA these factors play a much bigger role in determining what base pairings will take place. RNA structures can potentially be fluid, which can make crystallization difficult, and adjacent nucleotides become significant when determining the layout for the strand.

It is important to know the order of base pairing strength and preference based on thermodynamics. Here is the order of base pairing preference at standard salt concentrations: G-C > A-T > A-U > G-U > G-T. It is also important to know that when trying to determine the effect of two-dimensional structures on base pairing that loops > overhangs > mismatches. Without this knowledge, it would not be possible to engineer sequences that will obtain desired two-dimensional structures. Furthermore, the computer models are not perfect because there is too much variability with RNA folding, so sometimes human judgment is required to determine if a particular base-pairing predicted by a computer model is accurate by studying adjacent nucleotides and nearby two-dimensional structures.

Finally, the last strand to discuss is the RNA aptamer. Its sequence is shown in Figure 3.13 and contains two different segments. The first is called the linker hybridization region, and the second is the aptamer region. The linker hybridization region has the same six guidelines as the aptamer hybridization just described for the linker strand. In this case it is especially important to make sure that the nucleotide sequence in this region does not affect the three dimensional structure of the aptamer region. The aptamer itself was developed using the process called SELEX, as described in chapter 1. The sequence of nucleotides in this region cannot be modified, meaning that

the linker hybridization region has to be designed so that it has no influence on the structure and function of the aptamer. The computer modeling data for the same conditions showing only desired binding will occur can be seen in Figures 3.14 and 3.15. Additionally, this data also shows that the aptamer structure remains intact and unchanged when the linker hybridization region is attached to it.

Computer models are great tools for engineering nucleic acid platforms, but experimentation needs to be performed to have physical evidence that nucleic acid strands are binding as predicted. First, radioactively label the linker RNA strand and mix all possible combinations of the three strands. Then run these samples on a non-denaturing gel to determine if the right hybridization combinations are occurring by analyzing mobility shifts between all the samples. The data from this experiment is shown in Figure 3.16 and indicates homogeneous samples of the nucleic acid construct (protocol described in detail in the next section). This is the desired result and confirms that the computer models can be used for insight on what the two dimensional structure of the nucleic acid construct may look like.

It is always important to run a second experiment to confirm the first. Plus, the first experiment is not able to show if there are any interactions between the anchor and aptamer strands not accounted for by the computer models because only linker strand is visible from the radioactive label. Repeat the same non-denaturing gel experiment (data not shown) except this time use radioactively labeled aptamer. The result turned out to be the same as the first experiment indicating homogeneous sample of the desired nucleic acid construct without any hybridization occurring between the anchor and aptamer strands.

The aptamer chosen for these experiments is called Pegaptanib. It was chosen because it is currently the only aptamer available on the market for treating an ocular disease. The principles described in this chapter lay the foundation for creating a general nucleic acid platform that can be used for any future aptamers developed for treating other ocular diseases. Current SELEX technology has been advancing rapidly over recent years and it is now becoming more accessible to create successfully functional aptamers. There is great potential for many more aptamers targeting ocular diseases to be developed over the next several years.

3.2.2 Materials, Methods, and Protocols for DNA/RNA Experiments

Materials

Modified and unmodified oligonucleotides were synthesized by Integrated DNA Technologies (Coralville, Iowa). Gel extraction buffer, loading buffer, and all transcription kit components were purchased from Thermo Fisher Scientific (Waltham, MA). PCP and γATP was purchased from PerkinElmer (Waltham, MA). Spermadine, PEI cellulose paper, and PEI cellulose buffer were all purchased Sigma Aldrich (St. Louis, MO). PNK enzyme, RNA ligase, and ligase buffer were all purchased from New England Biolabs (Ipswich, MA). All other equipment and chemicals were of molecular biology grade and unless specified were purchased from VWR (Radnor, PA).

Purification of DNA Anchor Without Acrydite Modification

Make a 10% 19:1 acryl/bisacrylamide TBE/urea denaturing gel and pre-run it at 12watts for 30 min to heat the gel, use 1X TBE buffer for running. Take 10 µL's of purchased 1µM DNA Anchor and add 10 µL's of F buffer. Heat sample at 800C heat block for 3 min, then place on ice for at least 5 min. Prepare a blank sample by using 10 µL's of 1X TBE buffer + 10 µL's of F buffer. A blank sample will reduce the "smiling effect" caused by gels when loading large quantities of material in the wells. The "smiling effect" is when samples of the same material or size have different mobility's that curve on the edges, but in reality the samples are the same or at least the same size so the mobility should be the same as well. Divide the actual sample into four wells of 5 µL's each and run the gel at 12watts for 50 min.

Use a UV light source technique, called UV shadowing, to visually see the location of the DNA samples in the gel and cut out the bands from the gel using a sterile blade that is heated with a Bunsen burner. Put the cut gel pieces into an eppendorf tube, then take a pipette tip and use it to break up the cut gel pieces containing the DNA into many small pieces to increase the surface area of the gel. Soak the gel pieces with DNA gel extraction buffer (500 µL's in this case), then place on a rocker with 2.5 setting and let sit at room temperature overnight.

Remove DNA gel extraction buffer and place in a new eppendorf tube, leaving gel pieces behind. Add 150 µL's of DNA gel extraction buffer to the tube with the gel pieces, vortex for 1 min, then centrifuge at 13,200rpm for a few seconds. Remove the DNA gel extraction buffer from the tube with the gel pieces and combine it with the other tube containing the rest of the DNA gel extraction buffer, then discard the tube with the

gel pieces. Determine the volume of the sample (~620 µL's in this case). Add 5X the current volume of 100% cold EtOH and store at -20^{0}C overnight.

Centrifuge sample at 9000rpm for 15 min at 4^{0}C, remove supernatant, add 5X volume of 70% cold EtOH, and let sit on ice for 10 min. Centrifuge sample at 9000rpm for 15 min at 4^{0}C, remove supernatant, add 5X volume of 70% cold EtOH, and let sit on ice for 10 min. Centrifuge at 9000rpm for 15 min at 4^{0}C, remove supernatant, add 100 µL's of RH_2O, and let sit on ice for 10 min. Finally move the sample, now called anchor strand, to a new eppendorf tube to get rid of any remaining EtOH and store on ice. A 3 µL aliquot of the final anchor strand sample was again tested on a 10% 19:1 acryl/bisacrylamide TBE/urea denaturing gel alongside the unpurified original purchased DNA Anchor as a control and blank samples to confirm a purified product indicated by a single sharp band with mobility in the appropriate location.

Quantification of DNA Anchor

Absorbance of anchor strand sample was determined by taking a 2 µL sample and measuring with a nanodrop spectrophotometer. A230, A260, A280, and A320 values were recorded during the reading. A230 measures contamination of the sample with salts or solvents (when compared as a ratio to A260) such as phenol, A260 measures the concentration of nucleic acids, A280 measures contamination of the sample with proteins (when compared as a ratio to A260), and A320 measures turbidity adjusting for any other contaminates in the solution. The A260/A230 and A260/A280 ratios should both be greater then 1.8 for DNA (2.0 for RNA) to indicate a high quality sample; both of these ratios were around 1.88 for the anchor strand sample meaning the sample is considered

pure. The absorbance value at A260 should be subtracted by the value from A320 first before being used for quantification (A260-A320). The final absorbance after subtracting for turbidity was used for calculating concentration of the anchor strand. It should also be noted that the absorbance value needs to be between 0.1-3 for an accurate reading.. If the sample absorbance is above the value of 3, then it needs to be diluted and that dilution factor is then accounted for when calculating concentration of the sample.

Calculating concentration is done using the Beer-Lambert equation which is $C = A/(\varepsilon * L_p)$, where C is concentration, A is absorbance, ε is extinction coefficient, and L_p is path length. Extinction coefficient of the anchor strand is calculated using the IDT oligo analyzer and is based on the specific sequence and length of the anchor strand. This calculation was determined to be 149,500 L/(mol*cm). The path length is the distance of the signal for measurement by the machine and for the nanodrop used this value was 0.1cm according to the manual. The final concentration calculated for the anchor strand sample using this equation was 69nM. The anchor sample had the lowest concentration of the three nucleic acid strands, and therefore, the other two strands were diluted to match this value for the hybridization experiments.

Transcription of RNA Linker

An aliquot of 5 µL of 1µM L5prime (DNA template) + 5 µL of 1µM L3prime (DNA template), then removed 0.5 µL as a negative control. Placed sample on 80^0C heat block for 3 min, then in 37^0C incubator for 1h, after which added 85.5 µL TE buffer pH 8.0. This sample was called template. For negative control added 9.5 µL TE buffer pH 8.0 and 2 µL of 6X loading buffer. In a new eppendorf tube added 96 µL of 2X T7 buffer

-, 4 µL of spermadine, 50 µL of NTP's, 27 µL of RH_2O, and 20 µL of template. For second negative control removed 5 µL of this solution and added 1 µL of 6X loading buffer to that. Back to the sample added 4 µL of 1:50 T7 polymerase and 4 µL of Suparase. Place in 37^0C rolling incubator for 2h, after which this sample will be called DNA/RNA.

Next, the sample needed to undergo phenol extraction. Take 200 µL of DNA/RNA + 20 µL of 3M NAOAc pH 5.5 and put in 660 µL of 100% EtOH. For third negative control removed 2 µL and add 8 µL of RH_20 + 2 µL of 6X loading buffer. Back to the sample, added 98 µL of phenol pH 4.5, vortex for 1 min, then centrifuged at 13,200rpm for 2 minutes at room temperature. Extracted the top phase layer and put into a new eppendorf tube, then discarded the interface and bottom layers. Determined the volume of the top layer and add 1/10 of the current volume of 3M NaOAc pH 5.5. Then added 3X the new current volume of 100% cold EtOH. Inverted and flicked the tube, let sit on ice for 10 min, then stored at -20^0C overnight.

The next step was ethanol precipitation, which began by centrifuging the sample at 13,200rpm for 10 min at 4^0C. Discarded the supernatant and added the same volume of 70% cold EtOH. Flicked the tube, let sit on ice for 10 min, and then centrifuged the sample at 13,200rpm for 10 min at 4^0C. Discarded the supernatant and added the minimal amount of RH_2O needed to dissolve the pellet (in order to maximize concentration of sample), then let sit on ice for 10 min, this final product was called RNA transcript. Note: If final sample was too dilute, speed vacuum after freezing sample in -80^0C to concentrate sample. Took 2 µL of RNA transcript to use for the gel test and added 8 µL of RH_2O and 2 µL of 6X loading buffer.

Gel Test for RNA Linker

For gel controls: 8 µL of 0.1µM L5prime + 2 µL of TE buffer pH 8.0 + 2 µL of 6X loading buffer. 8 µL of 0.1µM L3prime + 2 µL of TE buffer pH 8.0 + 2 µL of 6X loading buffer. 40 µL of 0.5X TBE buffer + 8 µL of 6X loading buffer was created to use as a blank sample. Made a 15% Karzai gel by combining 12mL of 50% 19:1 Acryl/Bisacrylamide with 4mL of 5X TBE buffer and 24mL of double distilled water (ddH_2O). Then added 80 µL of TEMED followed by 60 µL of 50% ammonium persulfate (APS), gel took ~1h to polymerize. Use 0.5X TBE as the running buffer. Ran the gel at 100volts for ~12h at 4^0C. Gel was stained by soaking for 10 min on a rocker with a 2.5 setting in 100mL of ddH_2O and added 5 µL of ethidium bromide. Gel was then washed for 5 min on a rocker with a 2.5 setting in 100mL of ddH_2O. Stain and wash solutions were inactivated by using a pellet of NaOH and dissolved for 10 min on a rocker with a 2.5 setting. The samples that were loaded into the gel were as follows: blank, L5prime control, L3prime control, first negative, second negative, third negative, linker strand, and blank. Picture of gel was taken to confirm results of controls and sample.

Purification of RNA Linker

At this point the newly made RNA transcript was produced and separated from the proteins and salts, but now it needs to be separated from the DNA template and any free nucleotides that may still be in the sample. A DNase 1 experiment followed by gel extraction was performed to accomplish this goal. Volume of RNA transcript sample at

this point was 40 µL. To this sample added 10.8 µL of 5X DNase 1 buffer + 2.7 µL of DNase 1 enzyme. Placed sample in 37^0C incubator for 1h, then added 53.5 µL of F buffer, and put sample on heat block at 80^0C for 3 min, then ice for 5 min, prior to loading in a gel. Made a 10% 19:1 acryl/bisacrylamide TBE/urea denaturing gel and pre-ran it at 12watts for 30 min to heat the gel, used 1X TBE buffer for running. Divided the sample into several wells to get thinner bands, but loaded the entire 107 µL of sample in the gel. Ran the gel at 12watts for 50 min.

Used UV shadowing to visually see the location of the RNA samples in the gel and cut out the bands from the gel using a sterile blade that was heated with a Bunsen burner. Put the cut gel pieces into an eppendorf tube, then took a pipette tip and used it to break up the cut gel pieces containing the RNA into many small pieces to increase the surface area of the gel. Soaked the gel pieces with RNA gel extraction buffer (500 µL in this case), then placed on a rocker with 2.5 setting and let sit at room temperature overnight.

Removed RNA gel extraction buffer and placed in a new eppendorf tube, leaving gel pieces behind. Added 150 µL of RNA gel extraction buffer to the tube with the gel pieces, vortexed for 1 min, then centrifuged at 13,200rpm for a few seconds. Removed the RNA gel extraction buffer from the tube with the gel pieces and combined it with the other tube containing the rest of the RNA gel extraction buffer, then discarded the tube with the gel pieces. Determined the volume of the sample (~620 µL in this case). Added 5X the current volume of 100% cold EtOH and stored at -20^0C overnight.

Centrifuged sample at 9000rpm for 15 min at 4^0C, removed supernatant, added 5X volume of 70% cold EtOH, and let sit on ice for 10 min. Centrifuged sample at

9000rpm for 15 min at 4^0C, removed supernatant, added 5X volume of 70% cold EtOH, and let sit on ice for 10 min. Centrifuged at 9000rpm for 15 min at 4^0C, removed supernatant, added 100 µL of RH_2O, and let sit on ice for 10 min. Finally moved the sample, now called linker strand, to a new eppendorf tube to get rid of any remaining EtOH and stored on ice. 3 µL of the final linker strand sample was again tested on a 10% 19:1 acryl/bisacrylamide TBE/urea denaturing gel alongside the template strands as controls and blank samples to confirm a purified product indicated by a single sharp band with mobility in the appropriate location.

Quantification of RNA Linker

Absorbance of linker strand sample was determined by the same approach as the DNA anchor. This time the A260/A230 and A260/A280 ratios should both be greater then 2.0 for RNA, and both of these ratios were around 2.12, meaning the sample is considered pure. The extinction coefficient for the linker strand was determined to be 278,000 L/(mol*cm). The final concentration calculated for the linker strand sample was 595nM. The sample was not diluted to match the anchor strand at this point because it needed to be made radioactive first.

Preparation of Radioactively Labeled RNA Linker Strand

The first step was to make PCP, which is a Cytosine base with an extra phosphate that is radioactive. This PCP was added to the linker strand using a ligation reaction, which created a radioactive linker strand. Another possible method is to use [32P-α] ATP during the transcription process, which could have been used for this process as well, but

was not chosen. First was to combine 18 μL of PCP with 4 μL of radioactive γATP + 0.6 μL of free polynucleotide kinase (PNK) enzyme. Placed on a 37^0C incubator for 1h, then placed on a 95^0C heat block for 1.5 min to kill the enzyme, and stored in -20^0C.

Next, the PCP needed to be tested. Took 0.1 μL of PCP reaction mix and added it to 9.9 μL of RH_2O. Placed 0.5 μL of this sample onto PEI cellulose paper and allowed the sample on the paper to dry. Put the paper on a metal tray inside of a glass box and poured PEI cellulose buffer inside the glass box until just the bottom of the paper was dipped inside the buffer. Sealed the lid of the glass box by using vacuum grease to make the container airtight. Allowed the buffer to run up the gel paper to near the top; this process took approximately 1.5h. After this time, removed the paper from the glass box and wrapped it in saran wrap. Exposed the paper to Kodak film for ~3 min in the dark room, then developed the film to view the results. The film showed the radioactive PCP sample ran partially up the gel while the remaining unreacted γATP was visible at the initial point where the sample was placed; this indicated a successful reaction for creating radioactive PCP, which will now be called γPCP.

The final step was to label the linker strand with γPCP. It is important to note that the volume of the γPCP sample being added cannot exceed 1% of the total volume because it will inhibit the reaction. Since the desired total volume being prepared was 20 μL, the maximum volume for γPCP that can be used is therefore 2 μL. For this final sample, took 8 μL of RH_2O and added 4 μL of 5X ligase buffer + 2 μL of γPCP + 0.5 μL of RNA ligase, then placed the sample in 37^0C incubator for 1h. Took 1 μL of this final product, now called radioactive linker strand, and tested it on a 10% 19:1 acryl/bisacrylamide TBE/urea denaturing gel to make sure the reaction worked. Finally,

purified the radioactive linker strand from excess γPCP by using a gel following the same protocol described in the purification of RNA linker section (except no need to repeat the DNase 1 protocol portion described in the first three sentences of the first paragraph). Also instead of UV shadowing, the wet gel was covered with saran wrap and Kodak film was placed on the gel in the dark room to expose the location of the RNA in order to know where to cut the bands in the gel.

At this point the radioactive linker sample concentration was determined. This was done by using Cherenkov counting when putting the sample in a scintillation counter. Using the known cpm count from the original γATP sample plus a radioactive decay table to account for the time it took to make the sample, the concentration was determined based on the cpm count measured from the scintillation counter. The final concentration was calculated to be 88nM. From here, the sample was diluted to match the concentration of the anchor strand sample so that 1:1 volume ratios could be used for experiments involving hybridizing the strands together.

Transcription, Gel Test, Purification, and Quantification of RNA Aptamer

Production of purified RNA aptamer followed the exact same procedure as the RNA linker, except the starting DNA templates were different. A5prime and A3prime DNA templates were used at the start of the transcription protocol instead. Both the linker and aptamer sequences were designed to have their initial nucleotides be a guanine. It is known that transcription efficiency is increased significantly if the first nucleotide for each RNA sequence is a guanine. Since both strands were designed to have high

transcription efficiency, they both produced similar final concentrations for the same volume of sample.

The extinction coefficient for the aptamer strand was determined to be 385,000 L/(mol*cm). The final concentration calculated for the aptamer strand sample was 664nM. The sample was diluted to match the concentration of the anchor strand sample so that 1:1 volume ratios could be used for experiments involving hybridizing the strands together. Radioactive aptamer was also made following the same protocol as the linker as a second experiment to confirm appropriate hybridization between the anchor, linker, and aptamer. This data confirmed the result of the experiment using the radioactive linker, since this data gives the same result it was not shown.

Hybridization of Anchor, Linker, and Aptamer

Began by making a 15% Karzai gel by combining 12mL of 50% 19:1 Acryl/Bisacrylamide with 4mL of 5X TBE buffer and 24mL of double distilled water (ddH_2O). Then added 80 μL of TEMED followed by 60 μL of 50% ammonium per sulfate (APS), gel took ~1h to polymerize. Used 0.5X TBE as the running buffer. Ran the gel at 200volts for ~4h in 4^0C. Gel was dried using a heater and vacuum, then wrapped in saran wrap. A Kodak film was exposed to the gel to visualize the radioactive bands and produce the picture shown in Figure 3.16. The order of the samples loaded in the gel was shown in the picture, but consists of the following (bottom to top): radioactive linker strand only, anchor strand plus radioactive linker strand, radioactive linker strand plus aptamer strand, and anchor strand plus radioactive linker strand plus aptamer strand.

Here is described the preparation of the samples from the gel in Figure 3.16. Each sample contains an excess of radioactive linker strand to ensure maximum binding was detected. Radioactive linker strand only: 5 μL of RH_2O + 1 μL 10X binding buffer + 4 μL of radioactive linker strand. The 10X binding buffer is: 350 μL of RH_2O + 400 μL of 5M NaCl + 200 μL of 1M Tris/HCl pH 7.5 + 50 μL of 1M $MgCl_2$. This made a 2M NaCl, 200mM Tris/HCl pH 7.5, 50mM $MgCl_2$ solution inside the 10X binding buffer. Anchor strand plus radioactive linker strand: 2.5 μL of RH_2O + 2.5 μL of anchor strand + 1 μL 10X binding buffer + 4 μL of radioactive linker strand. Radioactive linker strand plus aptamer strand: 2.5 μL of RH_2O + 2.5 μL of aptamer strand + 1 μL 10X binding buffer + 4 μL of radioactive linker strand. Anchor strand plus radioactive linker strand plus aptamer strand: 2.5 μL of anchor strand + 2.5 μL of aptamer strand + 1 μL 10X binding buffer + 4 μL of radioactive linker strand. All four samples were placed in a 37^0C incubator for 15 minutes, then on ice for 5 minutes before loading into the gel.

3.2.3 Materials, Methods, and Protocols for Hydrogel Experiments

Materials

Modified and unmodified oligonucleotides were synthesized by Integrated DNA Technologies (Coralville, Iowa). Loading buffer was purchased from Thermo Fisher Scientific (Waltham, MA). γATP was purchased from PerkinElmer (Waltham, MA). HEMA, pHEMA, 2-hydroxy-2-methyl propiophenone (HMPP) were all purchased from Sigma Aldrich (St. Louis, MO). PEGDMA's were purchased from Polysciences Inc. (Warrington, PA). All other equipment and chemicals were of molecular biology grade and unless specified were purchased from VWR (Radnor, PA).

HEMA Gel Formulations

All percentages for HEMA, the various cross-linkers, and photoinitiator HMPP are mole percent's. The equation used for calculating the various HEMA percentages used were as follows: (1-0.01-X)*(molecular weight of HEMA)/(density of HEMA), where 0.01 was the percent for HMPP and X was the desired cross-linker percent in decimal form. The equation used for calculating the various cross-linker percentages followed similarly: (desired cross-linker percent in decimal form)*(molecular weight of cross-linker)/(density of cross-linker). Likewise, the equation for calculating the photoinitiator for polymerization, HMPP, was done in a similar manner: (0.01)*(molecular weight of HMPP)/(density of HMPP). HMPP was always kept constant at 1% for all experiments, and cross-linker percent was always the variable amount chosen for testing. The values from all three equations were then added together to create a total value; then each individual equation answer was divided by this total value. This resulted in an answer in μL for each component to add to make the desired mole percentages and give a total gel volume of 1mL. Radioactive free nucleotides (γATP) or radioactive DNA strands (43bp) were added to each gel at a total volume of 2 μL. The additional volume and material from nucleic acid samples was considered insignificant and therefore ignored in all calculations involving the gel formulation.

Values used for these equations are described in this paragraph. HEMA: molecular weight 130,000mg/mol, density 1073mg/mL. PEG600DMA: molecular weight 798,220mg/mol, density 1126mg/mL. PEG2000DMA: molecular weight 2,198,220mg/mol, density 730mg/mL. PEG8000DMA: molecular weight 8,198,220mg/mol, density 150mg/mL. pHEMA: molecular weight

~1,000,000,000mg/mol, density 1150mg/mL. HMPP: molecular weight 164,200mg/mol, density 1077mg/mL. All water percentages are based on volume instead of mole percent.

There are two ways this lens can be polymerized, either by radiation or redox. The radiation approach used UV light exposure for time period ranging from 2-10 minutes UV light has an efficiency of less than 5% for cross-linking or mutating DNA or RNA strands for extended periods of exposure [35]. Given that our time period is only 10 minutes or less, the effect of the UV light on the DNA or RNA in our lens solution should be negligible. The redox method used Ammonium persulfate (APS) and Tetramethylethylenediamine (TEMED) to polymerize the lens solution. This reaction was exothermic and the heat given off could potentially affect the hybridization of the nucleic acids, but the amount of APS and TEMED used can be controlled and therefore the rate of polymerization of heat given off can be controlled. If the reaction was allowed to run for an hour or longer before polymerization is completed, this would vastly reduce the amount of heat exposed to the nucleic acids at any one instant moment preventing any problems with hybridization that could potentially occur.

Preparation of HEMA Gel Experiments for Radioactive Free Nucleotides

Radioactive free nucleotides were used initially to test the compatibility of nucleotides with the HEMA gel. First, each of the three different PEGDMA sizes were made in formulations at 0.15% and vortexed, these formulations were then put in three contact lens molds each (all HEMA experiment samples were done in triplicate). Aliquots of 200 μL of each formulation were used per contact lens mold. These lenses also had radioactive free nucleotides of 2 μL added to each one and initial cpm counts

were measured on the scintillation counter for each gel. Each mold was then sealed with pincers and exposed to UV light for 2 minutes for polymerization. Then each polymerized gel was removed from the molds using tweezers and soaked in 1mL PBS solution. Every 30 min for the first 4h, the gels were placed in new 1mL PBS solution. After 4h all of the collected PBS solutions were measured in the scintillation counter, as well as the gel itself to determine how much sample was releasing from the gel at each time point and how much remained in the gel based on the initial cpm reading.

Based on the results from that experiment, PEG8000DMA worked the best and was then chosen for the next experiment, testing effect of cross-linker percent. Three different cross-linker percentages were chosen, 0.15%, 0.22%, and 0.45%, using PEG8000DMA and the gel formulations were made. Similar to the previous experiment, each gel was polymerized by the same method and soaked in the same manner. However, this experiment ran for 5h instead of 4h. All of the samples were collected and measurements of free radioactive nucleotides were calculated in the same manner.

The best result from the previous experiment was the 0.15% PEG8000DMA gel formulation, so therefore it was used for the next study testing the effect of water. Two different methods were tested for this approach. One was to introduce water into the gel formulation after the gel formulations were made, while the second method was to introduce additional water into each individual component before combining to make the gel formulation. Both methods had the same amount of water, but this was done because it was noticed that gel formulations would tend to have phase separation in the presence of water to a small degree when water was added directly into the gel formulation, but this did not happen if the water was added to the components before the gel formulation.

The result from this experiment showed no significant difference in release of radioactive free nucleotides, but it was worth checking. A third lens was made containing no additional water for comparing changes in release rate. Samples were soaked in 1mL PBS as usual and collected at 5 min, 15 min, 30 min, 60 min, 120 min, 180 min after which it was noticed nearly all of the material had released, one final time point was done at 24h to see if any of the small amount of remaining material would come out at different rates.

Preparation of HEMA Gel Experiments for Radioactive DNA Strand

The next step after testing compatibility of nucleotides with the HEMA gel formulation was to test release based on appropriate size to the desired aptamer. This was done by testing the release rate of radioactive DNA about 43bp long, a similar length to the RNA aptamer chosen for this project. RNA aptamer product was scarce, so DNA was used instead since the most important aspect was the size. Three different gel formulations were made, one using 0.15% PEG8000DMA cross-linker with 10% water, another using 0.15% PEG8000DMA cross-linker with no additional water (data not shown since result was 0% release), and the last was using 9% PEG8000DMA cross-linker; a relatively large increase just to see if the large amount would have a different effect then what was seen previously with smaller increases in cross-linker percent. Samples were soaked in 1mL PBS and collected every half hour for the first 6h, then once a day for up to 7 days.

After noticing the low release rate of the radioactive DNA, but viewing the trend that more HEMA and larger cross-linker size always meant more release, it was decided

to use pHEMA in order to keep the gel at 99% HEMA based material while increasing pore sizes. Unfortunately, there were limitations to the ratio of pHEMA that could be present in the gel formulation in order to obtain a, clear, mechanically durable, yet flexible gel similar in consistency to a standard contact lens. The highest amount of pHEMA that could be put in the gel formulation to meet these criteria was when the ratio of HEMA to pHEMA was 1.6:1.

It was decided that additional ratios of 2:1 and 3:1 would also be tested. The 10% water was not added to these gels for this experiment; the previous experiment showed 0% release of radioactive DNA when no water was present so this experiment when compared to that result will show the effect of pHEMA on release rate. pHEMA percentages were determined using the same equation as the PEGDMA cross-linkers. The only difference was that HEMA and pHEMA were determined together to make the selected ratios instead of choosing a desired cross-linker percent and then HEMA percent was decided based on that value. These gels were made and polymerized in the same manner as the previous gels using PEGDMA cross-linker. Samples were soaked in 1mL PBS and collected every half hour for the first 6h, new PBS solution was added at each collection, then collection continued once a day for up to 7 days.

The final experiment was testing the covalent binding of the Acrydite modification group on the anchor DNA to the HEMA gel. Contact lens solutions (98.85% HEMA, 0.15% PEG8000DMA, 1% HMPP) containing 2 µL of 0.1µM anchor DNA or 2 µL of 0.1µM anchor [acrd] DNA were polymerized into wells of an 8% TBE/urea denaturing gel and gel electrophoresis was performed. Gel was stained by soaking for 10 min on a rocker with a 2.5 setting in 100mL of ddH_2O and adding 5 µL of ethidium

bromide. Gel was then washed for 5 min on a rocker with a 2.5 setting in 100mL of ddH_2O. Stain and wash solutions were inactivated by using a pellet of NaOH and letting dissolve for 10 min on a rocker with a 2.5 setting.

ImageJ analysis software quantified amount of material released compared to amount remaining in the HEMA gel located in the well of the TBE/urea gel. The amount released was compared between the modified and unmodified anchor DNA samples to see the effect of the Acrydite modification on release. It is important to note that the anchor [acrd] strand was not purified before this experiment, so there was potentially unmodified anchor strands in that sample as well, which effected the percentage of release.

3.2.4 HEMA Gel Dynamic Release Study

The first step was to confirm that nucleic acids can be incorporated into a HEMA hydrogel without precipitating and that their release profile can be modulated by changes in lens solution composition and mesh size. Many lenses were crafted with free nucleotides and DNA to determine if the molecules are able to freely release from the hydrogel and dissolve in solution. After confirming that polymer lenses with nucleic acids were optically clear and formed a stable structure (images not shown), release studies were conducted with varying factors on the composition of the lens solution.

The lens solution used consisted of 98.85% HEMA, 0.15% PEG8000DMA, and 1% HMPP. Deviations from this recipe are explained in the data from this section below. Originally each experiment was performed using contact lenses polymerized by both the UV light and redox methods. However, the results were the same so only the UV light

method lens data are shown in this section. Every lens used for experiments was fully intact, maintained its structural integrity throughout.

Release studies were performed by using radioactively labeled nucleotides and DNA and measuring the amount of cpm's inside of a polymerized lens as recorded by a scintillation counter. At each point indicated in the respective data below, the solution soaking the lenses was removed and cpm's remaining were counted from the lens using the scintillation. A small volume was necessary for measurements using the scintillation counter. PBS was the chosen solution because it better mimics tear fluid compared to water. Every time point for every experiment in this section is an average of three lenses.

The first test was to vary cross linker size in order to see how sensitive the release of single nucleotides is inside of the HEMA gel lens solution. After testing PEGDMA cross linkers with sizes of 600, 2000, and 8000, it was clear that nucleotide release rates followed the expected trend as shown in Figure 3.17.

This result is what was expected and it can be seen that using PEG8000DMA, free nucleotides can be released from a polymerized hydrogel, even at a small cross-link percentage. The next step was to use the PEG8000DMA cross-linker and increase the percentage of cross linker. The free nucleotides released with the same profile as before using the 0.15% amount, but increasing the percentage of cross-linker resulted in a decreased release of free nucleotides, as can be seen in the data shown in Figure 3.18.

This is the expected result, as more cross-linker should allow more junctions to form reducing the mesh SIZE in the polymer. However, since HEMA percent is also changed when performing this study, the effect of HEMA should also be discussed. Therefore, another possible explanation is that because increasing the PEG cross-linker

percent results in a decreased percentage of HEMA, there is less HEMA to absorb water. It is possible that less water absorbed in the lens could decrease the release rate of free nucleotides in the hydrogel by reducing the free volume for transport.

Another study was done to see if water had a significant impact on the hydrogel, see Figure 3.19. Water was added to the 0.15% PEG 8000 HEMA gel lens solution so that 10% by volume was water. The release rate was tested and after 24 hours, 97.5% of the free nucleotides were removed from the lens (Figure 3.19 lens 1 and 2). The only difference between lens 1 formulation and lens 2 formulation was the order for when the water was added to the gel solution. The release percentage is comparable with the HEMA gel solution containing no additional water (lens 3). However, it is important to note that since the release was already near 100% and moving very rapid, the effect of water may have been masked. It is possible for samples releasing more slowly or at lower percentages that would water would have an effect on release rate. The image containing this data shows the radioactive cpm values of the hydrogel at each time point, instead of percentage, to show another viewpoint of the same release study.

Higher water percentages (20% and 40%) were also tested and nearly 100% of the free nucleotides were released in each case (data not shown). More water means polymer density is less so release rate will increase. In order to see if water is helping the release rate, additional experiments would need to be performed using a different lens solution composition that releases significantly less than 100% of the nucleic acids. However, that goes against the goal of this experiment to create a lens solution that achieves nearly 100% release of free nucleotides, and that was successful, so the avenue for testing water's effect on release rate was not studied any further.

After having successful results with free nucleotides incorporated into our HEMA gel lens formulation (98.85% HEMA, 0.15% PEG8000DMA, 1% HMPP), the next step was to test DNA strands that were approximately the same length as the RNA aptamer strand. DNA was used instead of RNA due to time and cost considerations for these experiments. The same experiments above were repeated and the results were drastically different than what was expected. The DNA strands released nearly 0% of the amount of DNA incorporated into the polymerized lens (data not shown). Using the same formulation with 10% by volume of water added, an increased release close to 9% was obtained. Testing the effect of increasing PEG cross-linker percent and decreasing HEMA percent resulted in even less of the DNA being released as expected, which can be seen from the data in Figure 3.20. This is the same trend seen in the data from Figure 3.18 with the free nucleotides.

Our data indicates that higher HEMA content results in a greater amount of DNA released from the hydrogel, so pHEMA was added instead of PEG cross-linkers.. Increasing the ratio of pHEMA to HEMA in the lens solution successfully increased the percentage of DNA released from the hydrogel, as can be seen in the data shown in Figure 3.21. Our final conclusions from these studies are that HEMA and increased water content improve the release of nucleic acids. Additionally, larger HEMA molecules such as pHEMA, also improved release. These properties are good to know for future experimentation with the effect of HEMA hydrogels on nucleic acids. Further release study experimentation will not be conducted, because the goal of this experiment was simply to test the behavioral effects of various lens solutions and options on nucleic acids, and that goal was accomplished.

The last experiment that needed to be conducted involving the polymer effect on nucleic acids is the Acrydite modification on the anchor DNA strand. Because the percentage of DNA released from the studies above was minimal, this experiment was conducted using gel electrophoresis to force the DNA out of the hydrogel. Contact lens solutions (98.85% HEMA, 0.15% PEG8000DMA, 1% HMPP) were polymerized into wells of an 8% polyacrylamide denaturing gel and gel electrophoresis was performed.

Percent release was measured by cutting out the HEMA gel from the well and the band of DNA that traveled through the polyacrylamide gel. Autoradiography was performed in order to see the location of the DNA that traveled through the gel. For the experiment, some lens solution samples contained DNA with the Acrydite modification, and the rest without. The same amount of DNA was loaded for both cases. If the Acrydite modification covalently binds to the HEMA gel, then there should be no DNA release from the modified DNA samples, but full release should occur with the unmodified DNA samples.

Results from this experiment indicate that the Acrydite modification is successful at covalently binding to the HEMA gel, as can be seen from the data in Figure 3.22. Only 35% of the Acrydite modified sample was released compared to nearly 100% of the unmodified sample. The 35% of DNA that was released from the HEMA gel could potentially be DNA in the sample ordered online that was not successfully modified, but was also not purified and removed before being shipped. Because the modified and unmodified DNA samples are almost the same size, it is difficult to test for this theory. Since the DNA samples purchased were not exposed to extensive purification protocol, there is a good chance that this is most likely the cause of the 35% of DNA released.

3.3 Conclusions

Engineering a nucleic acid construct for releasing drug from a contact lens is favorable for many reasons. First, there is only one RNase in the tear fluid allowing for specific control of RNA cleaving with minimal restrictions or concerns for total degradation during application *in vivo*. DNA can be cheaply modified with an Acrydite group for covalently binding to polymers commonly used in contact lenses. The contact lens polymer HEMA is hydrophilic and therefore is compatible with nucleic acids. Aptamers, such as Pegaptanib, can be developed to treat ocular diseases so creating an all nucleic acid construct for both a delivery platform and as the drug itself is possible.

Computer modeling is a helpful tool for engineering the nucleic acid platform. It is capable of predicting "likely" 2D structures to form based on Gibbs free energy. Though the structures are merely speculation and cannot be considered as fact, the Gibbs free energy calculations are able to confirm if a linear structure or 2D structure in general will form. Since these experiments were designed to create linear structures and not a specific 2D structure, the analysis used here based on the computer models is accurate and reliable for this purpose. The computer models can also be used to determine if a structure is expected to change, in the case of the aptamer, when additional nucleotides are added, but not to confirm an exact structure. The engineered sequences during the design process were regularly checked with the computer models for these effects, which can be accurately determined in this manner.

Release rate of free nucleotides was tested with different variables for optimization. Increasing PEG cross-linker size increased release rate as expected. This is due to increasing pore size. Increasing PEG cross-linker percentage decreased release rate

also as expected. Water content was also checked on the release, but because our free nucleotide samples already release nearly 100% at a rapid rate, no noticeable effect was detected. Water content did seem to have a positive effect on the release rate of DNA strands the same length as our aptamer, since the release rate was much lower for these samples.

The DNA strands showed the same behavior as free nucleotides in terms of HEMA percent resulting in an increase release rate compared to lower HEMA percent due to decreased PEG cross-linker percent. This second experimental result agreeing with the first helps confirm our experimental results. Finally, replacing the PEG cross-linker with pHEMA showed increase DNA strand release as pHEMA cross-linker percent increased. This test proved our hypothesis by demonstrating that HEMA is the main factor for increased release, and increasing the pore size by increasing the percent of pHEMA cross-linker further increased release rate as anticipated.

Future work is to test that the functionality of the aptamer remains after it is cut and released from the contact lens. This includes doing experiments that show the RNase 4 enzyme is capable of entering the polymerized lens and cleaving at the appropriate site. Finally, optimization of drug concentration and desired release rate profiles can be worked out by modulating the cut site and polymer composition in order to create a new ocular therapeutic delivery platform with highly tuned and extended drug release capabilities.

3.4 Tables & Figures

Table 3.1. Summary of important properties about the tear film layer of the eye. *Properties of the tear film necessary to know before engineering a drug delivery platform released by the tear fluid. In particular, there is only one RNase present in the tear film meaning there is only one cutting mechanism allowing for a more controlled release.*

Volume	**6-8 µl**
Rate of tear secretion	**1.2 µl/min**
Turn over rate	**16% per min**
RNase's present	**RNase 4**
pH	**7.2-7.7**
Central corneal temperature	**33°C-34°C**

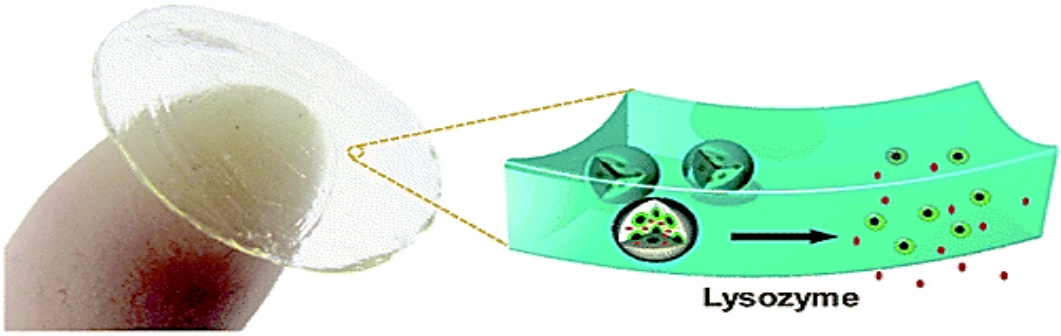

Figure 3.1. Enzyme cleavable polymers degrade lens affecting its properties. *This schematic demonstrates one potential drug delivery approach using contact lenses. There are a few drawbacks to this method including possible transparency issues and integrity of the lens being altered.*

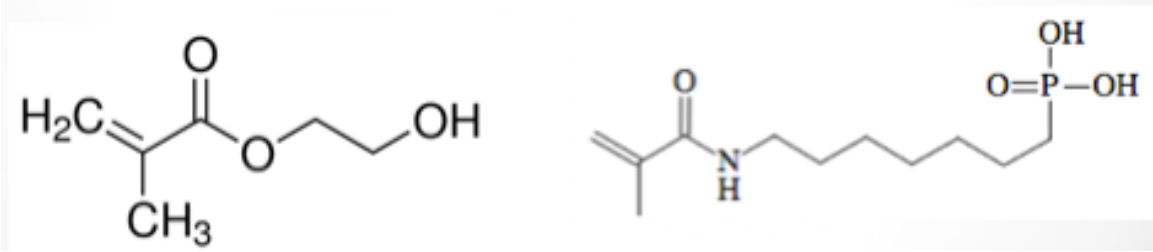

Figure 3.2. 2D Images of HEMA & acrydite molecules. *HEMA (**left**) and Acrydite (**right**) both have double bonded carbons capable of reacting together using UV light or redox.* Shown here are *2D molecular construct images of HEMA and Acrydite used in the polymerization of our DNA anchor to the polymer forming the hydrogel.*

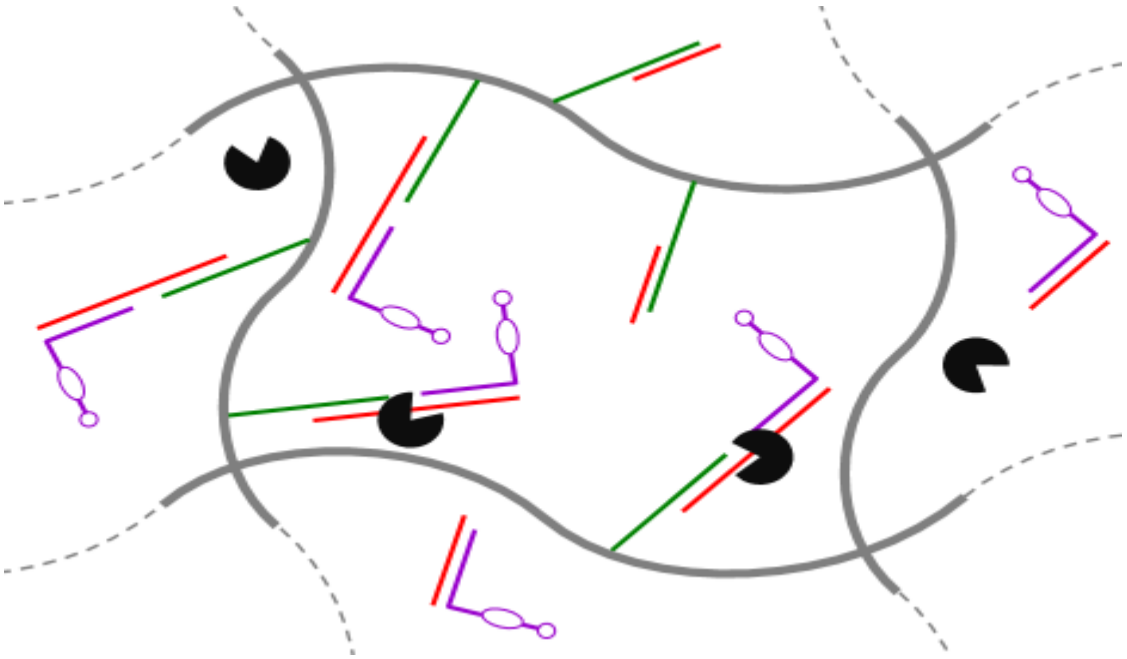

Figure 3.3. HEMA-nucleic acid drug delivery hybrid platform. *Schematic demonstration of the DNA/RNA construct bound inside the hydrogel. Black spheres represent RNase 4 inside the tear film. Anchor DNA (**green**) binds to the polymer network via an Acrydite group. A linker RNA strand (**red**) is engineered to hybridize to both the anchor DNA and the aptamer Pegaptanib (**purple**). The design of the linker strand is imperative to creating the ideal structure shown above. Pegaptanib is modified with a 5' tail to hybridize with the linker, but not alter its 3D structure.*

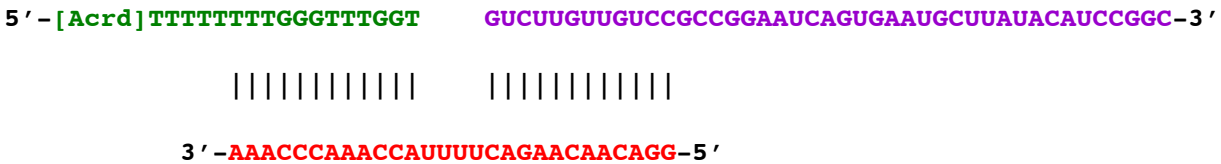

Figure 3.4. Nucleic acid construct. *Expected hybridization layout of DNA anchor (**green**) with RNA linker (**red**) and modified Macugen (**purple**). Here the sequences are shown that were used to ideally make a structure forming the exact construct shown in Figure 3.3. The 5' anchor DNA end up to the first 5 nucleotides as well as the sequences in the pegaptinib aptamer must remain unchanged. This means the linker strand must be engineered to work around these limitations when selecting the sequences for the hybridization portions. In addition, the linker also contains the cleavage site for releasing the drug, which is the series of U's found in the middle of the sequence. This can be the only portion where unmodified U's are located.*

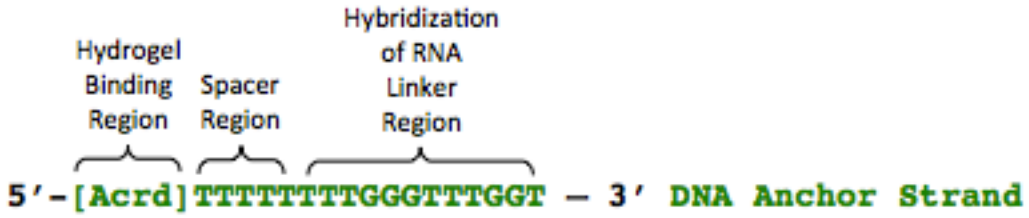

Figure 3.5. DNA anchor strand. *Designed with three regions to optimize properties for functionalization. 5' Acrydite modification allows for covalent binding of anchor strand to HEMA gel. Spacer region sequence minimizes potential hydrogen bonding and non-covalent interactions between the DNA and the polymer allowing for the DNA to stand up and have more surface area exposed for hybridization. Hybridization region complements binding site of RNA linker strand.*

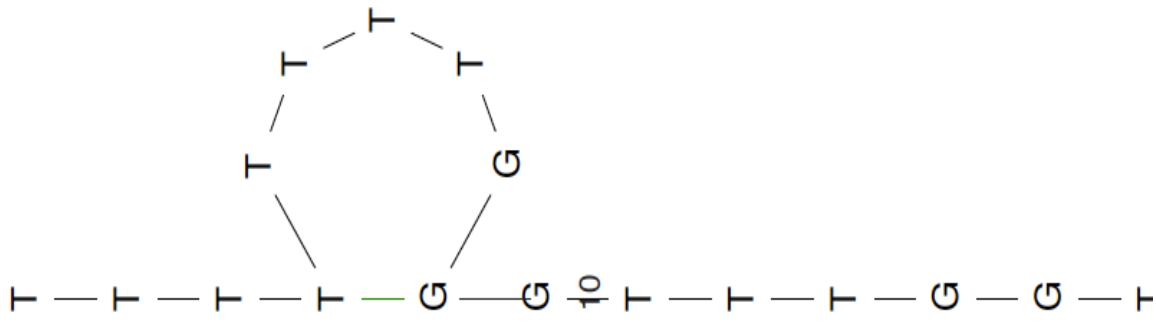

ΔG = 2.55 kcal/mol

Figure 3.6. Anchor strand intramolecular interactions. *Positive Gibbs free energy value indicates loop structure shown will not occur, meaning a linear structure will form as designed. The computer model shown is able to help predict the behavior of the anchor DNA by modeling structures most likely to form based on Gibbs free energy.*

TTTTTTTTGGGTTTGGT&TTTTTTTTGGGTTTGGT

. . . . . .&. . . . . .

Figure 3.7. Anchor strand intermolecular interactions. *Anchor DNA hybridizing with itself is not desired, since the preference is to bind with the linker. Dot bracket notation based on computer modeling is used to determine potential base pairing between two nucleic acid strands. Dots indicate no base pair for that nucleotide, while brackets indicate a base pair. The computer result of the anchor DNA sequence shows all dots underneath each nucleotide. This indicates no base pairing will occur between strands, which is is the desired outcome.*

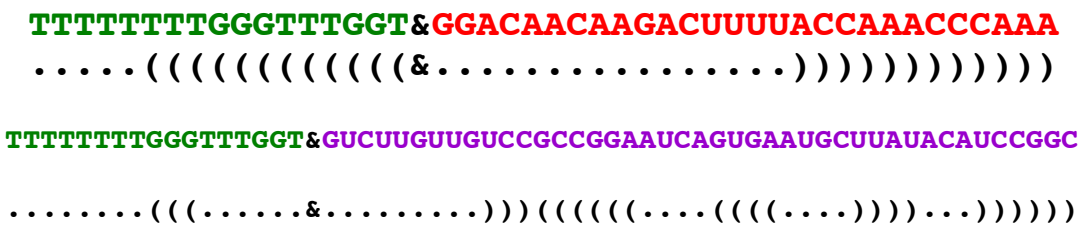

Figure 3.8. Anchor strand intermolecular interactions with linker and aptamer. *Desired hybridization between anchor (**green**) and linker (**red**) is predicted to occur (**top**), while undesired hybridization between anchor and aptamer (**purple**) is predicted not to occur (**bottom**). Anchor DNA is shown to only hybridize with linker in the appropriate designation, removal of hybridized region to see binding between the other areas showed little no binding between strands as well (not shown). This was done to make sure the dominant binding site is not masking other potential binding sites. Anchor DNA has 3 unwanted base pairs with the aptamer, but these reactions are weak and will dissociate in the presence of the linker molecule.*

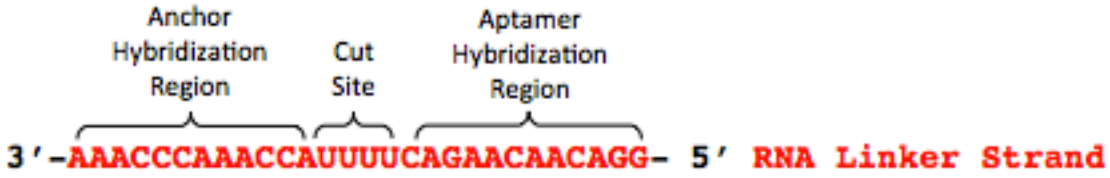

Figure 3.9. RNA linker strand. *Designed with three regions to optimize properties for functionalization. 3' Anchor hybridization region complements binding site of DNA anchor strand. Cut site allows for controlled release of aptamer strand from the hydrogel by varying the number of Uracil's and accessibility of RNase 4 to the cleavage site. This region can be either extended with A's to increase accessibility, or U's to increase number of cut sites. The 5' Aptamer hybridization region complements binding site of RNA aptamer strand.*

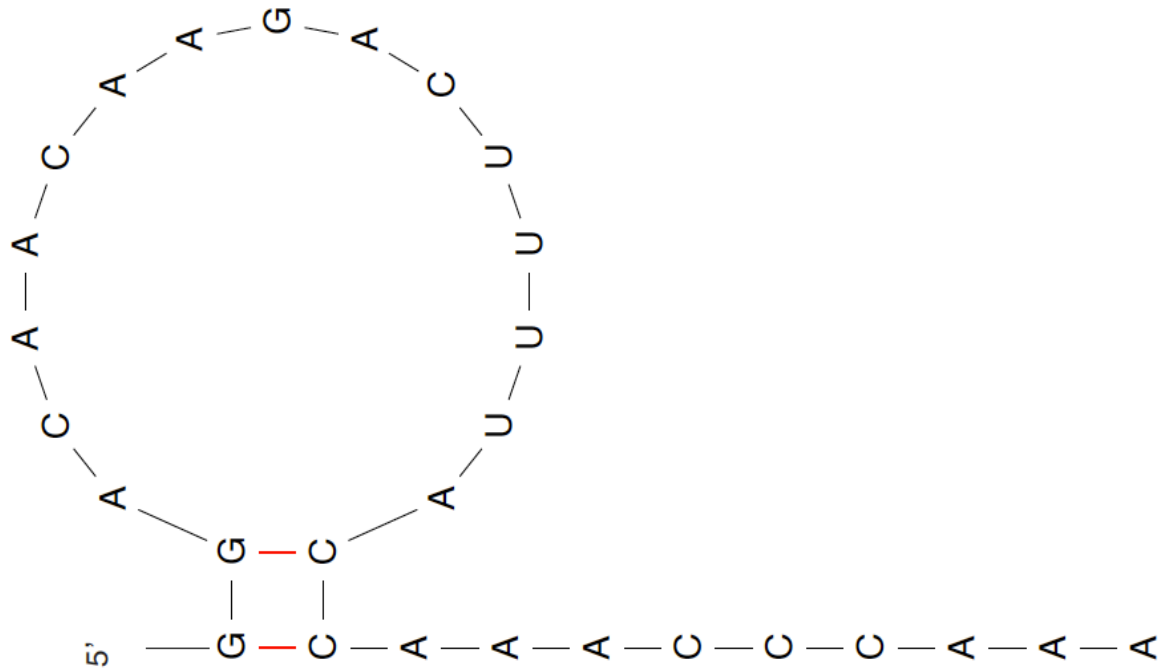

ΔG = 0.8 kcal/mol

Figure 3.10. Linker strand intramolecular interactions. *Positive Gibbs free energy value indicates loop structure shown will not occur, meaning a linear structure will form as designed. The two G-C base pairs are not stable enough to remain intact due to steric constraints caused by the large loop and free tail resulting in the formation of a linear structure under our specific environmental conditions.*

```
GGACAACAAGACUUUUACCAAACCCAAA&GGACAACAAGACUUUUACCAAACCCAAA

((.....(((.(((...((.........&)).....))).))))...)).........
```

Figure 3.11. Linker strand intermolecular interactions. *Dot-parenthesis notation indicates only weak hybridization will occur. In order to reduce this unwanted reaction, appropriate temperature conditions can be utilized to denature the interactions in the presence of anchor DNA and the aptamer allowing for proper binding with those strands. Since the difference in hybridization between the undesired binding shown here and the desired base pairing is staggering, the increased temperature method for melting the unwanted reaction will work in this case.*

GGACAACAAGACUUUUACCAAACCCAAA&GUCUUGUUGUCCGCCGGAAUCAGUGAAUGCUUAUACAUCCGGC

((((((((((((.................&))))))))))))((((((....((((....))))...))))))

Figure 3.12. Linker strand intermolecular interactions with aptamer. *Desired hybridization between linker (**red**) and aptamer (**purple**) is predicted to occur. Structure of aptamer is also predicted to remain intact indicating that additional hybridization to linker does not introduce any interference towards aptamer structure. Removal of designated binding site to check for other potential binding sites that might be masked by the dominant hybridization showed no other unwanted reactions (not shown).*

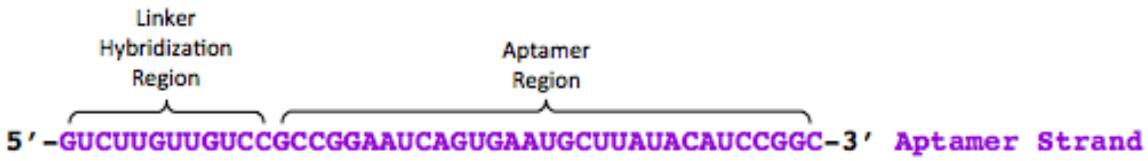

Figure 3.13. RNA aptamer strand. *Designed with two regions to optimize properties for functionalization. 5' Linker hybridization region complements binding site of RNA linker strand. Remaining nucleotides are the functional aptamer Pegaptanib, these nucleotides are the drug portion. The hybridization region is engineered to not interact with the aptamer.*

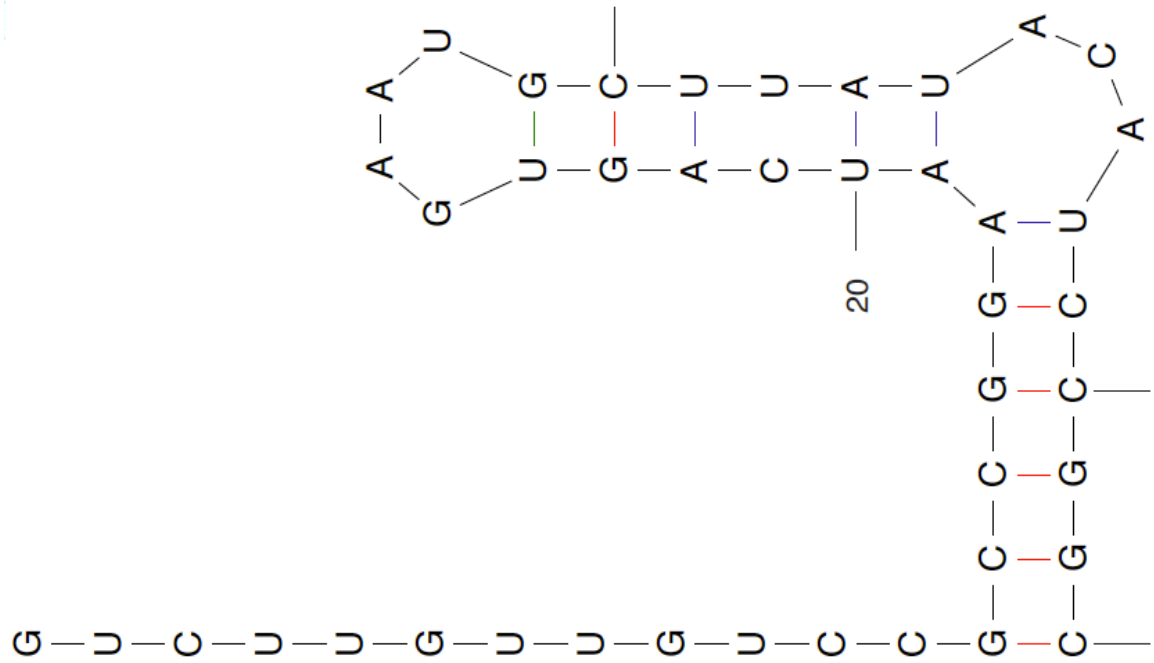

Figure 3.14. Aptamer strand intramolecular interactions. *Large negative Gibbs free energy value indicates loop structure shown is highly likely to occur; meaning the desired structure of aptamer shown will remain intact. The 5' tail is the linker hybridization region; its presence is shown not to change the structure of the aptamer, which is necessary to maintain the functionality of the aptamer.*

GUCUUGUUGUCCGCCGGAAUCAGUGAAUGCUUAUACAUCCGGC&GUCUUGUUGUCCGCCGGAAUCAGUGAAUGCUUAUACAUCCGGC

.....((((((....(((...((...(((.((((((&.....))))))....)))...))...)))...)))).))))))

Figure 3.15. Aptamer strand intermolecular interactions. *Dot-parenthesis notation indicates undesired hybridization will occur. However, utilizing appropriate temperature conditions this strand will prefer to bind in the correct structure (Figure 3.14) due to differences in thermodynamic stability between the option shown here compared to the intramolecular interaction. In addition, intramolecular interactions react faster then intermolecular ones, particularly in lower concentrations in the range of this study. This is due to the fact that intermolecular reactions need to see out another strand for binding.*

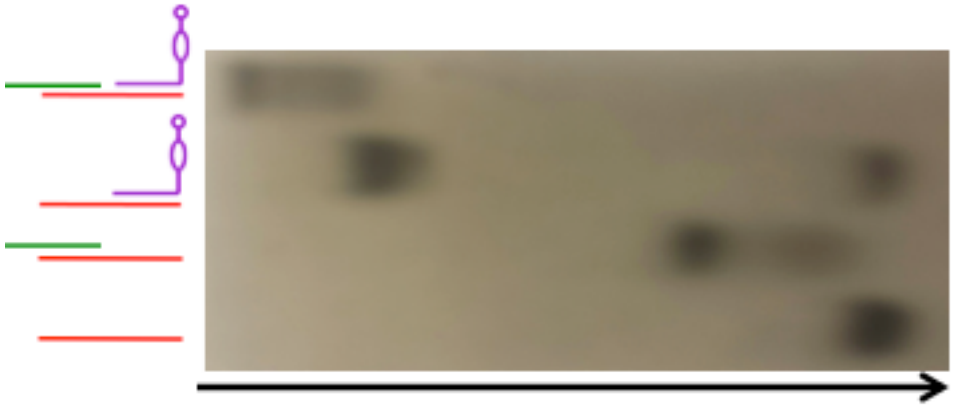

Figure 3.16. Homogeneous platform assembly confirmation. *Gel electrophoresis indicates successful anchor-linker-aptamer complex hybridization. Homogeneous bands indicate only one pairing is produced. Secondary bands are excess labeled linker, excess was added for a full reaction to take place. The linker strand is the one radioactively labeled since it binds to both anchor and aptamer; therefore it is the only detectable strand.*

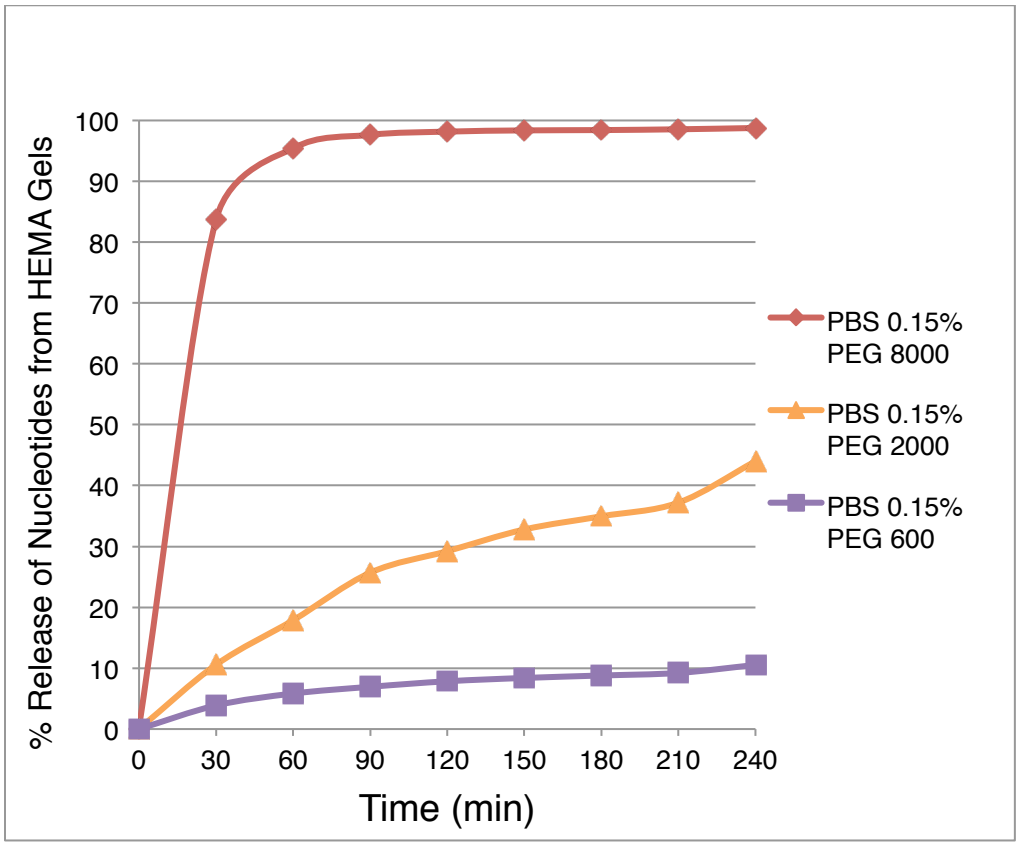

Figure 3.17. Cross linker size effect on release rate. *Free nucleotides release faster in a HEMA gel as cross linker size is increased. Cross linker concentration was kept constant at 0.15% by volume. Free nucleotides were used for each sample so that DNA size was kept constant. Release rate increased as PEG size increased, which is to be expected. This is because larger PEG molecules will create larger gel pores leading to faster release of DNA.*

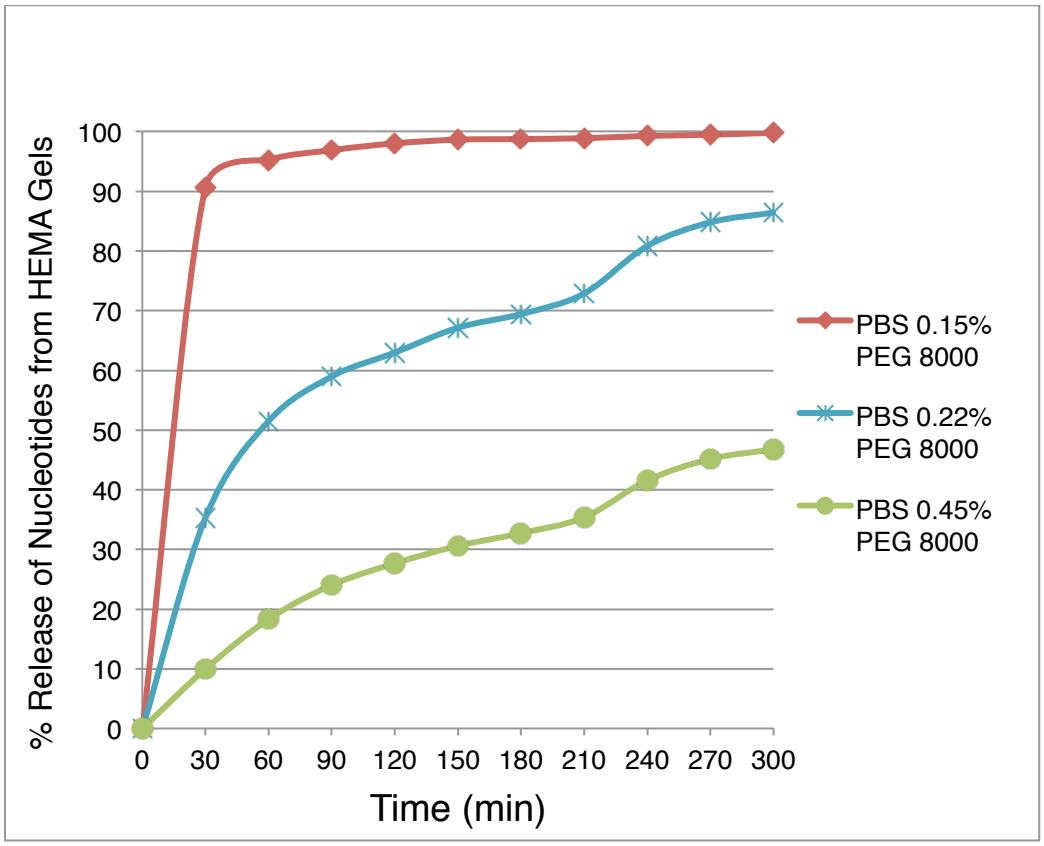

Figure 3.18. Cross linker percent effect on release rate. *Free nucleotides release faster in a HEMA gel as PEG cross linker amount is decreased. The Peg size was kept constant and largest PEG was chosen since it had the most release from the experiment in Figure 3.17. Free nucleotides were used for each sample so that DNA size was kept constant. Cross linker percent was varied based on volume. The decreasing release rate as cross linker increased is the expected result. It is believed that since the higher PEG cross linker percent gels contain less HEMA, there was less HEMA to absorb water and swell the gel, which is an additional factor that caused the release rate to decrease. This means that HEMA's ability to swell in the presence of water has further impact on release rate confirmed in Figure 3.20.*

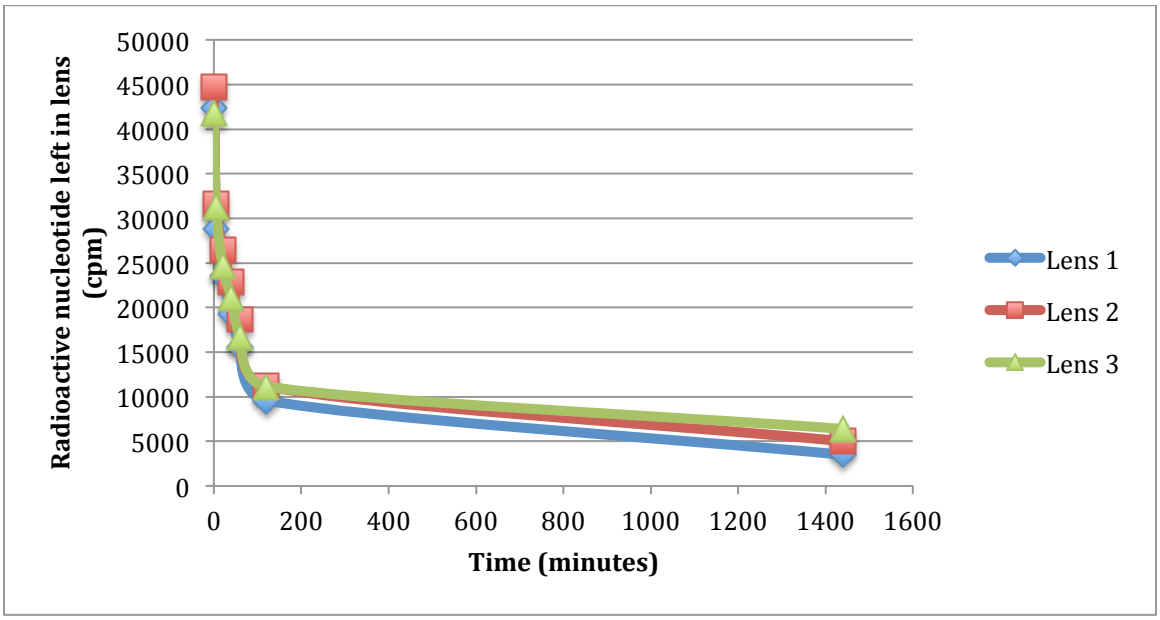

Figure 3.19. Effect of water on release rate. *Free nucleotides release at a comparable rate in 0.15% PEG 8000 HEMA gels plus 10% water (**lens 1,2**) as previous studies using no water (**lens 3**). Therefore, adding water to the lens solution of at least 10% will not change the kinetics of release for free nucleotides to any noticeable degree. There are a few factors at play that appear to cancel each other resulting in no noticeable change in release. The overall percentage of HEMA is reduced in the gels containing 10% water meaning there are fewer polymers to trap DNA and swell. However, more water in the system would further increase swelling for the polymers that are still in the sample, meaning that the ratio of water to polymer is greater. These two conflicting phenomenon appear to have equal, yet opposite effects on the gel, resulting in no change in release.*

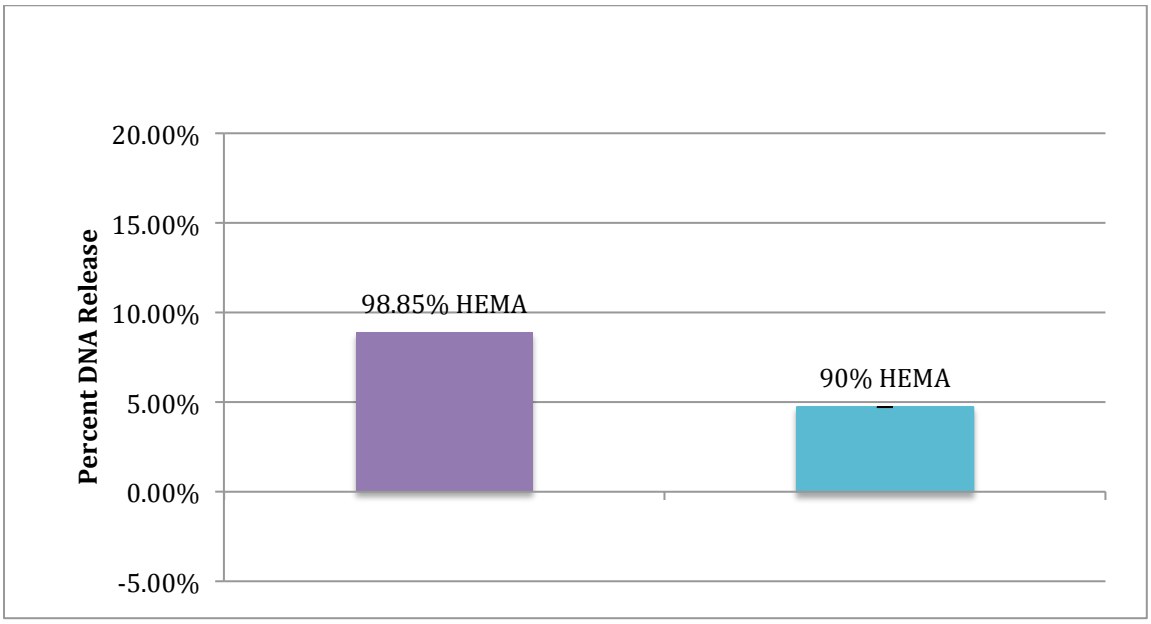

Figure 3.20. Release amount for DNA strands. *DNA strands of comparable length to our aptamer were released in HEMA lens containing 10% water (**left**). ~9% release was seen compared to 0% without water (not shown). Increasing PEG cross-linker percent resulted in a decrease in % DNA strand released (**right**) following previous trends. Once again this data demonstrates that the higher the percentage of HEMA present, the greater the release. Increasing PEG cross-linker percent decreased release in the same manner as previously shown in Figure 3.18. Interestingly, water percent had a difference in release rate for larger DNA compared to free nucleotides. This may be due to solubility of DNA strands compared to free nucleotides or simply the increased release molecule size is now in a range where change in release is distinguishable.*

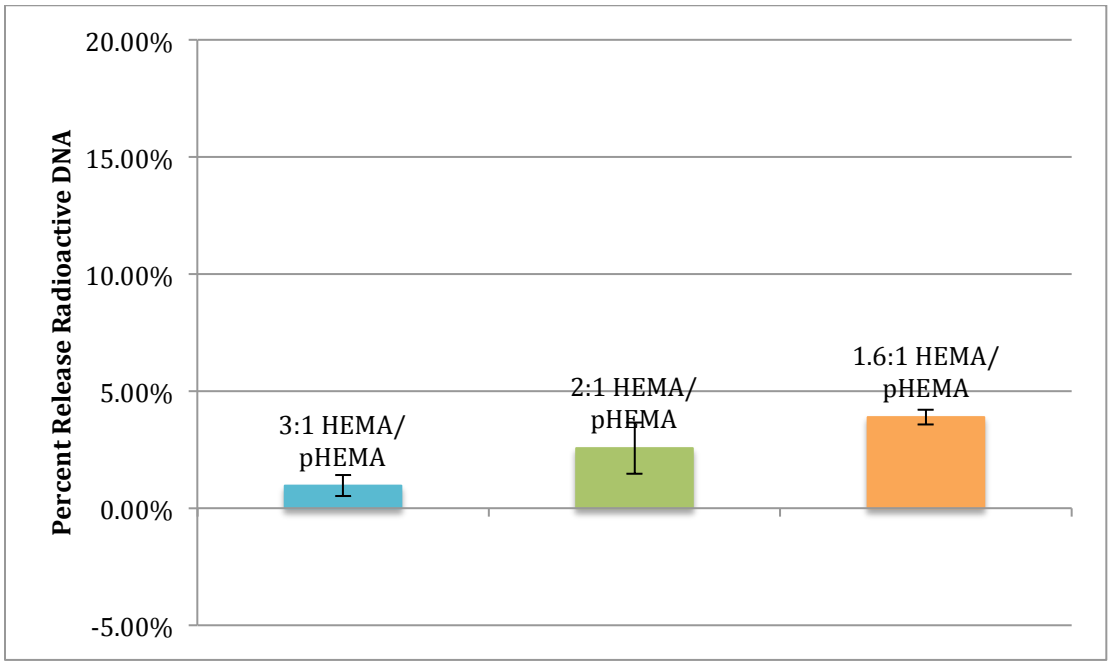

Figure 3.21. Effect of pHEMA on amount of DNA released. *pHEMA acts as a barrier to polymerization creating larger pore sizes. As the amount of pHEMA introduced increases, the total amount of DNA released also increased. No pHEMA resulted in a release of 0% (not shown). This follows the expected trend and indicates that pHEMA can be used to increase release rate of DNA. Using pHEMA was a way to increase pore size while also maintaining the same percentage of HEMA material present in the gel solution, instead of using a PEG cross-linker. The increased percent release of DNA confirms previous assumptions about the effect of the PEG cross-linker and HEMA's role in release rate. These gels do not include the 10% water by volume used in the previous experiment, indicating that the release rate can potentially be increased even further if pHEMA is combined with 10% water gel solutions.*

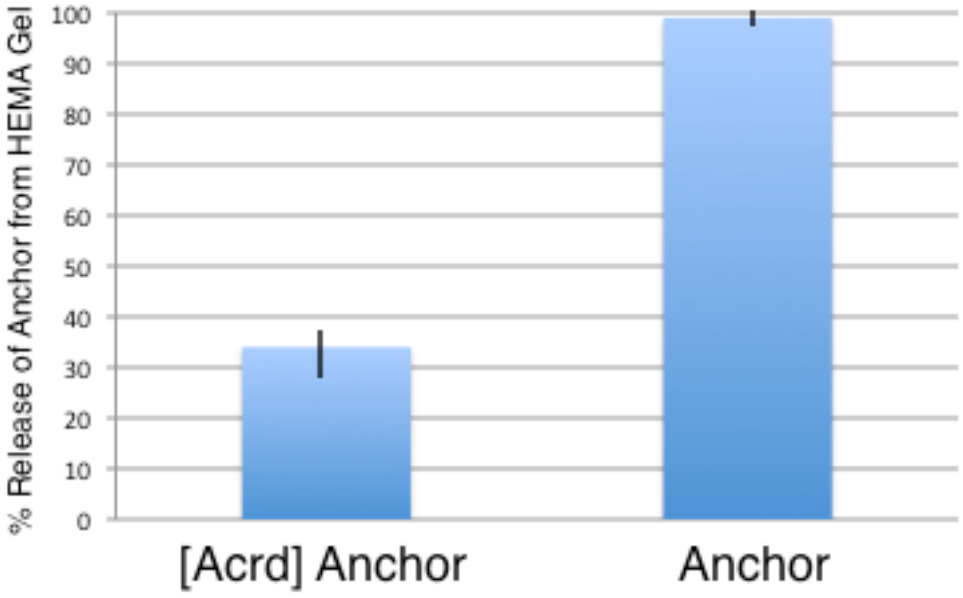

Figure 3.22. Effect of acrydite modification on amount of DNA released. *Gel electrophoresis was performed to drive non-covalently bound DNA out of the polymerized HEMA gel. Results indicate that Acrydite effectively holds DNA inside the polymerized gel compared to the same DNA strands without the modified group. Any DNA released from the Acrydite sample is most likely due to using an unpurified sample that probably contained some DNA strands without the Acrydite group attached.*

3.5 References

[1] https://www.smartvisionlabs.com/blog/why-vision-is-the-most-important-sense-organ. Smart Vision Labs. January 2017.

[2] Buwalda, S.; Vermonden, T.; Hennink, W. Hydrogels for Therapeutic Delivery: Current Developments and Future Directions. *Biomacromolecules* **2017**, 18, 316-30.

[3] https://www.quora.com/What-is-our-eyeball-size . Quora. March 2017.

[4] Fingeret, M.; OD, F.; Dickerson, J. The Role of Minimally Invasive Glaucoma Surgery Devices in the Management of Glaucoma. *Optom Vis Sci*. **2018**, 95(2), 155-62.

[5] https://www.slideshare.net/vijayjoshi311/tear-film-dynamics . Vijay Joshi. July 2013.

[6] Mishima, S.; Gasset, A.; Klyce, S.; Baum, J. Determination of Tear Volume and Tear Flow. *Invest Opthalmol*. **1966**, 5, 264-76.

[7] Brennan, N. Corneal Oxygenation during Contact Lens Wear: Comparison of Diffusion and EOP-based Flux Models. *Clin Exp Optom*. **2005**, 2, 103-8.

[8] Mirnezami, S.; Jafarabadi, M.; Abrishami, M. Temperature Distrubution Simulation of the Human Eye Exposed to Laser Radiation. *J Lasers Med Sci*. **2013**, 4(4), 175-81.

[9] Tiffany, J. Tears in Health and Disease. *Nature: Eye.* **2003**, 17, 923-6.

[10] Zhou, L.; Beuerman, R.; Tan, D. Characteristics of Human Tear Proteins Using High-resolution Mass Spectrometry. *Ann Acad Med Singapore*. **2006**, 35, 400-7.

[11] Gabelt, B.; Kaufman, P. Aqueous Humor Hydrodynamics. Adler's Physiology of the Eye. 9th. St. Louis, MO. Mosby, **2003**.

[12] Hollo, G.; Whitson, J.; Faulkner, R. Concentrations of Betaxolol in Ocular Tissues of Patients with Glaucoma and Normal Monkey after 1 Month of Topical Ocular Adminstration. *Invest Opthalmol Vis Sci*. **2006**, 47(1), 235-40.

[13] Shea, C. Distance Learning Course: Anatomy and Physiology of the Eye. *BSM Consulting*. **2012**.

[14] Mannermaa, E.; Reinisalo, M.; Urtti, A. Filter-cultured ARPE-19 Cells as Outer Blood-retinal Barrier Model. *Eur. J. Pharm. Sci*. **2010**, 40, 289-96.

[15] Vadlapudi, A.; Cholkar, K.; Dasari, S.; Mitra, A. Ocular Drug Delivery. In Drug Delivery. *Jones & Bartlett Learning*. Burlington, MA, **2015**, 219-63.

[16] Godse, R.; Singh, K.; Shrivastava, A.; Shinde, U. Polymeric Nanoparticulate Systems: A Potential Approach for Ocular Drug Delivery. *Nano-Biomaterials For Ophthalmic Drug Delivery*. **2016**, 351-87.

[17] Huang, A.; Tseng, S.; Kenyon, K. Paracellular Permeability of Corneal and Conjunctival Epithelia. *Invest Ophthalmol Vis Sci*. **1989**, 30(4), 684-9.

[18] Olsen, T.; Edelhauser, H.; Lim, J.; Geroski, D. Human Scleral Permeability: Effects of Age, Cryotherapy, Transscleral Diode Laser, and Surgical Thinning. *Invest Ophthalmol Vis Sci*. **1995**, 36, 1893-1903.

[19] Rabinovich-Guilatt, L.; Couvreur, P.; Lambert, G.; Dubernet, C. Cationic Vectors in Ocular Drug Delivery. *J Drug Target*. **2004**, 12(9-10), 623-33.

[20] Sahoo, R.; Biswas, N.; Guha, A.; Sahoo, N.; Kuotsu, K. Nonionic Surfactant Vesicles in Ocular Delivery: Innovative Approaches and Perspectives. *Biomed Research International*. **2014**, Article ID 263604, 12 pages.

[21] ElShaer, A.; Ghatora, S.; Alany, R. Contact Lenses as Drug reservoirs & Delivery Systems: the Successes & Challenges. *Ther. Deliv*. **2014**, 5(10), 1085-100.

[22] Lee, K.; Mooney, D. Alginate: Properties and Biomedical Appplications. *Prog Polym Sci.* **2012**, 31(1), 106-26.

[23] Kim, H.; Zhang, K.; Moore, L.; Ho, D. Diamond Nanogel-embedded Contact Lenses Mediate Lysozyme-dependent Therapeutic Release. *ACS Nano*. **2014**, 8, 2998-3005.

[24] Fonn, D.; Optom, D.; Optom, B. Silicone Hydrogel Material and Surface Properties. *Contact Lens Spectrum*. **2002**.

[25] Fuentes, R.; Fernandez, E.; Pascual, I.; Garcia, C. UV-Visible Transmittance of Silicone-Hydrogel Contact Lenses Measured with a Fiber Optic Spectrometer. *Proc. Of SPIE*. **2013**, 8785, 8785AZ-1.

[26] https://www.heritage-eyecar.com/contact-lens-overwear-syndrome . *Heritage Family Eyecare*. **2018**.

[27] Lee, S.; Kim, S.; Park, M. Oxygen Permeability of Soft Contact Lenses in Different pH, Osmolality and Buffering Solution. *Int J Ophthalmol*. **2015**, 8(5), 1037-42.

[28] Muntz, A.; Subbaraman, L.; Sorbara, L.; Jones, L. Tear Exchange and Contact Lenses: A Review. *J Optom*. **2015**, 8(1), 2-11.

[29] https://www.lentiamo.co.uk/blog/does-the-following-apply.html . Are Contact Lenses with Higher Water Content Better. *BlogLentiamo*. **2016**.

[30] Harthan, J.; Hom, M. It's All About the Tear Film. *Review of Cornea and Contact Lenses*. **2017**.

[31] Shigdar, S.; Macdonald, J.; Duan, W. Aptamers as Theranostic Agents: Modifications, Serum Stability and Functionalisation. *Sensors (Basel)*. **2013**, 13(10), 13624-37.

[32] Pendergrast, P.; Marsh, H.; Grate, D.; Stanton, M. Nucleic Acid Aptamers for Target Validation and Therapeutic Applications. *J Biomol Tech*. **2005**, 16(3), 224-34.

[33] https://synergeyes.com/wp-content/uploads/2017/06/70119-patient-instruction booklet-kc-and-clearkone-lens-rev.-c.pdf . *SynergEyes*. **2017**. Patient booklet.

[34] GPS Safety Summary 2-Hydroxyethyl Methacrylate (HEMA). July **2013**.

[35] West, S.; Deans, A. DNA Interstrand Crosslink Repair and Cancer. *Nat Rev Cancer*. **2011**, 11(7), 467-80.

[36] Kenney, M.; Ray, S.; Boles, T. Mutation Typing Using Electrophoresis and Gel-Immobilized Acrydite Probes. *Biotechniques*. **1998**, 25, 516-21.

[37] Vinores, A. Pegaptanib in the Treatment of Wet, Age-related Macular Degeneration. *Int J Nanomedicine*. **2006**, 1(3), 263-8.

Chapter 4: Quartz Crystal Microbalance in Biological Applications

The purpose of experiments using a quartz crystal microbalance (QCM) was to study the real-time assembly of DNA strands and drug loading and release kinetics on a gold surface.. Flowrate and concentration of DNA introduced can be precise and monitored at a given temperature. The goal is to assemble a drug loaded, DNA coated, gold nanoparticle capable of killing cancer cells with high efficacy. The QCM helps to character the behavior of DNA under similar conditions to better understand its physical properties and the engineering of the nanoparticles.

Dissipation can be tracked and used to determine how rigid or flexible the surface of the gold sensor becomes with changes to the surface This information can be directly related to DNA structure (i.e., analyze what may lead to either coil or stretching) Variables include salt concentration, DNA concentration, density of the packed surface, and binding of drug. It is hypothesized that details from this analysis will help lead to optimized DNA, salt, and drug concentrations to efficiently and effectively assembled ssDNA and maximize drug bound. This will then result in fewer drugs bound to the sensor. Once this behavior is understood, the next step is to implement these findings on the protocol for functionalizing gold nanoparticles with DNA.

4.1 Overview of Quartz Crystal Microbalance

A quartz crystal microbalance is an analytical tool that can detect small changes in mass with high precision. During the past few years, QCM has emerged as a critical tool in the development of biological assays. The ability to monitor reactions *in situ* in a tailorable, liquid environment provides vital information about biological surfaces in a

physiologically relevant medium. This chapter will present various methods that have been used to utilize QCM systems in biological assays and describe our experiments studying the binding of DNA to a gold surface as a representation of binding to gold nanoparticles. A diagram of the components found in a standard QCM system can be found in Figure 4.1.

The function of the QCM depends on the piezoelectric effect: that is, application of a voltage to a quartz crystal will result in mechanical deformations. In this case, the crystal will begin to oscillate and produce a standing shear wave that moves through the body of the crystal. This standing wave oscillates in time, but its peak amplitude does not propagate through space; this allows for high precision when detecting changes in frequency induced by thin film layers (see Figure 4.2A for graphic illustration). With careful consideration of the electrode material used to coat the quartz crystal, it is possible to deposit a range of molecules onto its surface. This mass deposition results in a disturbance of the crystal's resonance, leading to a subsequent shift in the frequency of oscillations. Commonly, the Sauerbrey equation is employed to directly relate frequency shifts to mass surface density. Under the assumption that a sufficiently thin and rigid film has been deposited homogenously across the crystal surface, the adsorbed layer is treated as an increase in the thickness of the resonating quartz and a mass to frequency correlation can be determined. These assumptions allow for extraction of relevant parameters about the deposited materials, in our case DNA.

Modern QCM systems can also measure energy dissipation, which is caused by thickness and viscoelastic properties of the adsorbed layer and can thus be used to

extrapolate behavior of the materials. Accurate analysis of data from the QCM also requires knowledge pertaining to the liquid media, including viscoelastic properties, as well as quantifying how much liquid is bound to the surface or trapped by the analyte. Methods for quantifying data include impedance or dissipation analysis, or *ex situ* optical techniques.

Using QCM with dissipation monitoring has allowed for observed formation of monolayers of biological materials such as nucleic acids, antibodies, proteins, and whole cells. These observations led to information about biological surface morphology, binding kinetics, drug release, biosensing and diagnostics, molecule targeting, and biocompatibility. QCM systems will prove to be indispensable in synthesizing and characterizing biomaterials and developing biological assays, such as detection of biomarkers in solution using antibody or aptamer sensors. In the future, this technological progression may lead to the manufacture of portable, pocket-sized sensors able to detect the presence of small amount of materials from a blood sample in a short amount of time.

4.1.1 Potential Impact of QCM on Biological Surface Science

As our breadth of knowledge regarding nanomaterials and nanotechnologies grow, innovative devices and novel applications are constantly emerging. One such application is in biosensing. The use of nanomaterials allows for more sensitive detection systems with significantly lower detection limits [1]. Nanomaterials or devices with controlled synthesis and homogenous layer composition allow for organized immobilization of a range of materials on their surface for the construction of biosensors [2]. Another application of nanomaterials is in the analysis of behaviors at biological

surfaces, such as the contact point between cells, immunological interactions, or nucleic acid structure formation. Biological surface science (BioSS) is interdisciplinary, with a broad range of applications, including medical implants, diagnostics, tissue engineering, bioelectronics, and biomimetic materials [3]. Growing from the progress made in surface science during the 1970s and 1980s, BioSS has developed to focus on the extensive strategies conducted to study the properties and processes at interfaces between biological environments (or biofunctional surfaces) and synthetic materials [3,4].

However, nanotechnology does not come without flaws. Many techniques are only applicable with the use of labels, or analysis is only possible *ex situ*. Additionally, immobilization is not always perfectly organized. Indeed, in many DNA-linked gold nanoparticles, there is concern for folding of the DNA strands to interact with the gold surface in unwanted ways. Methods to orient nucleic acids on gold nanoparticles can be complicated and time consuming [5]. Often supplementary techniques are needed to confirm structure and orientation. It is clear that a technology is needed that allows you to analyze nanomaterials for biosensing and biological surface analysis in real time, *in situ*, without the need for additional techniques. One strategy that has been promising recently involves use of the quartz-crystal microbalance.

4.1.2 Model Analysis of Quartz Crystal Microbalance

Application of voltage to a quartz crystal will result in mechanical deformation of the crystal, which in turn will produce an oscillatory motion. If the frequency of the applied voltage is equal to some multiple of the crystal's resonant frequency (overtones) then one can generate a standing wave [6]. Generally, a QCM system utilizes an AT cut

crystal to ensure that vibrations occur in thickness-shear mode. An AT cut crystal is inclined 35 ° 15' from the Z-axis; such a cut is advantageous due to temperature characteristics and its frequency range from 0.5 – 200 MHz. Typically the surface of the crystal is coated with an electrode, which is made of gold, silver, or platinum. The choice of surface electrode depends only on your desired adsorbate molecule.

Analyzing frequency shifts begins with identifying the resonant frequency of the quartz crystal sensor – typically, between 4- 6 MHz for most applications. The resonance frequency f_n will change depending on the surrounding media and adsorbed particles, and Δf is subsequently recorded by the machine. If the linear relationship between the resonance frequency and the resonator mass (derived by Sauerbrey [7]) cannot be assumed – either due to the presence of liquid medium or lack of rigidity in adsorbed layers - two other important parameters can be extracted from the QCM. First, impedance analysis [8] will reveal the bandwidth Γ_n of the crystal oscillations and is related to the viscosity of the medium, while second, QCM-D analysis [9] reveals the decay of the crystal oscillations as energy dissipates ΔD_n and is related to the adsorption kinetics of the bound particles. Note that bandwidth and dissipation are proportional in that $D_n = 2\Gamma_n / f_n$. These additional parameters allow for more accurate analysis of adsorbed film properties when viscoelastic mechanics are affecting the frequency of crystal oscillations. Due to this, QCM-D is generally the standard for assessment of biological phenomena using the QCM. Figure 4.3 provides an example of the relationship for dissipation and frequency data produced from the QCM.

Model analysis of QCM data will vary depending on the properties of the adsorbed particle layer. Adsorbed layers can be categorized in four ways: laterally

homogenous films or laterally heterogeneous films, each with either a large ΔD or small ΔD. For laterally homogenous films with little to no dissipation (ΔD < 1), the Sauerbrey equation can be used (see Figure 4.2B). This model provides a measurement of the areal mass density upon the electrode surface, including any solvent trapped within the film. For a list of model types available depending on the adsorbed layer see Table 4.1. Additional measurements such as surface plasmon resonance (SPR) or ellipsometry can be employed to determine the weight fraction of solvent within the film for a more accurate analysis. Films that exhibit significant ΔD, or films composed of discrete particles, can be analyzed using a number of viscoelastic models. These models are beyond the scope of this chapterbut are well described by Reviakine, I., Johannsmann, D. and Richter, R. P. [6].

4.1.3 Self Assembled Monolayers on Quartz Crystal Microbalance

Since the frequency shift in a QCM system is detected across the entirety of the electrode surface, it is important to ensure that any adsorbed film is organized and arranged as homogenously as possible. The study of homogenous films (including those composed of discrete particles) is directly related to the study of self-assembled monolayers (SAMs). SAMs are organized molecular assemblies of materials on a surface, formed from chemical reactions between individual molecules or groups of molecules and their reaction with the substrate. SAMs that have been characterized include fatty acids, organosilicon derivatives, alkyl substrates, phosphates, and organosulfur adsorbates [10]. Organosulfur particles, including alkanethiols, are of particular interest in QCM technology due to their application as monolayers on metals

and semiconductors. Alkanethiols are able to form dense, pseudocrystalline monolayers on some metals with high affinity and stability [11,12]. A great review on the assembly of thiolate SAMs on metals can be found by Love, J. C., Estroff, L. A., Kriebel, J. K., Nuzzo, R. G. and Whitesides, G. M. [13].

SAMs of biological materials have been studied extensively and are well accepted within the medical community - for example, blood glucose monitoring devices use biological SAMs and are one of the most popular biosensors used today. Other examples include the use of antibodies to manufacture immunosensors [14] and the use of nucleic acids to create affinity based sensors [15]. Furthermore, monolayers of enzymes have been used to create electrochemical biosensors that are able to produce an electrical signal [16]. These systems tend to be highly sensitive, but their performance can degrade over time due to fouling, or accumulation of material, at the sensor surface.

Some QCM applications utilize SAMs that do not bind densely, or do not organize easily, therefore subjecting the electrode surface to nonspecific binding. Monolayers of alkanethiols and nucleic acids have been shown to change their orientation as a result of variance in binding density [17,18]. Nonspecific binding can complicate QCM analysis through unwanted changes in frequency and dissipation. Additionally, the presence of trapped solvent within the monolayer plays a large role in analytical techniques, and characterization of the monolayer composition is imperative [19]. Many bioassays have employed blocking agents to reduce nonspecific binding. Blockers that have been studied include BSA, dextran, casein, and PEG. An ideal blocker should bind with high strength and stability while simultaneously preventing further surface reactions and avoiding interference with the adsorbate [20]. Therefore, care should be taken when

choosing a blocking agent with regards to your electrode surface, adsorbate particle, and solvent composition.

4.2 Methods of Immobilization

Many methods of biomolecule immobilization have been used in biosensors and nanoparticles. Table 4.2 provides a list of immobilization SAMs related to the topic discussed along with limit of detection and time characteristics. A popular approach is the use of a biotin layer paired with avidin/streptavidin. Subsequent layers can then be attached through biotinylation, a process that has been described for proteins, antibodies, and nucleic acids [21]. Biotin mediated immobilization on a QCM surface has been used for simple layer formation using bovine serum albumin as a blocking agent for extraction of stem cells from solution [22]. Previous groups have also utilized S-layer proteins as an immobilization layer. S-layer proteins are cell surface proteins that, when isolated from the cell, can self-assemble into a highly structured layer [23]. Others have used molecularly imprinted polymers (MIPs) to stamp an epitope into a polymer layer, providing a binding site for a particular analyte [24]. This section describes common techniques of biomolecule immobilization onto QCM surfaces.

4.2.1 Immobilization of Antibodies

Antibodies are indispensable biorecognition proteins in immunosensing devices and assays. Both monoclonal and polyclonal antibodies, either natural or synthetic [25], have been used to bind target molecules [26]. The strength of the antibody lies in its two adaptable antigen-binding regions: the fragment antigen binding region (Fab) and the

fragment crystallizable region (Fc) that binds to specific receptors and complement proteins. This property is key to orienting the antibody on a surface. When precautions for orientation are not taken, antibodies can bind to the sensor surface at random angles, limiting the exposure of the binding region to the antigen and decreasing the overall system efficiency.

For greatest detection of an antigen, the antibodies on a sensor surface should be packed as tightly as possible in (Fab)-up orientation. This configuration is possible with the help of SAMs, along with secondary molecules that help guide antibody binding. Using a monolayer of 1-dodecanethiol (DDT) and BSA as a blocking agent, Wiseman *et. al.* were able to monitor antibody binding orientation using two molecules specific for either the (Fab) or (Fc) sections of the antibody. At sufficient concentrations they were able to direct the orientation of the antibody to produce the highest affinity for the antigen [27].

Another method involved a monolayer of 11-mercapto-undecanoic acid (MUA) and 6-mer- capto-1-hexanol (MHL) treated with EDC/NHS, a common method to activate monolayers to react with aldehyde groups [28]. A polyclonal antibody was then oxidized with periodic acid to generate an aldehyde group within the (Fc) region, encouraging the antibody to orient itself onto the surface [29]. This method of oxidizing antibodies to react with an amine surface has also been shown by Makhneva *et al.* [30].

An obstacle to immobilization is the sometimes complicated and time-consuming practice of assembling and activating the monolayer. A method of immobilizing antibodies without surface treatment is therefore desired. As we will see with nucleic acids, this is simple with a thiol bond. Antibodies contain a number of disulfide bridges

that can be exploited by UV light to reveal a free thiol group. Using this method, Ventura *et al.* were able to selectively break the disulfide bridge within the (Fc) region of an antibody in order to orient it onto a gold QCM surface with no further surface treatment, see Figure 4.4 [31]. This "photon assisted immobilization" has remained untested on a wide range of antibodies, but due to the common disulfide groups it is expected to be successful for any antibody.

4.2.2 Immobilization of Nucleic Acids

Nucleic acids are utilized in QCM studies for their ability to couple with complementary DNA strands and modification capabilities, including thiol modifications [32]. Recently, nucleic acid aptamers have emerged as targeting molecules superior to antibodies, mainly due to their ability to target molecules outside of normal immunological pathways [33]. Methods of EDC/NHS chemistry and biotinylating are applicable when immobilizing nucleic acids [34], but by far the self-assembled thiolated monolayer is used most frequently due to its convenience and stability of the bond [35]. With nucleic acid layers, there are always concerns for orientation not being aligned due to nonspecific binding with the sensor surface. Additional thiols can be utilized as needed as blocking agents, either through a mixed solution [36] or by backfilling [32]. Shorter molecules, such as oligoethylene glycol (OEG) thiols have shown less impedance to nucleic acid binding accessibility [32].

The complementary binding of nucleic acids provides a platform for layer formation. Multilayer films consisting of complementary nucleic acids have previously been constructed on QCM surfaces [34]. Nucleic acids can be observed *in situ* with a

QCM system as they change structure under different environments– such as pH and temperature – or as polymerases modify base pair binding. This would provide invaluable data in the study of aptamers and nucleic acid stability *in vivo*; as aptamer function relies on its molecular structure, and the *in vivo* environment may differ from the environment in which the aptamer was discovered. It is imperative to characterize the aptamer's ability to retain its structure during the desired application. To date, no such work has been performed on a QCM system. Experiments in section 4.4 introduce preliminary data done in our lab to study this topic.

4.2.3 Whole Cell Immobilization

Whole cells have been successfully immobilized on a QCM surface by layering antibodies or aptamers specific for that cell. However, to more closely mimic an *in vivo* environment, it is necessary to construct a surface that mimics cell to cell adhesion. This involves layering sensors with substrates for the cell to attach to, which is often a mixture of extracellular matrix proteins. These substrates allow you to immobilize cells and modulate adhesion kinetics through surface modifications in order to observe cell adhesion under a variety of physiologically relevant conditions, see Figure 4.5 [37].

Additionally, cell studies can be completed on other biocompatible materials. Tantalum and chromium were used to observe cell spreading on metal oxide surfaces [38]. Titanium, gold, and fibrinogen-coated gold surfaces were used to distinguish adhesion characteristics between healthy and carcinogenic thyroid cells [39]. Guo *et al.* constructed a removable porphyrin film that was suitable for cell adhesion and allowed for reuse of the sensor [40]. Immobilizing cells onto QCM sensors of varying

composition can also provide valuable information regarding the *in vivo* reaction to implanted materials. Titanium and hydroxyapatite, materials common for hip and bone implants, are available as QCM sensor coatings; as such, this technology has probed the response of tissue layers at the interface between the body and an implant to extract relevant parameters regarding the cellular response to such implants [41].

4.3 Detection Sensitivity, Kinetics, & Future Impact of QCM

For all of the advantages that a QCM system provides, there is still a need to increase the sensitivity of the instrument. It has been shown that modulating the electrode surface of the quartz crystal as well as increasing the frequency of its oscillations can provide a more sensitive instrument [42]. A separate method for amplifying the signal of a particular analyte is mass amplification. In this method, a second particle is bound to the specific analyte on the QCM probe. This provides an amplified mass signal from the QCM that can allow for more sensitive detection and analysis. A schematic representation of these techniques for QCM mass amplification can be seen in Figure 4.6.

Use of novel amplification methods have shown the ability to detect immeasurably small amounts of molecules, even showing sensitivity down to a single unit of cholera toxin (CT). A sandwich-type sensing system immobilized CT to the sensor surface using a monolayer of anti-CT monoclonal antibodies. Next, a liposome functionalized with horseradish peroxidase and ganglioside GM1 – a molecule with affinity toward CT – was introduced. In this system, the presence of H_2O_2 allowed the horseradish peroxidase to biocatalyze oxidation of 4-chloro-1-naphthol leading to deposition of an insoluble product that was detectable even at low concentrations [43].

Gold nanoparticles functionalized with antibodies [44] and oligonucleotides [45] have also been used to amplify detection signals, although the incubation time of the amplification step may hinder the rapidness of detection that is normally associated with QCM studies.

4.3.1 Detecting Cell Adhesion

Detecting abnormalities in cell adhesion is critical in the diagnosis of a number of diseases. Defects in cell adhesion can disrupt cellular processes, including uncontrolled proliferation, which often leads to cancer [46]. Therefore, analysis of cell adhesion is essential for the understanding of cellular disorders that lead to further complications. Common techniques in cell adhesion studies utilize fluorescent labels, fixation solutions, or cell lysis. These techniques can produce environments for the cell that are not physiologically accurate, and at worst can cause cell death. They also do not reveal data about the mechanical strength of cell adhesion. QCM analysis is able to extract such data in a real-time, label free, and noninvasive manner.

Detection of cell adhesion to a QCM substrate relies on the ability of the acoustic wave of the machine to penetrate the basal region of the cell. Observation of the frequency shift reveals a three-step process of attachment, spreading, and adhesion of the cell, consistent with the three stages of the cell adhesion process [47]. Although Δf is acceptable to analyze dynamics of the cell adhesion, it is not sufficient to draw many conclusions. According to the size of the chosen cell, and due to the fluid nature of the cell membrane, adhered cells will behave like a soft material and will reveal a higher rate of dissipation than is acceptable for Sauerbrey analysis [48]. ΔD In the presence of cell

adhesion is complex, and since the exact cause of ΔD during this process is controversial, it is hard to predict. Hypotheses relating to ΔD during cell adhesion include liquid medium trapped beneath the cell, variations in structure of the complex between cell surface integrin receptors and the ECM, and restructuring of actin filaments [37]. Certain groups have utilized graphs of $\Delta D/\Delta f$, often as a function of time, to draw conclusions about the mechanical strength and structure of cells during the adhesion process, although fitting of the data to an appropriate model is still preferred for precise data [37].

There are two methods of QCM analysis of cell adhesion deemed "bottom-up" and "outside-in" approaches [37]. The bottom-up approach involves using QCM data to examine cell morphology and stiffness. These mechanical properties directly affect cell processes such as migration, differentiation, and motility. Studies using QCM have been able to detect cell morphology changes due to cytochalasin D mediated depolymerization of actin filaments in the cytoskeleton [49-51]. The QCM has also been used successfully to detect changes in microtubule stability [52,53]. The outside-in approach utilizes QCM to observe the workings of signal transduction pathways. EGFR in particular plays a large role in regulating cell adhesion, and abnormal levels of EGFR have been linked to certain types of solid tumors. Chen *et al.* used QCM to monitor the sequence of cell de-adhesion induced by EGFR [54]. Otto and Silhavy utilized a QCM to study the effect of the Cpx-signaling pathway on biofilm formation [55].

4.3.2 Detection of Viruses and Bacteria

QCM has also been used in the detection of viruses and bacteria. Rapid detection of these biological agents is beneficial to biological, medical, and environmental studies.

With a satisfactory recognition molecule, such as an aptamer or antibody, QCM has the potential to detect these biological agents at very low concentrations. Strains of the ebola virus have been detected using QCM at concentrations comparable to those of ELISA assays [56], but in minutes rather than hours. This method also provides high sensitivity and specificity for particular viruses, as the QCM is sensitive to detection of specific characteristic proteins.

Spores of *Bacillus anthracis* have successfully been detected at concentrations as low as 10^3 CFU/mL in less than 30 minutes using an antibody functionalized electrode surface [57]. Additionally, DNA probes were capable of successfully identifying *B. anthracis* in the presence of similar species *Bacillus thuringiensis*, using complementary DNA functionalized AuNps to bring the limit of detection as low as 3.5×10^2 CFU/ml. Successful QCM virus detection has been achieved using synthetic antibodies, soft lithography, and epitope imprinting, suggesting that the benefits of the QCM go beyond the real-time sensitivity of measurements and into the ability of sensor modification and functionalization [58].

Natural antibodies can be used in versatile ways. For example, ProLinker B, a calixcrown derivative, has been used to immobilize antibodies in a stable orientation on a gold QCM surface for the rapid detection of canine parvovirus [59] and H3N2 canine influenza [60]. Similar methods have been used to detect H5N1 avian influenza virus. A SAM of H5N1 antibodies was able to distinguish the H5N1 virus from three other non-specific subtypes at concentrations as low as 1.28 HA units (*hemagglutinin* units – a unit commonly used to measure the presence of viruses by detecting their ability to clump red blood cells) [61]. Ji *et al.* similarly were able to distinguish maize chlorotic mottle virus

from three other similar viruses when all four samples were mixed. The QCM was able to detect *maize chlorotic mottle virus* from crudely extracted plant samples at concentrations between 10-250 μg/mL [62].

4.3.3 Detecting Various Proteins, and Nucleic Acid Activity

Highly sensitive detection of enzymatic activity is advantageous in medical diagnostics as enzymatic activity can act as a biomarker for certain diseases [63]. Rapid detection of enzymatic events can therefore be applied in tests such as blood screening or biopsies to detect the presence of disease in early stages. However, many of the currently employed assays for enzymatic detection require complicated and laborious methods for application [64]. With a QCM system, Dong *et al.* were able to amplify an immobilized layer of synthetic peptides using gold nanoparticles. These peptides were designed with a known substrate for type IV collagenase activity [65], which would be cleaved upon contact and remove mass from the sensor surface. They were able to suitably detect enzymatic activity by a frequency shift, even in serum solutions diluted 30 fold, suggesting that such a technique could be used in clinical applications [64].

The behavior of cell membrane proteins has become a focus in cancer diagnostics and therapies. Certain glycoproteins have been identified that are overexpressed in breast cancer cells, and methods of detection and quantification have shown success in identifying pre-cancerous cell lines [66]. However, characterization of cell surface binding between cancer cells requires a more biologically accurate platform for observation. Utilizing the QCM, breast cancer cells can be grown directly onto a sensor surface and the liquid environment can be tailored to simulate a biologically relevant

environment. With this system, a series of lectins were used to screen for cell surface proteins activity on two different cancer strains in real-time without the need for labeling. With this system they were able to extract real-time thermodynamic data about surface protein activity without the need for *ex situ,* end-point detection techniques [67]. Table 4.3 shows how QCM directly compares to other common protein sensing techniques. The residence time for readings on the QCM is in the range of 15 min. It should be noted that QCM also has the ability to monitor in real time.

Detection of nucleic acids is also important for biosensing applications. It has already been previously discussed that aptamers can be used as SAMs to detect cells and toxins using QCM. Aptamers have emerged as an excellent targeting tool, and their effectiveness depends on their particular 3D structure; therefore, structural stability and orientation are of much interest [68]. Also, as aptamer development and SELEX methods improve with newer techniques and next generation technology, smaller functional aptamers can be created [69]. As stated before, adsorbed molecular layers on the sensor surface of sufficient thickness can provide additional data for analysis, but depending on the probing length of the particular QCM system, certain nucleic acid layers can be too thin or small. It has been shown that different adsorption phases can be distinguished by varying QCM signals [70]. In certain cases, the use of a monolayer can amplify the signal. For example, streptavidin has been used to immobilize single and double stranded DNA, providing insight into nucleic acid orientation for molecules as small as 34 base pairs [71]. This effect has also been exploited by incubating double stranded DNA with an intercalating drug in order to provide an amplified signal [72]. However, for more

precise characterization of nucleic acid structures more advanced techniques are necessary.

Hybridization is one way to ensure nucleic acid adhesion to the QCM surface. Bardea *et al.* have previously employed an antibody that only binds double stranded DNA to confirm hybridization of two strands in a system where the adsorbed monolayer was too thin for the QCM to identify hybridization events over single stranded immobilization [73]. Hybridization has also been used to detect the presence of the bacteria *Ehrlichia canis* in solution using immobilized complementary DNA [74]. Indeed, hybridization has been observed for nucleic acids strands as small as 30 base pairs, with the ability to construct multi-level layers by exploiting complementary base pairing [34]. This hybridization method can be used in the future for detection of various nucleic acid species. Experiments involving hybridization methods can be found in section 4.4.

4.3.4 Release Kinetics Utilizing the QCM

With low detection limit and rapid, real time analysis, QCM is excellent for observing drug release kinetics. Celik and Oksuz were able to differentiate the difference in release of ibuprofen from three different polymer systems using QCM [75]. Similar measurements were used to detect controlled release of chlorpromazine from a polymer film [76]. Due to the versatility of the QCM system, drug binding and release kinetics can be measured according to a number of variables, including temperature, liquid flow rate, and pH.

The small volume capability of the QCM lends itself nicely to the application of microfluidics. In this way, it can be applied as a microfluidic tool for drug release studies [77]. It has already been seen, for example, that using microfluidics to monitor drug release from a silicon contact lens while mimicking the physiological flow rate within the human eye is possible [78]. While these methods are effective, the real time mass change and sensitivity from the QCM has more potential. For example, binding of only two molecules of nogalamycin was detected using QCM on a layer of double stranded DNA [72]. Nucleic acids have been used as carriers for drugs on therapeutic nanoparticles [79,80]. The ability to analyze drug binding and release in a real-time liquid environment makes QCM technology invaluable for characterization of therapeutics.

4.3.5 Future Field Impact & Applications of QCM

QCM technology has provided a new, exciting avenue for developing biological assays, owing to its ability to operate *in situ* in a liquid environment. The ability to monitor biological processes in a more physiologically accurate environment such as that at the liquid interface within a QCM system is invaluable. The high sensitivity, real-time measurement, and label free sensing ability allows for simple observation of cellular and molecular behaviors that in previous studies required invasive techniques and *post hoc* quantification methods. As these systems are used more frequently, researchers will develop more novel applications for biosensing and biological surface science. It has been shown previously that an increase in the resonant frequency of quartz crystals can produce ultra-sensitive instruments [81]. This will be applicable in the future when

miniature QCM systems enter the market, leading to mobile detection units with no drop in performance.

Cooper *et al.* have used QCM technology to analyze the acoustic energy associated with separation of a bacteria and an antibody in a process they termed rupture event scanning (REVS). They demonstrated that this method could detect as few as 20 bacteria, with data that is not significantly affected by non-specific binding, and effective separation based on affinity to the surface [82]. There are also new QCM systems being developed that utilize other optical techniques, such as spectroscopic ellipsometry [19], and allow for more precise characterization of the adsorbed layer. This becomes beneficial in samples that show little energy dissipation.

Additionally, the development of new aptamers provides a vast range of new applications for the QCM. As more sophisticated methods for immobilizing nucleic acids onto QCM sensors emerge, aptamers can be used as detection markers as well as signal amplification tools. Already biosensors have been prepared using aptamers to detect the presence of *E. coli* and leukemia cells with limits of detection as low as 1.46×10^3 CFU/mL and 1160 cells/mL, respectively [83,84]. QCM technology has come a long way since its first inception in the mid-20^{th} century [85]. As new systems our developed, along with new methods of molecule recognition and detection, it is expected that QCM technology will be at the forefront of mobile, rapid particle detection systems.

4.4 Analysis of Various DNA Building Constructs on a QCM Surface

In order to synthesize stable and organized DNA-linked gold nanoparticles, extensive knowledge of the molecular interactions occurring at the AuNp surface are

necessary. Meanwhile, QCM technology can be used to observe molecular interactions on a flat, gold surface liquid environment in real-time. Therefore, observation of DNA layer formation and hybridization through the QCM may provide information regarding surface functionality and particle optimization. Additionally, the QCM has the ability to identify very small changes in mass deposition and monolayer properties. Using this capability, it is possible to accurately track the loading of drug, in our case Daunomycin, within dsDNA. The QCM reported behaviors of dsDNA layers introduced to Daunomycin, including mass changes and viscoelastic behaviors, can give insight into the intercalation of the drug we have previously observed on functionalized AuNps. From this study, conclusions can be drawn regarding the number of binding mechanisms for Daunomycin and effects that might influence release rate. Using a gold QCM sensor allows for the visualization of an AuNp surface in order to analyze these behaviors as they occur in real-time, in a system with more controlled variables.

According to the company QSense, based on diameter measurements, the QCM chip has an active sensor area of 0.9677cm^2. The hydrodynamic diameter of single stranded DNA for this system was calculated to be 6.6 nm^2; based on this knowledge, 107 DNA strands is the theoretical maximum of ssDNA that can be bound to a 15 nm gold nanoparticle surface [5]. Molecular weights of the custom DNA strands were calculated using the IDT oligo analyzer website [86], and the molecular weight of Daunomycin is known (x). With knowledge of these values, analysis of frequency shifts measured by the QCM could be converted directly to mass deposition, and furthermore total particle deposition could be calculated for all steps. All experiments were performed from a baseline QCM measurement using PBS, and all experimental samples were

suspended in PBS; therefore, we assumed liquid viscosity analysis was unnecessary. Finally, all experiments were performed at 37^{o}C.

4.4.1 Materials, Methods, & Protocols for QCM Use

The Q Sense quartz crystal microbalance and gold sensors were purchased from Nanoscience Instruments (Alexandria, VA). Daunomycin hydrochloride, PBS, and the DNA Polymerase I Large (Klenow) Fragment Mini Kit were purchased from VWR International, LLC (Radnor, PA). DNA oligonucleotides were purchased from Integrated DNA Technologies, Inc (Coralville, IA).

In order to detect binding on the QCM accurately the surface must be cleaned. .Researchers have previously done this by preparing gold electrode surfaces by heating in a peroxide solution [27,36], sonication with a detergent [87, 88], rinsing with ethanol [27, 57, 83, 87-89], and drying with N_2 [27, 36, 57, 83, 87, 88]. To ensure a clean surface, the crystals were soaked in peroxide solution (5:1:1 mixture of milliQ water, ammonia (25 %) and hydrogen peroxide (30 %) heated to 75°C) for 5 min according to manufacturer instructions. The sensors were subsequently immersed in a 2% Alconox solution within an ultrasonic water bath for 10 min. Following sonication, the sensors were rinsed with milliQ water followed by ethanol and dried with N_2. Sensor chambers and O-rings were cleaned using ethanol and dried with N_2. The input and output tubes were prepared by flowing a 10 mM SDS solution at 100 μL/min for 1 hour.

A baseline QCM measurement was performed using water (baseline is defined as $\Delta f < 1$ Hz). A second baseline was obtained using our binding buffer (0.8 M NaCl, 10 mM phosphate). Next, a 0.3 μM solution of reduced anchor DNA in binding buffer was

flowed through the system in an infinite loop at 100 μL/min [19, 27]. Our DNA solution contained 12.5X the amount of DNA to completely cover the gold surface (calculated from an active sensor surface diameter of 11.1 mm and single stranded DNA surface coverage of 6.6 nm^2). Measurements were taken until $\Delta f < 1$ Hz per hour was achieved, after which it was assumed that no more binding was occurring. With a DNA length of 19bp a thin, rigid film can be assumedThis was confirmed by observing a dissipation value $\Delta D < 1 \times 10^{-6}$ [27]. Such films can be evaluated using the Sauerbrey equation [7], which is based on the linear relationship between changes in the resonance frequency and the resonator mass. From this data, the mass per unit area of the film was calculated. Mass values can fluctuate depending on the bulk properties of the liquid medium and water retention within the active adsorbate particle. Further techniques, such as UV spectrophotometry, can be performed to determine the total mass of DNA bound to the gold sensor. Film thickness measurements require further optical measurements [6].

First, we tested the ability to bind and hybridize DNA to our anchor strands in situ using the QCM system. Thiolated anchor (ANC-SH) and non-thiolated anchor (ANC) were kept in a PBS solution at 0.3 μM. A flow rate of 100 μL/min was applied to the sensor. The samples were run in a loop until no further frequency change was observed and washed with PBS. Next, a 52bp DNA sequence with complementary nucleotides (J52) was flowed over both sensors. Again, the sample was flowed continuously until no further frequency change was observed. A subsequent PBS wash was performed to remove unbound DNA.

We then tested the application of a pre-hybridized DNA duplex called J52H. J52H was produced by incubating 50 μl aliquots of 6 μM ANC and 6 μM J52 DNA at

37^0C for one hour, followed by 5 minutes on ice. Added to the sample were 4mM dNTPs and 10X DNA polymerase reaction buffer. The samples were then diluted 10X with PBS to obtain a 0.3 μM solution. PBS was initially flowed through the Q Sense system to obtain a baseline measurement. For half of the sample, Klenow enzyme was introduced to encourage polymerization of a complete, double stranded complex with an anchor extension. The control sample received no enzyme. Hybridized DNA (with and without the Klenow enzyme) was flowed over the QCM sensor at 100 μL/min in a loop until no further frequency change was observed. PBS was applied as a wash to remove any unbound nucleotides.

ANC-SH and pre-hybridized J52H were diluted to 0.25 μM in 10mM PBS at a volume of 1mL. J52H was synthesized as described above. PBS was initially flowed through the Q Sense system to obtain a baseline measurement. DNA samples were then flowed through in a loop until there was no further frequency change observed. From there, maximum DNA binding was assumed, and a second PBS wash was applied to remove any unbound DNA. Next, a 1mL, 25 μM solution of Daunomycin in PBS was added in an infinite loop until a baseline was observed, followed by a third PBS wash step. This experiment was repeated at 10 μL/min and 100 μL/min.

4.4.2 Multiple Assembled DNA Complexes on QCM Sensor

Before starting our first experiment, we ran the QCM system in deionized water. This was to confirm that the sensors were properly cleaned and that no unwanted drift in frequency values was occurring within the system. Upon observation of an acceptable baseline measurement, the sensitivity of the QCM was confirmed as we observed a

frequency drop (or a mass increase) due to application of PBS. Once a baseline was reached with PBS, we began our experiment. The goal of the first experiment is in situ DNA hybridization using the QCM, see Figure 4.7A-B for schematic representation.

Initial data extraction is done by the Q-Sense system and reveals frequency shifts over time. The analyzer software packaged with the Q-Sense includes a built-in Sauerbrey equation function that is standardized for the particular system and the resonant frequency of the provided gold sensors; therefore, we were able to extract the data as mass bound per unit area (ng/cm^2) over time. The Sauerbrey equation is

$$\Delta m = -(C \cdot \Delta f)/n$$

where Δm = mass bound (ng/cm^2), C = 17.7 ng Hz^{-1} cm^{-2} for a 5 MHz quartz crystal, and n = the overtone number. The Sauerbrey equation is applicable to systems with thin, rigid films and change in energy dissipation of less than 1. It also assumes that mass is being deposited homogenously across the entire surface of the sensor. Note that observation of mass deposition over time reveals interesting trends that can be analyzed on their own; however, with knowledge of sensor surface area and molecular weights, further conclusions can be drawn with ease.

Additional ions found in PBS that are not found in deionized water caused a steep increase in mass, as can be in seen in Figure 4.8 (10-60min). This is important to observe initially as it highlights the sensitivity of the QCM system and the importance of keeping solvent composition static when controlling for single variables. The following mass increase, in Figure 4.8, observed at 60 mins is due to the addition of DNA samples ANC and ANC-SH (see Figure 4.7A for diagram explanation, ANC has no thiol bonds and

therefore does not have binding site shown). Oscillations in mass loading are observed, corresponding to fluctuations in mass bound to the sensor surface. As material is flowed over the sensor, it is expected that the adsorbed layer will go through multi-structural changes and intermolecular interactions.

ANC-SH reveals both mass loading and initial oscillations that are greater in value than ANC. The increase in total binding for ANC-SH is due to the covalent interactions of the thiol bond, along with the more organized, perpendicular binding that allows a denser surface coverage when compared to free floating ANC. The larger oscillations in the ANC-SH data from Figure 4.8 can be explained by asserting that the thiol-mediated monolayer can undergo organizational restructuring as more anchor strands are introduced. Next, a steep increase in mass is observed around 120 min, this occurred after application of a PBS wash. It is hypothesized that this is additional reorganization and untangling of loose DNA caused by the force induced by PBS flow.

The addition of complementary sequence J52, Figure 4.8 around 170 min, results in a final mass increase as it hybridizes with the bound ANC-SH layer (see Figure 4.7B for visualization). Assuming total, dense coverage of anchor strands in the initial loading, it is unlikely that J52 would have the space available to hybridize every anchor strand. However, it is clear from the data that some hybridization occurs, and unbound J52 is observed to release form the sensor surface after a final PBS wash, as can be seen from Figure 4.8. A small mass increase is observed for ANC upon addition of J52, likely due to further non-specific interactions between the phosphate backbone of the DNA and the gold sensor surface. Hybridization probably still occurs, however strands do not remain

bound in a tightly organized fashion and mostly wash off the sensor, as can be seen in Figure 4.8.

The next experimental study was to determine the effect of DNA loading due to buffer flow rate for ANC-SH and pre-hybridized J52H complexes (see Figure 4.7A and C-E for schematic representation of both). A decrease in flow rate resulted in a larger magnitude of DNA mass binding for both ANC-SH and pre-hybridized J52H molecules as can been seen from the results shown in Figure 4.9. Figure 4.9 represents a compilation of maximum loading values (after a wash step) observed over multiple tests involving DNA loading. Note that J52H results in greater mass binding overall, but is also about 5.6X larger than ANC-SH in molecular weight (34.17 kg/mol to 6.13 kg/mol, respectively). It is expected that organized formation of a thiol-mediated monolayer includes many phases of restructuring on a molecular level, and the higher flow rate of 100 μL/min may in fact be too forceful to allow tight, dense coverage due to higher velocity and shorter residence time. Reducing the flow rate to just 10% may allow for more appropriate methods of molecular assembly, explaining the increased binding seen in Figure 4.9. However, the most likely reason is the fact that the 10% flow rate sample interacted with the sensor surface 10 times longer to allow for the same amount of total sample to be exposed to sensor surface for both tests.

It is interesting that from the data in Figure 4.9, it appears that J52H loading results in a much greater deviation in total mass binding compared to ANC-SH (compare error bars). The increased size of the J52H molecule, along with the increased intramolecular complexity and probability of molecular entanglement may lead to variance in the monolayer formation. At slower flow rates, this can lead to random,

unwanted molecular interactions, which then produces the observed minimum and maximum loading values. ANC-SH, as a short, single stranded, poorly self-complementary molecule is much more consistent in its monolayer formation at both flow rates.

4.4.3 Detection of Real Time Polymerization of dsDNA

Next, the sensitivity of the Q-sense was put to the test with attempts to track real time polymerization of double stranded DNA from the Klenow reaction. The Klenow enzyme, when activated, is efficient at polymerizing complete DNA duplexes out of partially hybridized DNA strands in the presence of dNTPs. In solution, of course, mass is conserved, but the molecular weight of the DNA hybrids in question will be increased as polymerization runs its course. To assess the success of our Klenow mediated J52H hybridization, we analyzed QCM loading for ANC-SH + J52 hybrids incubated with and without the Klenow enzyme (see Figure 4.10 for schematic representation).

Because the Klenow (+) sample differs only by the presence of the enzyme, it is expected that initial QCM loading would reveal slightly greater mass loading than the Klenow (-) sample. Additionally, the subsequent wash step would reveal a decrease in mass for the Klenow (-) sample as all excess dNTPs are removed, and a much less pronounced decrease in the Klenow (+) sample as only excess dNTPs and Klenow enzyme are removed. Our data, shown in Figure 4.11, agrees with this expected outcome. It is important to note that a short, quick mass increase is observed around 140min (Figure 4.11), as flow was reversed to remove the presence of air bubbles in solution. This data is significant, as it demonstrates that successful Klenow mediated

hybridization of our J52H molecule is observable using QCM with expected mass differentials.

4.4.4 Daunomycin Binding & Quantification

Introducing a new variable to the system can yield further information. . It is important to determine if there are multiple drug binding mechanisms taking place with the DNA in order to analyze potential results later when this DNA-drug system is placed on an AuNp. Figure 4.12 is a schematic representation of this experiment demonstrating the inclusion of Daunomycin to the previously established DNA bound sensor systems and the potential drug binding behavior or impact on the construct. Daunomycin binding to both ANC-SH only and J52H sensors were compared and analyzed.

In order to isolate the effect of Daunomycin loading on the DNA functionalized QCM sensor surface, the initial time point that Daunomycin was introduced to the QCM system and the preceding mass loading values were both normalized to zero (see Figure 4.13 time point zero). Upon analysis of the data from Figure 4.13, it is conclusive that J52H loaded a greater amount of mass than ANC-SH upon introduction of Daunomycin. This is considered to be attributed to the mechanism of intercalation of Daunomycin into double stranded DNA, J52H. It is believed that nearly all interactions of Daunomycin with ANC-SH will be weak, ionic interactions with the phosphate backbone.

Indeed, oscillations in mass loading are observed after the initial Daunomycin introduction for J52H. This is potentially due to the nature of intercalation as Daunomycin first interacts with the phosphate backbone and then while it associates with

the minor groove of dsDNA, subsequently inserts itself between the base pairs [90]. The PBS wash, introduced around 65 min in Figure 4.13, reveals that Daunomycin is released from ANC-SH more rapidly than from J52H, presumably due to the interactions between the DNA and drug being much weaker. It is important to note that both samples approach the same value towards the end of the experiment after several washes.

Next, the data was further analyzed to determine the effect of flow rate on the number of DNA and Daunomycin molecules bound to each sensor. An important distinction between ANC-SH and J52H to consider is the molecular weight difference since the data output is in ng/cm^2. Using the molecular weight values of ANC-SH and J52H (6.13 kg/mol and 34.17 kg/mol, respectively), it was discovered that the sensor containing only a layer of ANC-SH loaded around 2.4 times more molecules of DNA than the J52H sensor, see Figure 4.14. This realization highlights the preferential loading of Daunomycin into dsDNA, as the greater mass value is more significant, and also suggests a greater tangling effect on the ANC-SH sensor – without this tangling effect, the differences in release time may have been even greater.

The mass loading values for both DNA and Daunomycin bound to the QCM sensor surface requires several assumptions, but most notably; that liquid retention within the adsorbed layer is equivalent for both sensors, and that these values are negligible. The increased mass and complexity of J52H when compared to ANC-SH may lead to some inaccuracies due to this assumption. Number of Daunomycin and DNA particles bound for both J52H and ANC-SH functionalized sensors can be analyzed at various flow rates from data shown in Figure 4.14. An important conclusion to draw from this data is that

regardless of flow rate, ANC-SH sensors bound more DNA than J52H sensors, and with lower Daunomycin loading.

As expected, Daunomycin prefers to intercalate between dsDNA rather than associating with ssDNA backbones, and will load more mass initially and retain higher loading after a wash step. At 100 μL/min, the force of the flow rate is expected to have removed a large portion of Daunomycin from both sensors; this explains not only the reduced loading values but also the comparable loading between ANC-SH and J52H (see Figure 4.14), as the Daunomycin was not able to intercalate entirely at such a high flow rate. At 10 μL/min, the difference in total Daunomycin bound is more distinguishable between ANC-SH and J52H. Here, a significantly larger Daunomycin loading amount is observed for J52H, as the low amount of force imbued by the solvent does not seem to perturb the Daunomycin mechanism of intercalation.

The next analysis involves comparing the ratio of Daunomycin bound per DNA complex(Table 4.4). From this table it is clear that the difference in Daunomycin molecules/DNA bound is much more pronounced at the slower flow rate when comparing ANC-SH to J52H. Interestingly, the Daunomycin molecules/DNA bound ratio is greater for both samples at 100 μL/min. One hypothesis could be that the increased flow rate may exacerbate the tangling effect of the DNA functionalized sensors as Daunomycin interacts with DNA backbones and is therefore crowded at a more rapid pace.

4.4.5 Energy Dissipation

One last analysis conducted, in an effort to determine if there are multiple binding mechanisms for Daunomycin in our DNA system, was to extract data regarding energy dissipation for both ANC-SH and J52H. Energy dissipation is measured in the QCM system by regularly stopping the applied voltage and analyzing the degradation of the frequency with the equation:

$$D = E_{lost} / 2\pi E_{stored}$$

Where E_{lost} is the energy lost (dissipated) during one oscillation cycle and E_{stored} is the energy stored within the oscillating crystal. Generally, adsorbed layers with $\Delta D < 1$ correspond to a thin, rigid film that is analyzed using the Sauerbrey equation. For layers with $\Delta D > 1$, it is assumed that some viscoelastic properties may be having an effect on mass binding values and further modeling or optical techniques are required. Methods of analysis for distinct adsorbed layers must be analyzed appropriately according to frequency and dissipation values. Dissipation can be caused by an increase in layer density or viscoelasticity (through either entangled molecules or interactions with the adsorbed particles) or through increases in the layer thickness, e.g. the length of the adsorbed molecules. This dissipation response is artistically rendered for our system in Figure 4.15.

Analyzing the data in Figure 4.16B, at 100 μL/min, dissipation values are virtually identical. As the introduced Daunomycin sample was the same for both sensors, most of the dissipation is attributed to nonspecific, tangle-induced interactions. It can be seen from initial dissipation oscillations that some intercalation occurs for J52H at 100

μL/min, however final values are comparable. In contrast, at 10 μL/min (Figure 4.16A), the dissipation induced by Daunomycin binding for J52H is higher than that observed for ANC-SH.

It is expected that this increased energy dissipation may be due to two effects: 1) increase in molecular weight of each individual DNA molecule from drug binding, and 2) lengthening of each individual DNA molecule due to drug intercalation. Again, we observe an oscillating effect upon introduction of Daunomycin for J52H, as the Daunomycin undergoes its biphasic intercalation. Note that upon intercalation into the J52H strands, dissipation values occasionally oscillate and approach values slightly greater than $\Delta D = 1$. This suggests that the Daunomycin intercalation may be imparting some viscoelastic properties onto the adsorbed DNA layer due to its stabilization of slight extension of the DNA. However, many measured values remain under $\Delta D = 1$; therefore, the Sauerbrey equation was used for analysis of all the previously discussed data.

4.5 Conclusions

QCM outputs frequency and dissipation, which calculates mass accumulated and rigidity of the sample on a gold sensor surface based on these measurements. In order for these calculations to be performed, a type of film layer expected based on your sample must be determined first. Fortunately, this determination is also based on the frequency and dissipation values from the output. Depending on the range the values , a mathematical model can be used to calculate mass accumulated and changes in rigidity of the sample. These models of course come with assumptions and their applicability will vary depending on the specific values of frequency and dissipation measured, even within

their particular target range. Based on the frequency and dissipation values measured for our DNA and drug loaded gold sensor system, the Sauerbrey model for non-dissipative response was determined to be the most accurate representation. This particular Sauerbrey model is indicative of a thin, rigid, homogeneous film layer on the gold sensor surface.

The QCM is capable of working with a variety of SAMs depending on time range needed and detection limits. It also has one lowest detection limits and shortest measure time for protein sensing, while adding the benefit of real-time monitoring. The QCM has many capabilities, such as flow rate of a sample over the sensor can be controlled by a pump, as well the possibility to load up to four sensors at once for multiple tests. The Q-sense has an analyzer that uses a simple interface for tracking frequency changes and energy dissipation.

Quartz crystal microbalance, as the name suggests, uses a quart crystal as the physical material. A voltage is applied to the quartz crystal coated with a gold surface, and due to the piezoelectric effect, this voltage will generate a standing wave within the crystal. As mass is either bound or removed from the sensor surface, a frequency change in this standing wave will be induced, which is used to determine mass and energy dissipation. These changes are sensitive enough to even track cell adhesion to the sensor in real-time. Additionally, many common techniques to prevent undesired binding of a target molecule to the sensor surface can be used without damaging the sensor. Finally, the signal for the QCM can be amplified or reduced within the system, such as introducing secondary molecules, similar to other detection methods.

The assembly of the DNA and drug complex on the gold sensor was done using two different approaches. First, a pre-hybridization method where anchor DNA was base paired with *J52* DNA and then a double stranded region was extended using the Klenow enzyme was assembled and purified before being introduced to the sensor. The second method was a post-hybridization approach where anchor DNA was first bound to the sensor, unbound washed, *J52* DNA added with unbound washed, then the Klenow reaction was performed with one last wash. The drug, Daunomycin, was introduced after the complexes were already bound to the sensors for both methods. Bound DNA and drug was quantified for both methods and results were similar. The post-hybridization method was able to show the assembly in real-time so the results for this method are shown as a preference.

Interestingly, the real-time DNA assembly of the double stranded region during the Klenow reaction was detected and tracked, with an obvious difference between sensors with and without the Klenow enzyme being present for the reaction. Sensors with the enzyme showed more mass was attached overtime after washing. Another test was the effect of the flow rate of two samples with the same concentration of salt and DNA. A flow rate 10 times slower then the other bound approximately twice the amount of DNA to its surface. There are several possibilities as to why this may have happened, but most likely it is due to the fact that the sample was exposed to the surface 10 times longer to account for the 10 times slower speed rate to make sure the sample amount of total sample was exposed to each sensor.

The next test was Daunomycin binding to bare sensors, anchor DNA only sensors, and the full dsDNA complex sensors. Daunomycin binding occurred for all sensors, but

the DNA coated sensors bound significantly more drug, especially after washing. Daunomycin appeared to bind more on the dsDNA sensor compared to the anchor only sensor initially, but after washing the results were nearly the same. However, the Daunomycin washed off of the anchor only sample at a faster rate compared to the full dsDNA sensor. This could potentially indicate the difference in affinity for the drug between the two samples and the mechanism for binding. It is hypothesized that the anchor only sensor was binding drugs either through tangling or interactions with the backbone, while the dsDNA sensor had both of these mechanisms plus intercalation, the latter of which will bind Daunomycin more strongly, causing a slower delay in release of drug from the sensor during the wash.

Energy dissipation can be used to determine if there is a different behavior in drug binding between these two samples based on its effect on the DNA when bound. The 10 times slower sample showed an increase in dissipation for the dsDNA sensor but only negligible change for the anchor only sensor after drug loading (normalization before the drug was loaded was done for each sensor), indicating the DNA rigidity has changed for the dsDNA sensor. Daunomycin is known to increase stability of dsDNA and tighten the strands to decrease diameter, this matches with the data and is in agreement with our hypothesis.

The 10 times faster flow rate sample showed no change in dissipation for both sensors. It is possible that the force from the faster flow rate was an additional factor in removal of Daunomycin bound to the DNA, which would explain this result. Overall, the 10 times faster flow rate bound more drugs for both the anchor only (many times greater) and dsDNA (only slightly more) sensors. However, the 10 times slower flow rate sample

had a much greater ratio in drug bound when comparing dsDNA vs anchor only sensors with a ratio of 30.5 compared to only 2.67 for the 10 times faster flow rate sample. This means the impact of intercalation from the presence of the dsDNA region is greater when working with the slower flow rate.

QCM technology operates *in situ* in a liquid interface environment that can be monitored for biological processes. In the future, as this technology further improves, there is potential to one day have a pocket sized Q-sense with rapid detection rates and high sensitivity in ranges of picomolar or lower. QCM is currently being developed to be compatible with other types of optical techniques, such as spectroscopic ellipsometry. These new properties will further allow for more precise characterization of absorbed layers. QCM will increase in use over time and may one day be at the forefront of mobile, rapid particle detection systems, coming along way since its inception in the mid-20^{th} century.

4.6 Tables & Figures

Table 4.1. Mathematical model selection based on adsorbed layer and dissipation. *Depending on the attached material to the sensor, different mathematical models are a better fit. Assumptions must first be made before selecting model. Sauerbrey was chosen for the experiments performed in our study.*

Type of film	Dissipative response	Model/Approach	Output
laterally homogeneous film	$\Delta\Gamma_n \ll -\Delta f_n$, or[a] low dispersion in $\Delta f_n/n$	Sauerbrey equation	• areal mass density (may include solvent inside the film)
	$\Delta D > 0$	viscoelastic model	• areal mass density (may include solvent inside the film) • viscoelastic properties (frequency dependent loss and storage moduli or compliances)
		intrinsic viscosity	• $\Delta\Gamma_n/-\Delta f_n$ ratio has been used to obtain structural information about the molecules in the film.[24]
monolayer of discrete particles or other nanosized objects	ΔD is small, or [a] low dispersion in $\Delta f_n/n$	Sauerbrey equation	• areal mass density (including liquid inside the film)
		empirical trapped-liquid coat model	
	$\Delta D \geq 0$	FEM simulation of hydro-dynamics	• local mechanical properties (linker stiffness) • in principle also particle size, shape and coverage. Quantitative predictions limited by computational resources.
		model-independent	• $\Delta\Gamma_n/-\Delta f_n$ ratio has been used to obtain adsorbed particle size in a model-independent fashion[26]

[a] Either of the two criteria can be applied, though the criteria of low dispersion in $\Delta f_n/n$ is more stringent.

Table 4.2. List of SAMs with LOD and time. *Various immobilization tactics that can be used depending on time range needed and detection limits. Information here provides a list for common options.*

Probe	Target	Immobilization	LOD	Time	Reference
Antibody	*A. hydrophila*	Oxidized IgG	6.25 ug/mL	5m	Hong et al 2017 [29]
Antibody	AFB1	Direct (Activated Monolayer)	1.625 ng/mL	-	Ertekin etal 2016 [91]
Antibody	*Anthracis* spore	Protein A on Mixed Monolayer	10^3 CFU	<30m	Hao et al 2009 [57]
Antibody	*C. Jejuni*	Direct (Activated Monolayer)	150 CFU/mL	9m	Masdor et 2016 [92]
Antibody	*E. Coli DH5α*	Sulfo-SMCC crosslinker	8 x 10^4 CFU/mL	10m	Farka et al 2015 [93]
Antibody	HSA	Amine-rich Polymer	5 µg/ml	-	Makhneva 2016 [30]
Antibody	Ochratoxin A	Direct (Activated Monolayer)	17.2 ng/mL	10m	Pirinçci et 2018 [94]
Antibody	rhIL-1ra	Capture Ligand (Protein G)	25 ng/mL	-	Carrigan et 2005 [95]
Aptamer	AIV H5N1 virus	Thiolated ssDNA in Nanowells	2^{-4} HAU/50uL	10m	Wang et al 2017 [96]
Aptamer	CCRF-CEM cells	Thiolated ssDNA	1160 cells/mL	30m	Shan et al 2014 [84]
Aptamer	Collagenase	Thiolated Peptide	0.96 ng/mL	10m	Dong et al 2017 [64]
Aptamer	*B. Anthracis DNA*	Thiolated ssDNA	3.5×102 CFU/mL	30m	Hao et al 2011 [97]
Aptamer	*E. Canis* DNA	Thiolated ssDNA	4.1 x 10^9 molecules/uL	-	Bunroddith 2018 [74]
Aptamer	*E. Coli DNA*	Biotinylated Aptamer	1.46×10^3 CFU/mL	50m	Yu et al 2017 [83]
Aptamer	Salmonella	Thiolated ssDNA	10 CFU/mL	<10m	Ozalp et al 2015 [98]
Aptamer	Thrombin	Avidin-Biotin	1nM	10m	Hianik et al 2005 [99]
Aptamer	Thrombin	Thiolated ssDNA	0.1nM	-	Chen et al 2010 [36]
MIP	Bilirubin	Imprinted Bilirubin	0.45 µg/mL	25m	Çiçek et al 2016 [24]
MIP	*E. Coli*	Imprinted *E. Coli*	3.72 x 10^5 CFU/mL	56s	Yilmaz et 2015 [100]
Penicillinase	Penicillin	Virus particle scaffolds	50 µM	-	Poghossian,18 [101]

Table 4.3. Protein sensing between common detection methods. *Reported detection limits of common protein sensing techniques. The advantage of QCM analysis lies in its real-time monitoring capabilities and in situ environment. This provides more accurate observation of certain processes even when detection limits are not the lowest.*

Detection Method	Target	Detected Using:	Sensitivity	Time
QCM	IgE	Aptamers immobilized on avidin surface	2.5 ng/mL[102]	15 min
ELISA	IgE	Antibody-linked ELISA plates	8.5 ng/mL[103]	1 - 4h
Capillary electrophoresis	IgE	Fluorescence	46 nmol/mL[104]	< 1 min
Western Blot	Transferrin	Semiconducting polymer dots	< 50 pg[105]	0.5-2h
UV Spectroscopy	BSA	UV absorbance	1.2µg/mL	< 2 min

Table 4.4. Ratio of Daunomycin particles per DNA molecule bound. *Flow rates of 10 µL/min (left) and 100 µL/min (right) showed different ratios of drug bound per DNA molecule for both ANC-SH and J52H. Both DNA samples bound a greater amount of Daunomycin at the faster flow rate. There is an increasing difference in the ratios seen between ANC and J52H at the slower flow rate compared to the faster flow rate.*

Daunomycin Particles Bound per DNA Molecule Bound		
ANC-SH	0.77	10.33
J52H	23.49	27.61
	10 µL/min	**100 µL/min**

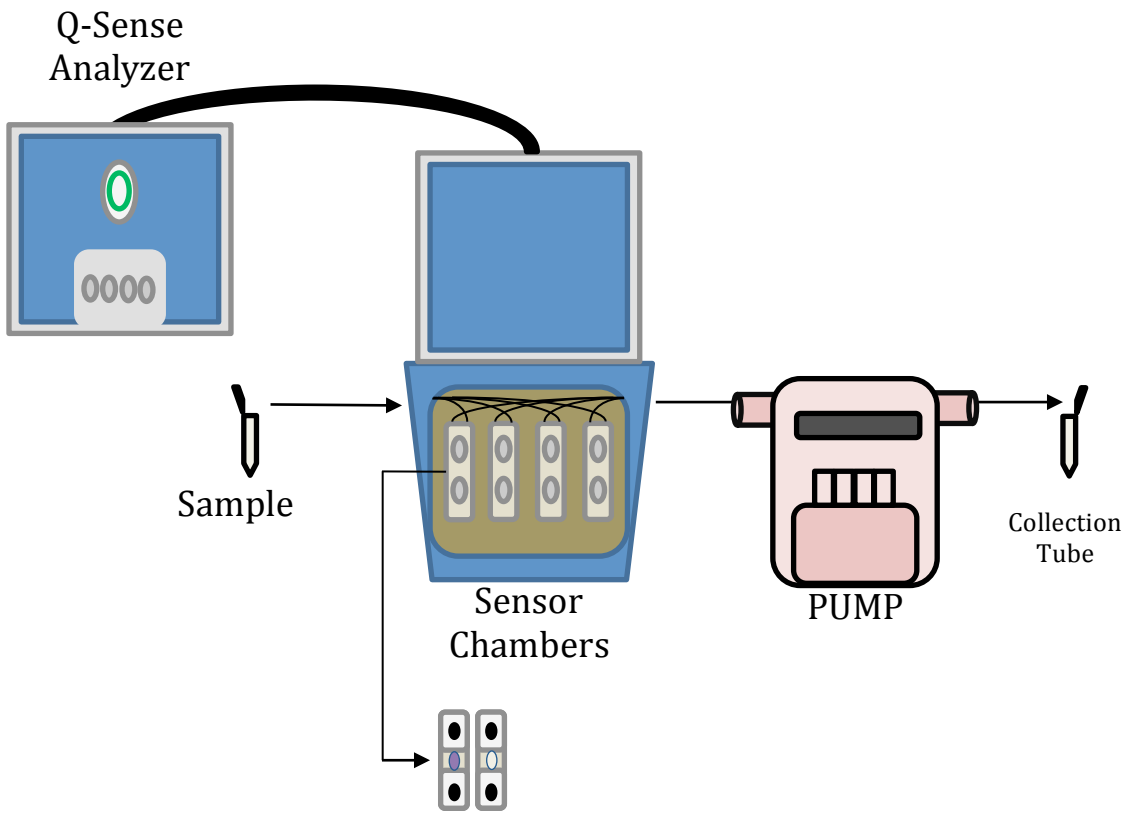

Figure 4.1. Diagram of components in Q-sense system. *Within the main body of the system lies mounts for four sensor chambers in which your chosen sensor type will be set. A variable speed pump is used to direct liquid flow in either direction over each QCM sensor, from your input sample to your output collection tube. The Q-Sense analyzer comes equipped with a simple interface for tracking frequency changes and energy dissipation in real-time. The Qtools software included with the device also has the capability of plotting your data according to a variety of built-in mathematical models.*

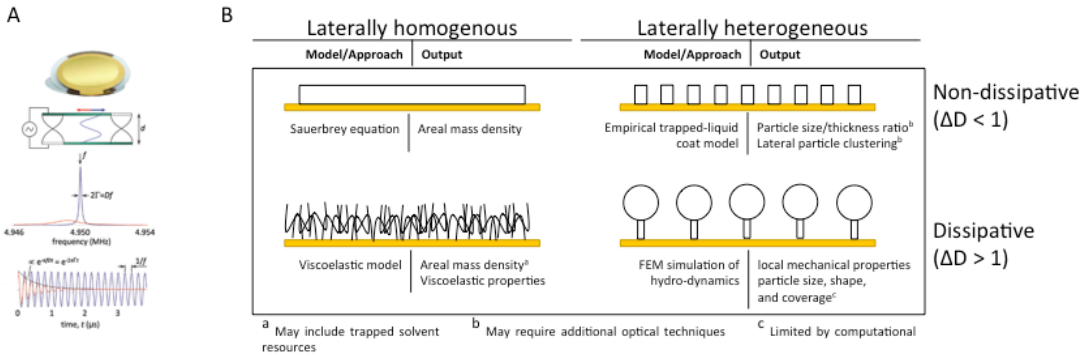

Figure 4.2. Model QCM standing wave and absorbed layers. *(**A**) Function of a quartz crystal microbalance (QCM) involves application of a voltage to a quartz crystal surface coated with a chosen material (in this picture, gold). Top: due to the piezoelectric effect, this voltage generates a standing wave within the crystal. Binding/removing mass from the crystal sensor surface will induce a frequency change in the standing wave. Bottom: many modern QCM systems are also able to extract data about energy dissipation (ΔD). (**B**) In general, absorbed layers can be laterally homogenous (left) or heterogeneous (right), and dissipative (ΔD > 1) (bottom) or non-dissipative (ΔD < 1) (top). For non-dissipative layers, such as the system used in this study, the Sauerbrey equation can be employed to relate frequency shift (Δf) to areal mass density (ng/cm^2).*

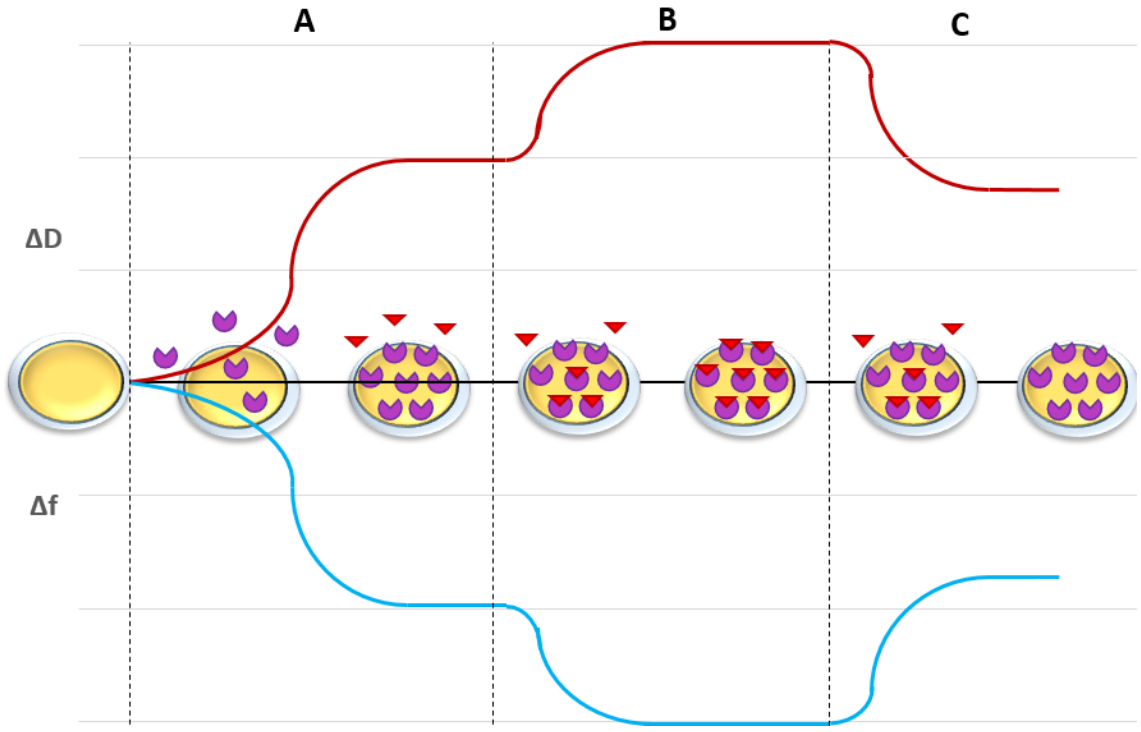

Figure 4.3. Illustrated QCM data. *This schematic demonstrates likely data seen when using a QCM. Δf is shown in blue, ΔD is shown in red. Note that shifts may not be to scale, and not all binding will cause a shift in dissipation.* ***(A)*** *An initial shift in frequency as a monolayer is bound to the sensor surface.* ***(B)*** *An additional shift as the target molecule binds to the monolayer.* ***(C)*** *A shift in the opposite direction as the target molecule is released from the complex.*

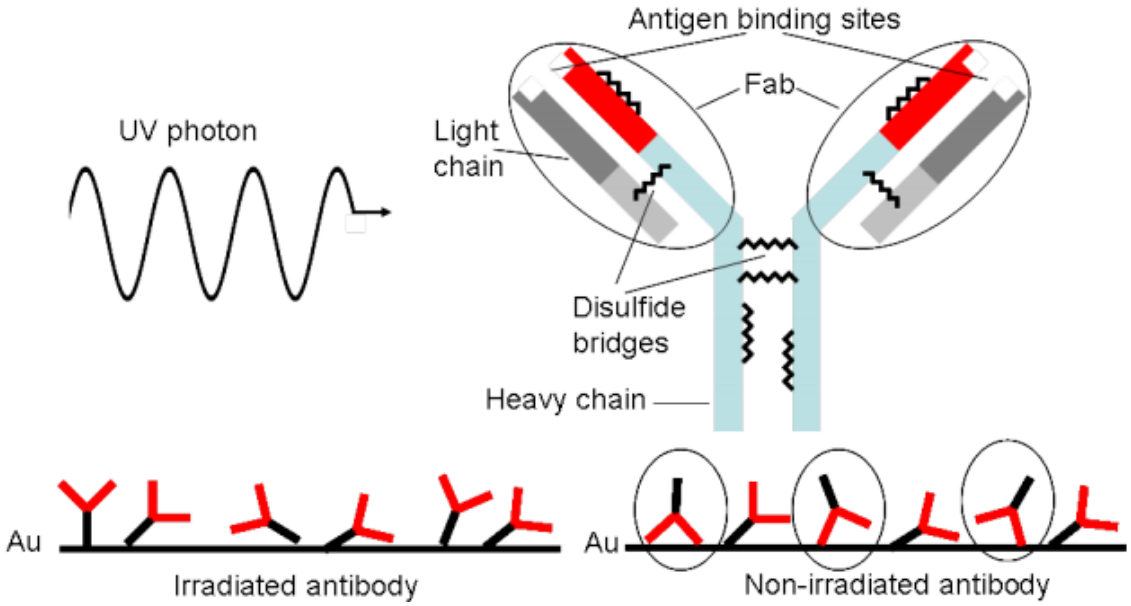

Figure 4.4. Photon assisted immobilization. *UV light is used to exploit the disulfide bridges present in an antibody. With this technique, a free thiol group is revealed and a monolayer of antibodies can be constructed without further surface modifications. Adapted from [31].*

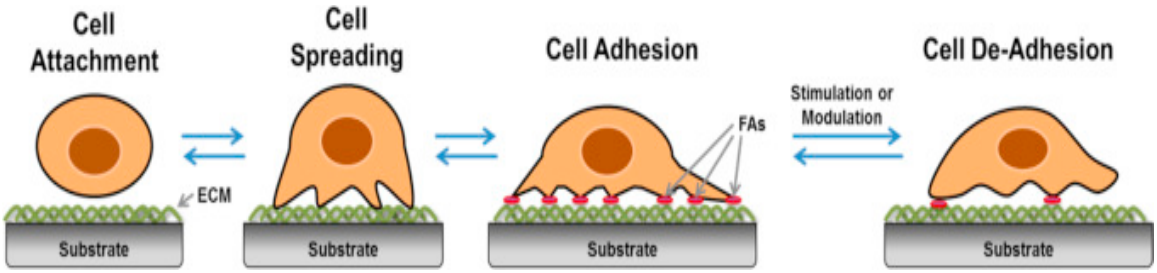

Figure 4.5. Stages of cell adhesion. *Cell adhesion normally occurs in three steps: attachment, spreading, and adhesion. QCM systems are able to monitor these processes in real time. De-adhesion can also be monitored in response to different stimulations. Adapted from [37].*

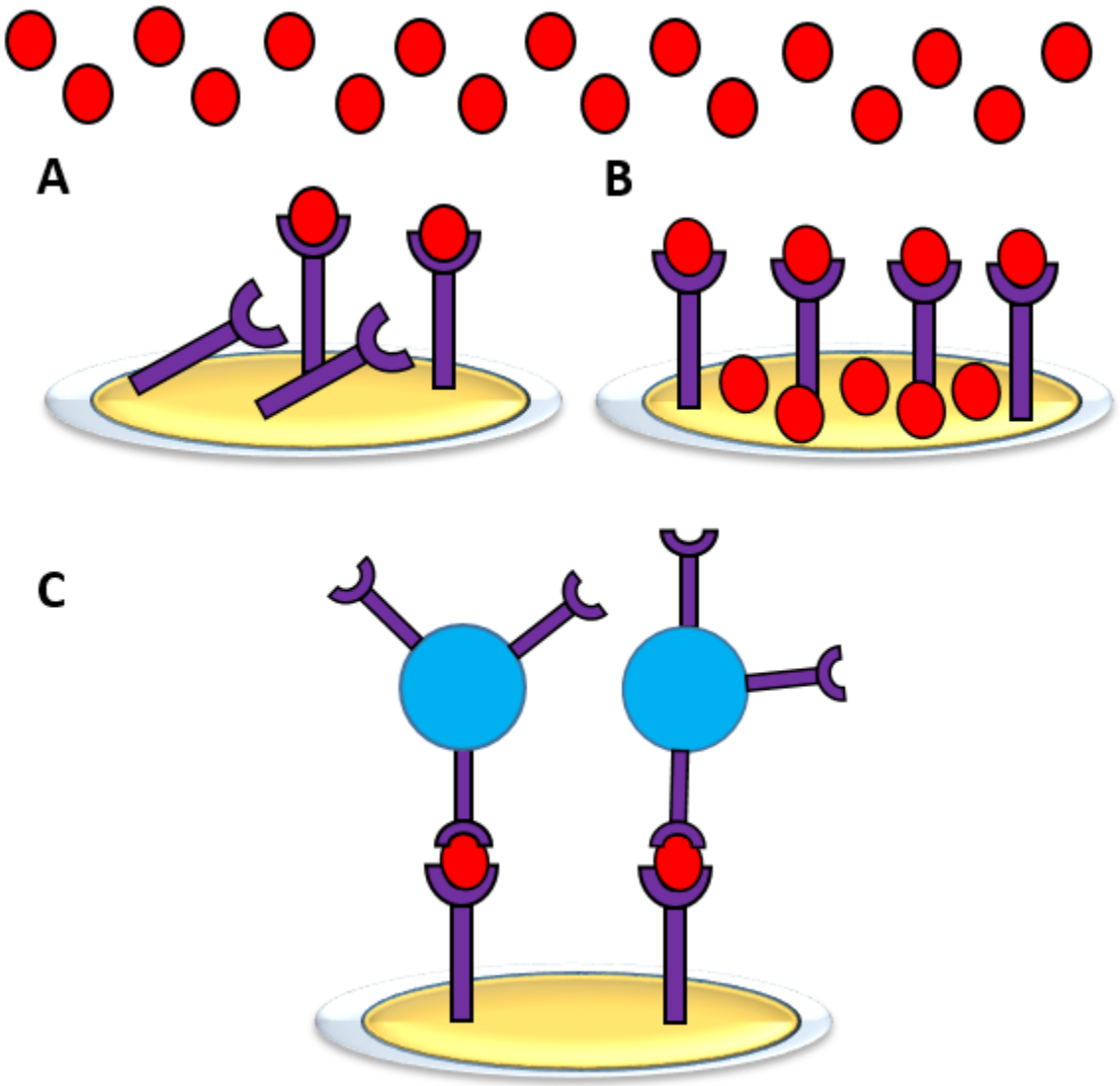

Figure 4.6. Common causes for QCM data amplification or reduction. *Demonstrates three common ways QCM data can be amplified or reduced.* ***(A)*** *Non-oriented molecules will cause a reduced signal when exposed to a target.* ***(B)*** *Nonspecific binding, or trapped liquid on the sensor surface will cause a signal shift.* ***(C)*** *Mass amplification can be achieved using nanoparticles, or other higher mass materials.*

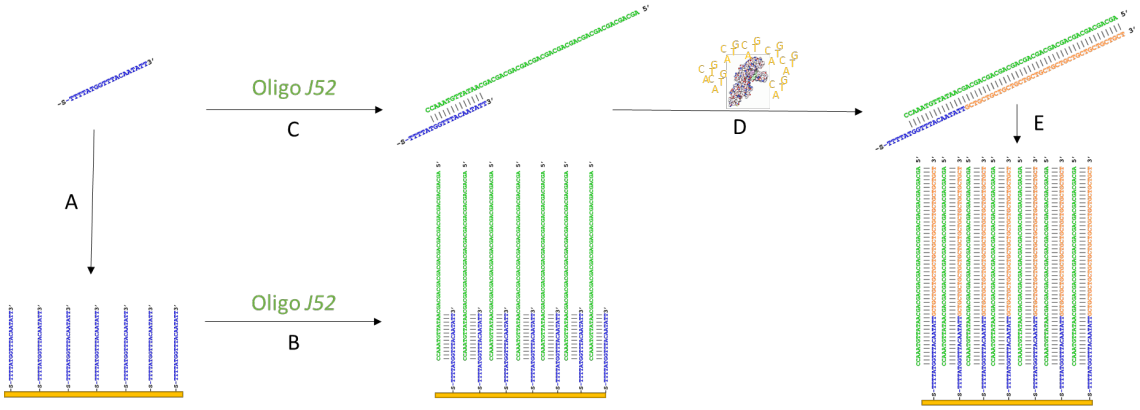

Figure 4.7. Schematic of multiple DNA assemblies tested on a QCM gold sensor. *Flowing 5' thiol-modified anchor strand (ANC-SH) over a gold-coated QCM sensor to observe formation of a monolayer of small thickness (**A**). Observation of real time hybridization of the partially complementary DNA strand, oligo J52, to ANC-SH (**B**). Hybridization of ANC-SH to oligo J52 ex situ (**C**) and subsequent polymerization of a complete double stranded DNA duplex using the Klenow enzyme (**D**). Binding of the double stranded duplex to the QCM sensor surface (**E**).*

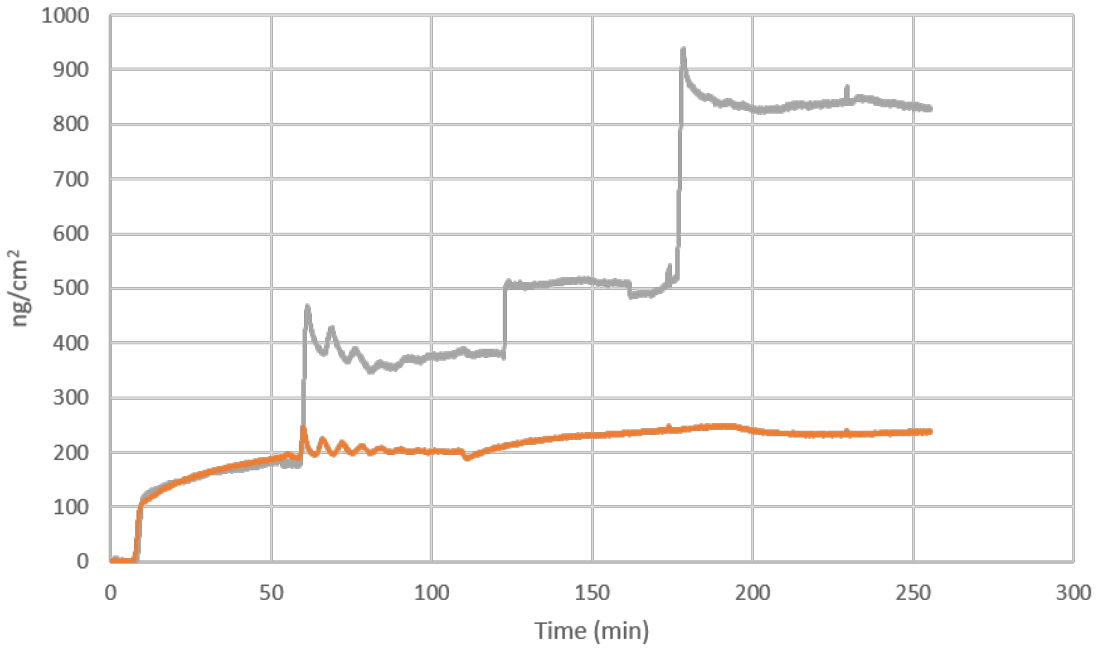

Figure 4.8. In situ DNA hybridization using a QCM. *(■)Thiolated anchor DNA (0.3 µM) was flowed over a QCM sensor in PBS (60 min). An initial increase of mass is observed due to diH_2O being replaced with PBS (10-60 min). Complementary ssDNA (J52) (0.3µM) was added (170 min) until another baseline was reached and a final PBS wash was applied. (■) Non-thiolated anchor (0.3 µM) was also applied (60 min) to observe hybridization without a thiol-mediated monolayer and J52 was added the same as just described..* ***Time points:*** *0min – H_2O; 10 min – PBS; 60 min – ANC(SH); 110 min – PBS wash; 170 min – J52; 230 min – PBS wash.*

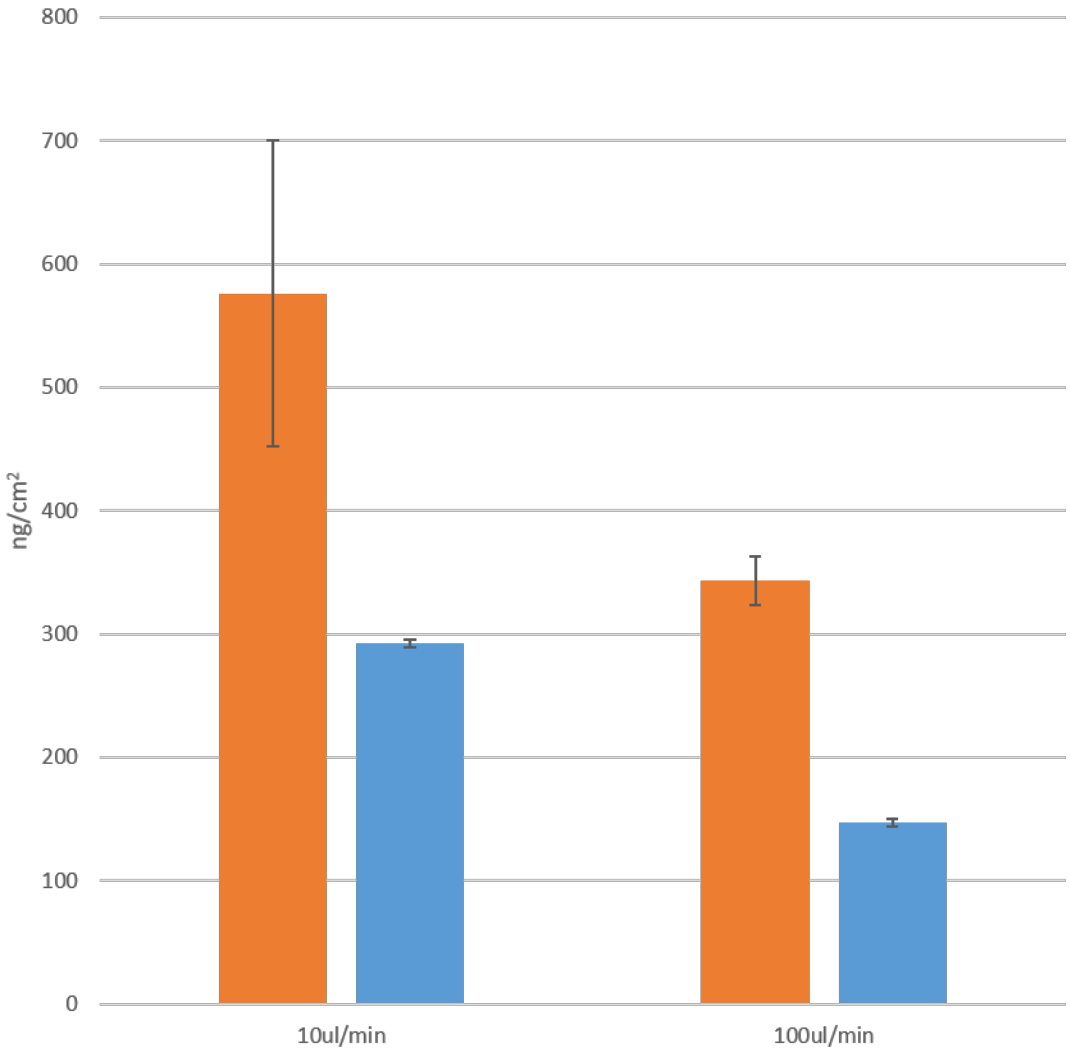

Figure 4.9. DNA loading at various flow rates using a QCM. *Pre-hybridized (J52H) (■) and anchor (ANC-SH) (■) DNA with a thiol modification at the 5' end were flowed over a QCM sensor at 10 µL/min (left) and 100 µL/min (right). The slower flow rate of 10 µL/min led to increased binding for both. The larger amount of deviation in J52H loading values is likely a result of the increased size and complexity of the molecule leading to a more pronounced tangling effect.*

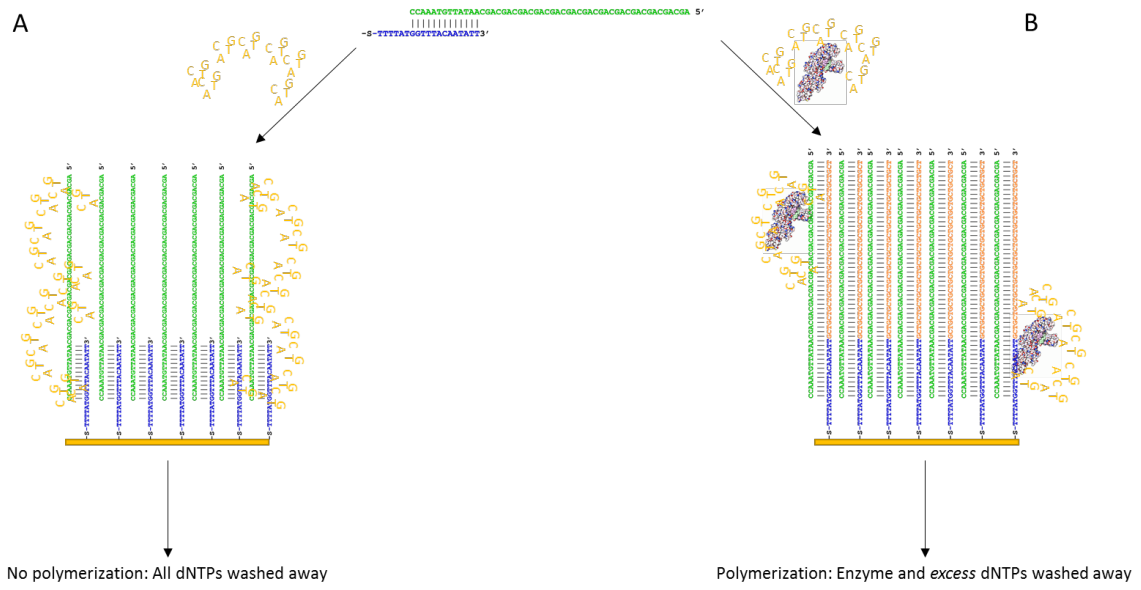

Figure 4.10. Schematic of real time detection of Klenow polymerized DNA hybrids. *Klenow-mediated polymerization is observable by viewing mass loading of partially complementary DNA duplexes plus dNTPs incubated without (A) and with (B) the enzyme. (A) Initial increase in mass density upon the QCM sensor will quickly reduce in value dNTPs are removed from the sensor surface during PBS wash steps. (B) Initial increase in mass density upon the QCM sensor will reduce in value less during PBS wash steps due to the addition dNTPs polymerizing onto the DNA construct as a result of the presence of the enzyme.*

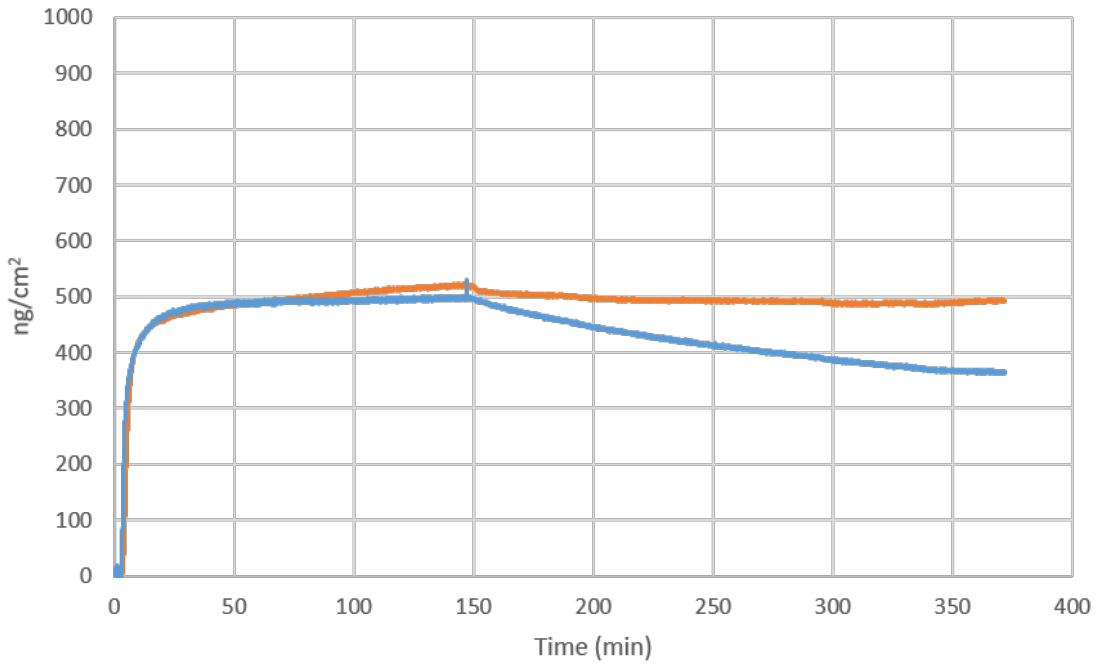

Figure 4.11. Real time detection of DNA polymerization using QCM. *Real time binding of hybridized DNA duplexes (J52H), polymerized with and without the Klenow enzyme. Klenow (+) samples (■) show slightly increased mass binding initially due to the presence of the Klenow enzyme in the solution. The wash step shows mass reduction from removal of enzyme along with any excess, un-polymerized dNTPs. Klenow (-) samples (■) had a much more pronounced mass reduction after the wash step as most excess dNTPs were removed.* ***Time points:*** *5min – J52H; 140min – PBS wash.*

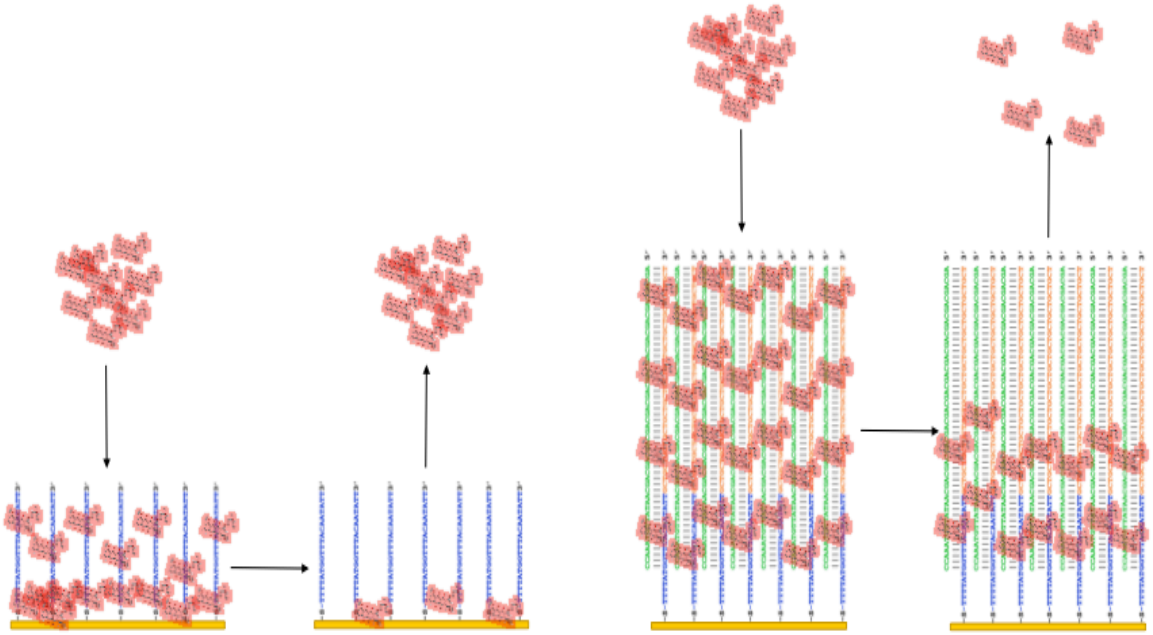

Figure 4.12 Schematic representation of daunomycin inclusion and wash effects. *Ionic interactions with the DNA phosphate backbone and the gold surface can lead to weak interactions, and a resulting dense layer of molecules may cause a sterically induced tangling effect. These effects potentially result in higher drug binding for the ANC-SH coated QCM sensor then expected (far left). Wash step removed most of the bound Daunomycin observed within minutes (middle left). Higher amounts of Daunomycin bound to the J52 duplexes comparative to ANC-SH (middle right). Wash steps also rinsed away a large portion of Daunomycin, but at a slower rate (far right).*

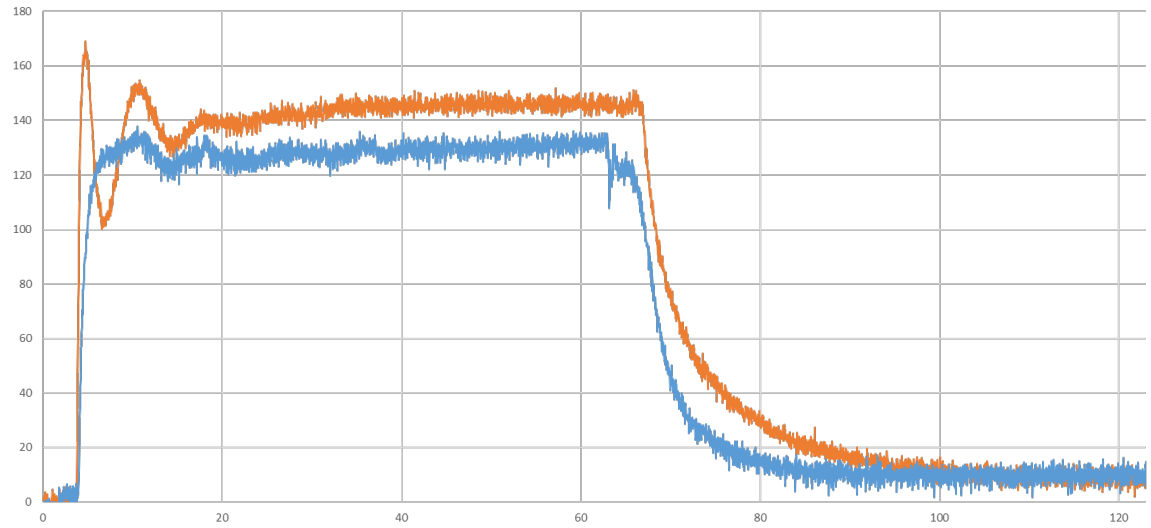

Figure 4.13. Loading daunomycin onto a nucleic acid functionalized QCM sensor. *Daunomycin loading was observed on both J52H (■) and ANC-SH (■) functionalized surfaces (flow rate = 100 µL/min). DNA coated sensors were normalized to zero before subsequent Daunomycin loading onto each DNA layer (time = zero). J52H contains initial variation in mass when Daunomycin was introduced (time = 5 min). The fairly smooth loading of Daunomycin onto the ANC-SH layer indicates different drug binding mechanisms comparatively. J52H bound approximately 10% more Daunomycin in total than ANC-SH, calculated by taking the averaging mass values from 15-65 min. Mass removed more rapidly from the ANC-SH sensor compared to J52H as can be seen from time points 65-90 min.*

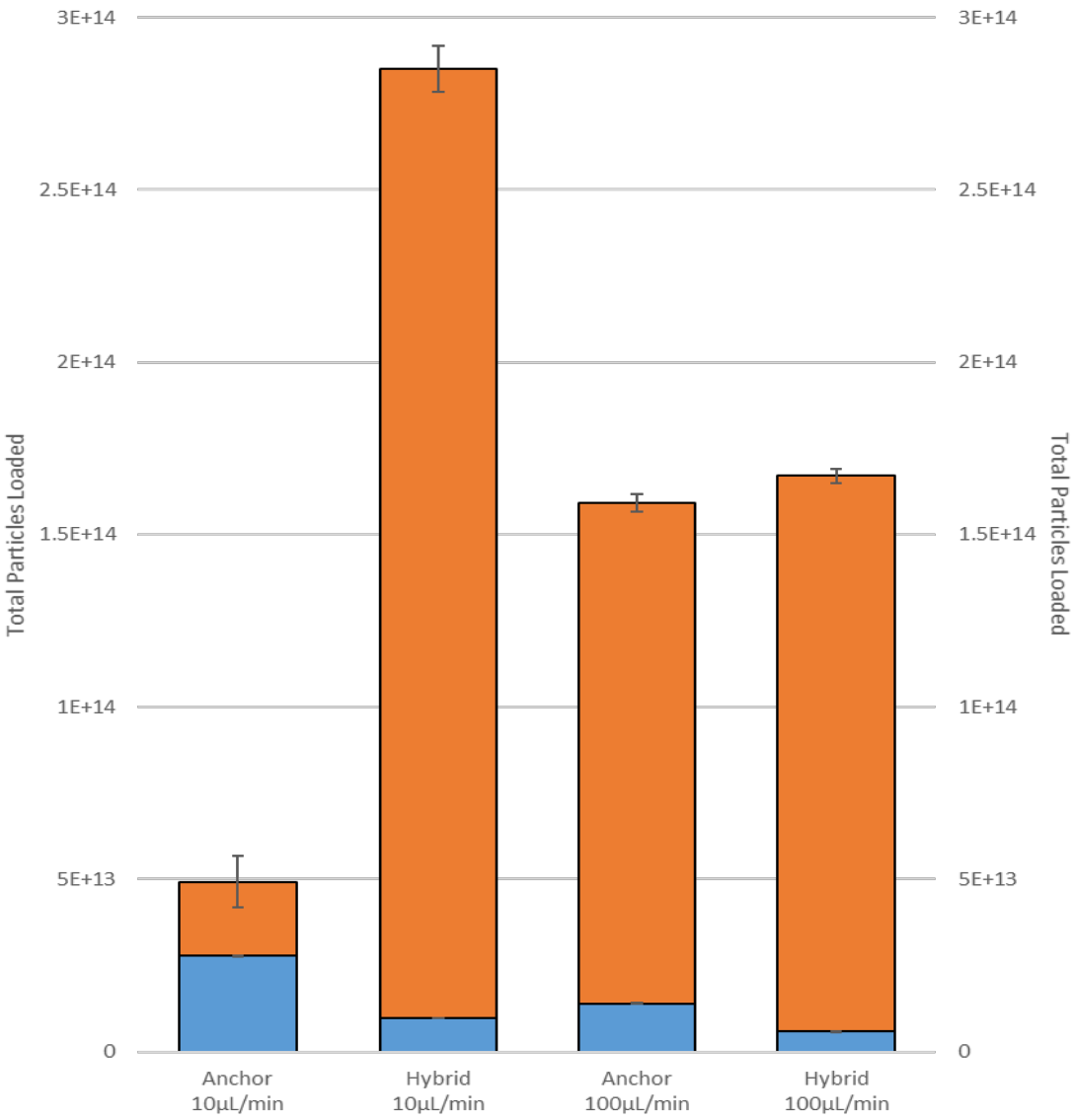

Figure 4.14. QCM monitored daunomycin & DNA quantification. *Total DNA binding (□) and total Daunomycin binding (□) are shown and calculated based on molecular weights of each molecule. ANC-SH bound more DNA molecules than J52H at both speeds (10 µL/min, left, 100 µL/min right). J52H loaded a greater amount of Daunomycin molecules than ANC-SH at both flow speeds. The discrepancies in loading for both DNA and Daunomycin are much more pronounced at the slower flow rate.*

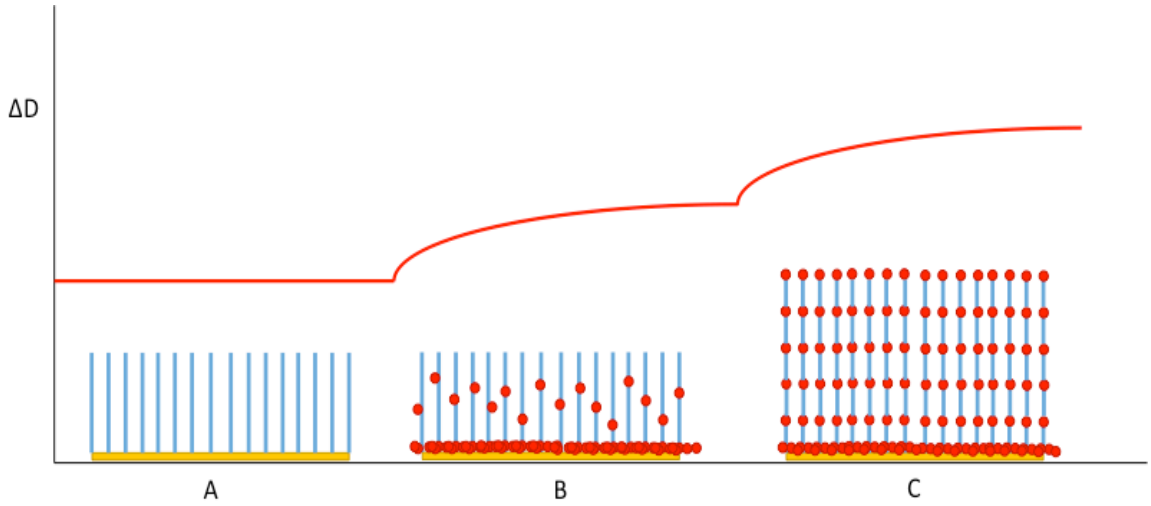

Figure 4.15. Schematic of an energy dissipation curve measured in the QCM system. *Energy dissipation stabilizes at a particular value for the functionalized DNA coated sensor (**A**). Additional dissipation can be induced in multiple ways, including an increase in layer density or viscoelasticity, which can be caused by entangled molecules or interactions with adsorbed particles (**B**); or through increases in the layer thickness or the length of the adsorbed molecules (**C**).*

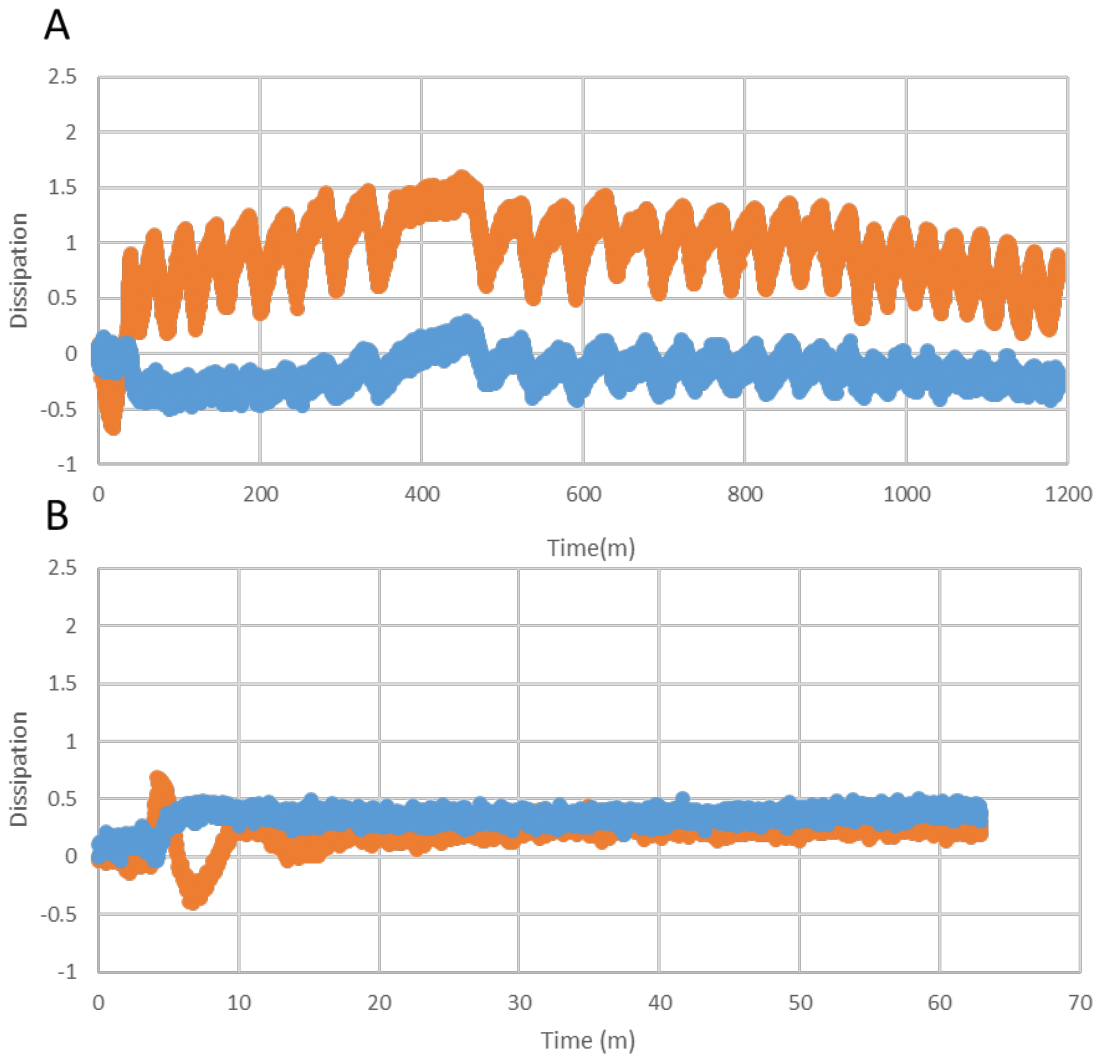

Figure 4.16. Energy dissipation recorded due to Daunomycin binding. *Increased dissipation observed in J52H (□) compared to ANC-SH (□) at 10 µL/min (**A**) suggests that Daunomycin is binding with a different mechanism between samples. However, dissipation between Daunomycin loaded ANC-SH and J52H is very similar at 100 µL/min (**B**). It is suspected that the increased flow rate prevents Daunomycin from remaining intercalated, reducing the dissipative effect.*

4.7 References

[1] Holzinger, M., Le Goff, A. & Cosnier, S. Nanomaterials for Biosensing Applications: A Review. *Front. Chem.* **2,** 1–10 (2014).

[2] Putzbach, W. & Ronkainen, N. J. Immobilization Techniques in the Fabrication of Nanomaterial-Based Electrochemical Biosensors: A Review. 4811–4840 (2013). doi:10.3390/s130404811

[3] Kasemo, B. Biological Surface Science. *Surf. Sci.* **500,** 656–677 (2002).

[4] Hook, F., Kasemo, B., Grunze, M. & Zauscher, S. Quantitative Biological Surface Science : Challenges and Recent Advances. *Nano* **2,** 2428–2436 (2008).

[5] Hurst, S. J., Lytton-Jean, A. K. R. & Mirkin, C. A. Maximizing DNA Loading on a Range of Gold Nanoparticle Sizes. *Anal. Chem.* **78,** 8313–8318 (2006).

[6] Reviakine, I., Johannsmann, D. & Richter, R. P. Hearing What You Cannot See and Visualizing What You Hear. *Anal. Chem.* **83,** 8838–8848 (2011).

[7] Sauerbrey, G. Use of Quartz Crystals for Weighing Thin Layers and for Microweighing. *Phys* **155,** 206–222 (1959).

[8] Beck, R., Pittermann, U. & Weil, K. G. Impedance Analysis of Quartz Oscillators, Contacted on One Side with a Liquid. *Reports of the Bunsen Society Phys. Chem* **92,** 1363–1368 (1988).

[9] Rodahl, M., Höök, F., Krozer, A., Brzezinski, P. & Kasemo, B. Quartz Crystal Microbalance Setup for Frequency and G Factor Measurements in Gaseous and Liquid Environments. *Review of Scientific Instruments* **66,** 3924–3930 (1995).

[10] Ulman, A. Formation and Structure of Self-Assembled Monolayers. *Chem. Rev.* **96,** 1533–1554 (1996).

[11] Bain, C. D. *et al.* Formation of Monolayer Films by the Spontaneous Assembly of Organic Thiols from Solution onto Gold. *J. Am. Chem. Soc.* **111,** 321–335 (1989).

[12] Laibinis, P. E. & Whitesides, G. M. Self-Assembled Monolayers of n-Alkanethiolates on Copper Are Barrier Films That Protect the Metal Against Oxidation by Air. *J. Am. Chem. Soc.* **114,** 9022–9028 (1992).

[13] Love, J. C., Estroff, L. A., Kriebel, J. K., Nuzzo, R. G. & Whitesides, G. M. Self-Assembled Monolayers of Thiolates on Metals as a Form of Nanotechnology. *Chemical Reviews* **105,** (2005).

[14] Ronkainen-Matsuno, N. J., Thomas, J. H., Halsall, H. B. & Heineman, W. R. Electrochemical Immunoassay Moving into the Fast Lane. *TrAC - Trends Anal. Chem.* **21,** 213–225 (2002).

[15] Takenaka, S., Yamashita, K., Takagi, M., Uto, Y. & Kondo, H. DNA Sensing on a DNA Probe-Modified Electrode Using Ferrocenylnaphthalene Diimide as the Electrochemically Active Ligand. *Anal. Chem.* **72,** 1334–1341 (2000).

[16] Ronkainen, N. J., Halsall, H. B. & Heineman, W. R. Electrochemical Biosensors. *Chem. Soc. Rev.* **39,** 1747–1763 (2010).

[17] Furukawa, M. *et al.* Geometrical Characterization of Pyrimidine Base Molecules Adsorbed on Cu(1 1 0) Surfaces: XPS and NEXAFS Studies. *Surf. Sci.* **532–535,** 261–266 (2003).

[18] Mateo-Martí, E. *et al.* Self-Assembled Monolayers of Peptide Nucleic Acids on Gold Surfaces: a Spectroscopic Study. *Langmuir : the ACS journal of surfaces and colloids* **21,** 9510–9517 (2005).

[19] Rodenhausen, K. B. *et al.* Combined Optical and Acoustical Method for Determination of Thickness and Porosity of Transparent Organic Layers Below the Ultra-Thin Film Limit. *Rev. Sci. Instrum.* **82,** 1–10 (2011).

[20] Reimhult, K., Petersson, K. & Krozer, A. QCM-D Analysis of the Performance of Blocking Agents on Gold and Polystyrene Surfaces. *Society* 8695–8700 (2008). doi:10.1021/la800224s

[21] Diamandis, E. P. & Christopoulos, T. K. The Biotin-(Strept)avidin System: Principles and Applications in Biotechnology. *Clin. Chem.* **37,** 625–636 (1991).

[22] Maglio, O. *et al.* A Quartz Crystal Microbalance Immunosensor for Stem Cell Selection and Extraction. *Sensors* **17,** 2747 (2017).

[23] Weinert, U. *et al.* S-layer Proteins as an Immobilization Matrix for Aptamers on Different Sensor Surfaces. *Engineering in Life Sciences* **15,** 710–720 (2015).

[24] Çiçek, Ç., Yılmaz, F., Özgür, E., Yavuz, H. & Denizli, A. Molecularly Imprinted Quartz Crystal Microbalance Sensor (QCM) for Bilirubin Detection. *Chemosensors* **4,** 21 (2016).

[25] Deyev, S. M. & Lebedenko, E. N. Modern Technologies for Creating Synthetic Antibodies for Clinical Application. *Acta Naturae* **1,** 32–50 (2009).

[26] Lipman, N. S., Jackson, L. R., Trudel, L. J. & Weis-Garcia, F. Monoclonal Versus Polyclonal Antibodies: Distinguishing Characteristics, Applications, and

Information Resources. *ILAR J.* **46,** 258–268 (2005).

[27] Wiseman, M. E. & Frank, C. W. Antibody Adsorption and Orientation on Hydrophobic Surfaces. *Langmuir* **28,** 1765–1774 (2012).

[28] Fischer, M. J. E. Surface Plasmon Resonance. **627,** 55–73 (2010).

[29] Hong, S. R., Kim, M. S., Jeong, H. Do & Hong, S. Development of Real-Time and Quantitative QCM Immunosensor for the Rapid Diagnosis of Aeromonas hydrophila Infection. *Aquaculture Research* **48,** 2055–2063 (2017).

[30] Makhneva, E., Manakhov, A., Skládal, P. & Zajíčková, L. Development of Effective QCM Biosensors by Cyclopropylamine Plasma Polymerization and Antibody Immobilization using Cross-linking Reactions. *Surf. Coatings Technol.* **290,** 116–123 (2016).

[31] Della Ventura, B., Schiavo, L., Altucci, C., Esposito, R. & Velotta, R. Light Assisted Antibody Immobilization for Bio-sensing. *Biomed. Opt. Express* **2,** 3223 (2011).

[32] Zhang, X. & Yadavalli, V. K. Surface Immobilization of DNA Aptamers for Biosensing and Protein Interaction Analysis. *Biosens. Bioelectron.* **26,** 3142–3147 (2011).

[33] Jayasena, S. D. Aptamers: An Emerging Class of Molecules that Rival Antibodies in Diagnostics. *Clin. Chem.* **45,** 1628–1650 (1999).

[34] Caruso, F., Rodda, E., Furlong, D. N., Niikura, K. & Okahata, Y. Quartz Crystal Microbalance Study of DNA Immobilization and Hybridization for Nucleic Acid Sensor Development. *Anal. Chem.* **69,** 2043–2049 (1997).

[35] Herne, T. M. & Tarlov, M. J. Characterization of DNA Probes Immobilized on Gold Surfaces. *J. Am. Chem. Soc.* **119,** 8916–8920 (1997).

[36] Chen, Q. *et al.* Amplified QCM-D Biosensor for Protein Based on Aptamer-Functionalized Gold Nanoparticles. *Biosens. Bioelectron.* **26,** 575–579 (2010).

[37] Chen, J. Y., Penn, L. S. & Xi, J. Quartz Crystal Microbalance: Sensing Cell-Substrate Adhesion and Beyond. *Biosens. Bioelectron.* **99,** 593–602 (2018).

[38] Modin, C. *et al.* QCM-D Studies of Attachment and Differential Spreading of Pre-Osteoblastic Cells on Ta and Cr Surfaces. *Biomaterials* **27,** 1346–1354 (2006).

[39] Chronaki, D., Stratiotis, D. I., Tsortos, A., Anastasiadou, E. & Gizeli, E. Screening Between Normal and Cancer Human Thyroid Cells through Comparative Adhesion Studies using the Quartz Crystal Microbalance. *Sens. Bio-Sensing Res.*

11, 99–106 (2016).

[40] Guo, M. *et al.* Enhanced adhesion/Spreading and Proliferation of Mammalian Cells on Electropolymerized Porphyrin Film for Biosensing Applications. *Biosens. Bioelectron.* **23,** 865–871 (2008).

[41] Westas, E. *et al.* Using QCM-D to Study the Adhesion of Human Gingival Fibroblasts on Implant Surfaces. *Journal of Biomedical Materials Research - Part A* **103,** 3139–3147 (2015).

[42] Marx, K. A. Quartz Crystal Microbalance: A useful Tool for Studying Thin Polymer Films and Complex Biomolecular Systems at the Solution - Surface Interface. *Biomacromolecules* **4,** 1099–1120 (2003).

[43] Alfonta, L., Willner, I., Throckmorton, D. J. & Singh, A. K. Electrochemical and Quartz Crystal Microbalance Detection of the Cholera Toxin Employing Horseradish Peroxidase and GM1-Functionalized Liposomes. *Anal. Chem.* **73,** 5287–5295 (2001).

[44] Chu, X., Zhao, Z. L., Shen, G. L. & Yu, R. Q. Quartz Crystal Microbalance Immunoassay with Dendritic Amplification using Colloidal Gold Immunocomplex. *Sensors Actuators, B Chem.* **114,** 696–704 (2006).

[45] Patolsky, F., Ranjit, K. T., Lichtenstein, A. & Willner, I. Dendritic Amplification of DNA Analysis by Oligonucleotide- Functionalized Au-nanoparticles. *Chem. Commun.* **1,** 1025–1026 (2000).

[46] Bendas, G. & Borsig, L. Cancer Cell Adhesion and Metastasis: Selectins, Integrins, and the Inhibitory Potential of Heparins. *Int. J. Cell Biol.* **2012,** (2012).

[47] Saitakis, M. & Gizeli, E. Acoustic Sensors as a Biophysical Tool for Probing Cell Attachment and Cell/Surface Interactions. *Cell. Mol. Life Sci.* **69,** 357–371 (2012).

[48] Lord, M. S. *et al.* Monitoring Cell Adhesion on Tantalum and Oxidised Polystyrene using a Quartz Crystal Microbalance with Dissipation. *Biomaterials* **27,** 4529–4537 (2006).

[49] Wegener, J., Seebach, J., Janshoff, A. & Galla, H. J. Analysis of the Composite Response of Shear Wave Resonators to the Attachment of Mammalian Cells. *Biophys. J.* **78,** 2821–2833 (2000).

[50] Li, F., Wang, J. H. C. & Wang, Q. M. Monitoring Cell Adhesion by using Thickness Shear Mode Acoustic Wave Sensors. *Biosens. Bioelectron.* **23,** 42–50 (2007).

[51] Kandel, J. *et al.* Chemically Grafted Fibronectin for use in QCM-D Cell Studies.

Biosens. Bioelectron. **58,** 249–257 (2014).

[52] Marx, K. A., Zhou, T., Montrone, A., Schulze, H. & Braunhut, S. J. A Quartz Crystal Microbalance Cell Biosensor: Detection of Microtubule Alterations in Living Cells at nM Nocodazole Concentrations. *Biosens. Bioelectron.* **16,** 773–782 (2001).

[53] Marx, K. A., Zhou, T., Montrone, A., McIntosh, D. & Braunhut, S. J. A Comparative Study of the Cytoskeleton Binding Drugs Nocodazole and Taxol with a Mammalian Cell Quartz Crystal Microbalance Biosensor: Different Dynamic Responses and Energy Dissipation Effects. *Anal. Biochem.* **361,** 77–92 (2007).

[54] Chen, J. Y., Shahid, A., Garcia, M. P., Penn, L. S. & Xi, J. Dissipation Monitoring for Assessing EGF-Induced Changes of Cell Adhesion. *Biosens. Bioelectron.* **38,** 375–381 (2012).

[55] Otto, K. & Silhavy, T. J. Surface Sensing and Adhesion of Escherichia coli Controlled by the Cpx-Signaling Pathway. *Proc. Natl. Acad. Sci.* **99,** 2287–2292 (2002).

[56] Yu, J. S. *et al.* Detection of Ebola Virus Envelope using Monoclonal and Polyclonal Antibodies in ELISA, Surface Plasmon Resonance and a Quartz Crystal Microbalance Immunosensor. *J. Virol. Methods* **137,** 219–228 (2006).

[57] Hao, R. *et al.* Rapid Detection of Bacillus anthracis using Monoclonal Antibody Functionalized QCM Sensor. *Biosens. Bioelectron.* **24,** 1330–1335 (2009).

[58] Afzal, A. *et al.* Gravimetric Viral Diagnostics: QCM Based Biosensors for Early Detection of Viruses. *Chemosensors* **5,** 7 (2017).

[59] Kim, Y. K. *et al.* A Novel Assay for Detecting Canine Parvovirus using a Quartz Crystal Microbalance Biosensor. *J. Virol. Methods* **219,** 23–27 (2015).

[60] Kim, Y. K. *et al.* Detection of H3N2 Canine Influenza Virus using a Quartz Crystal Microbalance. *J. Virol. Methods* **208,** 16–20 (2014).

[61] Li, D. *et al.* A Nanobeads Amplified QCM Immunosensor for the Detection of Avian Influenza Virus H5N1. *Biosens. Bioelectron.* **26,** 4146–4154 (2011).

[62] Ji, F. (Haifeng), Xu, J., Huang, X., Zhu, S. & Chen, H. Quartz Crystal Microbalance Based Biosensor for Rapid and Sensitive Detection of Maize Chlorotic Mottle Virus. *Anal. Methods* **6,** 4530–6 (2014).

[63] Efsen, E., Særmark, T., Hansen, A., Bruun, E. & Brynskov, J. Ramiprilate Inhibits Functional Matrix Metalloproteinase Activity in Crohn's Disease Fistulas. *Basic Clin. Pharmacol. Toxicol.* **109,** 208–216 (2011).

[64] Dong, Z. M., Jin, X. & Zhao, G. C. Amplified QCM Biosensor for Type IV Collagenase Based on Collagenase-Cleavage of Gold Nanoparticles Functionalized Peptide. *Biosens. Bioelectron.* **106,** 111–116 (2018).

[65] Liu, H., Liang, G., Abdel-Halim, E. S. & Zhu, J. J. A Sensitive and Selective Quantum Dots-Based FRET Biosensor for the Detection of Cancer Marker Type IV Collagenase. *Anal. Methods* **3,** 1797–1801 (2011).

[66] Wang, Y. *et al.* Membrane Glycoproteins Associated with Breast Tumor Cell Progression Identified by a Lectin Affinity Approach. *J. Proteome Res.* **7,** 4313–4325 (2008).

[67] Li, X. *et al.* Real-Time and Label-Free Analysis of Binding Thermodynamics of Carbohydrate-Protein Interactions on Unfixed Cancer Cell Surfaces using a QCM Biosensor. *Sci. Rep.* **5,** 1–9 (2015).

[68] Lakhin, A. V., Tarantul, V. Z. & Gening, L. V. Aptamers: Problems, Solutions and Prospects. *Acta Naturae* **5,** 34–43 (2013).

[69] Dassie, J. P. Systemic Administration of Optimized Aptamer-siRNA Chimeras Promotes Regression of PSMA-Expressing Tumors. **134,** 1–10 (2009).

[70] Höök, F., Rodahl, M., Brezezinski, P. & Kasemo, B. Energy Dissipation Kinetics for Protein and Antibody - Antigen Adsorption under Shear Oscillation on a Quartz Crystal Microbalance. *Langmuir* **14,** 729–734 (1998).

[71] Aung, K. M. M., Ho, X. & Su, X. DNA Assembly on Streptavidin Modified Surface: A Study using Quartz Crystal Microbalance with Dissipation or Resistance Measurements. *Sensors Actuators, B Chem.* **131,** 371–378 (2008).

[72] Pope, L. H. *et al.* Probing DNA Duplex Formation and DNA-Drug Interactions by the Quartz Crystal Microbalance Technique. *Langmuir* **17,** 8300–8304 (2001).

[73] Bardea, A., Dagan, A., Ben-Dov, I., Amit, B. & Willner, I. Amplified Microgravimetric Quartz-Crystal-Microbalance Analyses of Oligonucleotide Complexes: A Route to a Tay-Sachs Biosensor Device. *Chem. Commun.* **12,** 839–840 (1998).

[74] Bunroddith, K., Viseshakul, N., Chansiri, K. & Lieberzeit, P. QCM-Based Rapid Detection of PCR Amplification Products of Ehrlichia canis. *Anal. Chim. Acta* **1001,** 106–111 (2018).

[75] Celik, G. & Oksuz, A. U. Controlled Release of Ibuprofen From Electrospun Biocompatible Nanofibers With In Situ QCM Measurements. *J. Macromol. Sci.* **52,** 76–83 (2015).

[76] Hepel, M. & Mahdavi, F. Application of the Electrochemical Quartz Crystal Microbalance for Electrochemically Controlled Binding and Release of Chlorpromazine from Conductive Polymer Matrix. *Microchem. J.* **56,** 54–64 (1997).

[77] Damiati, S., Kompella, U. B., Damiati, S. A. & Kodzius, R. Microfluidic Devices for Drug Delivery Systems and Drug Screening. *Genes (Basel).* **9,** (2018).

[78] White, C., SA, D. & Byrne, M. Controlled Release of Multiple Therapeutics from Silicone Hydrogel Contact Lenses. *Optom Vis Sci* **93,** 377–386 (2017).

[79] Luo, Y. L., Shiao, Y. S. & Huang, Y. F. Release of Photoactivatable Drugs from Plasmonic Nanoparticles for Targeted Cancer Therapy. *ACS Nano* **5,** 7796–7804 (2011).

[80] Sundaram, P., Wower, J. & Byrne, M. E. A Nanoscale Drug Delivery Carrier using Nucleic Acid Aptamers for Extended Release of Therapeutic. *Nanomedicine Nanotechnology, Biol. Med.* **8,** 1143–1151 (2012).

[81] Lin, Z., Yip, C. M., Joseph, I. S. & Ward, M. D. Operation of an Ultrasensitive 30-MHz Quartz Crystal Microbalance in Liquids. *Anal. Chem.* **65,** 1546–1551 (1993).

[82] Cooper, M. A., Dultsev, F. N., Ostanin, V. P. & Klenerman, D. Separation and Detection of Bacteria using Rupture Event Scanning. *Anal. Chim. Acta* **702,** 233–238 (2011).

[83] Yu, X., Chen, F., Wang, R. & Li, Y. Whole-Bacterium SELEX of DNA Aptamers for Rapid Detection of E.coli O157:H7 using a QCM Sensor. *J. Biotechnol.* **266,** 39–49 (2018).

[84] Shan, W. *et al.* An Aptamer-Based Quartz Crystal Microbalance Biosensor for Sensitive and Selective Detection of Leukemia Cells using Silver-Enhanced Gold Nanoparticle Label. *Talanta* **126,** 130–135 (2014).

[85] Mason, W. P., Baker, W. O., Mcskimin, H. J. & Heiss, J. H. Measurement of Shear Elasticity and Viscosity of Liquids at Ultrasonic Frequencies. *Phys. Rev.* **75,** 936–946 (1949).

[86] https://www.idtdna.com/calc/analyzer (2018).

[87] Shumaker-Parry, J. S., Aebersold, R. & Campbell, C. T. Parallel Quantitative Measurement of Protein Binding to a 120-Element Double-Stranded DNA Array in Real Time using Surface Plasmon Resonance Microscopy. *Anal. Chem*. **76** (7), 2071–2082 (2004).

[88] Dunn, K. E., Trefzer, M. A., Johnson, S. & Tyrrell, A. M. Investigating the Dynamics of Surface-Immobilized DNA Nanomachines. *Scientific Reports* **6**, article number: 29581 (2016).

[89] Zhou, X., Liu, L., Hu, M., Wang, L. & Hu. J. Detection of Hepatitis B Virus by Piezoelectric Biosensor. *J Pharm Biomed Anal*. **27**(1-2), 341-345 (2002).

[90] Barone, G. *et al.* Intercalation of Daunomycin into Stacked DNA Base Pairs. Dft Study of an Anticancer Drug.*J. Biomol. Struct. Dyn.* **26,** 115–129 (2008).

[91] Ertekin, Ö., Öztürk, S. & Öztürk, Z. Z. Label free QCM Immunobiosensor for AFB1 Detection using Monoclonal IgA Antibody as Recognition Element. *Sensors (Switzerland)* **16,** 1–12 (2016).

[92] Masdor, N. A., Altintas, Z. & Tothill, I. E. Sensitive Detection of Campylobacter jejuni using Nanoparticles Enhanced QCM Sensor. *Biosens. Bioelectron.* **78,** 328–336 (2016).

[93] Farka, Z., Kovář, D. & Skládal, P. Rapid Detection of Microorganisms Based on Active and Passive Modes of QCM. *Sensors (Switzerland)* **15,** 79–92 (2015).

[94] Pirinçci, Ş. Ş. *et al.* Label-free QCM Immunosensor for the Detection of Ochratoxin A. *Sensors (Switzerland)* **18,** (2018).

[95] Carrigan, S. D., Scott, G. & Tabrizian, M. Real-time QCM-D Immunoassay through Oriented Antibody Immobilization using Cross-linked Hydrogel Biointerfaces. *Langmuir* **21,** 5966–5973 (2005).

[96] Wang, R. *et al.* A Nanowell-based QCM Aptasensor for Rapid and Sensitive Detection of Avian Influenza Virus. *Sensors Actuators, B Chem.* **240,** 934–940 (2017).

[97] Hao, R. Z. *et al.* DNA Probe Functionalized QCM Biosensor Based on Gold Nanoparticle Amplification for Bacillus anthracis Detection. *Biosens. Bioelectron.* **26,** 3398–3404 (2011).

[98] Ozalp, V. C., Bayramoglu, G., Erdem, Z. & Arica, M. Y. Pathogen Detection in Complex Samples by Quartz Crystal Microbalance Sensor Coupled to Aptamer Functionalized Core-shell Type Magnetic Separation. *Anal. Chim. Acta* **853,** 533–540 (2015).

[99] Hianik, T., Ostatná, V., Zajacová, Z., Stoikova, E. & Evtugyn, G. Detection of Aptamer-protein Interactions using QCM and Electrochemical Indicator Methods. *Bioorganic Med. Chem. Lett.* **15,** 291–295 (2005).

[100] Yilmaz, E., Majidi, D., Ozgur, E. & Denizli, A. Whole Cell Imprinting Based Escherichia coli Sensors: A Study for SPR and QCM. *Sensors Actuators, B Chem.* **209,** 714–721 (2015).

[101] Poghossian, A. *et al.* Field-effect Biosensor using Virus Particles as Scaffolds for Enzyme Immobilization. *Biosens. Bioelectron.* **110,** 168–174 (2018).

[102] Yao, C. *et al.* Aptamer-based Piezoelectric Quartz Crystal Microbalance Biosensor Array for the Quantification of IgE. *Biosens. Bioelectron.* **24,** 2499–2503 (2009).

[103] Strouse, R. J., Anderson, D. W. & Argentieri, D. C. Rapid Detection of Antigen-Specific Mouse IgE by Enzyme-linked Immunosorbent Assay (ELISA). *J. Immunoass.* **12,** 113–141 (1991).

[104] German, I., Buchanan, D. D. & Kennedy, R. T. Aptamers as Ligands in Affinity Probe Capillary Electrophoresis. *Anal. Chem.* **70,** 4540–4545 (1998).

[105] Ye, F., Smith, P. B., Wu, C. & Chiu, D. T. Ultrasensitive Detection of Proteins on Western Blots with Semiconducting Polymer Dots. *Macromol Rapid Commun* **34,** 247–253 (2013).

Chapter 5: Application of a DNA Nanoparticle Drug Delivery System

By exploiting the binding mechanism of nucleic acids, we have developed a novel nanoparticle drug carrier with high therapeutic payload, controllable release, and the potential for active tumor targeting (Figure 5.1). It consists of 15 nm gold nanoparticles (AuNPs) conjugated with short, single-stranded thiolated anchor DNA (ANC-SH) at high surface density. These anchor strands are programmable to bind DNA via complementary base pairing. We used DNA oligonucleotides with regions complementary to ANC to optimize DNA loading onto our AuNP platform, with an experimental quantification of 106 DNA complexes per AuNP. Klenow enzyme is employed to impart a drug binding DNA region, and we have detected for the first time the degradation products that arise from variability in the route of polymerization by this method.

We utilize the natural intercalating behavior of Daunomycin into DNA base pairs to load the drug on our platform (Figure 5.1). This schematic illustrates the effect of surface plasmon resonance on the color of our gold nanoparticles as one method for confirming binding of ANC-SH. It also shows the hypothesized structure of the nanoparticle platform. Engineered DNA sequences (green) will hybridize to ANC-SH (blue) by complementary base pairing, then the Klenow reaction will be performed to create uniform double stranded binding regions (orange) capable of intercalating Daunomycin. At the bottom of Figure 5.1 is an example of how Daunomycin stacks within base pairs of double stranded DNA.

Using this platform layout obtained a high therapeutic payload of > 1,000 drug molecules per AuNP, one of the highest loadings reported in literature to date. We have engineered unique DNA sequences to alter binding affinity and control release of

Daunomycin for over 48 hours. Cell studies showed higher cell death using our drug-loaded nanocarriers when compared to equivalent concentrations of free Daunomycin. We have also explored cell internalization mechanisms (clathrin-mediated endocytosis, caveolae mediated endocytosis, and lipid-raft endocytosis) to identify the pathways by which our AuNPs enter the cell.

This nanocarrier is in the ideal size range of 16-100 nm in diameter and is capable of passive targeting of cancer cells *in vivo*, utilizing the enhanced permeability and retention effect while resisting renal clearance and leakage into healthy tissue through capillaries. Our AuNP platform is effective as a therapeutic drug delivery device and can easily incorporate any DNA of choice through complementary base pairing. The work demonstrated in this chapter has produced an innovative nanoscale drug delivery platform with the capability of providing personalized cancer therapies through careful selection of complementary DNA and an adjustable drug release profile.

5.1 Introduction to Nanoparticles and Aptamers as Therapeutic Tools

Progress in the field of nanotechnology has led to a number of breakthroughs in the study of cancer therapy [1,2]. Nanoparticle drug carriers offer potential to direct the delivery of chemotherapeutic drugs to avoid a host immune response, increase bioavailability in the blood, and reduce healthy cell cytotoxicity. The *in vivo* fate of a nanoparticle can be regulated to a certain degree by adjusting the composition, size, and surface properties [3]. Ideally, the nanoparticle would be larger than the upper pore size limit in capillary walls – 15nm [4] – and smaller than the pore size limit within the liver

and spleen – 150 to 200nm [5] – to avoid rapid clearance from the blood and detection by fixed macrophages within the reticuloendothelial system (RES).

Retaining a size smaller than the pore size of cancer cell vasculature, which is between 100 to 600nm [6], will allow for preferential accumulation at tumor sites, taking advantage of the enhanced permeability and retention effect and the lack of effective lymphatic drainage in tumors [7–9]. Thus, a nanoparticle with a diameter in the range of 16 to 100nm would be capable of passive targeting to tumor cells. Additional functionalization with an aptamer can be used to provide active targeting abilities.

Nucleic acid aptamers have proven to be excellent targeting agents in recent years. Complex intramolecular reactions allow oligonucleotides to form unique three-dimensional structures that are able to bind a variety of macromolecules with high specificity. Aptamers are developed and screened through a process called systematic evolution of ligands by exponential enrichment (SELEX), a protocol that has since become standard in characterizing and synthesizing aptamers [10–12]. In short, large pools of random-sequence oligonucleotides are incubated with target molecules, and subsequent wash steps effectively isolate sequences with specificity and affinity to the target for cloning and amplification.

Aptamers retain distinct advantages over antibodies including molecule size, targeting specificity, minimized immune response, and capacity for modification [13]. They are also capable of binding with specificity to multiple molecules [14]. A variety of therapeutic aptamers have been developed since their discovery in 1990, including one already approved for market [15]. However, the use of aptamers as targeting components rather than therapeutic agents has proven to be more economical [16].

5.1.1 Hypothesis of Aptamer, AuNP, and Drug Emergence Potential

Aptamers have been studied for targeted drug delivery in tandem with a number of nanoparticle platforms, including lipid based delivery systems [16–18], polymerosomes [19,20], carbon nanotubes [21], mesoporous silica nanoparticles (MSNs) [18,22], and gold nanoparticles (AuNPs) [23–25]. These and other types of nanoparticles are capable of binding DNA as well as other types of ligands (Figure 5.2), but AuNPs are ideal for multiple reasons: biological inertness provides little to no immune response, optical properties impart imaging capabilities *in vitro* and *in vivo* [26], and photothermal properties can be used to damage tumor cells [27] and release drug payloads [28,29]. Nucleic acids can be conjugated to AuNPs using a thiol bridge [30] and subsequent work by Mirkin *et al.* has developed methods of maximizing surface coverage of these particles [31].

Although nanoparticles have been used for controlled drug release in the past, thus far no literature has reported the ability to control drug delivery using the aptamer itself. This works shows a synthesized flexible platform by coating the surface of a AuNP with short, thiolated anchor oligonucleotides that are able to link one or several oligonucleotides on a single nanoparticle through complementary base pairing. Careful selection of the nucleotide sequence within this base paired region allows us to control loading and release of chemotherapeutic drugs.

Our drug of choice is the chemotherapeutic drug Daunomycin. Daunomycin is an anthracycline antibiotic that intercalates into DNA base pairs in order to inhibit DNA replication [32]. It also emits natural fluorescence that is quenched when in complex with double stranded DNA, making for a simple method of quantification. We utilize

Daunomycin's intercalation mechanism by using double stranded DNA as a carrier for the drug. The nucleic acid sequence of this region can be altered to provide binding sites of varying affinity to the drug, effectively controlling our drug release (Figure 5.3). The engineering of the sequences is explained in greater detail in section 5.3.2.

It is hypothesized that manipulating the orientation of such a motif could lead to affinity variance. DNA is conjugated through complementary base pairing to ANC-SH and then treated with Klenow enzyme to engineer a binding region for the drug. This chapter discusses the synthesis and characterization of our novel drug delivery nanoparticle, with focus on why such a platform is advantageous and how it can be optimized in the future.

5.1.2 Review of AuNP-DNA Platform

Gold nanoparticles are well accepted for their potential use in biology and medicine [37], with much focus on cancer treatment and immunotherapy [38]. Indeed, a AuNP platform that relies on the enhanced permeability and retention (EPR) effect for therapeutic activity has already been approved for clinical trials (Aurimune [39]), suggesting that the prospect of synthesizing customizable AuNP drug delivery platforms is not only obtainable but industrially viable. The novelty of the platform reported in this study is two-fold: our AuNPs are customizable for use with theoretically any aptamer one may choose, and they allow us to control drug payload behavior using the aptamer conjugates rather than altering the base platform onto which they attach.

Nucleic acid monolayers on AuNP surfaces have already been studied in the past [31]; indeed, such monolayers are so highly organized that they are capable of forming

macroscopic assemblies with themselves through sequence engineering and complementary base pairing [40]. Furthermore, engineering spacer regions within each conjugated nucleic acid can modulate oligonucleotide loading. We have exploited here the use of a series of thymine (polyT) spacers which has the lowest affinity toward gold surfaces [41], to minimize non-specific interactions and encourage orientation outward from the AuNP. Mirkin *et. al*. [31] also explored the use of poly(ethylene glycol) (PEG) spacers, showing that they can significantly increase oligonucleotide loading on AuNPs compared to nucleotide spacers.

Addition of PEG segments can also contribute *in vivo* stability by hindering the interactions of endogenous opsin proteins employed by the RES system [42] and the increased extension from the AuNP surface using both PEG and nucleotide spacers has shown to increase the aptamer's ability to bind a target [43,44]. A problem with increasing the spacer region length is that we wish to retain a nanoparticle size less than 100 nm in diameter; anything greater may remove our passive targeting in accordance with the EPR effect. Theoretical and experimental data from our lab revealed AuNP platforms between 60 – 70 nm when using polyT spacers and 52 bp DNA conjugates, while addition of a 3-monomer PEG chain should theoretically add < 7 nm to the total diameter (roughly the same length as 10 additional nucleotide bases on all sides) [31]. However, there are characterized aptamer sequences much shorter than 52 bp in length [45,46], so it should be possible to retain our desired size range.

The greatest obstacle in clinically applying aptamer-based nanoparticles is the aptamer stability. Complex nucleic acid structures can be sensitive to environmental changes and are quite fluid in structure, leading to low reproducibility in some aptamer

based biosensors [47]. Indeed, addition of a complementary ANC-SH binding sequence and subsequent conjugation risks altering the aptamer structure and therefore its function, although some researchers have shown the ability to identify the active regions of aptamer sequences and alter surrounding nucleotide composition without affecting performance [48]. Furthermore, densely conjugated aptamers may interact with neighboring strands to produce structural changes due to electrostatic repulsion. This phenomena has been shown to reduce the performance of aptamer-based biosensors [49].

In this work, we noticed that application of DNA conjugates to a gold nanoparticle conjugated with thiolated anchor DNA (AuNP-ANC) platform leads to unwanted binding between molecules. These observed interactions led to aggregate clusters of AuNPs, as noted by the increased polydispersity in dynamic light scattering (DLS) measurements after synthesizing our platform. The increased G/C content of our strands, meant to promote Daunomycin affinity toward the particle, had the unwanted effect of encouraging AuNP-AuNP interactions and neighboring strand interactions. Such interactions could prevent this platform from achieving homogeneity and stability in clinical use. To remedy this impedance would involve controlling aptamer loading on the AuNP surface in order to determine optimal aptamer density. Our lab has already revealed the ability to control DNA loading on our AuNP platforms, and future work will attempt the same result using an aptamer.

This AuNP platform is expected to show an ability to kill cancer cells *in vitro* with a higher efficiency than free Daunomycin at equivalent concentrations. Nanoparticle platforms have shown the ability to exploit active endocytotic pathways improving efficacy and controlling unwanted side effects of drug therapies [50]. Effective

internalization allows for a more localized payload delivery, and increasing the payload size can increase the efficiency of the drug delivery platform. Our AuNP platform described in this chapter is observed to release Daunomycin into solution, which must be contributing to its ability to kill cells. However, it is hypothesized that the drug loaded AuNPs will induce more cell death than free Daunomycin, supporting the notion that drug loaded AuNP uptake delivers more drug into cells internally than free Daunomycin uptake..

Another consideration is that it is suspected the aggregation of AuNPs caused by DNA interactions may be accelerating this effect of our particles. It is hypothesized that this phenomenon will be negligible, resulting in the hypothesis that the drug delivery efficiency of our functionalized AuNP platform is the driving force behind high cell death efficacy. Current studies in our lab involve quantifying aptamer loading onto our unique platform using both polyT and PEG spacers. Controlled release of Daunomycin from these platforms and the ability to target cancerous cells are also being explored.

5.2 Nanoparticle Characterization, Optimization, and Quantification

Materials

Gold nanoparticles of 15 nm diameter were purchased from TedPella (Redding, California). These nanoparticles are coated with citric acid, but additional procedures are needed to remove the citric acid. Synthesis of DNA onto the gold nanoparticle surface is capable of replacing the citric acid due to the surface chemistry between the Thiol bond and gold surface. The citric acid is then removed from the system during the wash steps. Modified and unmodified oligonucleotides were synthesized by Integrated DNA

Technologies (Coralville, Iowa). NAP-5 and NAP-10 columns (Sephadex G-25 DNA grade) were purchased from VWR (Radnor, Pennsylvania). Tissue culture treated 96-well plates with lids and 6-well plates were purchased from VWR (Radnor, Pennsylvania). Human breast adenocarcinoma cells (MCF7), basal cell culture medium (EMEM) and supplements (penicillin/streptomycin, fetal bovine serum, 0.25% Trypsin/EDTA and non-essential amino acids) were purchased from ATCC (Manassas, Virginia). All other equipment and chemicals were of molecular biology grade and unless specified were purchased from VWR.

Preparation of Nanocarriers

The anchor oligonucleotide with thiol group at the 5' end was suspended in Tris EDTA (TE) buffer to 1 mM final concentration. To cleave the disulfide functionality on the oligonucleotide, 4μL of ANC was combined with 60μL of 0.2 M phosphate-buffer solution at a pH of 7.3 with 4μL of 1 M dithiothreitol (DTT) for 3 hours at 37^{o}C, followed by adding 32μL of deionized water to reach a final volume of 100μL. Desalting of ANC on a Sephadex grade F resin G-25 illustra microspin column (50μL per column) was performed according to manufacturer's specifications. The concentration of desalted oligonucleotides was determined by measuring absorbance at 260nm and found to be 14.6μM.

Gold nanoparticles were purchased at 15nm in diameter; diameter was measured using dynamic light scattering. Concentration of AuNPs was provided by TedPella and was listed as $1.4x10^{12}$ particles/mL. Absorbance spectrum was analyzed for AuNPs to confirm sample used was pure. AuNP absorbance at 520nm was found to be 0.288. This

value was used to calculate percent of AuNPs lost during experimental procedure and monitor concentration.

Functionalization of AuNPs with ANC-SH began with taking 1mL of AuNPs and adding 1μL of 10% sodium dodecyl sulfate (SDS), 15 μL of reduced ANC-SH, and 50μL of 0.2 M phosphate buffer (pH 7.3). ANC-SH was covalently bound to AuNPs using the salt aging procedure developed by Hurst. et al [35]; in short, NaCl is added slowly over time to a final concentration of 0.4M, with 10s of sonication after each salt addition.

Confirmation of successful ANC-SH bound to AuNPs was confirmed by three methods. First is the surface plasmon resonance effect. At the 0.4M NaCl concentration used for synthesis of these functionalized particles, if the DNA was not binding to gold nanoparticles by the surface chemistry between the thiol bond and gold, then the nanoparticles would change colors from red to blue. Second is by mobility in an agarose gel. When loading a gold nanoparticle sample in a gel electrophoresis apparatus, the gold nanoparticles will not move in the presence of an electric current if no ANC-SH is bound. Movement of gold nanoparticles through the gel indicates attachment of ANC-SH to the gold nanoparticles. The last method is by transmission electron microscope (TEM). Under TEM, gold nanoparticles will aggregate, but if ANC-SH is bound to the surface, the gold nanoparticles will remain separated. Additionally, a very faint halo surrounding each gold nanoparticle will be visible. Figure 5.4 shows this behavior confirming successful assembly of AuNP-ANC via a TEM.

5.2.1 DNA Anchor Loading and Behavior on Gold Nanoparticles

The salt-aging protocol employed allowed us to load a high surface density of ANC oligonucleotides. By varying the concentration of ANC-SH in solution when functionalizing the AuNPs, we were able to modulate the loading of double stranded DNA onto the AuNP surface. Radioactive labeling allowed us to observe dsDNA loading ranging from 79 (± 3) to 141 (± 6) strands per AuNP (Figure 5.5). Excess DNA is the lower band in each lane, while the upper bands were cut from the gel and placed in a scintillation counter. The DNA was then quantified using Cherenkov counting.

A significant mobility shift is observed in agarose gel electrophoresis when functionalizing AuNPs with dsDNA as can be seen from Figure 5.6 (bands 1 and 6 being AuNP-ANC vs bands 2 thru 5 being Klenow reacted nanoparticles). Smaller shifts can also be observed between AuNPs with various dsDNA loading values when comparing the first and last bands in Figure 5.6. Schematics of each nanoparticle complex are shown for each band in the gel.

Presence of the radioactive label located with the AuNP sample in the gel indicates successful hybridization of the dsDNA to the AuNP-ANC complex; since the hybridized DNA sample binding to ANC-SH is what contains the radioactive label. It should be noted that the theoretical maximum number of DNA possible to bind to a 15nm AuNP based on surface area is ~107 DNA strands. Since our samples bound a greater number then this in some of the cases (Figure 5.5), this means that either there is non-specific DNA-DNA interactions binding additional DNA strands to the particles, the particles are larger in size then anticipated, or some combination of both. Another consideration is the behavior of parallel DNA interactions. On the gold nanoparticle, each

5’ end of the ANC-SH DNA is locked in placing allowing neighboring strands to interact with each other in a parallel manner. Parallel DNA interactions are not well understood so unknown behavior between these strands may also play a role in the increased ANC-SH binding on the gold nanoparticle surface.

Dynamic light scattering was performed to confirm nanoparticle size, as well as the size once ANC-SH and dsDNA were attached. Dynamic light scattering, discussed in more detail in the following section, indicated that the nanoparticles are in fact slightly larger with a size of 18.7nm (Figure 5.7) compared to the manufacture listed value of 15nm. This difference in size is the justification for concluding that particles of larger size then anticipated is the main reason for observed number of DNA strands per nanoparticle containing values higher then the theoretical maximum (Figure 5.5). Theoretical sizes for AuNP-ANC and DNA-AuNP were also slightly larger then predicted based on calculations from DNA size (for exact values see Figure 5.7). The larger sizes, however, were only marginal and within a range that can be explained by crowding and charge repulsion forces stretching out the DNA on the densely packed surface of the AuNPs. The close sizes to the calculated values are another good indication that the nanoparticles are assembling in the proper manner predicted.

5.2.2 Dynamic Light Scattering Analysis

Dynamic Light Scattering

Diameter measurements of our AuNP platforms were recorded by dynamic light scattering using a Zetasizer Nano ZS90 (Malvern, Westborough, MA). DLS uses a beam of light to detect the scattering angle induced by particles moving under Brownian

motion. Using the Stokes-Einstein relationship, diffusion of particles through this beam can be correlated to a function to produce a range of hydrodynamic diameters observed in a sample. The Stokes-Einstein equation uses assumptions that the particles undergo Brownian motion in a quiescent fluid at uniform temperature, *van't Hoff's law* for osmotic pressure is equally applicable to pressure associated with a suspension of Brownian particles, and that stokes drag applies. All of these assumptions are within reason for our nanoparticle suspension. DLS measurements are temperature controlled and factor in information regarding the viscosity of your solvent to produce size profiles and polydispersity of suspended particles. Comparing DLS reports of AuNP samples before, during, and after nanocarrier synthesis allows you to observe particle construction as the diameter of the particles increase; DLS will also report a range of particle diameters at relative signal intensities, revealing more about the uniformity of synthesized nanocarriers.

AuNP-ANC Size Profiles – Modifying DNA and NaCl Concentration

While beginning the ANC-SH reduction process described previously, initial ANC-SH concentrations were varied to produce increased concentrations of reduced ANC samples. ANC-SH concentrations – both after reduction and while diluted in AuNP solution – are provided in Table 5.1. These values needed to be determined because sample is lost using the G-25 columns after the reduction process, explaining the nonlinear changes in concentration between samples. The ANC-SH concentration values from Table 5.1 are the concentration when the reduced samples are added to the 1mL AuNP solution. The various ANC-SH samples are identified according to the volume (in µl) of stock solution that was used in the reduction process (*from 2µl – 10µl → ANC2 –*

ANC10). A 50µl aliquot from each ANC-SH sample was added to 1mL of AuNPs and synthesized as described above.

The results of this experiment provided us with a range of ANC-SH concentrations that provide the most desirable size profile. The concentration for the *4µl* sample was determined to be sufficient, and additional ANC-SH was reduced and diluted to that concentration (reduced ANC-SH = 30µM). These samples were then used to synthesize another series of AuNP-ANC platforms; in this experiment, ANC-SH was added at identical volumes and concentrations to 1mL of just AuNPs. NaCl solutions were prepared at increasing concentrations, selected so that equal volumes can be added during AuNP synthesis while obtaining final salt concentrations from 0 – 1M. Therefore, a series of AuNP-ANC platforms were synthesized with an identical protocol while varying both DNA and salt concentration. Purified AuNP-ANCs were quantified by measuring absorbance at 520nm and comparing results to the baseline measurement to identify the percentage of particles lost; size profiles were obtained by measuring the solution using DLS.

Testing the Effect of DNA Interactions on Particle Size Profile

A sample of AuNP-ANC synthesized in 1M NaCl was measured using DLS. The sample was then treated with heat in three subsequent steps: heating at 80^{o}C for 5 min, heating to 80^{o}C for 10 min followed by 5 min on ice, and finally heating at 95^{o}C for 3 min followed by 5 min on ice. DLS measurements were taken after every heating step. All DLS measurements are temperature controlled at 24^{o}C.

Results & Analysis of DLS Experiments

Hydrodynamic diameter of AuNP-ANC constructs in solution is reported by DLS as relative signal intensities with an average value given for your sample (Table 5.2). These values varied from what was expected, going up and down at the lower salt concentrations, but overall the average size values began to steadily approach the theoretical value at the higher salt concentrations (compare Table 5.2 to Figure 5.7 for AuNP-ANC). Success in AuNP-ANC synthesis involves average intensities at or close to theoretical particle diameters and thin, sharp peaks representing homogenously synthesized AuNP-ANC platforms. Figures 5.8 and 5.9 show DLS measurements of AuNP-ANC platforms with variable ANC-SH or NaCl concentrations; these figures serve as a measure of AuNP-ANC uniformity and stability (*i.e.*, resistance to aggregation).

Size profiles of AuNP-ANC platforms synthesized at various ANC-SH concentrations are shown in Figure 5.8. The increasing concentrations of ANC-SH were used to observe AuNP-ANC size profiles as we increased the concentration gradient to drive ANC-SH to the gold surface. Encouraging more AuNP-ANC interactions at the beginning of synthesis will provide a greater probability that ANC-SH is available to block AuNP-AuNP interactions as NaCl is added. It is already known that increasing NaCl concentration will induce aggregation of non-functionalized AuNPs; we also see that non-functionalized AuNPs in 0M NaCl will aggregate after centrifugation (Figure 5.8A) – this aggregation is not reversible by vortexing or resuspension. This suggests that any AuNP-AuNP interactions caused by centrifugation will be detectable by measuring synthesized particles before and after centrifugation (note that DLS measurements of non-centrifuged AuNP-ANC particles contain excess ANC-SH molecules). It is observed in that as ANC-SH concentration is increased during synthesis, the majority of AuNP-

ANC particles approach diameter values close to our theoretical expectations from Figure 5.7.

Additionally, as ANC-SH concentration increases (Figure 5.8B-F), diameter values seem to group more precisely around the peak value creating more homogeneous samples, as can be observed by the decreasing width of the DLS reported diameter range. This supports the hypothesis that increasing the ANC-SH → AuNP gradient provides a more homogenous mixture of AuNP-ANC platforms. Furthermore, we see more agreement between pre-centrifuge/post-centrifuge size profiles as ANC-SH concentration increases; supporting the assertion that increased ANC-SH concentrations can effectively block AuNP-AuNP interactions induced by the centrifuge steps. From this data we conclude that the ANC-SH layer is likely acting as a barrier to AuNP aggregation, and methods of increasing ANC-SH layer density will improve the uniformity and stability of our particles. Bare nanoparticles with no DNA or NaCl are shown as a control for each set of data in Figure 5.8.

Size profiles of AuNP-ANC platforms synthesized at various final NaCl concentrations are shown in Figure 5.9 (increasing NaCl concentration going from A-H). A 50µl aliquot of ANC-SH (30µM) was added to 1mL AuNPs. NaCl stocks were prepared at increasing concentrations to ensure equal volumes could be added to each sample while modifying the final NaCl concentration. We observe some level of influence between NaCl concentration and final size profile; however, there does not seem to be any form of control. Diameter values for each AuNP-ANC sample fluctuate depending on the NaCl concentration. It has been shown that increasing salt leads to an increase of ANC-SH bound to each AuNP surface; this led to our expectation that

increasing salt concentration would lead to more controllable AuNP-ANC synthesis by demonstrating a lower range of nanoparticle sizes (similar to the effect of increasing ANC-SH concentration, Figure 5.8).

However, that is clearly not the case as each data set from Figure 5.9 has a similar profile regardless of NaCl concentration. It is possible that this is due to the varying concentration of our NaCl stock solutions. In an attempt to preserve volume, AuNP-ANC synthesized at higher NaCl concentrations experienced greater increases of NaCl at each step. Experimental observations have shown that successful AuNP-ANC synthesis requires careful attention during all steps of synthesis, especially when adding NaCl (*e.g.*, immediate sonication is necessary after each addition). It is possible that steeper increments of NaCl leads to non-ideal behavior, unchecked by the included sonication steps. There is also the fact that increasing NaCl efficiently increases ANC-SH loading, and that the increased diameter spread observed in Figure 5.9 is due to ANC-ANC interactions rather than AuNP-AuNP interactions.

Parts of each sample are at increasingly larger diameters then expected suggesting aggregation of particles; either through salt-mediated gold surface contact or DNA mediated interactions. We hypothesize that gold-gold interactions are the driving force for aggregation, either induced during synthesis or due to centrifugation with DNA effects considered minimal; this hypothesis is tested in Figure 5.10 by observing changes in size when attempting to remove any unwanted DNA-DNA interactions. Because it can be argued that aggregation can also be induced by ANC-ANC interactions, due to increasing DNA density and centrifugation; this would force us to alter our assumption of the ANC-SH layer as a protective barrier on the AuNP surface.

To test the effects of ANC-ANC interactions on particle size profile, we exposed a highly size-dispersed, high density ANC-SH loaded particle (AuNP-ANC, 1M NaCl sample) to increasingly intense heat and compared the subsequent DLS reported size profile (Figure 5.10). It is expected that intensively heating the AuNP-ANC sample and cooling on ice will break any base pairing or entanglement induced by ANC-ANC interactions but will be unable to reverse AuNP-AuNP attachments; therefore, we should see some significant change in DLS measurements at the end of the experiment if ANC-ANC interactions are causing increase in diameter size for the nanoparticles.

Figure 5.10 shows the size profile of AuNP-ANC (1M NaCl sample) after multiple heating steps. We see a slight increase in peak diameter – along with an increase in the peak intensity value – after heating at 80^{o}C for 5 min and cooling to room temperature. Heating again at 80^{o}C for 10 min followed by cooling on ice reduced the peak intensity value of AuNP-ANC. The size profile is then generally unchanged after heating to 95^{o}C followed by cooling on ice. The results conclude that ANC-ANC interactions have a slight effect on peak height and width as measured by the DLS, but since the sample profiles did not change drastically, most likely AuNP-AuNP interactions are the main culprit for larger diameter sizes being detected.

5.2.3 Klenow Reaction Creating Drug Binding Region

Daunomycin binding nucleic acid sequences (*L52, J52, M52, H52*) were denatured at 80^{o}C for 10 min followed by cooling on ice for 5 min. They were then hybridized to AuNP-ANC at 37^{o}C for one hour. A Klenow reaction was performed on the DNA functionalized AuNPs by adding 2μL individual nucleotides (dNTPs, 4mM), a 10X

reaction buffer, and 1μL Klenow enzyme (2U/μL) followed by incubation at 37^{o}C for 3 hours, after which the completed AuNP-ANC-DNA were purified by centrifugation. Completed platforms were again measured for dynamic light scattering spectrum and absorbance. Confirmation of successful Klenow reaction was done using an agarose gel test (Figure 5.11). AuNP-ANC was run on an agarose gel as a control. DNA-AuNP samples for *L52, J52, M52,* and *H52* were each tested with all components for the Klenow reaction except (-) and (+) the Klenow enzyme (two lanes for each sample). The far right lane for each DNA sample shows a large mobility shift indicating successful Klenow reaction (Figure 5.11).

Application of the Klenow enzyme to our dsDNA functionalized AuNPs allowed us to extend the double stranded region of the DNA strands to increase drug loading in a uniform and homogeneous manner. If a complementary strand was attached to create the double stranded region, there are many ways in which it could hybridize. However, using the Klenow reaction method ensures that only one particular double stranded complex is formed, the one shown in the schematic in Figure 5.1.

Using autoradiography imaging, we observed a series of degraded products included with our Klenow reacted AuNPs after stripping and removal of the AuNPs (Figure 5.12). We hypothesize that these products are due to degradation of nucleotides on the 3' end of each DNA strand by the Klenow enzyme, leading to a less densely packed AuNP surface (Figure 5.12A). Since the radioactive label is on the 5' end of the DNA, in order for the bands to be visible, this side must be unaffected by degradation, meaning the 3' end is being degraded. Figure 5.12B shows this degradation occurring experimentally and several different bands varying each by one nucleotide ranging from

+2 to -11 nucleotides being add/removed from the default amount of 52. This phenomenon occurring is another indication that the surfaces of the AuNP's are densely packed. It is likely that the Klenow enzyme is having trouble getting to the surface of the gold nanoparticle due to crowding. To our knowledge this is the first observation of the synthesis and degradation products of the Klenow reaction in this manner. This behavior and discovery has potential for future researchers to use the Klenow enzyme for many other applications.

5.3 Daunomycin Quantification & Affinity to Designed DNA Sequences

This section explains in detail all protocols and experiments performed using the cancer therapeutic drug Daunomycin. Materials, methods, and protocols for daunomycin had to take into consideration properties of the drug itself. Due to its hydrophobic nature, it would precipitate out of our buffer solution if stored at room temperature at a concentration greater then 80μM. Another issue is that adding too high of a concentration of daunomycin to the nanoparticles would cause them to precipitate out of solution, these considerations are the reasoning behind why the drug concentrations used were chosen.

In order to maximize binding of drug to DNA, the concentrations of DNA also had to be limited to fit the constraints of daunomycin use; this is the justification for the concentrations chosen for the DNA samples. The length of the DNA chosen at 52 base pair (bp) was selected to attempt to maintain a small nanoparticle size for additional use of passive targeting into cancer cell membranes over normal cells. Even though larger sequences could have been chosen and still meet this criteria, it is desired that they system be readily applicable to attachment of an aptamer for cell targeting for future

experiments in the lab going forward, which will further increase the size, restricting the size of DNA chosen to 52bp for these experiments.

The experiments performed in this section are quantification of drug bound per DNA sequence selected, binding affinity, drug bound per gold nanoparticle, and variation in release rate of drug from the DNA-nanoparticle platforms. Overall these experiments show that there are differences in binding behavior between single and double stranded DNA, as well as release rates in gold nanoparticles depending on what DNA is functionalized onto them. The data presented here also shows that intramolecular binding between self-complementary DNA strands can also bind Daunomycin at high rates. Finally, affinity for drug binding is more difficult to control then simply modifying DNA sequence as structural properties also have a large impact on drug binding.

5.3.1 Methods, & Protocols for Daunomycin Loading

Four DNA sequences (*L52, J52, M52, H52*; see Figure 5.3) with variations of AGC triplicates and their complements were suspended separately in Tris EDTA (TE) buffer to 1mM final concentration. Each DNA sequence and complement were diluted 100 times in a binding buffer (10mM phosphate, 0.2M NaCl, pH 7.3). The absorbance of each strand was measured, and further dilutions were done to bring all four samples to a fixed concentration (2.94μM). The DNA sequences and their complements were hybridized by incubating the single stranded oligonucleotides with their complement at 95^{o}C in a water bath followed by slow cooling to room temperature over a period of several hours.

Double stranded structures were confirmed by analyzing hybridization on an 8% non-denaturing polyacrylamide gel (Figure 5.13). A ladder was used to identify sizes of DNA based on mobility; markers for 300bp, 100bp, and 10bp can be seen on the ladder lane. Each engineered DNA sequence was tested for its single strand, complement, and hybridized forms. The gel shows intramolecular behavior for *J52*, *M52*, and *H52* indicated by differences in mobility compared to *L52* and moving at a rate just above the 10bp marker. Unwanted reactions for each DNA sample are also present in the form of either intermolecular interactions or other hybridization reactions that are not preferred. ImageJ software analysis of the gel stained using "stains all" (a fluorescent dye capable of quantification for DNA) indicates percentage of desired hybridization for each sample, this is important because it will affect the final results of the experiment (see Table 5.3).

Single-stranded DNA was heated to 80^{o}C and cooled on ice for 5 min. All four DNA duplexes, including their single stranded controls, were brought to a fixed concentration (0.74μM based on DNA content) in a binding buffer (10mM phosphate, 0.2M NaCl, pH 7.3) for a total of 12 samples. DNA concentrations were determined by measuring absorbance at 260nm and diluting to desired values. Each DNA sample was incubated with increasing molar ratios of Daunomycin (0.25, 0.5, 1, 2, 5, 10, and 50 equivalence). A DNA control was prepared with no Daunomycin, and for each drug solution a control was prepared with no DNA. The fluorescence of each sample was read at an excitation of 490nm and an emission of 595nm using a NanoDrop 3300 fluorospectrometer (Thermo Scientific, Waltham MA). The fluorescence of the Daunomycin controls was compared to Daunomycin bound to DNA to produce a percent

bound ratio. This ratio was used to quantify the amount of Daunomycin molecules bound per DNA duplex.

5.3.2 Justification for Sequence Selection

Daunomycin can interact with the phosphate backbone of DNA, but it will also intercalate between base pairs of double stranded DNA for a much stronger bond. Studies in literature have concluded that Daunomycin will bind with the highest affinity between G/C base pairs flanked by an A/T within a DNA double helix [34]. For sequences *J52*, *M52*, and *H52*, AGC repeats were arranged in sequence along a single strand, or in combination between two strands to modulate Daunomycin binding affinity (Figure 5.3). Sequence *L52* contained a designed sequence without this motif. Due to the heavy G/C content of *J52*, we experienced unwanted base pairing between single strands. Additionally, the palindromic nature of the *M52* and *H52* strands led to complications in single strand preparation and hybridization.

Computer simulations of base pairing and thermodynamic favorability is modeled in Figure 5.14 and explains what led to increased Daunomycin binding to single strands in those three sequences because of the presence of base paired regions. Gibbs free energy (ΔG) calculations based on computer models indicates the likelihood that intra/intermolecular interactions will occur. *L52* and *L52C* had ΔG of -0.84 and -1.13kcal/mol, respectively, and when analyzing where base pairing can occur, this data indicates that intramolecular interactions for this sequence are unlikely to be present. *J52* and *J52C* however, are likely to have intramolecular interactions with ΔG values of -5.53 and -11.06kcal/mol respectively. This is also true for *M52, M52C, H52*, and *H52C*, but

with even greater impact due to lower ΔG values of -9.86, -11.81, -21.02, and -20.83kcal/mol, respectively.

Intermolecular interactions for each DNA strand were also tested and each one had high enough Gibbs free energy values to indicate these unwanted reactions would occur. These values followed the same trend with ΔG numbers decreasing going from *L52, L52C, J52, J52C, M52*, *M52C, H52C*, to *H52* (-9.72, -14.85, -34.08, -37.55, -48.51, -49.13, -79.81, and -79.89kcal/mol respectively). In order to determine the effect that these reactions may have on the desired hybridization, the Gibbs free energy for this reaction is determined and these values can be compared. *L52H, J52H, M52H,* and *H52H* had ΔG values of -92.38, -112.63, -108.76, and -104.56kcal/mol respectively. When comparing the differences in these values to their intermolecular counterparts, it can be seen that *L52* has the greatest thermodynamic favorability to behave as desired. *J52* also has significantly more favorability to the desired hybridization reaction compared to intermolecular interactions. *M52* and *H52*, however, have their desired and undesired Gibbs free energy values closer to each other and as a result, these DNA sequences are more vulnerable to unwanted reactions affecting the behavior of desired hybridization (see Figure 5.14 for all Gibbs free energy values and theoretical structures).

In theory, the molecular structure of Daunomycin would allow it to intercalate within every 3-nucleotide base pairs. As our sequences are 52bp in length, and minus the ends due to the lack of flanking base pairs and the random "breathing" of DNA base pairs [35], we predict that a theoretical maximum of 15 Daunomycin molecules can bind to each DNA strand.

5.3.3 Daunomycin Binding Quantification and Affinity Per Sequence

The fluorescence of the Daunomycin controls was compared to free Daunomycin in each DNA sample after degradation by deoxyribonuclease (DNase). This ratio was used to quantify the percent of Daunomycin bound to DNA and further extrapolate data regarding Daunomycin molecules bound per DNA duplex. For every DNA sequence, hybridized DNA duplexes bound greater amounts of Daunomycin at higher drug ratios (Figure 5.15). All hybrid strands bound an average of 14-15 drug molecules at the highest concentration of Daunomycin, approximately equal to the theoretical maximum predicted. The ssDNA for each hybrid sample (except L52) also carried similar amounts of drug, this is in agreement with the Gibbs free energy calculations and computer modeling predicting formation of self-hybridization.

Interestingly, there is a significant decrease in Daunomycin binding for *L52* when comparing its ssDNA to its hybridized sample. It is also the only sequence not expected to have total self-hybridization (Figure 5.14) based on the computer models, which could explain this phenomenon and the comparisons in drug loading for the other three sequences (Figure 5.15). Furthermore, each of the hybrid samples has some single stranded complexes remaining in the samples as well; *M52* and *H52* having the highest amount are the most effected by this fact (see Table 5.3). This means that it is possible that averages for drug quantification can be slightly lower for these samples because of this fact.

From this point, the data from Figure 5.15 was then plotted according to the Hill equation:

$$\log\left(\frac{\theta}{1-\theta}\right) = n\log[\mathrm{L}] - \log K_d$$

Where θ = the fraction of DNA that bound Daunomycin, n = the Hill coefficient, L = the concentration of free Daunomycin, and K_d = dissociation constant. The Hill plot reveals a number of important quantities: the Hill coefficient measures the cooperativity of Daunomycin binding (see Table 5.4), which should be slightly greater then a value of 1 to show slight positive cooperative, this is found in our data for the double stranded complexes agreeing with data found from other literature. The single stranded complexes exhibit different behavior (except for *H52* and *H52C*), but that is to be expected and gives further credence that Daunomycin is binding via intercalation in the double stranded complexes. H52 and H52C behave like double stranded duplexes according to the Hill coefficient, since these samples have the highest Gibbs free energy values (meaning the most stable structure) of all the single strands and comparable values to the hybridized samples, this could explain the similarity in behavior to the double stranded samples. The reciprocal of K_d gives the average binding affinity value (see Table 5.5).

Analysis of the Hill plot using a one-way ANOVA test revealed that there is no significant difference in binding affinities (Table 5.5) for Daunomycin toward our unique DNA sequences. All double stranded complexes had binding affinities greater then any of the single stranded DNA sequences by a statistically significant amount. Surprisingly, *J52* had the highest binding affinity value of 2.78/μM, followed my *M52* (2.58/μM), *H52* (1.81/μM), and *L52* (1.28/μM). Except for *L52*, which had the lowest binding affinity as expected, the other samples did not behave as anticipated.

The amount to which the affinity data is skewed by intra/intermolecular base pairing between strands seen from our gel (Figure 5.13, with values in Table 5.3) within each DNA sample is unknown, but this could be the reason why *M52* and *H52* did not have higher binding affinities then *J52*. Intermolecular interactions are particularly high for *M52* (41.2%), *M52C* (40.8%), *H52* (16%), and *H52C* (30.5%) plus large amounts of unwanted side reactions for *M52H* (19.8%) and *H52H* (13.9%). In addition the non-denaturing gel (Figure 5.13) showed intramolecular binding behavior by differences in mobility in ssDNA for *J52*, *M52*, and *H52*. All of these factors were not accounted for when calculating Daunomycin binding affinity, which may explain why *M52* and *H52* did not work as well as *J52* since that sample did not have these problems.

It was expected that *H52* would have the highest affinity, followed by *M52*, *J52*, and *L52*. Since all of the calculations for each sample assumed 100% hybridized samples and no nanoparticle aggregation, this actually has a negative impact on the calculations and lowers the affinity values calculated for each sample, but more so for *M52* and *H52* in particular. If there was a way to determine the amounts of drug bound from the intramolecular interactions and AuNP aggregation only, remove those amounts, and then recalculate affinity, we hypothesize there would most certainly be an increase in affinity values for both of these samples. *L52* and *J52* were not effected by this problem as severely and therefore the affinity data calculated is more reliable, yet still all samples are in agreement with the range of affinity values found in the literature for Daunomycin bound to other DNA fragments.

5.3.4 Daunomycin Binding Per DNA Nanoparticle Construct

A 10μL aliquot of each DNA-AuNP platform was soaked in Daunomycin solution (80μM Daunomycin) overnight. Unbound drug was removed by centrifugation and bound drug was quantified. Daunomycin exhibits a natural fluorescence that is quenched when in complex with DNA. Therefore, quantification required purification of drug loaded DNA followed by extraction of bound Daunomycin. After removing unbound Daunomycin from the AuNPs and resuspending them in our binding buffer, we had to strip the AuNPs of their bound DNA. DTT was added to the AuNPs to a concentration of 0.05M and incubated overnight. The supernatant containing the stripped DNA duplexes was saved. We then treated the DNA duplexes with DNase at 37^{o}C for three hours to degrade them and reveal the fluorescence of the bound Daunomycin, since Daunomycin does not fluorescence when bound to DNA.

Fluorescence values were measured on a spectrophotometer against a fluorescence standard curve of known Daunomycin concentrations. The standard curve was made by measuring absorbance of several daunomycin samples to calculate concentration, and then fluorescence was measured to determine equivalent values. Daunomycin concentration was compared to nanoparticle concentration to determine Daunomycin/AuNP values. A nanoparticle functionalized with anchor DNA only was used as a control (AuNP-ANC). All daunomycin binding engineered platforms were able to bind over 1,000 Daunomycin molecules per AuNP while bare and ANC-SH only AuNps were not (Figure 5.16).

Daunomycin has shown to interact with the surface of gold nanoparticles. Measurements of drug loading on bare AuNPs showed there were 117 (± 3) drug

molecules per particle (see Figure 5.16). Normally, bare AuNps should not be able to bind any Daunomycin, the value found here demonstrates excess molecules that were either attached to the walls of the eppendorf tubes, or remained in solution after three washes. Since these nanoparticles were treated with the same protocol as all the other samples, this value of 117 (± 3) can be treated as a background value that can be subtracted as bound drug from each of the samples. In our case, because these samples were going to be added directly for further studies with cells, the drug is still present in the sample, and therefore was not subtracted since concentration of drug present is most important.

The addition of nucleic acids can increase daunomycin binding significantly. AuNP-ANC showed a drug-loading rate of 966 (±7) molecules per particle. It is expected that the interaction with the phosphate backbone of the single stranded ANC-SH strands allowed this drug loading. Although the loading is somewhat comparable to the loading of our functionalized nanocarriers, it is expected that drug release would occur more readily from AuNP-ANC when compared to our engineered sequences because the intercalation of Daunomycin provides a much stronger bond when compared to the binding seen on AuNP-ANC. This also explains why drug loading for engineered AuNP platforms is higher than the AuNP-ANC control.

Our dsDNA functionalized nanocarriers showed increased loading when compared to bare AuNP and AuNP-ANC (Figure 5.16). *J52* consistently showed the greatest rate of Daunomycin loading at 1449 (± 237) drug molecules per AuNP; followed by *L52* (1156, ± 35 drug/AuNp), *H52* (1073, ± 32 drug/AuNp), and *M52* (1038, ± 40 drug/AuNp). *J52* performed the best at Daunomycin loading, even more then *M52* and

H52, which again was unexpected. We hypothesize that the palindromic regions in *M52* and *H52* may have led to complications in the organized assembly of our nanocarriers, likely disrupting the Klenow enzyme and leading to decreased Daunomycin loading. Furthermore, the combination of large amounts intermolecular interactions for *M52* and *H52*; along with the intramolecular interactions led to some nanoparticle aggregation and precipitation out of solution for these samples. All of these factors were not accounted for when quantifying Daunomycin bound per DNA-AuNP (Figure 5.16), which may explain why *M52* and *H52* did not work as well as *J52* since that sample did not have these problems.

5.3.5 Dialysis Indicating Daunomycin Release Rate from Nanoparticles

Using seven 6-well plates as containers, each well was filled with 10mL of deionized water. On top of each well floated a dialysis membrane (pore size 25nm). This pore diameter is large enough for drug diffusion but too small to allow passage of AuNPs. Then 100μL of drug loaded AuNPs was pipetted onto the surface of each dialysis membrane. AuNPs with only anchor (AuNP-ANC) and AuNPs with each of the four DNA sequences were tested.

Initial drug concentration was quantified, and then concentration was monitored at 1, 2, 4, 12, 24, 48, 144 hours (see Table 5.6). The AuNP-ANC platform released drug at a rapid rate, as expected, and ~90% of loaded drug was released in only 4 hours (Table 5.6). The AuNP platforms with sequences *M52* and *H52* remained a little more stable, retaining their payload and releasing ~81% and ~75% of loaded Daunomycin in 4 hours, respectively. The AuNP platforms with sequences *L52* and *J52* retained the greatest

payload stability, and released only ~57% and ~52% of their payload after 4 hours respectively. The rapid release from AuNP-ANC is likely due to the weak binding of Daunomycin to the single stranded DNA on the AuNP. Our functionalized AuNP platforms retained a majority of the drug payload within the dsDNA duplex, which is a stronger interaction and takes longer to release. *L52* and *J52* showed similar release profiles, with *J52* releasing at a slightly slower rate than *L52*. This result was expected, as *L52* lacks the AGC motif found on *J52*. *M52* released drug at the highest rate of the four-engineered sequences; *H52* acted similarly.

We hypothesize that the particular DNA sequences present on *M52* and *H52* AuNP platforms may have affected organized DNA-AuNP structure and encouraged base pair interactions between particles. This would lead to entanglement of Daunomycin within AuNP clumps rather than controlled intercalation. This was also visible in the samples as these two had some slight aggregation from with the nanoparticles so that some of the sample would slowly fall out of solution, possibly resulting in the explanation for why these samples did not work as well as *L52* and *J52*. *J52* retained the highest amount of Daunomycin after 4h (time for incubation with cancer cells). It was considered to be the best working sample and therefore will be used for further experiments involving cell culture. The efficacy of the nanoparticles on cell death will be greatly impacted by the release rate of the drug from them; therefore *J52* should be the most successful nanoparticle in terms of cell death since it gives the nanoparticles more time to enter the cells before a majority of the drug is released.

5.4 Analysis of DNA Constructs on Cell Cultures

Since the drug loaded DNA-nanoparticle constructs have been quantified, optimized, and analyzed, in vitro analysis was undertaken. The in vitro study was to determine effect on cell death for MCF-7 breast cancer cells. Questions addressed in this section are 1) do the constructs kill cancer cells more efficiently then free drug, and 2) can internalization of nanoparticles be tracked by inhibition? Future applications for this research are limitless, as research continues to progress towards subcellular targeting in order to reduce total drug amounts necessary for cancer treatments. Researchers studying new methods for lowering drug quantities to cancer patients to reduce side effects of treatment will be interested in learning more about the results of these experiments.

This section includes a detailed description of materials, methods, and protocols for cell culture passaging of MCF-7 breast cancer cells, XTT cell viability, and various cell internalization inhibition assays. Cell viability was tested with free drug and was directly compared to cell death from the DNA coated nanoparticle platform in order to determine if this novel platform performs better then free drug. Furthermore, the answers to the questions asked above are described in detail and new insight on our nanoparticle behavior platform is learned. The groundwork laid out here for analyzing the behavior of these DNA coated nanoparticle platforms is applicable for all types of nucleic acid platforms in the future.

5.4.1 Materials, Methods, & Protocols for Cell Culture

MCF-7 Breast Cancer Cells Passage Protocol

Human breast adenocarcinoma cells (MCF7), basal cell culture medium (EMEM) and supplements (penicillin/streptomycin, fetal bovine serum, 0.25% Trypsin/EDTA and non-essential amino acids) were purchased from ATCC (Manassas, Virginia).

Took EMEM media from fridge and place in 37^0C water bath. Open biological fume hood, turn on the blower and light, set up rack and pipette tips. Grabbed 1X PBS and trypsin centrifuge tubes, removed parafilm. Took cells from $37^0C/CO_2$ incubator, and determined confluency under microscope. Turned on vacuum and aspirate media from plate. Added 5 mL of 1X PBS solution at the edge of the plate, and mixed solution by rotating hands. Aspirated 1X PBS solution from plate. Added 5 mL of 1X PBS solution at the edge of the plate, and mixed solution by rotating hands. Aspirated 1X PBS solution from plate. Added 1 mL of Trypsin in the center of the plate, and mixed solution by rotating hands. Put plate back in $37^0C/CO_2$ incubator for 5 minutes. Put parafilm over trypsin tube and put it away, grabbed and labeled a centrifuge tube C. S (for cell suspension). Took plate and put back under biological fume hood.

Added 5 mL of 1X PBS solution, use pipette to suck up solution and put in C. S. tube. Added 5 mL of 1X PBS solution, use pipette to suck up solution and put in C. S. tube. Centrifuged cell suspension @ 1500rpm for 5 minutes. Put parafilm over 1X PBS tube and put it away, grabbed media bottle, wiped water off outside. Got out a new plate, updated plate label and increased the passage number by one. Threw away old plate, added 5 mL of fresh media to new plate & coated surface entirely by mixing. Dumped exhausted media from C. S. tube into waste container swiftly. Added 2 mL of fresh media onto pellet and mixed vigorously with pipette. Transferred 1 mL of new cell suspension into new plate, mixed by rotating hands. Checked cells under microscope, then placed

back in $37^0C/CO_2$ incubator. Threw away remaining cell suspension, or kept for lab experiments in an eppendorf tube. Sprayed biological fume hood with 70% Isopropanol (IPA) and wiped everything clean. Closed biological fume hood, turned off blower, and turned on UV light.

XTT Cell Viability Assay for Free Daunomycin

This protocol was a four-day process for determining cell viability. First, coated 36 wells from a 96- well plate with 25 µL of Gelatin for 2 hours. During this period passaged the MCF-7 cells. Used Hemocytometer to count number of cells per mL. Diluted cell suspension (dcs) with media so that there were 20000 cells per 50 µL's of media. Added 50 µL of dcs to 33 wells; added 50 µL of fresh media to 3 wells. Let samples adhere to plate for 20 hours @37°C.On the second day, added 50 µL of drug diluted in media at the following concentrations (3 of each): Blank (50 µL of fresh media), 0 nM (no drug, negative control), 100-1400nM (in increments of 100nM), and 70% isopropanol (no drug, positive control). Let samples incubate with drug for 4 hours @37°C. Removed drug/media mixture from all 36 wells. Washed all wells with 100µL of fresh media. Washed all wells with 100µL's of fresh media. Added 100µL of fresh media to each well and placed in 37°C incubator for 24 hours.

On the third day, measured each well on a plate reader @475nm & 660nm after shaking for 5 seconds. Heated up XTT solution @37°C to remove any sediment. Added 10µL of activation reagent to 2000µL of XTT solution (creating activated solution). Mixed and added 25µL of activated solution to each of the 36 wells. Immediately measured each well on a plate reader. Repeated measurements every hour during the next 24 hours. On the final day, proceeded to required calculations and created a graph of the

cell viability data. After results were finalized, removed media from each well and discarded plate.

5.4.2 Methods, & Protocols for Cell Viability Analysis

Previous tests revealed the amount of Daunomycin that can be loaded onto each AuNP. From this information, we were able to determine the drug concentration in each AuNP sample, and then the XTT cell viability assay was repeated for the drug loaded AuNP samples. All concentrations in our cell viability assay correspond to Daunomycin concentration (nM). Concentration of AuNPs will vary depending on loading efficiency between each DNA strand tested. AuNP platforms showed a higher rate of cell death at all concentrations when compared to free Daunomycin. *J52* showed the highest rate of cell death at three of the four concentrations that it was tested. *L52* showed the highest cell death at concentrations below 300nM. AuNP-ANC showed slightly increased cell death at 700 and 1100nM compared to free Daunomycin. For this reason, *J52* was chosen for the cell internalization studies described below.

DNA Nanoparticle Cell Internalization Study Using MCF-7 Breast Cancer Cells

In order to characterize cell internalization pathways of our AuNP platforms, various agents were used to inhibit isolated endocytotic mechanisms within a cell. Sucrose is used to inhibit clathrin-mediated endocytosis, Methyl-Beta-Cyclodextrin (MβCD) is used to inhibit lipid-raft endocytosis, and nystatin is used to inhibit caveolae mediated endocytosis. MCF-7 human breast cancer cells were seeded on a 96-well tissue

culture plate at 20,000 cells/well for 24 hours. Once the cells had adhered, the media was removed and each well was washed three times with PBS. The samples were then pretreated with various endocytotic inhibitors (protocol adapted from Jiang *et al*, 2015) by incubating them with 50μL of sucrose (450mM), nystatin (180nM), or methyl-β-cyclodextrin (MβCD, 10mM) in serum-free media for one hour. A negative control was performed on cells with no inhibitors and the incubation occurred at 4^{o}C. This temperature shuts down all energy-driven internalization pathways, ensuring that no AuNPs can enter.

After 1 hour, Daunomycin loaded *J52*-AuNPs were added to each well, in the presence of the inhibitors, at three drug concentrations (315nM, 700nM, 1100nM) for each of our variables (untreated cells, sucrose-treated cells, nystatin-treated cells, MβCD-treated cells, and repeated for cells at 4^{o}C). The plates were left in a 37^{o}C incubator for 4 hours (excluding the plates kept at 4^{o}C). Then the wells were washed again with PBS, and an XTT Cell Viability assay was applied to track cell death over the next 48 hours. Cells alone and cells incubated with 70% IPA were used as negative and positive controls for the assay. All inhibitors were tested with cells without the addition of AuNPs to ensure that they do not induce toxicity. Functionalized *J52*-AuNPs with no drug were incubated with cells on both plates to observe the effect on the cells due to the functionalized nanoparticles without drug. Equivalent molar ratios of free drug were tested on the 4^{o}C plate as a control to compare to functionalized *J52*-AuNP samples on the same plate.

5.4.3 Nanoparticle Versus Free Drug Experiment

An XTT Cell Viability assay was performed to determine the efficiency of the functionalized drug loaded AuNP platforms at killing cancer cells. Human breast adenocarcinoma cells (MCF7) in EMEM liquid cell culture medium were seeded on a gelatin coated well plate at 20,000 cells/well and allowed to grow for 24h. Free Daunomycin in solution was pipetted into each well at concentrations ranging from 0-1400nM (increments of 100nM). A 70% isopropyl alcohol solution was used to kill all cells as a marker for the viability assay. It was observed that AuNP platform loads Daunomycin at various amounts. Daunomycin concentration on each individual particle was calculated, and this allowed us to measure Daunomycin concentration as a function of AuNP concentration. With this information we incubated seeded cells with our AuNP platforms at various drug concentrations from 128-1,100nM. Cells were allowed to incubate with the Daunomycin for 4h then washed and placed in media overnight, after which an XTT cell viability was performed and results measured using a spectrophotometer. Cell viability using our AuNPs was plotted against cell viability using free Daunomycin as a measure of platform efficacy (see Figure 5.17).

By this method we are able to directly compare the effectiveness of our drug loaded functionalized AuNP platform to free Daunomycin at different drug concentrations (Figure 5.17). It is expected that our AuNPs in solution will naturally release some Daunomycin into the surrounding liquid. As seen in our dialysis membrane study, AuNP-ANC released 90% of its drug payload in only 4 hours. When compared to equivalent concentrations of free Daunomycin, AuNP-ANC showed only slightly higher

rates of cell death, consistent with the observation that a majority of the drug is released quickly.

All AuNP platforms showed more cell death than free Daunomycin and AuNP-ANC at equivalent drug concentrations with *J52*-AuNP performing the best (see Figure 5.17). It is hypothesized that due to the high, local concentration of Daunomycin on each AuNP a small rate of internalization will produce more rapid cell death than freely diffusing drug molecules as demonstrated by the schematic in Figure 5.18. Figure 5.18A shows free drug diffusing into a cell, requiring several molecules to independently be taken up by a cell. Figure 5.18B demonstrates that one nanoparticle entering a cell, either by active or passive transport, has the potential to release upwards of 1,000 drug molecules into a cell. This illustrates the power of a high-localized drug concentration on potential delivery through a cell membrane and instigating cell death.

5.4.4 Internal Mechanism Study

The most efficient AuNP platform (*J52*-AuNP) was used to evaluate methods of cell internalization of the nanoparticles. Human breast adenocarcinoma cells (MCF7) were seeded onto a gelatin coated well plate at a concentration of 20,000 cells/well, as described above. The Eagle's Minimum Essential Medium (EMEM) media was removed and PBS was used to wash each well. We then added serum-free media to each well containing certain endocytotic inhibitors in accordance with the protocol performed by Li and Monteiro-Riviere [33]. Our inhibitors included: tests at 4^{o} C to reduce cell metabolism and inhibit active transport, sucrose (450mM) to inhibit clathrin-mediated

endocytosis, nystatin (180nM) to inhibit caveolae mediated endocytosis, and methyl-β-cyclodextrin (MβCD, 10mM) to inhibit lipid-raft endocytosis.

Cells were incubated with the inhibitors for one hour. Next, *J52*-AuNP was added to each respective well at equivalent Daunomycin concentrations of 315nM, 700nM, and 1100nM for 3h. Cells were monitored with all inhibitors without addition of drug-loaded AuNPs to ensure they have no cytotoxic effects. Free Daunomycin and *J52*-AuNP without Daunomycin were also incubated with cells at 4°C to observe auxiliary effects of the reduced metabolism. After 3h, the wells were washed again with PBS and incubated in inhibitor-free, serum-free media for 24h. Finally, another XTT Cell Viability assay was applied to track cell death. Results were compared to cell viability involving *J52*-AuNP with drug containing untreated cells (data from Figure 5.17) to calculate percent inhibition for each test (Figure 5.19).

Inhibition due to cells being exposed to a temperature of 4°C is the highest at ~79%. It is expected that this environment would produce the highest rate of inhibition, as our particles are expected to be internalized due to active transport based on their size. Additionally, this is the only mechanism that loses inhibition at higher concentrations. The variance in inhibition percentage at higher concentrations is explainable when one considers that AuNPs will aggregate at low temperatures, and more AuNPs are present in the solution for the higher concentrated samples.

These aggregate clusters may be negatively affecting the cells and inducing cell death and therefore was tested. Additional control experiments using *J52*-AuNP (with no drug) lead to the conclusion that this effect is likely the issue (data not shown). The highest concentration of *J52*-AuNP with no drug (identical to concentration for

nanoparticles with drug) tested at 4ºC increased death by about 8%. Comparing this to percent inhibition between the lowest and highest concentrations for 4ºC nearly matches the difference in cell death. The middle concentration of 700nM also showed an increased death rate of 3% agreeing with change in percent inhibition. These control experiments explain why percent inhibition changes with concentration at 4ºC, but not for the inhibitors, as should be the case.

The three-inhibitor systems however, should ideally maintain a consistent inhibition rate since drug concentration does not affect functionality of the inhibition markers, and this result is seen in our data as evident from no change in percent inhibition as concentration is increased (comparing across the x-axis in Figure 5.19). MβCD is the second most efficient inhibitor of internalization at ~65%. It is likely that our AuNP platforms are mostly internalized through the lipid-raft pathway judging from this data. Sucrose internalization has been shown to be size dependent for similar AuNPs and can be preferential for particles < 200nm [36].; indeed, the size distribution of our particles agrees with studies in literature regarding clathrin-inhibition [33]. Our results indicate ~55% inhibition for this mechanism with the expectation that this value will decrease with increasing particle size, and conversely increase with decreasing particle size.

Nystatin, inhibiting only a fraction of total lipid-raft formation, resulted in the lowest rate of internalization inhibition at ~33%. Although it seems that lipid-rafts are the most likely internalization pathway, *caveolae-mediated* lipid-raft endocytosis may be a secondary internalization mechanism for our platform. Note that in all cases, it is possible that free drug is being released from the AuNPs. However, it is expected that any effect on cell viability imparted by free drug release will remain constant across each test with

J52, and it has already been seen that AuNP platforms outperform free Daunomycin at killing cultured cancer cells. From this realization, it is accepted that these data are indicators of our AuNP platforms' internalization pathway.

5.5 Conclusions

This chapter describes a programmable, nanoscale drug carrier capable of delivering therapeutics to kill cancer cells. The dense coverage of anchor oligonucleotides provides flexibility to bind large quantities of one or more aptamers to each nanoparticle. The hydrodynamic diameter of the nanoparticle can reduce the rate of renal clearance, thus increasing bioavailability, and enhance passive targeting to tumor cells with AuNP platforms of < 100 nm in diameter. This factor paired with active, aptamer-mediated targeting is expected to greatly reduce off-target absorption and toxicity of the drug.

Loading studies with the chemotherapeutic drug Daunomycin revealed a payload much higher than previously reported with nanoparticles of similar size. The kinetic release studies observed drug release from the nanoparticle for over 48 hours. Initial release is extended due to the intercalation of Daunomycin into DNA duplexes compared to bare AuNPs and AuNP-ANC. The release time also seems to be slightly tailorable by engineering specific nucleic acid sequences on the particle surface; although more in depth analysis will be necessary to explore the amount of control possible when using an aptamer with targeting functions.

Drug delivery to tumors can be achieved both actively and passively using this platform when aptamers are employed. Our nanoparticles have proven to induce cell

death in breast cancer cells at a higher efficiency than free Daunomycin at all tested concentrations. The size and targeting capabilities of the particle will increase its therapeutic value for *in vivo* use. One consideration to make is the innate immune system response. This mechanism uses receptors that recognize conserved microbial DNA/RNA features in order to combat foreign nucleic acids. Sometimes these systems can attack native nucleic acids when not working properly leading to various types of autoimmune or autoinflammatory diseases. In order to reduce this concern, the length of the DNA strands selected for binding lots of Daunomycin was kept below 100 base pairs. Even though longer DNA strands would allow for increased drug binding, the increased size would potentially create other undesired effects *in vivo*. Current studies in our lab include characterization and optimization of this unique platform in tandem with aptamer sequences extracted from literature.

This chapter further highlights the potential for the synthesis and characterization of drug delivery nanoparticles with high therapeutic payload for multi-faceted targeting capabilities. This technology has the potential to lead to groundbreaking cancer therapies. The anchor layer of the particle allows for conjugation of several aptamers for specific targeting of multiple cells or molecules. The high payload of Daunomycin suggests that loading therapeutic doses of multiple drugs is within the realm of possibility. Thus, our technology may be utilized in the future to develop simple, safe, and highly effective nanoparticles that can be intelligently engineered for personalized cancer therapies.

5.6 Tables & Figures

Table 5.1. ANC-SH concentrations used during AuNP-ANC synthesis. *ANC concentrations were modified by increasing the ANC volume used during DTT reduction; each sample is identified by its oligo ID based on µL of stock sample. ANC concentrations are shown here as concentration after reduction and concentration at the start of AuNP-ANC synthesis (AuNP concentration: $1.4x10^{12}$ particles/mL; 1 mL volume used for synthesis).*

Oligo ID	**ANC2**	**ANC4**	**ANC6**	**ANC8**	**ANC10**
Reduced ANC (µM)	13.26	30.38	39.22	55.48	64.62
ANC (with AuNPs) (µM)	0.47	1.08	1.39	1.97	2.29

Table 5.2. Size measurements of AuNPs functionalized with anchor DNA by DLS.
Increasing concentrations of NaCl showed changes in nanoparticle size. Peak values represent the diameter at which the highest percentage of the sample lies as reported by DLS measurements.

ANC								
Avg (nm)	88.73	28.55	47.68	76.82	50.15	36.85	45.96	40.95
Salt (M)	**0**	**0.1**	**0.3**	**0.4**	**0.6**	**0.7**	**0.9**	**1**

Table 5.3. ImageJ analysis of non-denaturing gel for engineered DNA sequences. *This data represents analysis of intramolecular interactions and double stranded hybridization percentage for engineered DNA sequences. Incomplete and undesired reactions for each single and hybridized sample can explain why each engineered sequence did not behave as anticipated. All calculations for Daunomycin quantification and affinity do not take into account the behaviors for each sample shown here.*

Reaction Type	L52	L52C	L52H	J52	J52C	J52H	M52	M52C	M52H	H52	H52C	H52H
Self Reaction	0.0%	2.0%		5.9%	6.3%		41.2%	40.8%		16.0%	10.5%	
Incomplete Hybridization			0.0%			1.8%			19.8%			13.9%

Table 5.4. Hill coefficient for each DNA sequence. *A Hill coefficient n > 1 refers to positive cooperativity, while n < 1 refers to negative cooperativity. It is seen that Daunomycin imparts slightly positive cooperativity on hybridized DNA while it imparts a slightly negative cooperativity on most single strands. This behavior agrees with what is reported in the literature except for H52 and H52C. One reason that these might behave differently is because these strands bind with themselves to such a strong degree.*

Hill Coefficient			
0.834	0.884	0.934	1.18
L52	**J52**	**M52**	**H52**
0.828	0.921	0.963	1.09
L52C	**J52C**	**M52C**	**H52C**
1.34	1.17	1.30	1.28
L52H	**J52H**	**M52H**	**H52H**

Table 5.5. Binding affinity constants calculated using the Hill plot. *Daunomycin intercalation to DNA has ranged from 0.23 μM^{-1} for 6 bp long molecules to 7 μM^{-1} for studies involving genomic DNA. These sequences, being longer than 6 bp but shorter than genomic DNA, exhibit binding affinity within this range. A one-way ANOVA test reported no statistical significance between affinity values for any two strands; p-values range from 0.07 (L52H and M52H) to 0.8 (J52H and M52H).*

Binding Affinity (μM^{-1})			
0.13 (±0.04)	0.54 (±0.07)	0.48 (±0.12)	0.44 (±0.06)
L52	**J52**	**M52**	**H52**
0.15 (±0.04)	0.65 (±0.14)	0.58 (±0.11)	0.36 (±0.14)
L52C	**J52C**	**M52C**	**H52C**
1.28 (±0.66)	2.78 (±1.61)	2.58 (±0.64)	1.81 (±0.53)
L52H	**J52H**	**M52H**	**H52H**

Table 5.6. Dialysis membrane release of Daunomycin from functionalized AuNPs. Drug release at room temperature, pH 7, over 6 days. Percentages are out of total drug loaded onto nanoparticles. The 4h time point is considered for incubation time with cancer cells, therefore release here is most significant. AuNP-ANC released over 90% of its drug payload in only four hours. Conversely, J52 only released 52% of its drug payload during the same time period. The dialysis release data seems to agree with the Daunomycin loading data in that the AuNP constructs that bound the greatest amount of drug had the slowest drug release rate.

Time (h)	AuNP-ANC	AuNP-L52	AuNP-J52	AuNP-M52	AuNP-H52
1	51% (± 2.8)	36% (± 1.3)	30% (± 0.6)	47% (± 0.5)	43% (± 1.2)
2	84% (± 3)	45% (± 0.4)	41% (± 0.4)	72% (± 0.5)	64% (± 1.4)
4	89% (± 3.9)	57% (± 1.3)	52% (± 2.7)	81% (± 3.3)	75% (± 0.8)
12	96% (± 1.5)	69% (± 0.1)	64% (± 1.1)	88% (± 0.3)	84% (± 0.6)
24	99% (± 1.2)	79% (± 0.2)	75% (± 0.1)	91% (± 0.3)	90% (± 0.1)
48	99% (± 0.6)	88% (± 0.8)	87% (± 0.1)	97% (± 0.6)	96% (± 0.4)
144	100% (± 0.1)	99% (± 0.3)	98% (± 0.3)	100% (± 0.5)	99% (± 0.3)

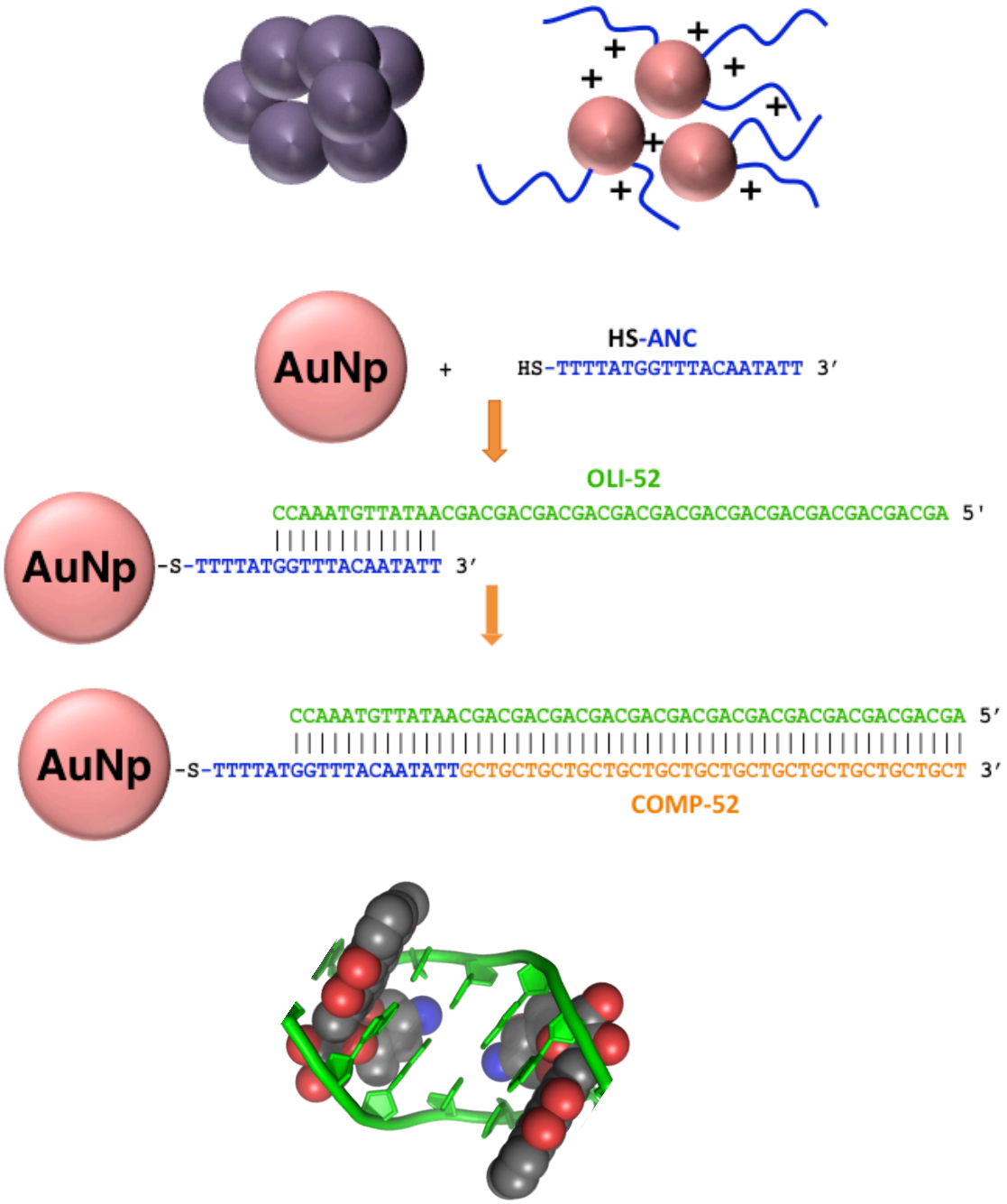

Figure 5.1. Schematic of AuNP platform behavior and hypothesized assembly. *Nanoparticles (red) will turn dark blue in the presence of salt if no DNA is bound due to surface plasmon resonance. This is used to indicate successful ANC (blue) binding to AuNPs. From there, an engineered drug binding DNA strand (green) is capable of attaching to the AuNP through complementary base pairing with ANC. This double stranded region can be extended in a uniform manner using a Klenow enzyme (orange). Finally, 3-D model (bottom) of Daunomycin intercalation into the double stranded DNA region. Daunomycin is only fluorescent when not bound to DNA. The sugar group of the Daunomycin molecule sticks outwards towards the backbone of the DNA.*

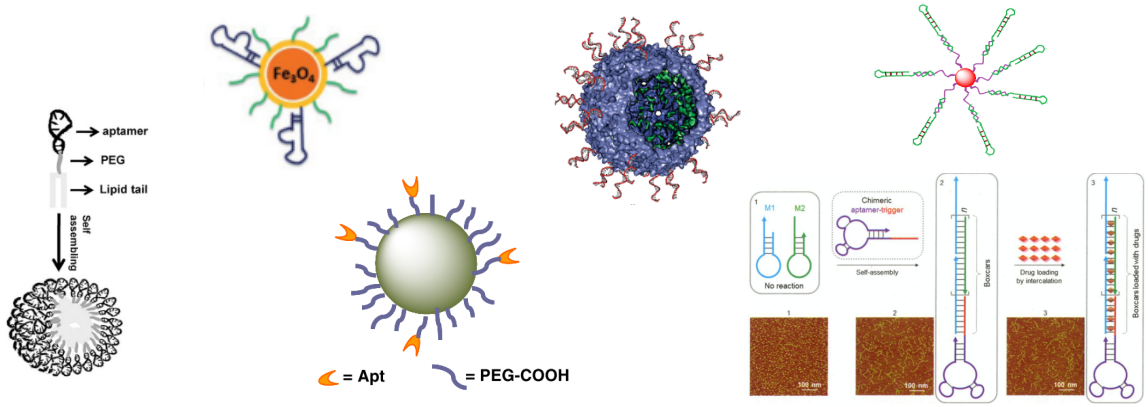

Figure 5.2. Schematic of various types of nanoparticles and bound ligands. *There are many types of nanoparticles capable of binding DNA. Gold nanoparticles were chosen because their interactions with DNA and binding behavior being well documented. Furthermore, controlled binding, and optimization for DNA loading have been researched in detail and these properties fit perfectly with the goals of the research performed. Adapted from [26].*

L52	CAA ATC CTC TTC CAA ACT CCT AAT CCA GTG TAA CTC ACC GTT TAG GAG AAG GTT TGA GGA TTA GGT CAC ATT GAG TGG
J52	**AGC AGC AGC AGC AGC AGC AGC AGC AGC AGC AGC AGC AGC** TCG TCG TCG TCG TCG TCG TCG TCG TCG TCG TCG TCG TCG
M52	**CGA** TCG **CGA** TCG **CGA** TCG **AGC AGC AGC AGC AGC AGC AGC** GCT **AGC** GCT **AGC** GCT **AGC** TCG TCG TCG TCG TCG TCG TCG
H52	**CGA** TCG **CGA** TCG **CGA** TCG **CGA** TCG **CGA** TCG **CGA** TCG **CGA** GCT **AGC** GCT **AGC** GCT **AGC** GCT **AGC** GCT **AGC** GCT **AGC** GCT

Figure 5.3. Engineered Daunomycin binding sequences. *Each sequence is 52 nucleotides long, with 13 nucleotides complementary to the anchor strand (not shown). The remaining 39 nucleotides and their complement strands are shown above. Daunomycin is known to preference intercalation in between two G/C base pairs flanked by an A/T. The four sequences are manipulated into different formations to alter drug-binding affinity. J52 contains this triplet sequence (shown in bold) across the entirety of its sequence. M52 and H52 contain the triplet sequence on alternating strands in different patterns to assess the effect orientation has on binding affinity.*

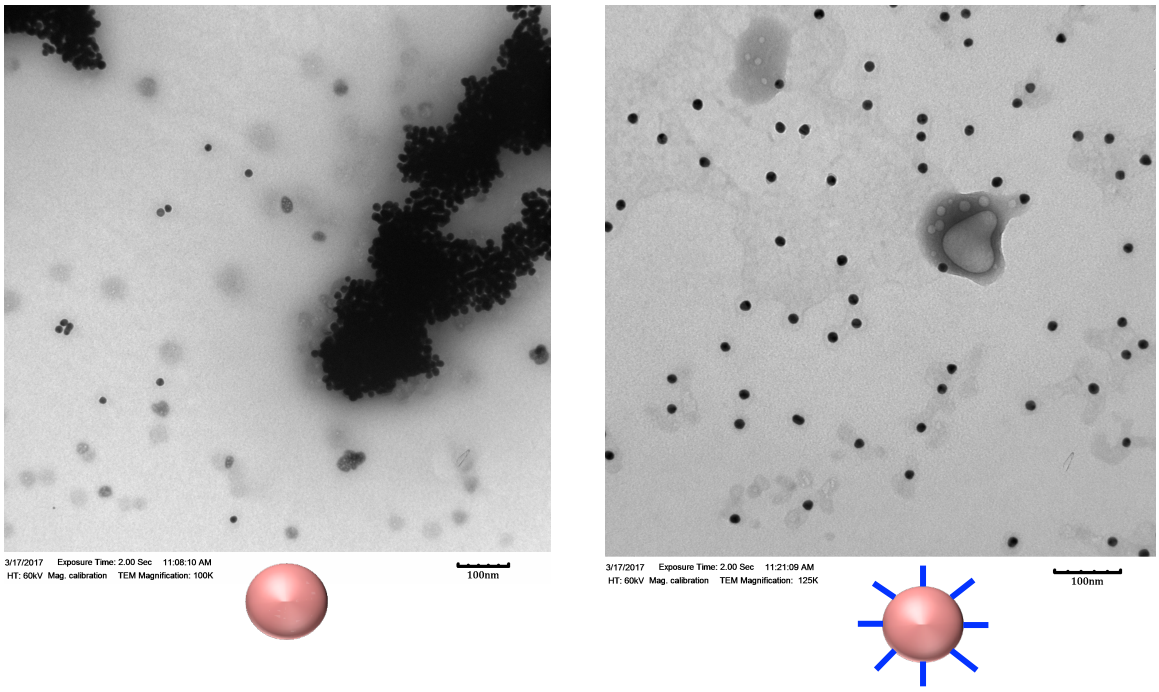

Figure 5.4. TEM images of gold nanoparticles*. Gold nanoparticles without ANC-SH aggregate under the conditions required for imaging via TEM (left). When ANC-SH is attached to gold nanoparticles, they remain separated and a small halo can be seen surrounding each one (right). This one of three ways confirmation of ANC-SH bound to AuNPs is shown experimentally.*

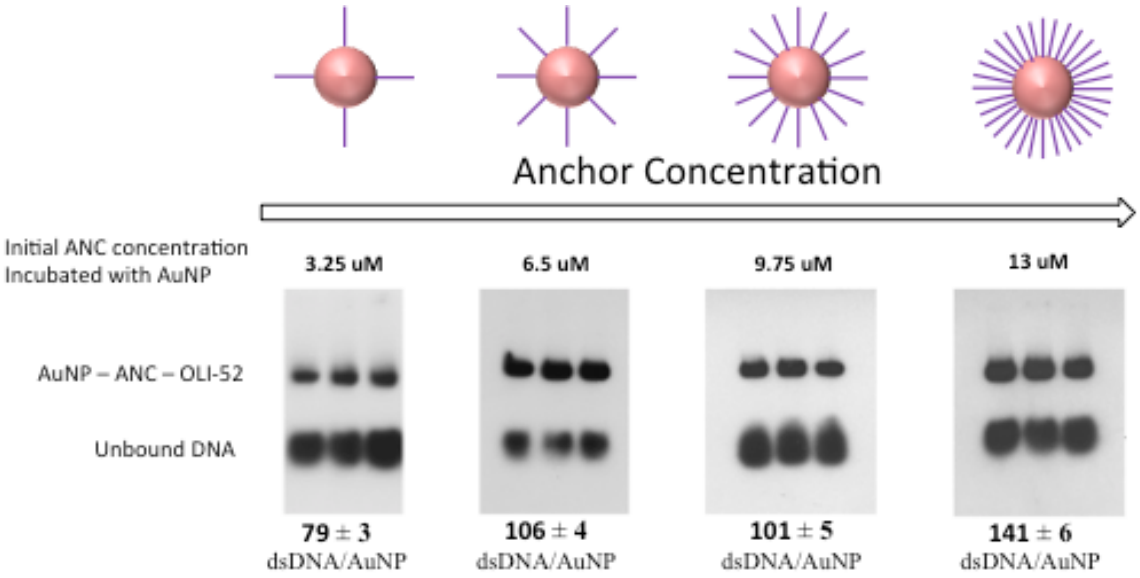

Figure 5.5. Engineered DNA sequence quantification on gold nanoparticle. *Autoradiography images quantifying the amount of complementary oligonucleotides (dsDNA) bound to each nanoparticle. Loading was influenced by the initial concentration of ANC incubated with each gold nanoparticle sample. As the binding mechanism of complementary DNA relies on base pairing, it is clear that an increase in ANC loading leads to an increase in dsDNA loading. The loading amount for dsDNA loading seems to have a buffer range where varying ANC concentration (6.5-9.75μM) maintains the same rate of binding. This is helpful to maintain a consistent assembly of nanoparticles between new batches. The highest concentration tested gives a value greater then the theoretical maximum of 107. The most likely explanation is that the nanoparticles are larger then 15nm estimate given by TedPella.*

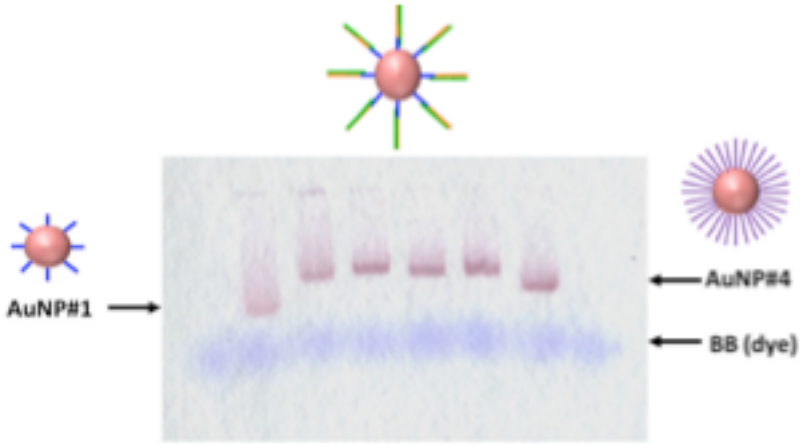

Figure 5.6. Agarose gel showing mobility shift. *Nanoparticles containing hybridized engineered DNA sequences and Klenow reaction (four middle lanes) compared to AuNp-ANC only (first and last samples) are shown to have differences in mobility. AuNP-ANC#1 (3.25μM) is also shown to run faster down the gel compared to AuNP-ANC#4 (13μM), showing the sensitivity of this gel for detecting changes in mass to nanoparticle surface. All four Klenow reacted samples have mobility shifts indistinguishable from each other, which is to be expected, but all have a slower mobility then the AuNP-ANC only samples confirming hybridization of engineered DNA sequences.*

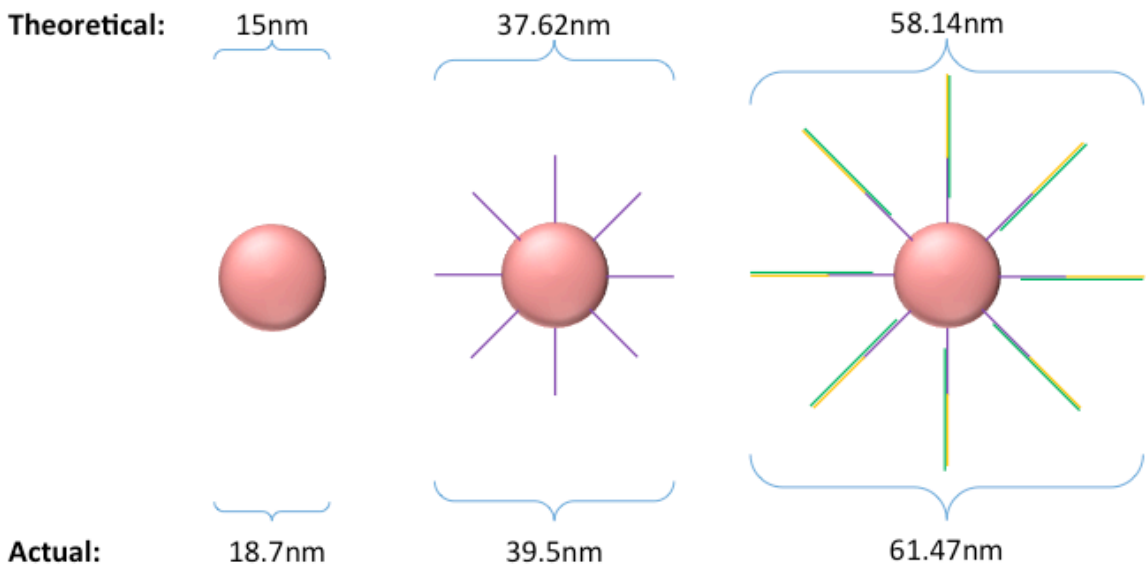

Figure 5.7. Theoretical diameters of AuNPs at each stage of synthesis. *Bare nanoparticles of 15 nm diameter were purchased initially, and DLS sizing on a Zetasizer revealed an average diameter of ~18.7nm. From this calculation a new theoretical size estimate for AuNP-ANC was determined to be ~31.62nm. Actual readings were ~7nm larger then calculated, most likely this is due to stretching of the DNA from a crowded environment and charge repulsion forces acting on each DNA strand. Using the actual value, again a theoretical size estimate for attachment of each 52-nucleotide long engineered DNA strand was calculated and determined to be ~58.14nm. The trend remained constant as the actual value from DLS reported a size ~3nm larger. However, this value is close to expected and can easily be explained by some slight stretching and charge repulsion of DNA strands in close proximity to one another on the gold nanoparticle surface. Actual values being close to theoretical values is one indication that the expected assembly behavior of the DNA is behaving as designed and anticipated.*

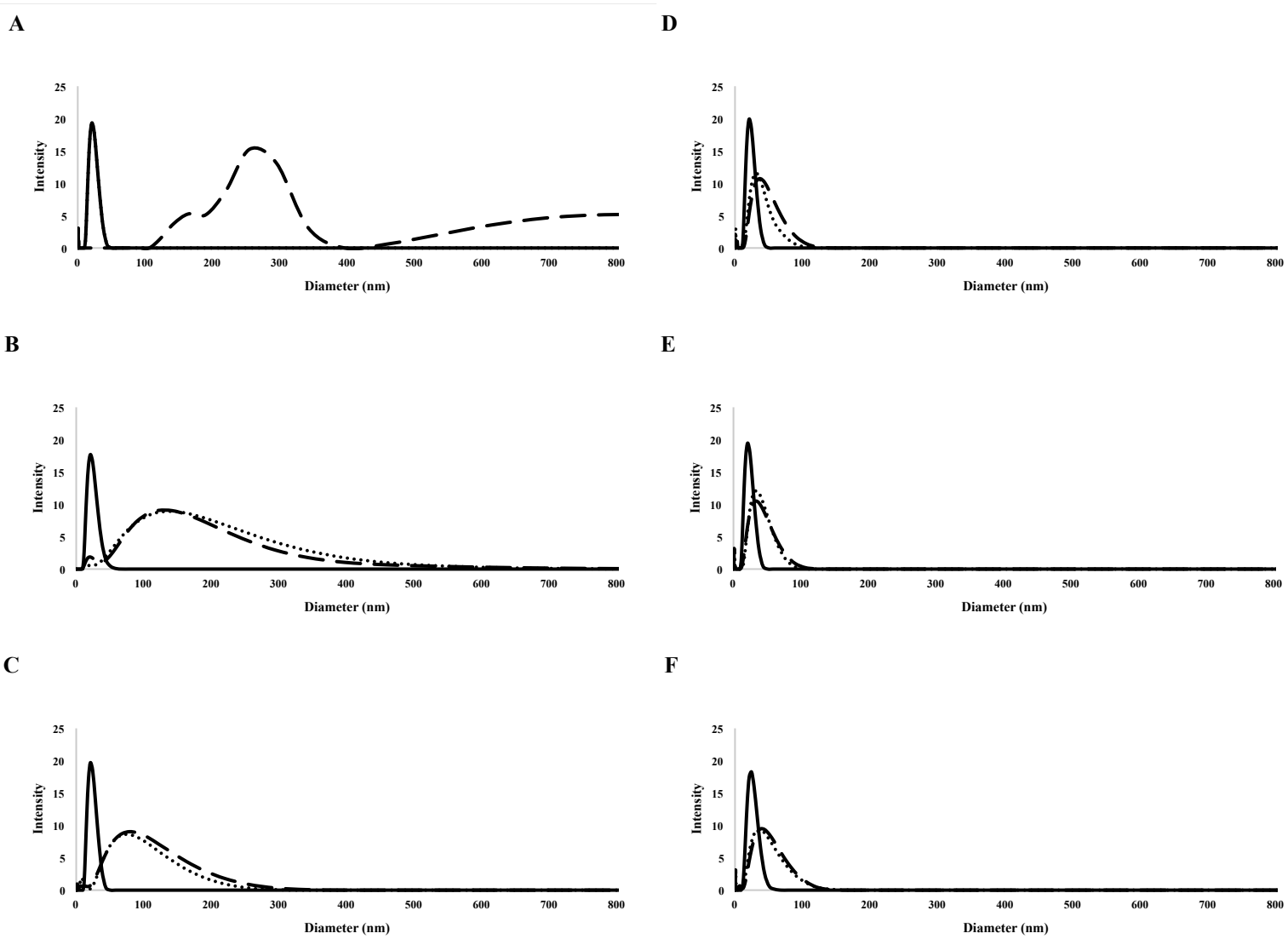

Figure 5.8. Size profiles for AuNP-ANC with increasing DNA concentration. *AuNPs were functionalized with short, thiolated DNA oligonucleotides (ANC) at various DNA concentrations according to our salt-aging protocol (final concentration of NaCl = 0.5M). Size profiles of unmodified AuNPs are shown for comparison purposes only. DLS size profiles are reported for AuNP-ANC both before and after centrifugation/resuspension. Unmodified AuNPs (———), AuNP-ANC (pre-centrifugation; ● ● ●), AuNP-ANC (resuspended; — — —); Reduced ANC concentrations:* ***A*** *- 0μM;* ***B*** *– 13.26μM;* ***C*** *– 30.38μM;* ***D*** *– 39.22μM;* ***E*** *– 55.48μM;* ***F*** *– 64.62μM.*

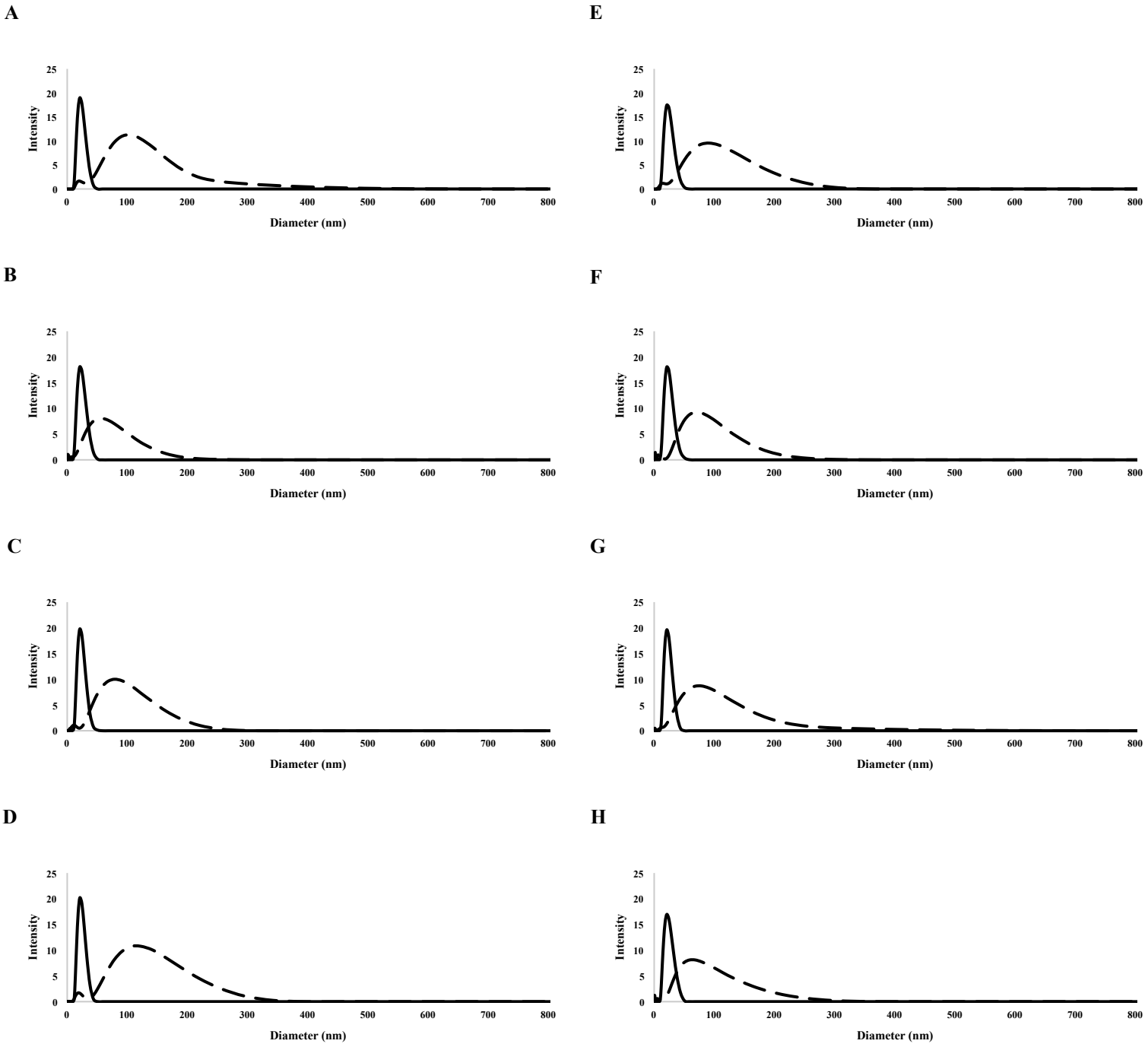

Figure 5.9. Size profiles for AuNP-ANC with increasing NaCl concentration. *AuNPs were functionalized with short, thiolated DNA oligonucleotides at various NaCl concentrations according to our salt-aging protocol. Size profiles of unmodified AuNPs are shown for comparative purposes only with those of synthesized AuNP-ANC platforms. Unmodified AuNPs (———), AuNP-ANC (— — —). Final NaCl concentrations: A - 0M; B – 0.1M; C – 0.3M; D – 0.4M; E – 0.6M; F – 0.7M; G – 0.9M; H – 1M).*

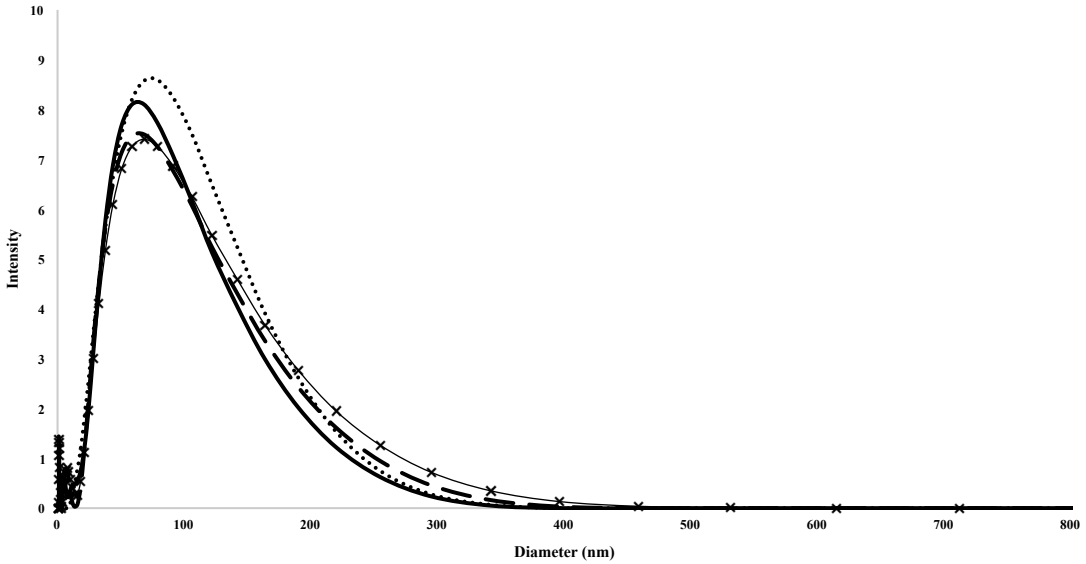

Figure 5.10. Size comparisons of AuNP-ANC after different heating treatments. *DLS measurements of synthesized AuNP-ANC platforms (AuNP-ANC, 1M NaCl) were compared over multiple heating steps. Here we compare the size profile of one AuNP-ANC sample (——) after the following treatments (in order): heating at 80°C for 5 min (● ● ●), heating at 80°C for 10 min and ice for 5 min (— — —), and heating at 95°C for 3 min and ice for 5 min (—x—)*

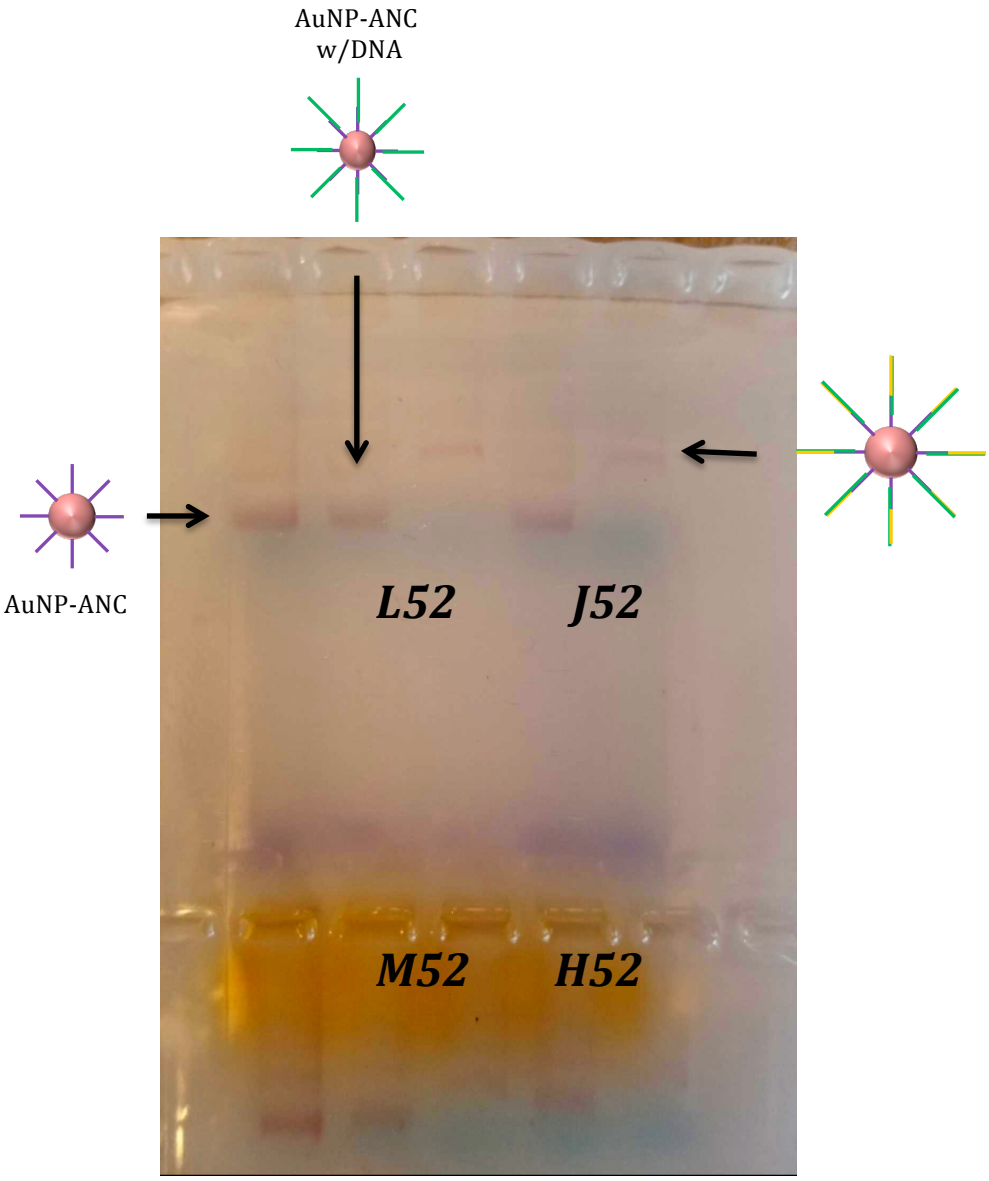

Figure 5.11. Agarose gel confirmation of successful Klenow reaction*. Mobility shift for nanoparticles containing all the same components except the Klenow enzyme (- and + lanes for each DNA sample) AuNP-ANC was also run as an additional control. The decreased mobility rate is proof that the Klenow reaction was successful for each DNA-AuNP sample.*

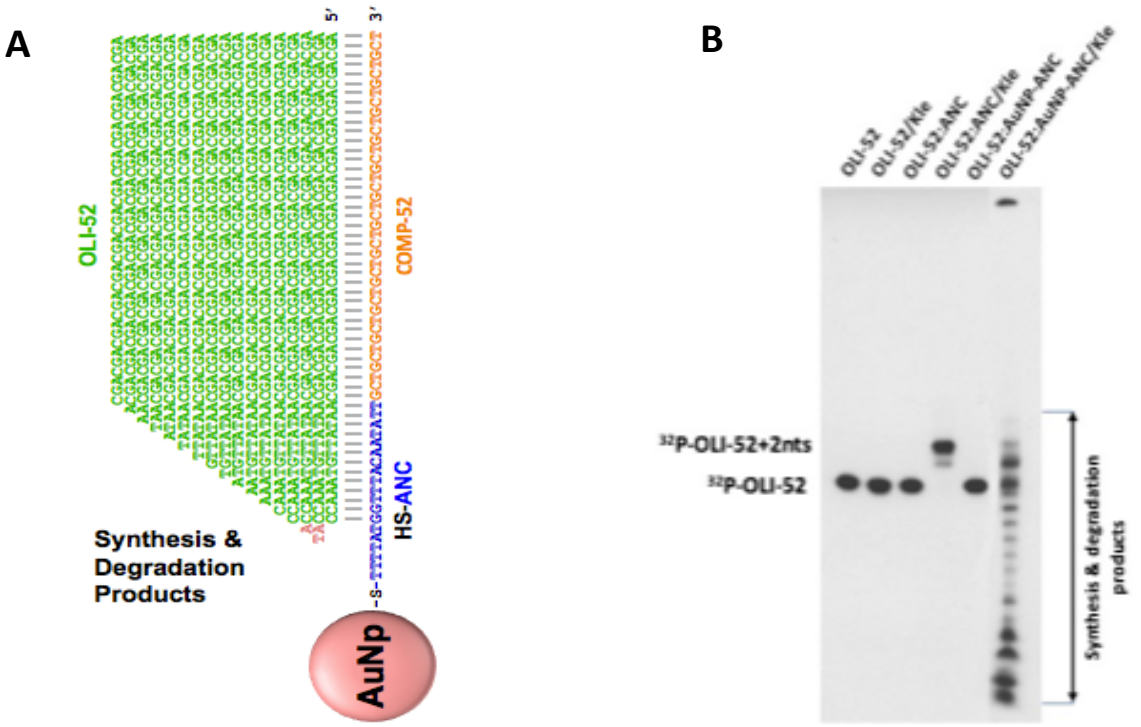

Figure 5.12. Synthesis and degradation products of Klenow reaction. *The behavior of the Klenow enzyme in the presence of our nanoparticle leads to a series of degraded DNA sequences shown schematically* ***(A)*** *and experimentally after stripping off the nanoparticle* ***(B).*** *Degradation from cleaving mediated by the Klenow enzyme may commence at different locations on the DNA strand according to steric hindrance on the AuNP in proximity for each unique strand. This can lead to a series of variable DNA complexes across the surface of our AuNP. The product of this degradation can be seen in the autoradiograph* ***(B)****. From the image, it is clear that the Klenow enzyme produced a number of distinct structures of various sizes and molecular weights. Since the 5' end is labeled radioactively, all visible degradation must be occurring on the 3' end, which is the side near the surface of the AuNP.*

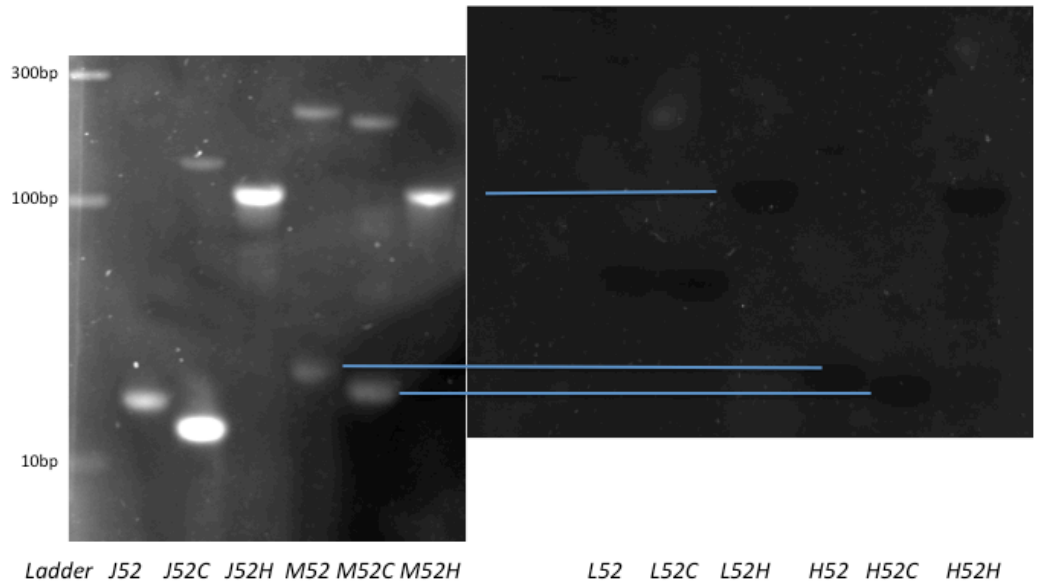

Figure 5. 13. 8% non-denaturing gel of engineered DNA sequences*. Hybridization rate of each strand was calculated by running each sample through a gel, comparing sizes of bands with a ladder, and using ImageJ to scan the bands in the image. This gel shows ssDNA for J52, M52, and H52 have a similar mobility, while L52 behaves drastically different. This agrees with computer simulation data. Unwanted hybridization reactions are shown in this gel and therefore can be used as justification for Daunomycin binding and affinity behavior differing from expected result. Percent values are shown in Table 4.3.*

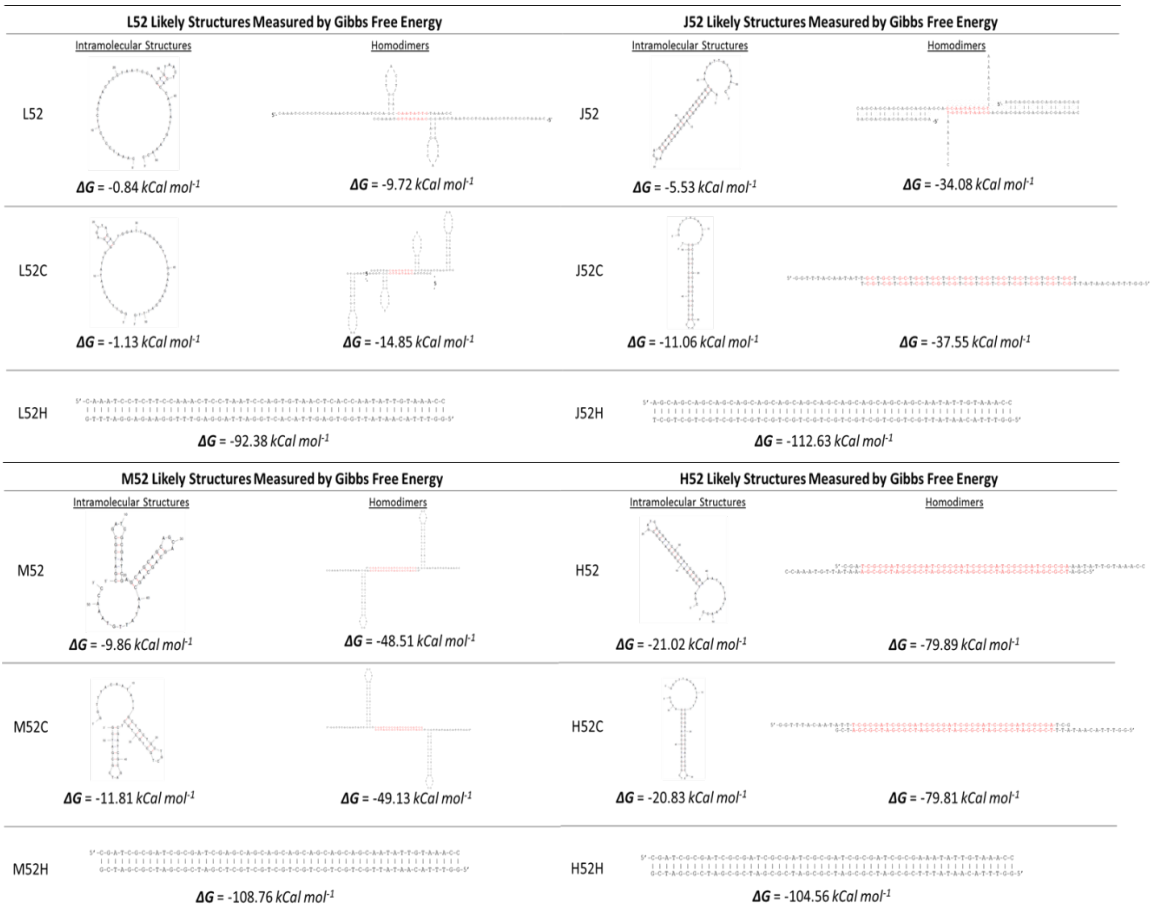

Figure 5.14. Most thermodynamically favored engineered DNA structures. Mfold and RNAcofold nucleic acid modeling software predict the structures most likely to form and calculate thermodynamically the odds of each structure forming. Modeling was performed for single strands (X52), complements (X52C), and hybridized DNA duplexes (X52H). Due to the high G/C content of J52, M52, and H52, these structures have a higher probability of self-reacting to produce intramolecularly base paired single strands. Furthermore, all single strands in solution are likely to form homodimers between identical single strands. This is the most logical explanation as to why single-stranded DNA bound Daunomycin in our binding studies. Note that all strands are preferentially favored to hybridize with their respective complement, as seen in the significantly lower Gibbs free energy of the hybridized strand complexes.

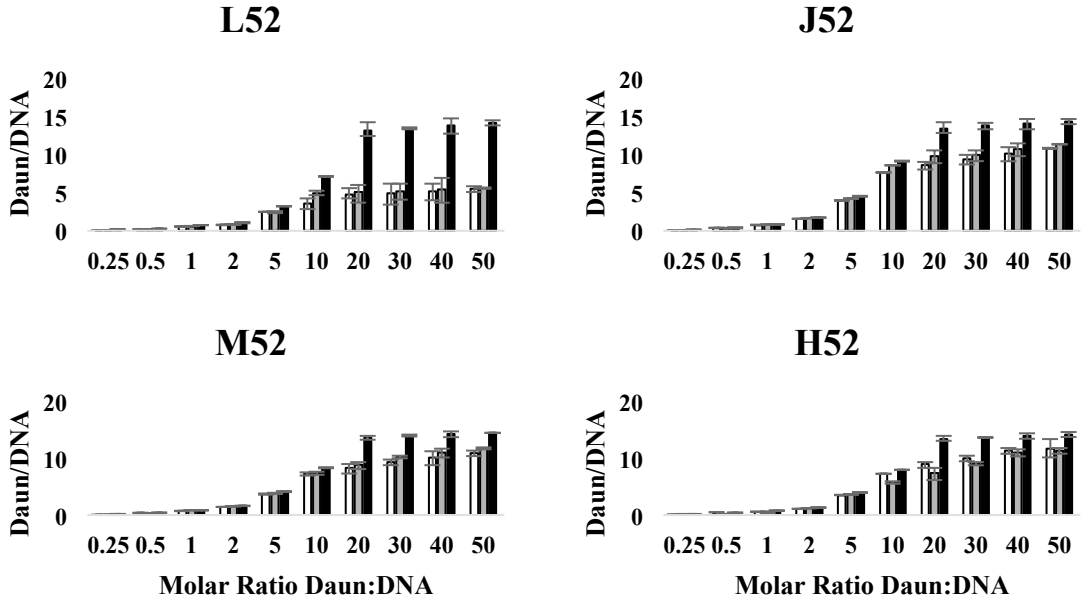

Figure 5.15. Quantification of Daunomycin binding using engineered DNA sequences.
Binding of Daunomycin to four engineered DNA sequences as a function of increasing molar ratio of drug. Binding was calculated for single stranded DNA (□), complementary DNA (■), and double stranded DNA (■). Single stranded controls were heated to 80°C and cooled on ice to reduce intramolecular formations; however, the formation of homodimers was unavoidable and is likely to have occurred, explaining the Daunomycin binding observed for single stranded DNA. Hybridized DNA duplexes showed higher Daunomycin binding than their controls. Maximum loading was assumed, as all hybrid strands loaded around the maximum of ~15 molecules each at molar ratios of 20 and higher.

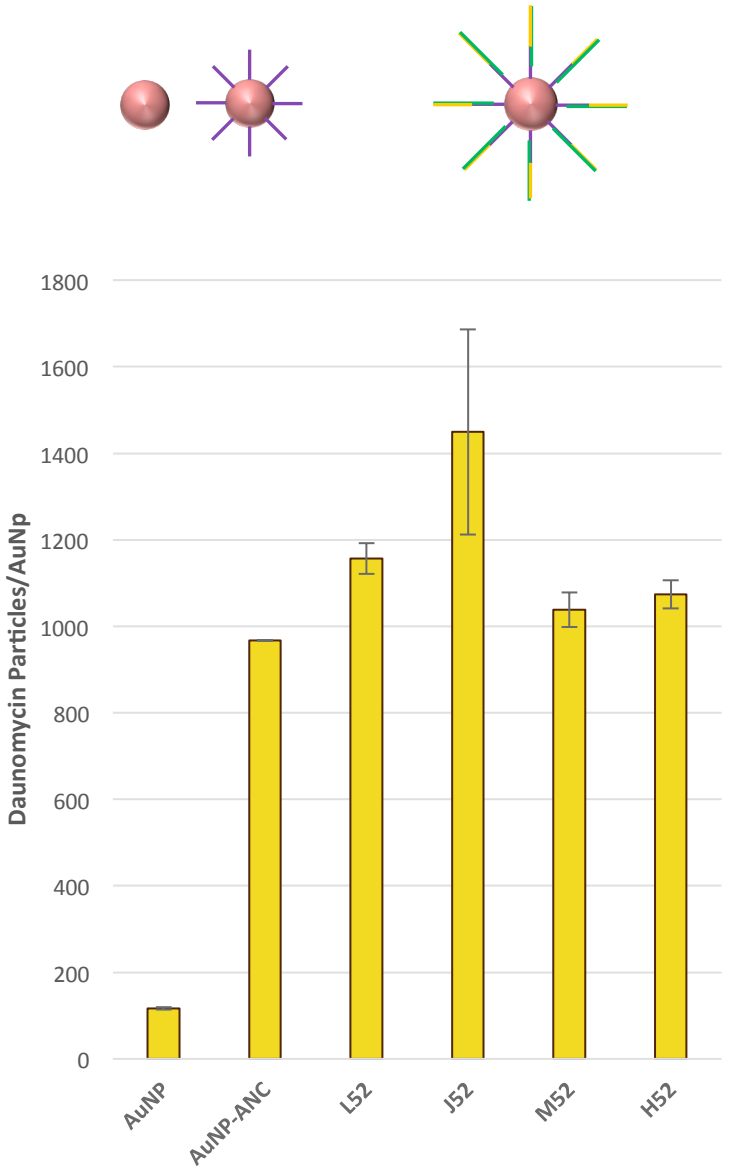

Figure 5.16. Daunomycin binding with DNA-AuNp platforms. *Daunomycin loading onto AuNPs functionalized with each engineered DNA sequence. AuNP represents a bare gold nanoparticle. Bare nanoparticles underwent the same protocols for each as the DNA-AuNPs, except buffer was used in place of NaCl and DNA. Inability to completely remove all unbound Daunomycin during wash steps, as well as any natural Daunomycin binding to eppendorf tube walls or the AuNP surface results in Daunomycin remaining in the sample. Therefore, the Bare AuNP bound value of 117 ± 3 can be subtracted from each nanoparticle when determining actual amounts bound as a result of the DNA. However, for this experiment it was more important to quantify total drug in the sample for further experiments, therefore the values indicated in the table show the total amount of drug per particle (from binding to DNA and other remaining drug. AuNP-ANC bound a much greater amount, due to a combination of non-specific interactions with the DNA phosphate backbone and, we expect, some entanglement within the ANC layer. All AuNP-X52 platforms bound a greater amount of Daunomycin than AuNP and AuNP-ANC. M52 and H52 bound a comparable amount of Daunomycin, lower than both L52 and J52. We observed small amounts of particle aggregation during the experiment, which we expect is due to the palindromic, self-complementary nature of these two sequences. This most likely explains the reduced loading, as the platforms lacked complete, even hybridization for Daunomycin to intercalate. L52 loaded the second greatest amount of Daunomycin. J52 bound the greatest amount of Daunomycin.*

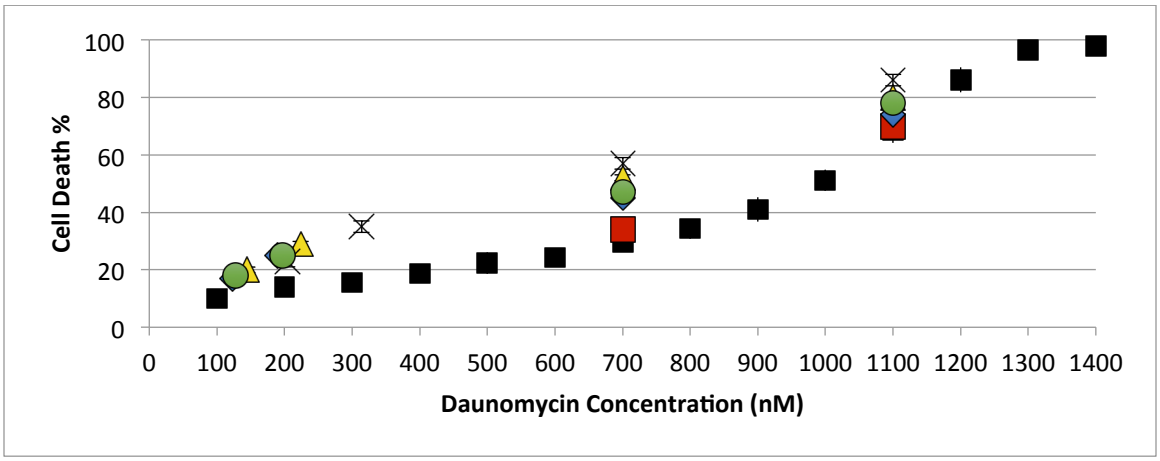

Figure 5.17. Cell viability of MCF-7 cells: free drug v drug loaded nanoparticles. *Results of XTT cell viability tests over varying concentrations of Daunomycin using MCF-7 breast cancer cells. Free drug (■), AuNP-ANC (■), AuNP-L52 (▲), AuNP-J52 (X), AuNP-M52 (♦), and AuNP-H52 (●). Daunomycin concentration was calculated from known drug/AuNP data. All nanoparticle drug carriers showed increased cell death at equivalent Daunomycin concentrations. It is hypothesized that the large, local concentration of drug on the AuNPs allows Daunomycin to enter the cell at a higher concentration than normal diffusion. Note that Daunomycin concentration is measured here, not AuNP concentration; AuNP platforms with lower drug loading required increased AuNP concentration to achieve equivalent drug concentrations. The increased AuNP presence does not affect the cell in a noticeable way, as AuNP-J52 performed better than other platforms at similar drug concentrations yet has the lowest AuNP concentration in this study.*

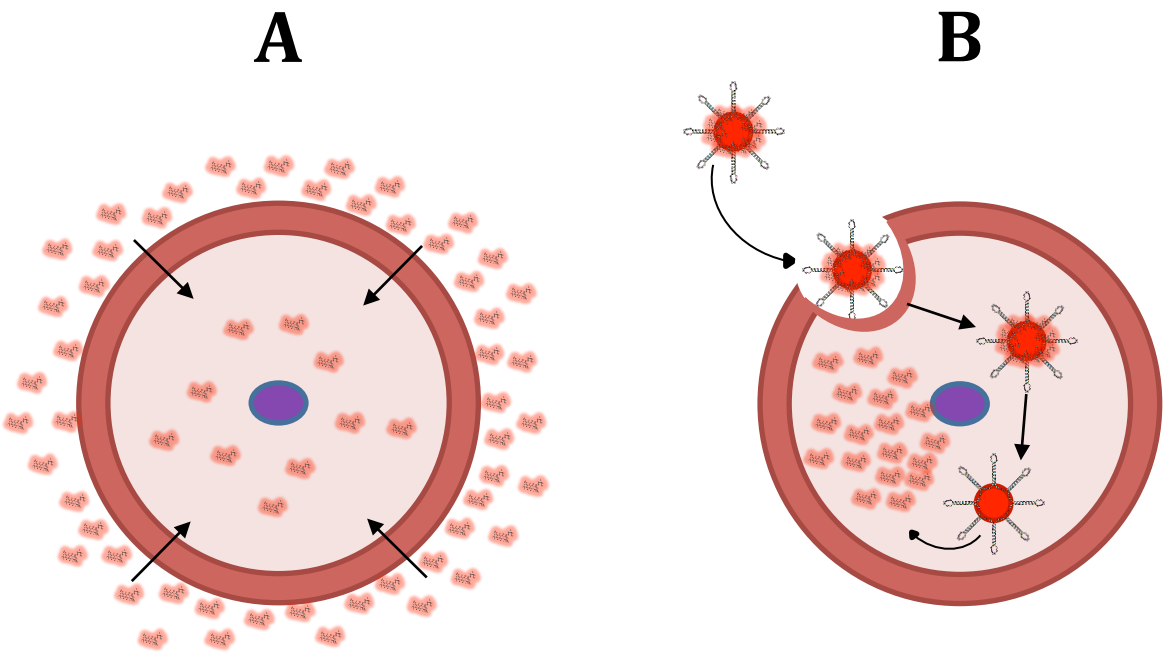

Figure 5.18. Localized concentration of Daunomycin on AuNPs v free drug approach. *Due to its small size, Daunomycin will passively diffuse across the cell membrane in accordance with random motion, and over time will cause a buildup of drug within the cell* ***(A)****. However, internalization of a single AuNP can result in a very high, local concentration of Daunomycin, leading to the AuNP platforms being more efficient than free drug* ***(B)****.*

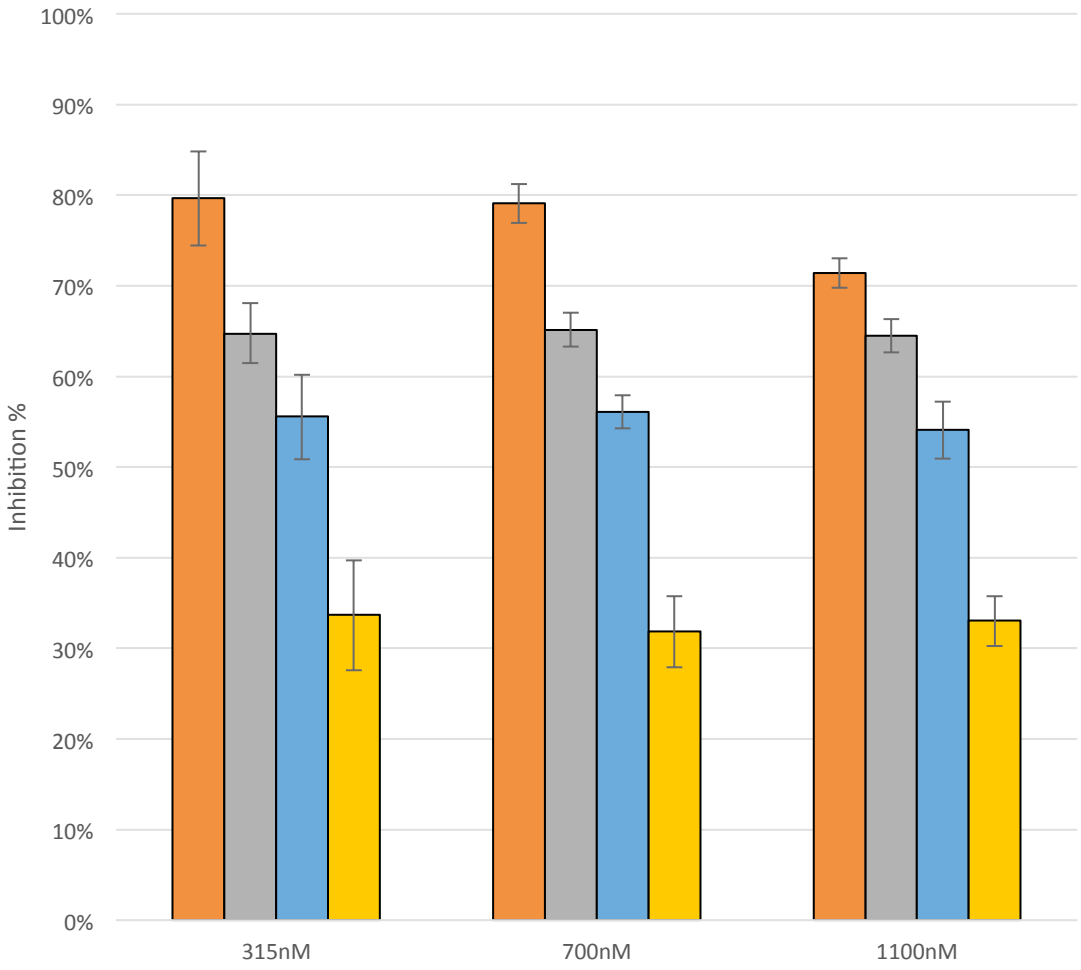

Figure 5.19. Cell internalization mechanism study. *Inhibition of cell death from various endocytotic inhibitors to track internalization pathways of the AuNPs. As these are drug-loaded nanoparticles, it is expected that cell viability is correlated with particle internalization. The endocytotic inhibitors tested include: test at 4°C (■) to lower cell metabolism and inhibit active transport, methyl-beta-cyclodextrin (MβCD, ■) to inhibit all lipid-raft endocytosis, sucrose (■) to inhibit clathrin mediated endocytosis, and nystatin (□) to inhibit caveolae mediated lipid-raft endocytosis. Data was normalized to the results of cell viability tests involving AuNP-J52 with no inhibitors. From this we were able to effectively deduce percent inhibition. The effect at 4°C is greatest since it limits all active transport, and additionally it is the only variable that loses inhibition at higher concentrations. The variance in inhibition percentage at higher concentrations is explained when one considers that AuNPs will aggregate at low temperatures which may be inducing further cell death or different nanoparticle behavior. MβCD is the most efficient inhibitor of internalization and is likely the main pathway for our AuNP platforms. Sucrose internalization has been shown to be size dependent for similar AuNPs and is the second best inhibitor for particles of our size. Nystatin, inhibiting only a fraction of total lipid-raft formation, resulted in the lowest rate of internalization inhibition.*

5.7 References

[1] Gu, F. X. *et al.* Targeted Nanoparticles for Cancer Therapy. *Nano Today* **2,** 14–21 (2007).

[2] Brigger, I., Dubernet, C. & Couvreur, P. Nanoparticles in Cancer Therapy and Diagnosis. *Adv. Drug Deliv. Rev.* **64,** 24–36 (2012).

[3] Alexis, F., Pridgen, E. & Molnar, L. K. Factors Affecting the Clearance and Biodistribution of. *Mol. Pharm.* **5,** 505–515 (2008).

[4] Sarin, H. Physiologic Upper Limits of Pore Size of Different Blood Capillary Types and Another Perspective on the Dual Pore Theory of Microvascular Permeability. *J. Angiogenes. Res.* **2,** 1–19 (2010).

[5] Cho, K., Wang, X., Nie, S., Chen, Z. & Shin, D. M. Therapeutic Nanoparticles for Drug Delivery in Cancer. *Clin. Cancer Res.* **14,** 1310–1316 (2008).

[6] Yuan, F. *et al.* Vascular Permeability in a Human Tumor Xenograft: Molecular Size Dependence and Cutoff Size1. 3752–3757 (1995).

[7] Jain, R. K. Transport of Molecules, Particles, and Cells in Solid Tumors. *Annu. Rev. Biomed. Eng* **01,** 241–263 (1999).

[8] Jain, R. K. Delivery of Molecular Medicine to Solid Tumors: Lessons from In Vivo Imaging of Gene Expression and Function. *J. Control. Release* **74,** 7–25 (2001).

[9] Gao, X., Cui, Y., Levenson, R. M., Chung, L. W. K. & Nie, S. In Vivo Cancer Targeting and Imaging with Semiconductor Quantum Dots. *Nat. Biotechnol.* **22,** 969–976 (2004).

[10] Tuerk, C. & Gold, L. Systematic Evolution of Ligands by Exponential Enrichment: RNA Ligands to Bacteriophage T4 DNA Polymerase. *Science* **249,** 505–510 (1990).

[11] Ellington, Andrew D., J. W. S. In Vitro Selection of RNA Molecules that Bind Specific Ligands. *Nature* **346,** 818–821 (1990).

[12] Robertson, D. L. & Joyce, G. F. Selection In Vitro of an RNA Enzyme that Specifically Cleaves Single-Stranded DNA. *Nature* **344,** 467–468 (1990).

[13] Jayasena, S. D. Aptamers: An Emerging Class of Molecules that Rival Antibodies in Diagnostics. *Clin. Chem.* **45,** 1628–1650 (1999).

[14] White, R. *et al.* Generation of Species Cross-Reactive Aptamers using 'Toggle' SELEX. *Mol. Ther.* **4,** 567–574 (2001).

[15] Sundaram, P., Kurniawan, H., Byrne, M. E. & Wower, J. Therapeutic RNA Aptamers in Clinical Trials. *Eur. J. Pharm. Sci.* **48,** 259–271 (2013).

[16] Cao, Z. *et al.* Reversible Cell-Specific Drug Delivery with Aptamer-Functionalized Liposomes. *Angew. Chemie - Int. Ed.* **48,** 6494–6498 (2009).

[17] Wu, Y., Sefah, K., Liu, H., Wang, R. & Tan, W. DNA Aptamer-Micelle as an Efficient Detection/Delivery Vehicle Toward Cancer Cells. *Proc. Natl. Acad. Sci.* **107,** 5–10 (2010).

[18] Gao, L. *et al.* Selective Recognition of Co-assembled Thrombin Aptamer and Docetaxel on Mesoporous Silica Nanoparticles Against Tumor Cell Proliferation. *Chem. - A Eur. J.* **17,** 13170–13174 (2011).

[19] Aravind, A. *et al.* AS1411 Aptamer Tagged PLGA-lecithin-PEG Nanoparticles for Tumor Cell Targeting and Drug Delivery. *Biotechnol. Bioeng.* **109,** 2920–2931 (2012).

[20] Wu, J. *et al.* Nucleolin Targeting AS1411 Modified Protein Nanoparticle for Antitumor Drugs Delivery. *Mol. Pharm.* **10,** 3555–3563 (2013).

[21] Farokhzad, O. C. *et al.* Targeted Nanoparticle-Aptamer Bioconjugates for Cancer Chemotherapy In Vivo. *Proc. Natl. Acad. Sci.* **103,** 6315–6320 (2006).

[22] Yang, X. *et al.* Near-Infrared Light-Triggered, Targeted Drug Delivery to Cancer Cells by Aptamer Gated Nanovehicles. *Adv. Mater.* **24,** 2890–2895 (2012).

[23] Luo, Y. L., Shiao, Y. S. & Huang, Y. F. Release of Photoactivatable Drugs from Plasmonic Nanoparticles for Targeted Cancer Therapy. *ACS Nano* **5,** 7796–7804 (2011).

[24] Wang, J. *et al.* Assembly of Aptamer Switch Probes and Photosensitizer on Gold Nanorods for Targeted Photothermal and Photodynamic Cancer Therapy. *ACS Nano* **6,** 5070–5077 (2012).

[25] Sundaram, P., Wower, J. & Byrne, M. E. A Nanoscale Drug Delivery Carrier Using Nucleic Acid Aptamers for Extended Release of Therapeutic. *Nanomedicine Nanotechnology, Biol. Med.* **8,** 1143–1151 (2012).

[26] Cao, X., Ye, Y. & Liu, S. Gold Nanoparticle-Based Signal Amplification for Biosensing. *Anal. Biochem.* **417,** 1–16 (2011).

[27] Hirsch, L. R. *et al.* Nanoshell-Mediated Near-Infrared Thermal Therapy of Tumors Under Magnetic Resonance Guidance. *Proc. Natl. Acad. Sci.* **100,** 13549–13554 (2003).

[28] Yavuz, M. S., Cheng, Y., Chen, J., Cobley, C. M. & Zhang, Q. Gold Nanocages Covered by Smart Polymers for Controlled Release with Near-Infrared Light. *Bio Protoc.* **8,** 935–939 (2009).

[29] Kang, H. *et al.* Near-Infrared Light-Responsive Core-Shell Nanogels for Targeted Drug Delivery. *ACS Nano* **5,** 5094–5099 (2011).

[30] Sandström, P., Boncheva, M. & Åkerman, B. Nonspecific and Thiol-Specific Binding of DNA to Gold Nanoparticles. *Langmuir* **19,** 7537–7543 (2003).

[31] Hurst, S. J., Lytton-Jean, A. K. R. & Mirkin, C. A. Maximizing DNA Loading on a Range of Gold Nanoparticle Sizes. *Anal. Chem.* **78,** 8313–8318 (2006).

[32] Hortobagyi, G. N. Anthracyclines in the Treatment of Cancer. (1997).

[33] Li, Y. & Monteiro-Riviere, N. A. Mechanisms of Cell Uptake, Inflammatory Potential and Protein Corona Effects with Gold Nanoparticles. *Nanomedicine* **11,** 3185–3203 (2016).

[34] Quigley, G. J. *et al.* Molecular Structure of an Anticancer Drug-DNA Complex: Daunomycin Plus d(CpGpTpApCpG). *Proc. Natl. Acad. Sci. U. S. A.* **77,** 7204–7208 (1980).

[35] Alexandrov, B. S. *et al.* DNA Breathing Dynamics Distinguish Binding from Nonbinding Consensus Sites for Transcription Factor YY1 in Cells. *Nucleic Acids Res.* **40,** 10116–10123 (2012).

[36] Rejman, J., Oberle, V., Zuhorn, I. S. & Hoekstra, D. Size-Dependent Internalization of Particles via the Pathways of Clathrin- and Caveolae-Mediated Endocytosis. *Biochem. J.* **377,** 159–169 (2004).

[37] Giljohann, D. A. *et al.* Gold Nanoparticles for Biology and Medicine. *Angew Chem Int Ed Engl* **49,** 3280–3294 (2010).

[38] Evans, E. R., Bugga, P., Asthana, V. & Drezek, R. Metallic Nanoparticles for Cancer Immunotherapy. *Mater. Today* **21,** 673–685 (2018).

[39] Libutti, S. K. *et al.* Phase I and Pharmacokinetic Studies of CYT-6091, a Novel PEGylated Colloidal Gold-rhTNF Nanomedicine. *Clin. Cancer Res.* **16,** 6139–6149

(2010).

[40] Mirkin, C. A., Letsinger, R. L., Mucic, R. C. & Storhoff, J. J. A DNA-Based Method for Rationally Assembling Nanoparticles into Macroscopic Materials. *Nature* **382,** 607–609 (1996).

[41] Storhoff, J. J., Elghanian, R., Mirkin, C. A. & Letsinger, R. L. Sequence-Dependent Stability of DNA-Modified Gold Nanoparticles. *Langmuir* **18,** 6666–6670 (2002).

[42] Unsworth, L. D., Sheardown, H. & Brash, J. L. Protein-Resistant Poly(ethylene oxide)-Grafted Surfaces: Chain Density-Dependent Multiple Mechanisms of Action. *Langmuir* **24,** 1924–1929 (2008).

[43] Balamurugan, S., Obubuafo, A., McCarley, R. L., Soper, S. A. & Spivak, D. A. Effect of Linker Structure on Surface Density of Aptamer Monolayers and their Corresponding Protein Binding Efficiency. *Anal. Chem.* **80,** 9630–9634 (2008).

[44] Lao, Y. H., Peck, K. & Chen, L. C. Enhancement of Aptamer Microarray Sensitivity through Spacer Optimization and Avidity Effect. *Anal. Chem.* **81,** 1747–1754 (2009).

[45] Hua, X., Zhou, Z., Yuan, L. & Liu, S. Selective Collection and Detection of MCF-7 Breast Cancer Cells Using Aptamer-Functionalized Magnetic Beads and Quantum Dots Based Nano-bio-probes. *Anal. Chim. Acta* **788,** 135–140 (2013).

[46] Cheng, A. K. H., Su, H., Wang, Y. A. & Yu, H. Aptamer-Based Detection of Epithelial Tumor Marker Mucin 1 with Quantum Dot-Based Fluorescence Readout. *Anal. Chem.* **81,** 6130–6139 (2009).

[47] Jeddi, I. & Saiz, L. Three-Dimensional Modeling of Single Stranded DNA Hairpins for Aptamer-Based Biosensors. *Sci. Rep.* **7,** 1–13 (2017).

[48] Dassie, J. P. Systemic Administration of Optimized Aptamer-siRNA Chimeras Promotes Regression of PSMA-Expressing Tumors. **134,** 1–10 (2009).

[49] White, R. J., Phares, N., Lubin, A. A., Xiao, Y. & Plaxco, K. W. Optimization of Electrochemical Aptamer-Based Sensors via Optimization of Probe Packing Density and Surface Chemistry. *Langmuir* **24,** 10513–10518 (2008).

[50] Akinc, A. & Battaglia, G. Exploiting Endocytosis for Nanomedicines. *Cold SPring Harb Perspect Biol* **5,** (2013).

Chapter 6: Conclusions

The goal of the research presented in this dissertation was to develop nucleic acid-based tools for precision medicine. First, it was important to study what has already been done with nucleic acids and what issues are in the most need to be addressed. The two main issues with nucleic acid drug and targeting platform development is the instability of their structure and susceptibility to degradation *in vivo*.

SELEX, the main method for developing nucleic acid therapeutic tools called aptamers, has several issues that are slowly being fixed with time. Limits to the complexity of a structure that can form based on sequences not being truly "random" is still a work in progress. For example, a nucleic acid strand will start to take a structure while it is still being extended with nucleotides during the process of creating the large library at the first step of SELEX. Because this happens, nucleotides that will be placed sequentially will favor a particular nucleotide that will lower the overall complexity of the structure and Gibbs free energy. As one understands this behavior, certain nucleotide positions along a nucleic acid strand based on its length can be pinpointed and specific nucleotide can be forced into these positions by the researcher. Understandingly entirely the potential for how to locate these positions and which nucleotides to insert is still an on-going process.

There are several more issues with SELEX that were analyzed and addressed at the beginning of this document, most of these deal with the fact that post modifications, necessary for stabilization of an aptamer *in vivo*, can potentially reduce efficacy of the original aptamer or even stop functionality entirely. Other concerns involve the use primers, one issue being the sequence might have an impact on functionality, and another

being there presence might block potential targets that favor binding to the ends of an aptamer. Certain types of structures that take similar shapes to a “lollipop” are also inhibited from forming to some degree because of the location of primers being on the 5’ and 3’ ends of an aptamer being developed. However, on a brighter note, new discoveries with using endonuclease cleave site based primers are currently becoming more wide spread to help reduce this problem of aptamers developed even just a few years ago. Next gen technology is also improving the SELEX process and new issues introduced from this approach, such as handles, are also becoming more aware and researchers are actively seeking new developmental methods to alleviate these problems.

This work presetned how thermodynamics, in particular Gibbs free energy, can be used to indicate structural changes of DNA and determine how salts, solvents, and DNA proximity based on concentration effect this value. Furthermore, modifications to nucleic acids were studied that can be used to increase resistance to degradation as well as attach nucleic acids to gold nanoparticles. The use of a gold nanoparticle can help reduce degradation of DNA, while providing a stable platform for nucleic that can reduce the amount of modifications necessary for delivery *in vivo*, therefore, protecting structure and function.

It is important to understand how DNA and RNA these molecules stabilize themselves, such as base stacking for ssDNA and hybridization at sites that optimize G-C and A-T base pairs. Secondary structures such as hairpins, help align as many of these ideal base pairs and lower Gibbs free energy overall, but require some energy themselves during formation. Computer models can be used to calculate Gibbs free energy, which in

turn, indicates the likelihood of a particular nucleic structure existing in a specific environment, mostly based on type of salt and concentration.

The third chapter of this dissertation takes the information gathered to this point and begins applying it to an experiment of my own design. This begins with attempting to develop a nucleic acid platform. The plan was to engineer a DNA anchor strand binding with a HEMA gel, to an RNA developed aptamer already on the market. Therefore, the goal was to design an RNA linker strand to connect these two strands, anchor and aptamer, to each other. First, it is important to note that the reason the anchor and aptamer cannot be connected with each other directly is because of the mechanism for release of the aptamer. This aptamer is designed to treat an ocular disease, and since the platform is based on the surface of the eye, the goal was to design a release mechanic based on the tear fluid of the eye. Because the aptamer needs to be fully modified to prevent degradation, it cannot be degraded and release naturally from biological components in the tear fluid.

It is possible to create a short cleavage site that is recognized by the only RNase present in the tear fluid of the eye, RNase 4, and simply attach that sequence to the modified aptamer by a ligase enzyme. This would in theory eliminate the need for a linker strand. However, this short sequence would need to be modeled specifically for this one particular aptamer and would therefore only be applicable for this one situation. One of the goals of this nucleic acid based platform was to create a general setup that can quickly be adapted and applied to multiple types of aptamers that may be potentially developed in the future for ocular disease treatment. This is the main reason why a linker strand was chosen to be made and to assemble the nucleic acid platform in this manner.

Engineering this nucleic acid platform required understanding of linear nucleotide sequence dictating structure, which dictates function. The final sequence selected for the aptamer is highly sensitive to structural change. Even changing just one nucleotide at almost any position drastically affects the delicate balance of desired reactions to undesired ones at the high ratio currently obtained. There were several considerations that restricted the design and computer model simulations were tested repeatedly dozens, if not hundreds of times, to get the Gibbs free energy values shown at a significantly higher amount for the desired reaction, compared to all the undesired ones.

The linker strand had to hybridize to both the anchor and aptamer with a particular strength that would allow it to potentially separate at eye temperatures, but at low amounts, while at the same time controlling the cleavage site for the endonuclease to a single location. Structurally, the linker needed to be designed not to hybridize with itself, either intra or intermolecularly, while only hybridizing in the appropriate locations with the anchor and aptamer. The binding with the aptamer even had an additional condition in that the hybridization could not affect its structure, which could alter its function.

After finally assembling this structure and creating the RNA strands by transcription in the lab, the complex was confirmed to be homogeneous, meaning only one size variation is being built, as seen on a non-denaturing polyacrylamide gel. At this point the compatibility of DNA was tested with a common contact lens formulation and basic tests on manipulation of the HEMA gel components were done to see the feasibility on controlled release of the nucleic acids from this approach. These studies showed that the nucleic acids are indeed compatible in a HEMA gel and different aspects of the gel

can also be changed to modulate release of nucleic acids. The experiments fulfilled this purpose and therefore continued experimentation to optimize the gel was not required, as it is out of the scope of the nucleic acid science. This project showed that there is potential for aptamer development and use in ocular therapeutics via surface modalities.

There was also discussion on various types of nanoparticles and how nucleic acids can be implemented into platforms combining the two. Nanoparticles are a great way to add more functions to nucleic acids without altering their already sensitive structures. For example, detection can be an added function from the incorporation of a nanoparticle. Furthermore, multiple nucleic acids can be grouped together, this can improve their affinity using an effect called avidity, plus it allows for either drug carrying or targeting nucleic acids to be combined together into one platform without having to create one nucleic acid strand capable of all of these functions.

Gold nanoparticles were chosen to be combined with nucleic acids because of their detection capabilities, little to no toxicity *in vivo*, and already well characterized behavior with nucleic acids taking advantage of work already done by other researchers. A thiol bond can be cheaply and easily modified onto a DNA strand for covalent binding to the gold surface. The surface plasmon resonance effect of gold nanoparticles even allows for confirmation of DNA functionalization to the surface just from the naked eye. Protocols for maximizing DNA loading onto gold surfaces have already been developed, and these also account for purity of the sample and reducing loss of materials by monitoring aggregation of nanoparticles, which is not desired.

Even with all of these great studies, however, there is still unknown behavioral phenomenon between nucleic acids and gold surfaces, especially the effect of density of

aptamers on binding, not everything has yet been studied leaving an opportunity for someone to further study DNA and gold interactions. Having learned a lot about nucleic acid behavior and what effects structure, it was realized that this is an important issue that needs to be understood before experimenting with nucleic acids and gold nanoparticles. Thus, before beginning experiments attaching nucleic acids to nanoparticles, a quartz crystal microbalance with energy dissipation was used to investigate behavior of DNA with gold surfaces and how density of binding may effect structure and reduce binding of nucleic acids. Salt and DNA concentration, as well as time of exposure of DNA to gold surface, will all impact binding quantity and conformation of DNA, and these properties were analyzed.

The QCM works with a variety of SAMs and has one of the lowest detection limits and shortest measure times, but most importantly it offers real-time analysis. Flow rate of sample can be controlled, multiple samples can be performed at the same time, and its interface is compatible with other technology. Detection is highly sensitive, in that it can even track cell adhesion in real time, plus the signal can be amplified or reduced in the presence of other materials at the discretion of the researcher.

The QCM outputs frequency, which is then used to calculate mass, and dissipation, used to determine conformational changes in nucleic acids bound to the surface. After reviewing literature, the Sauerbrey equation was determined to be the best model for the anchor DNA hybridized with dsDNA and drug complex being assembled on the gold sensor from these experiments. The frequency and dissipation values also registered within the ranges necessary to confirm that this model is appropriate for our

system as well. This particular Sauerbrey model for non-dissipative response is indicative of a thin, rigid, homogeneous film layer on the gold sensor surface.

Several experiments were performed using the Q-sense, real-time binding analysis of dsDNA and Klenow reaction, quantification of anchor and dsDNA binding, effect of flow rate on nucleic acid binding, quantification of Daunomycin loading, and its effect on energy dissipation. First, real-time binding analysis based on frequency was able to determine mass of both anchor and dsDNA bound to the gold sensor surface, with peaks being clearly visible when each one bound. The mass was found to be 295ng/cm^2 and 580ng/cm^2 respectively. Number of anchors and aptamers bound to the sensor surface can then be calculated by using known values: molecular weight of anchor DNA is 6.13 kg/mol, molecular weight of dsDNA is 34.17 kg/mol, Avogadro's number is $6.022*10^{23}$ molec/mol, and surface area of the sensor is 0.9677 cm^2. The number of anchors bound is calculated to be $2.80*10^{17}$, and aptamers $9.89*10^{36}$, meaning there are ~2.84 anchors per aptamer bound on the surface. This number helps understand the limitations of dsDNA hybridization to the anchor under current salt and DNA concentrations, as well surface area available for binding.

Flow rate speed had an effect on the number of DNA strands bound and the ratio of anchor to dsDNA. When the flow rate speed was increased 10 times faster, it was found that the number of anchors bound was $1.38*10^{37}$ and dsDNA was $5.71*10^{36}$ with the ratio of anchor to dsDNA being ~2.41. This indicates that increased flow rate (and reduced exposure time to the sensor surface as a result) causes a reduction in the amount of DNA strands bound. Anchor was reduced by more than half (1/2.03), but dsDNA was affected less with a reduction less then half (1/1.73). The lower ratio of anchor to dsDNA

indicates that a faster flow rate improves the correlation between anchor and dsDNA, but most likely this improvement was because of lower density between samples since approximately half the total amount of DNA bound to the sensor compared to the slower flow rate.

Interestingly, the extension of the dsDNA with the Klenow enzyme was detected in real-time on the Q-sense. This is shown by the fact that after washing the sensors, the mass for the Klenow reacted sample only decreased slightly, while the sample not containing the enzyme had its mass decrease dramatically. The decrease in mass is a result of free nucleotides being washed out of the sensor environment. The sample containing the Klenow enzyme maintained this mass because the free nucleotides were incorporated into the dsDNA due to the reaction and therefore less mass was lost in when the sample solutions were washed away.

Another aspect to consider is the amount of Daunomycin binding and the effect of its binding on the conformation of the DNA. Daunomycin can interact with DNA by multiple mechanisms, but most significantly via intercalation. However, if the concentration of Daunomycin is excessive, the gradient force can cause weaker binding to DNA other then intercalation as well as other factors such as ionization and crowding from a high-density environment. These factors were tested by comparing Daunomycin binding on anchor DNA with dsDNA. Our results indicated that more Daunomycin is interacting with the sensor surface for dsDNA then anchor DNA only, but not by much, only about 16% increase. After washing, this is when the differences become more apparent between the two samples.

It is important to remember that the anchor only sample binds more DNA then the dsDNA sample; so therefore, it is necessary to convert to drug per complex when comparing the two samples. Once this is considered it can be seen that the dsDNA does indeed bind more drug then the anchor only sample. The slower flow rate binds 30.5 times more daunomycin on its dsDNA sample compared to the anchor only sample, while the faster flow rate only binds 2.67 times more drug on its dsDNA sample. This shows that the faster flow rate is affecting Daunomycin's ability to bind to the DNA more so then the slower flow rate indicating that either flow rate or exposure time influences Daunomycin binding. The faster flow rate bound slightly more Daunomycin per dsDNA complex then the slower flow rate, 27.6 v 23.5 respectively, but since the slower flow rate binds 1.73 times more DNA, it still bound more total drug overall.

During this experiment another intriguing phenomenon was noticed, the release profile of the drug during the wash step. Daunomycin bound to the dsDNA sample washed away more slowly then the anchor only sample. This is not because of there was more drug bound to the dsDNA sensor either because that is not the case. Since the anchor only sample binds more DNA to its surface, the amount of drug bound only differed by ~16% as already explained previously. The drastic change in the release profile between these two samples must be due to the mechanism of binding being different. In order to check mechanism binding, conformation change in DNA was tracked using energy dissipation.

The faster flow rate only had a difference of 2.67 more drugs per complex, therefore, no significant difference in dissipation between the two samples was found unfortunately. However, the slower flow rate showed a drastic difference in dissipation

during its binding of 30.5 times more Daunomycin for dsDNA compared to the anchor only sample. This difference in dissipation means that a conformational change has occurred within the DNA because the film layer characteristics have shifted. Since no change is seen for the anchor only sample, the mechanism for Daunomycin must be interacting with the already existing conformation of the DNA without altering to a noticeable amount. The dsDNA sample, on the other hand, must be performing some reaction with Daunomycin that causes structural change with the DNA, for example intercalation. All of the data is in agreement with this analysis. Understanding this behavior will provide insight to how the DNA may behave for both anchor only, and dsDNA when comparing results with gold nanoparticles moving forward.

Next, the nanoparticle platform was further explored. Four main experiments were performed: characterization of nanoparticle size, Daunomycin binding affinity to various dsDNA sequences, drug release rates and quantification from DNA coated gold nanoparticles, and cell internalization studies and cell viability.

Gold nanoparticle plus dsDNA size can be theoretically calculated, and then dynamic light scattering can determine the actual measured size based on using the Stokes-Einstein equation. The results indicated that the measured nanoparticle sizes were only a few nanometers larger then theoretical amounts. These values are within expected results when accounting for the fact that DNA in a dense environment will tend to stretch due to repulsion forces from neighboring negative charges. DLS also showed peaks and with width indicated that samples were mostly homogeneous. Salt and DNA concentrations were optimized until DLS results showed closer and closer diameter sizes to expected values and thickness of peak began to shrink.

After this optimized protocol was developed, using these salt concentrations for free dsDNA strands without the presence of gold nanoparticles, Daunomycin affinity was tested against four different DNA strands that each varied a triplicate sequence known to be the best for intercalating Daunomycin. These strands were, in expected order from worse to best: *L52* – no triplicate sequence, *J52* – triplicate sequence all on one of the two DNA strands, *M52* – half of one DNA strand was the triplicate sequence, then the other half was staggered between the two DNA strands, and *H52* – triplicate sequence was staggered entirely between two strands.

After quantification of drug per DNA complex and using the Hill equation to determine binding affinity, *L52* had the lowest affinity as expected, but surprisingly *J52* had the highest. In an attempt to discover why *M52* and *H52* did not perform as well as expected, computer models showed that these two sequences were highly likely to have intramolecular interactions with themselves. This would reduce the amount of dsDNA complexes in these samples, and since the affinity calculations assumed that 100% of the DNA was forming the desired dsDNA complex, this resulted in lower affinity values. The palindromic nature of the *M52* and *H52* sequences make it nearly impossible to completely eradicate the intramolecular interactions. Several hybridization methods involving slow cooling and varying temperatures before placing on ice helped reduce these unwanted reactions to a better degree then initial results, but even the final results shown in this chapter still had some of these intramolecular interactions occurring.

Next, it was decided to test these four sequences on a gold nanoparticle and determine which platform bound the most drugs per particle and has the most desired release rate profile. Agreeing with the previous data, J52 bound the most drugs per

particle with 1449 (± 237), however, after this the data was different. *L52* bound 1156 (± 35), *H52* 1073 (± 32), and *M52* 1038 (± 40). Why is it that *M52* and *H52* bound fewer drugs per particle then *L52* when bound to nanoparticles? It was noticed that *M52* and *H52* always appeared to have some nanoparticle aggregation that could be broken up when vortexing, but would reappear if samples were allowed to sit, this was not seen for *L52* and *J52*. This slight aggregation with portions of these samples would explain why these platforms have fewer drugs per particle then *L52* because the quantification calculation assumed that all of the nanoparticles were separate entities fully soluble in the salt solution, but why do these two platforms aggregate?

Once again turning to computer models it can be seen that *M52* and *H52* are much more likely to have intermolecular interactions with neighboring strands then *L52* and *J52*. Since the double stranded region on the nanoparticles was created with the Klenow enzyme, as opposed to already existing as it was in the previous data without nanoparticles, it is possible that during the hybridization process, *M52* and *H52* preferred to hybridize with other strands from neighboring nanoparticles. One strand alone would be a weak enough reaction to break these particles apart, but due to the avidity effect, if dozens of these strands on two neighboring nanoparticles performed intermolecular interactions, these reactions may be too strong to break apart. This then causes some nanoparticle aggregation as a result.

These nanoparticles then underwent release rate testing using a dialysis membrane. The release rates performed from best to worst in the same order as the quantity of drug bound to each platform that was just described. It is desired to incubate these nanoparticles with breast cancer cells for 4h; therefore, this time point was the

focus of discussion. *J52* released only 52% (± 2.7) of drug after 4h, followed by *L52* 57% (± 1.3), *H52* 75% (± 0.8), and *M52* 81% (± 3.3). Furthermore, *J52* only released 75% of its drug content after 24h. It is important that as much of the drug remains on the nanoparticles as possible to increase the local drug concentration when performing the cell viability tests; therefore *J52* having the most drugs per particle and slowest release rate is expected to kill the most breast cancer cells.

Bare nanoparticles and anchor only gold nanoparticles were also quantified for drug per particle and release rate checked to see how they would compare to the dsDNA nanoparticle platforms. Bare nanoparticles showed 117 (± 3) drugs per particle with a 98% release rate after only 1h. Anchor nanoparticles showed 966 (±7) drugs per particle with a release rate of 89% (±3.9) after 4h. The amount of drug bound to bare nanoparticles after three washes is most likely excess drug still remaining in the solution that could not be properly removed without risking losing nanoparticle sample.

Since these nanoparticles went through the same process as the DNA nanoparticle platform samples, it can be assumed that those samples have approximately the same amount of drug not technically bound to them. However, because the drug is still located inside of the solution, it will be exposed to the breast cancer cells, therefore, it would be inaccurate to subtract this number when determining concentration of drug exposed to the cancer cells. The anchor only sample bound fewer drugs per particle then all of the DNA nanoparticle platforms, but it was not much lower, therefore it is important to ask why is the dsDNA platform necessary. The answer has to do with the release rate profile. Just as the bare nanoparticles released nearly all of its drug in 1h, the anchor only samples

released 89% after 4h. Compare this to *J52*, which released only 52% in the same amount of time.

All of the dsDNA nanoparticle platforms had slower release rates. This will greatly impact the efficacy of the anchor only platform in killing cancer cells. Indeed, experimental data comparing all four dsDNA nanoparticle samples plus the anchor only sample on breast cancer cells at the same drug concentration consistently showed that the anchor only sample performed the worst at killing the cells. Since the drug concentration was matched, the anchor only samples had more gold nanoparticles with the cancer cells because it had the fewest drugs per particle. Furthermore, it was already shown from the Q-sense data that the anchor only samples bind Daunomycin with a different mechanism then the dsDNA and these release rate results agree with those findings. *J52* also killed the cancer cells better then the other platforms, agreeing with all the other data, when each of the samples were tested at the same drug concentrations with the cells.

All of the nanoparticle platforms killed more cancer cells then free drug of equivalent concentrations, controls with no drug showed no cell death. This means that the DNA coated nanoparticles are a better method for killing breast cancer cells in an *in vitro* environment. Since *J52* performed the best, Daunomycin loaded J52 nanoparticles were then subjected to cell internalization studies in order to determine how they were entering the cells. Three different mechanisms of internalization were inhibited: all lipid-raft endocytosis, clathrin-mediated endocytosis, and caveolae mediated lipid-raft endocytosis. All lipid-raft endocytosis demonstrated the highest amount of inhibition (~65%), meaning that this mechanism is the main entry pathway for the DNA coated

nanoparticles to enter breast cancer cells. This agrees with other literature performing experiments with gold nanoparticles and negative charged ligands of a similar size.

Clathrin-mediated endocytosis was second best of the three with ~55% inhibition. Studies in literature have shown that clathrin-mediated endocytosis is the most sensitive of these three pathways to particle size. As particle size decreases, this pathway will become more dominant. The caveolae mediated lipid-raft endocytosis had an inhibition rate of ~33%. This is still a good amount of nanoparticles entering through this pathway, revealing that all three of these mechanisms are responsible for nanoparticles getting inside the breast cancer cells, but at varying degrees. A temperature of 40^0C was also tested and since this inhibits all metabolic pathways, it showed more inhibition then the three pathways with a rate of ~79%.

This work presented a novel platform for potentially treating breast cancer cells better then current chemotherapeutic treatments. Work began with learning about nucleic acid as a tool for precision medicine and potential for integrating additional functionalities via a nanoparticle. From here, understanding how to engineer nucleic acids and their behavior as a result of their environment was learned and tested in a platform by itself. Then analysis of nucleic acid interactions with gold surfaces was analyzed and characterized, before finally testing DNA combined with gold nanoparticles.

The novel platform developed in this dissertation showed an increase in efficiency for killing breast cancer cells compared to free drug. This project laid the groundwork and foundation for developing a versatile, and “smarter” therapeutic treatment platform for cancer. Nucleic acids indeed have great potential to be used for cancer treatment. In

the future, nucleic acids may be engineered for personalized cancer therapy based on an exact tumor profile relating to specific patients, leading to more efficacious therapy.